Studies of Zinc Oxide Nanocrystals: Quantification of Capping Ligands and the Coupling of Protons and Electrons

Carolyn N. Valdez

A dissertation

submitted in partial fulfillment of the

requirements for the degree of

Doctor of Philosophy

University of Washington

2015

Reading Committee:

James M. Mayer, Chair

Daniel R. Gamelin

Brandi M. Cossairt

Lilo D. Pozzo

Program Authorized to Offer Degree:

Chemistry

University of Washington

Abstract

Studies of Zinc Oxide Nanocrystals: Quantification of Capping Ligands and the Coupling of Protons and Electrons

Carolyn N. Valdez

Chair of the Supervisory Committee:
Professor James M. Mayer
Department of Chemistry

The energetics of semiconductors are widely relevant to technologies ranging from chemical- and photo-catalysis to charge injection in photovoltaic materials. In these processes involving electron transfer, protons often play a critical but overlooked role in facilitating charge transfer. For example, the conduction band energies of most metal oxides in contact with an aqueous solution demonstrate a Nernstian pH dependence, an observation that cannot be explained by surface protonation models. Given that a Nernstian dependence is typically attributed to proton coupled electron transfer (PCET), we are interested in determining if the reduction of metal oxides can also be described by PCET. Zinc oxide (ZnO) nanocrystals (NCs) were chosen as a model system given the broad range of previous research on bulk and nanocrystalline forms of

ZnO, the relative ease of synthesis and characterization, and their use in developing a fundamental understanding of interfacial electron transfer. We demonstrate that photochemically reduced NCs react with hydrogen-atom acceptors, indicating that both electrons and protons are transferred by the NCs. To isolate the influence of a proton coupled to the extra electron in the conduction band, the NCs have also been reduced chemically. Addition of an excess of the one-electron reductant $CoCp^*_2$ (Cp* = pentamethylcyclopentadienyl, -1.94 V vs. Fc/Fc^+) gives NCs that contain extra electrons in the conduction band, without protons that arise from photoreduction. Protons can also be individually added stoichiometrically to the NCs by either a photoreduction/oxidation sequence or by addition of acid. Using these methods, we have shown that the presence of one extra proton drastically alters the redox potential of the NCs. With the addition of acid the NC orbitals are lowered, allowing the systematic variation of driving force for electron transfer from the reductant to the NCs. In the presence of excess reductant and acid, the number of electrons per NC ($<n_{e^-}>_{max}$) reaches a maximum, beyond which the addition of more acid has no effect. This $<n_{e^-}>_{max}$ varies with the NC radius with an r^3 dependence, so the density of electrons ($<N_{e^-}>_{max}$) is constant over a range of NC sizes. The approximately 1:1 relationship of $<n_{e^-}>$ with protons per NC, and the dramatic dependence of $<N_{e^-}>_{max}$ on the nature of the cation (H^+ vs. $MCp^*_2{}^+$) suggest that the protons intercalate into the NCs under these conditions. These studies illustrate the strong coupling between protons and electrons in ZnO NCs and show that proton activity is a key parameter in nanomaterial energetics.

TABLE OF CONTENTS

LIST OF FIGURES

LIST OF SCHEMES

LIST OF TABLES

ACKNOWLEDGMENTS

Putting together this thesis and working for these past five years were equal parts transformative and trying experiences. But just like raising kids, it takes a village, and I owe so many people thanks for their help and encouragement.

I have to start by thanking my adviser Professor Jim Mayer. When I first joined the group, Jim immediately treated me as an equal even though I had (and have) so much to learn from him. He is one of the smartest people I have ever met, but cares about his students with a passion that seems endless. In our day to day interactions, his passion for science flows out of him at a high pace, but he always takes the time to ask about our day and respond to our needs. Jim was there to push me when I was distracted, offer encouragement when I felt like I didn't deserve to be in graduate school, and does a spectacular job at his primary role being a scientific partner in the development of my research. It has been a pleasure to work with Jim, and I will forever appreciate his mentorship and friendship.

I also have to thank my undergraduate research advisers, Professors Harry Gray (Caltech) and Jillian Dempsey (UNC Chapel Hill). My first year in college was filled with absolute confusion and so much catching up with my peers. Harry gave me a place to work and made me feel like I could accomplish anything. Jillian is probably the reason that I am in science today. She taught me many specific skills in the laboratory and to work hard for what I want. Jillian is a spectacular mentor and individual. Harry and Jillian took the time to teach, encourage, and promote me as a scientist even when I was an absolute beginner. I wouldn't be here without them.

I also have to thank Lee Syer, my chemistry teacher in high school. Lee enchanted me with stories of his experiments (explosions) as a kid and encouraged me to apply to a summer program at Caltech and to take the SAT's. Without him, I may not have gone to college, and I certainly wouldn't be finishing my thesis.

To my committee members, Professors Brandi Cossairt, Lilo Pozzo, Xiaosong Li, and Daniel Gamelin. Thank you for your guidance and assistance getting me to this point. I know that you're already such intensely busy and overworked, but I have appreciated all of the time that you have spent with me.

At the University of Washington, I had the privilege to work and befriend many brilliant and beautiful scientists including Kate Allen, Shoshanna Barnett, Johanna Blacquiere, Miriam Bowring, Colin Carver, Michael Coggins, Alicia Cohn, Ben Glassy, Ellen Hayes, Rebecca Hayoun, David Lao, Elizabeth Mader, Todd Markle, Brad McKeown, Alex Miller, Mike Pegis, Tom Porter, Mitsuhashi Ryoji, Ian Rhile, Carlos Rodriguez del Rio, Alina Schimpf, Joel Schrauben, Adam Tenderholt, Chih-Chin Tsou, Derek Wasylenko, and Jessica Wittman. Joel Schrauben really helped to get this project started, and is so calm and intelligent. Thank you as well to Paul Miller for help and humor in running experiments on the ICP and NMR spectrometers - if someone could get it done - it was him. To the undergrads that I had the pleasure of mentoring, Ashley Soria, Margaux Pinney, and Hayli Larsen, it was a rewarding experience to help you to understand science and work with you in the lab. You taught me to think carefully about my own science, challenged me to truly understand how things work, and enriched my experience as a scientist.

There are a few other individuals who stick out in my mind at UW as people that I have forged especially strong relationships and really helped to shape me into who I am today. Caroline Saouma was a force in the lab, on a bike rides, and as a human being. I admire her for her passion for science, for baking, and for people. To David Lao, for teaching me so many practical skills in the laboratory and for being such a generous soul. To Tristan Tronic, for being a calm presence during my first few years of graduate school and always knowing what to say. To Miles Braten, for taking on these five years together with me and always willing to lend a listening ear. There was nothing that we couldn’t talk about.

I am also lucky to have formed meaningful and lasting friendships with many of my colleagues. Tyler Stevens and Erica Chong kept me sane through many years with weekly coffee dates, where we decompressed and caffeinated. I couldn’t have asked for a better way to spend my downtime at work. To my dear friend Wilson Bailey, thank you for being such an excitable and encouraging person, from riding bikes with me and Tyler and planting plants, and introducing me to Cecily. To my ex-husband Benjamin Leipzig, thank you for all of your years of support and encouragement. We helped each other through the majority of graduate school, and you have one of the kindest and gentlest souls I have ever met, I know you will be great wherever life takes you. And finally, to my dear, dear friend and soul-sister Sophia Tran, who

understands my heart more than anyone else. At a workplace I expected to find acquaintances and even good friends, but I never thought that I would find someone as funny, genuine, and loveable as Sophia. She has been a constant source of love, encouragement, wisdom, listening, cooking advice, and overall fun for all five years. I love you like a sister, and I know that we'll be friends for many long years. To everyone else in the department that helped in numerous ways, thank you.

To the new colleagues at Yale: Gannon Connor, Delina Damatov, Julia Darcy, Onyu Jung, Scott Kolmar, Janelle Lora, and Catherine Wise, I have enjoyed working with each of you and you have made coming to work every morning pleasant, even in the snow. To my best friend in Connecticut, Jennifer Peper, a sweet and level headed person, who was my rock and friend through trying times. She gracefully helped me in my transition to New Haven and has an especially frank way of "saying it like it is" that I admire. She juggles way more than any individual I know, is outlandishly generous, and always has a word of encouragement. I also wouldn't be where I am not without the help and love of my partner Wesley Morris. He has asked questions about my research, gone on adventures with me, and been supportive of all of my possible career paths. I love you and can't believe you put up with all my crazy writing this thesis.

And of course I have to thank my family. I have aunts, uncles and cousins that have loved and celebrated with me every step of this way. I wouldn't be who I am today without the guidance of my late grandmother, Ena Moss. She taught me to bake, cook, sew, and garden. She taught me history and mathematics even before I was old enough to be in school, and I credit my success in early school to her. I have to thank my sister, Crystal Valdez. We're cheerleaders for each other's careers, and she was always an ally at family gatherings when no one seemed to know why the heck we were still in school. She is a beautiful, intelligent, creative, and fun person. To my parents, Vicki and Ed Valdez, thank you for raising me and for pushing me to want more. Thank you for allowing me the freedom to do a lot of life on my own, and loving me no matter what.

I am grateful and humbled by the love and generosity of all these fine people, and am lucky to have them in my life.

DEDICATION

To my parents

Vicki and Ed

for working so that I could be where I am today.

"Only a life lived for others is a life worthwhile"
— Albert Einstein, 1932

Chapter 1. INTRODUCTION

1.1 METAL OXIDES

Metal oxides (MO_x) make up a specific class of semiconductor materials that are widely studied due to their relatively low cost, low toxicity, high stability, and ease of preparation. Noteworthy applications of metal oxide materials include dye-sensitized solar cells (DSSCs), photocatalytic oxidation of organics in wastewater remediation, and the positive terminal of lithium ion batteries.[1-3] Metal oxides are also good catalysts for many redox reactions, ranging from photoelectrochemical water splitting to the production of commodity chemicals such as the oxidation of propylene.[4-6]

More specifically, zinc oxide (ZnO) will be discussed for the majority of this thesis. ZnO has been widely studied since 1935, is categorized as a II-VI, direct band gap semiconductor, and has long attracted interest for its electronic, optical, and photochemical properties.[7-9] It has also been used to develop a fundamental understanding of interfacial ET in electrochemical cells.[10] A recent surge in the use of ZnO in electronic and optoelectronic devices has arisen because of processing advances in the preparation of ZnO into high quality epitaxial layers and single crystals. Along with these pristine architectures, ZnO can be easily prepared in bulk, films, and nanostructures.[11] We will focus on ZnO nanocrystals (NCs) that are easily synthesized and characterized, which allow the study of reaction chemistry in solution.

The experiments described in this thesis aim to provide an understanding of proton-coupled electron transfer (PCET) reactions at the interface of metal oxides and solutions using ZnO NCs as a model system. It is divided into four sections: reactions with photochemically reduced NCs, reactions with chemically reduced NCs, capping ligands, and finally a chapter that describes experiments that contributed to our understanding of these NCs. Each of these sections is accompanied by a more specific introduction, and the aim of this more general introduction is to describe the motivation for the research and describe some of the body of work that came before it.

1.2 Charge Balance: Proton Coupled Electron Transfer

Oxidation and reduction reactions of metal oxide materials are crucial to emerging energy technologies, as well as other processes such as photocatalytic wastewater remediation and self-cleaning surfaces.[2] Often these reactions take place in solution at the surface of the material. Such "interfacial" reactions play a critical role in a wide range of chemical processes, and are generally described solely in terms of electron transfer (ET). For example, the extensive literature on photochemical and electrochemical water splitting by metal oxides is focused on the ET between surface-bound species and the valence and conduction bands of the solid.

Underlying the electron transfer in metal oxides is the importance of protons, which often act as the counter charge to the electron. For example, it was demonstrated that thin films composed of ZnO NCs have higher differential capacitances when exposed to protic vs. aprotic solutions, which indicates that protons play an important role in ET.[12] In addition, the conduction band energies of metal oxide NCs have demonstrated a Nernstian pH dependence (60 mV/pH),[13,14] an observation that cannot be explained by conventional, surface-protonation models because the range of pH where this is true extends beyond the proton accepting ability of the surface. A specific example of this is from Lyon and Hupp,[15] where they reported that the energy of the conduction band of TiO_2 varied linearly over 30 pH units. As an alternative to the conventional model, they suggest that intercalation of protons, rather than surface protonation, occurs when a potential is applied.[15] Although several $H^{\bullet}$ doped metal oxides have been suggested,[16-18] a tight coupling between the electron and proton has yet to be established.

Proton coupled electron transfer (PCET) processes involve the simultaneous transfer of a proton and an electron. In the Mayer laboratory, PCET reactions are studied for applications ranging from photocatalysis to the development of a theoretical framework. The compounds used for these studies are typically small molecules such as porphyrins, transition metal complexes, and organic molecules. Our goal is to extend this understanding to metal oxide NCs. Because a Nernstian dependence on pH is usually attributed to PCET, we are interested in determining if electron transfer on the surface of metal oxides is better described as PCET. Does this mechanism conflict with current description of the conduction band of metal oxides? How do protons function as counterions for the extra electron in the conduction band? A more thorough understanding of localized redox reactions at the interface of semiconductor metal

oxides and solution, especially with earth-abundant and inexpensive metals, will be essential in the development of more effective and sustainable chemical technologies. Although our work does not specifically aim to make devices, this atomic-level understanding could help in the future optimization of metal oxide photovoltaics. The broader understanding gained from this research could be used to inform solar cells, light emitting devices, luminescent biological labels, and we hope many other applications.

1.3 THERE'S NOTHING WRONG WITH BEING SMALL: THE NANO REGIME

Nanomaterials, so named because their diameters are less than/on the order of a few hundred nanometers, have special properties when compared to their bulk material counterparts. One general characteristic of nanomaterials is that there is a much higher percentage of the atoms at the surface, and surface material typically has different reactivity than the interior (due to dangling bonds, lower coordination numbers, etc.). Nanomaterials come in a variety of sizes and geometries, a few examples are: nanotubes, nanowires, nanoribbons, nanodisks, nanosheets, core-shell geometries, and likely the most common, nanoparticles (the simplest configuration, roughly spherical). Broadly speaking, there are two classes of nanoparticles categorized by the method of synthesis; nanoparticles formed in solution via "wet" (benchtop) methods, or epitaxial nanoparticles that are generated via vapor deposition.[19] The latter are predominantly used by physicists as this procedure generates more uniform and often defect-free nanoparticles, while the former is most often used by chemists, and is the only type discussed herein.

Some nanoparticles are termed "quantum dots", coined by the physicist Mark Reed in the early 1990's,[20] because the energy levels in their conduction and valence bands are quantized, as orbitals are in atoms and molecules. One can picture this as a particle in a box problem, where quantum mechanics tells us that an electron will have wavelike properties. When confined in a nanoparticle, the boundaries for this wave are the edges of the nanoparticle. According to Heisenberg's uncertainty principle, as the position of the electron becomes more restrained (fixed inside a small spherical particle), the momentum must therefore be less certain. A wider range of momentum thus leads to higher energies.[20] This can lead to quantum confinement effects, which arise when the nanoparticles are smaller than the corresponding electron wavefunction (Bohr radius). At radii smaller than the Bohr radius, the nanoparticles are in the quantum confined regime, where there is an inverse relationship of semiconductor band gap

(energy) and nanoparticle size. In other words, smaller particles have higher energy levels, and the energy of a material can be easily tuned by making different sizes of particles.

The preparation of quantum dots was pioneered in the 1980's by Louis Brus (then at Bell labs),[21,22] and nanoparticles have since been studied extensively. Colloidal semiconductor nanocrystals (NCs), the crystalline version, are now widely used in solar cells, light emitting devices, luminescent biological labels, and for many other applications.[23] Nanocrystals lie at the interface of small molecules (that chemists generally work with) and materials (usually used by physicists and materials scientists). They possess the processability and approachability for use with analytical tools such as NMR spectroscopy, reaction chemistry, and other solution based spectroscopies, coupled with the electronic structure more similar to a semiconductor material. The energy of the nanocrystals can be finely tuned by small changes in size. For these reasons, we have chosen to use semiconductor NCs to study properties of the interface between solution and semiconductors. ZnO NCs in particular are used because of their relative ease of preparation and characterization developed in the Gamelin lab in the early 2000's.[24,25]

1.4 Doping of Nanocrystals

Another interesting property of semiconductor materials is that carriers (electrons or holes) can be added to the lattice, also called doping *n*- or *p*-type. Understanding the effect of these extra charges and being able to manipulate the carriers is necessary for a variety of reasons. Charge carriers can control the magnetism of a material,[26] tune chemical reactivity,[27] and affect device performance.[28] There are currently five methods to generate reduced (*n*-type) NCs: (1) electrochemical, (2) hydrogen gas, and (3) photochemical, (4) aliovalent, and (5) chemical (remote) doping.

Photochemical doping is perhaps the most commonly used method, which involves the absorption of light to promote an electron across the band gap of the semiconductor material, generating an electron-hole pair. The hole that is formed can be "quenched" (filled) by a sacrificial reductant, generally an alcohol. Photodoping has been studied in ZnO, and many other materials since the 1980's.[29-31] Electrochemical reduction involves deposition of the NCs onto a surface, where charge is then transported in a steady state from the electrode to the NCs.[32-35] Aliovalent doping describes nanocrystals with a lattice site occupied by a vacancy or a dopant atom with a different oxidation state. For example, ZnO can be doped with Al^{3+} to give stable, *n*-

type nanocrystals that are air-stable. The electrons are charge-compensated by Al^{3+} (compared to Zn^{2+}).[36] Similarly, hydrogen gas can be used to insert charge into semiconductor materials (bulk).[37,38] This is given its own category because the protons (H^+) follow the electron into the lattice, and likely take up intersitial sites.[17] Chemical reduction, however, utilizes an outer sphere electron donor whose resulting cation balances the eletron charge from the exterior of the NC. Examples of chemical doping include the reduction of ZnO and CdSe with sodium biphenyl[23] and PbS and PbSe with cobaltocene.[39]

1.5 Zinc Oxide Nanocrystals: Previous Work

Five years ago in our lab, Dr. Rebecca Hayoun began working on ZnO NCs with the assistance of Dr. Kelly Whitaker who had recently completed her Ph.D. in the Gamelin group. Together they performed studies on Mn^{2+}-doped ZnO NCs via electron paramagnetic spectroscopy (EPR). In general, Mn^{2+} atoms show a characteristic multiline EPR signal. As has been demonstrated in the Gamelin lab, Mn^{2+} doping into the lattice of ZnO NCs broadens the EPR signal.[43,44] Dr. Hayoun used this broadening to probe electron transfer between doped and undoped NCs.[40]

Dr. Hayoun and Dr. Whitaker also demonstrated facile ET between colloidal ZnO NCs of different sizes.[41] Using stopped flow optical spectroscopy, they determined that the electron transfer from NC to NC was rapid and complete within the time of mixing, which indicates a bimolecular rate constant greater than 10^7 $M^{-1}s^{-1}$. At the time, this was very surprising given that the NCs are capped with dodecylamine (1.5 nm in length) which for thin films greatly reduces the conductivity.[42] This experiment demonstrated quantum confinement using inter-nanocrystal electron transfer, moving electrons from smaller (higher energy) to larger (lower energy) NCs. These experiments also demonstrated that these photoreduced NCs can be treated like molecular reductants.

Dr. Hayoun also performed preliminary experiments that demonstrated that photoreduced ZnO NCs react with hydrogen atom acceptors (TEMPO and $^tBu_3ArO^\bullet$) by donating a hydrogen atom (discussed in more detail in Chapter 3). The work presented herein builds off of these initial studies using ZnO NCs as molecular reagents.

1.6 NOTES TO CHAPTER 1

(1) Hagfeldt, A.; Boschloo, G.; Sun, L.; Kloo, L.; Pettersson, H. *Chem. Rev.* **2010**, *110*, 6595.

(2) Fujishima, A.; Zhang, X.; Tryk, D. A. *Surf. Sci. Rep.* **2008**, *63*, 515.

(3) Whittingham, M. S. *Chem. Rev.* **2004**, *104*, 4271.

(4) Xu, H.; Zhang, R. Q.; Ng, A. M. C.; Djurišić, A. B.; Chan, H. T.; Chan, W. K.; Tong, S. Y. *J. Phys. Chem. C* **2011**, *115*, 19710.

(5) Khan, M. M.; Adil, S. F.; Al-Mayouf, A. *J. Saudi Chem. Soc.*

(6) Nakagawa, T.; Beasley, C. A.; Murray, R. W. *J. Phys. Chem. C* **2009**, *113*, 12958.

(7) Look, D. C. *Mater. Sci. Eng., B* **2001**, *80*, 383.

(8) Klingshirn, C. *Chemphyschem* **2007**, *8*, 782.

(9) Huss, A. S.; Bierbaum, A.; Chitta, R.; Ceckanowicz, D. J.; Mann, K. R.; Gladfelter, W. L.; Blank, D. A. *J. Am. Chem. Soc.* **2010**, *132*, 13963.

(10) Hamann, T. W.; Gstrein, F.; Brunschwig, B. S.; Lewis, N. S. *Chem. Phys.* **2006**, *326*, 15.

(11) Jagadish, C.; Pearton, S. J. *Zinc Oxide Bulk, Thin Films and Nanostructures*; Elsevier Ltd.: Amsterdam, 2006.

(12) Roest, A. L.; Germeau, A.; Kelly, J. J.; Vanmaekelbergh, D. l.; Allan, G.; Meulenkamp, E. A. *ChemPhysChem* **2003**, *4*, 959.

(13) Morrison, S. R. *Electrochemistry at Semiconductor and Oxidized Metal Electrodes*; Plenum Press: New York, 1980.

(14) *Semiconductor Electrodes*; Finklea, H. O., Ed.; Elsevier: New York, NY, 1988; Vol. 55.

(15) Lyon, L. A.; Hupp, J. T. *J. Phys. Chem. B* **1999**, *103*, 4623.

(16) Carlsson, P.; Holmstrom, B. *J. Electrochem. Soc.* **1982**, *129*, 1851.

(17) Van de Walle, C. G. *Phys. Rev. Lett.* **2000**, *85*, 1012.

(18) Hofmann, D. M.; Hofstaetter, A.; Leiter, F.; Zhou, H.; Henecker, F.; Meyer, B. K.; Orlinskii, S. B.; Schmidt, J.; Baranov, P. G. *Phys. Rev. Lett.* **2002**, *88*, 045504.

(19) Reddy, M. V.; Subba Rao, G. V.; Chowdari, B. V. R. *Chem. Rev.* **2013**, *113*, 5364.

(20) Reed, M. A. *Scientific American* **1993**, *268*, 118.

(21) Rossetti, R.; Nakahara, S.; Brus, L. E. *J. Chem. Phys.* **1983**, *79*, 1086.

(22) Ekimov, A. I.; Efros, A. L.; Onushchenko, A. A. *Solid State Commun.* **1985**, *56*, 921.

(23) Shim, M.; Guyot-Sionnest, P. *Nature* **2000**, *407*, 981.

(24) Schwartz, D. A.; Gamelin, D. R. *Proc SPIE-Int Soc Opt Eng* **2003**, *5224*, 1.

(25) Schwartz, D. A.; Norberg, N. S.; Nguyen, Q. P.; Parker, J. M.; Gamelin, D. R. *J. Am. Chem. Soc.* **2003**, *125*, 13205.

(26) Ochsenbein, S. T.; Feng, Y.; Whitaker, K. M.; Badaeva, E.; Liu, W. K.; Li, X.; Gamelin, D. R. *Nat Nano* **2009**, *4*, 681.

(27) Cohn, A. W.; Janßen, N.; Mayer, J. M.; Gamelin, D. R. *J. Phys. Chem. C* **2012**, *116*, 20633.

(28) Anikeeva, P. O.; Madigan, C. F.; Halpert, J. E.; Bawendi, M. G.; Bulović, V. *Phys. Rev. B* **2008**, *78*, 085434.

(29) Koch, U.; Fojtik, A.; Weller, H.; Henglein, A. *Chem. Phys. Lett.* **1985**, *122*, 507.

(30) Bahnemann, D. W.; Kormann, C.; Hoffmann, M. R. *J. Phys. Chem.* **1987**, *91*, 3789.

(31) Hoffmann, M. R.; Martin, S. T.; Choi, W.; Bahnemann, D. W. *Chem. Rev.* **1995**, *95*, 69.

(32) Wehrenberg, B. L.; Guyot-Sionnest, P. *J. Am. Chem. Soc.* **2003**, *125*, 7806.

(33) White, M. A.; Weaver, A. L.; Beaulac, R.; Gamelin, D. R. *ACS Nano* **2011**, *5*, 4158.

(34) Liu, H.; Keuleyan, S.; Guyot-Sionnest, P. *J. Phys. Chem. C* **2011**, *116*, 1344.

(35) Diroll, B. T.; Gordon, T. R.; Gaulding, E. A.; Klein, D. R.; Paik, T.; Yun, H. J.; Goodwin, E. D.; Damodhar, D.; Kagan, C. R.; Murray, C. B. *Chem. Mater.* **2014**, *26*, 4579.

(36) Schimpf, A. M.; Ochsenbein, S. T.; Buonsanti, R.; Milliron, D. J.; Gamelin, D. R. *Chem. Commun.* **2012**, *48*, 9352.

(37) Samson, S.; Fonstad, C. G. *J. Appl. Phys.* **1973**, *44*, 4618.

(38) Ip, K.; Overberg, M. E.; Heo, Y. W.; Norton, D. P.; Pearton, S. J.; Stutz, C. E.; Luo, B.; Ren, F.; Look, D. C.; Zavada, J. M. *Appl. Phys. Lett.* **2003**, *82*, 385.

(39) Koh, W.-k.; Koposov, A. Y.; Stewart, J. T.; Pal, B. N.; Robel, I.; Pietryga, J. M.; Klimov, V. I. *Sci. Rep.* **2013**, *3*, 2004.

(40) Hayoun, R. *Studies of Metal Oxides in Organic Redox Reactions: Zinc Oxide Nanoparticles as Chemical Reductants in Electron Transfer and Hydrogen Atom Transfer Reactions and the Use of Osmium Tetroxide to Oxidize Higher Alkanes*, Ph.D. Thesis, University of Washington, 2011.

(41) Hayoun, R.; Whitaker, K. M.; Gamelin, D. R.; Mayer, J. M. *J. Am. Chem. Soc.* **2011**, *133*, 4228.

(42) Talapin, D. V.; Lee, J.-S.; Kovalenko, M. V.; Shevchenko, E. V. *Chem. Rev.* **2010**, *110*, 389.

(43) Liu, W. K.; Whitaker, K. M.; Kittilstved, K. R.; Gamelin, D. R. *J. Am. Chem. Soc.* **2006**, *128*, 3910.

(44) Ochsenbein, S. T.; Feng, Y.; Whitaker, K. M.; Badaeva, E.; Liu, W. K.; Li, X.; Gamelin, D. R. *Nat Nano* **2009**, *4*, 681.

Chapter 2. LOW CAPPING GROUP DENSITY ON ZINC OXIDE NANOCRYSTALS

2.1 INTRODUCTION

Colloidal semiconductor nanocrystals (NCs) are widely investigated for use in solar cells, light emitting devices, luminescent biological labels, and many other applications.[1-3] NCs are unique materials, combining the tunable electronic structure and photochemical properties associated with bulk materials with the synthetic accessibility and spectroscopic convenience of small molecules.[4,5] Most NC preparations in nonpolar solvents use capping ligands to control solubility, photoluminescence, and other properties.[6,7] The capping ligand density of each system is an important parameter to a range of chemical and physical properties of NCs, from stabilizing colloids in solution to influencing the inner sphere reactivity of NCs with hole acceptors[8] and proton-coupled electron transfer (PCET) acceptors,[9,10] as well as interparticle electron transfer.[11]

Recent studies show that the capping ligands on semiconductor NCs are more complex and dynamic than the traditional image of a fairly dense shell.[8-17] Kahn et al. identified different types of DDA that compose the ligand shells of ZnO NCs (prepared by a different synthetic method),[15] but they did not quantify the number of capping ligands per NC. The literature of capping groups on other semiconductor NCs, especially CdSe, is much more extensive.[13,16,18-20] In particular, Weiss *et al.* have reported that the density and dynamics of the capping groups strongly influence the chemical reactivity of chalcogenide NCs.[8]

Of the variety of techniques that have been used to examine the chemistry of capping ligands, including inductively coupled plasma mass spectrometry (ICP-MS), IR and NMR spectroscopy, X-ray photoelectron spectroscopy (XPS), energy-dispersive X-ray spectroscopy (EDS), and thermogravimetric analysis (TGA),[16,21] NMR spectroscopy is especially powerful tool. NMR spectroscopy is an in situ and non-destructive analysis that provides information about the organic molecules interacting with NCs in solution.[13] The in situ nature of NMR spectroscopy is particularly valuable for examining the capping ligands under conditions that parallel reactivity and spectroscopic studies. Diffusion-ordered NMR spectroscopy (DOSY) and

related pulsed field gradient experiments have been used to investigate the interaction of ligands with NC surfaces[15,22] and to extract overall sizes using the Stokes-Einstein relation.[15,23]

The dodecylamine (DDA) ligand shells of a series of ZnO NC samples suspended in toluene were studied by a variety of NMR spectroscopies. A method to quantify capping group densities was developed. NMR spectroscopic data implicate a model with strongly bound, weakly associated, and free DDA. The strongly bound DDA ligands cover only 10-20% of the estimated number of surface Zn atoms and account for less than 25% of the maximum coverage predicted for a self-assembled monolayer. Figure 2.1 is a semi-quantitative illustration of the measured density, roughly to scale. It shows a quarter of a d = 3.8 nm NC with its roughly ten strongly-bound DDA ligands and fewer weakly-associated DDA groups. Thus these NCs have very incomplete surface shells of capping ligands, which contrasts with the typical view of a fully saturated surface. Annealing the NCs causes an increase in the coverage of the strongly bound ligands and a decrease of weakly associated ligands. Since annealing causes the loss of water, this result supports the hypothesis that strong binding of DDA is blocked by surface protons (hydroxide ligands).

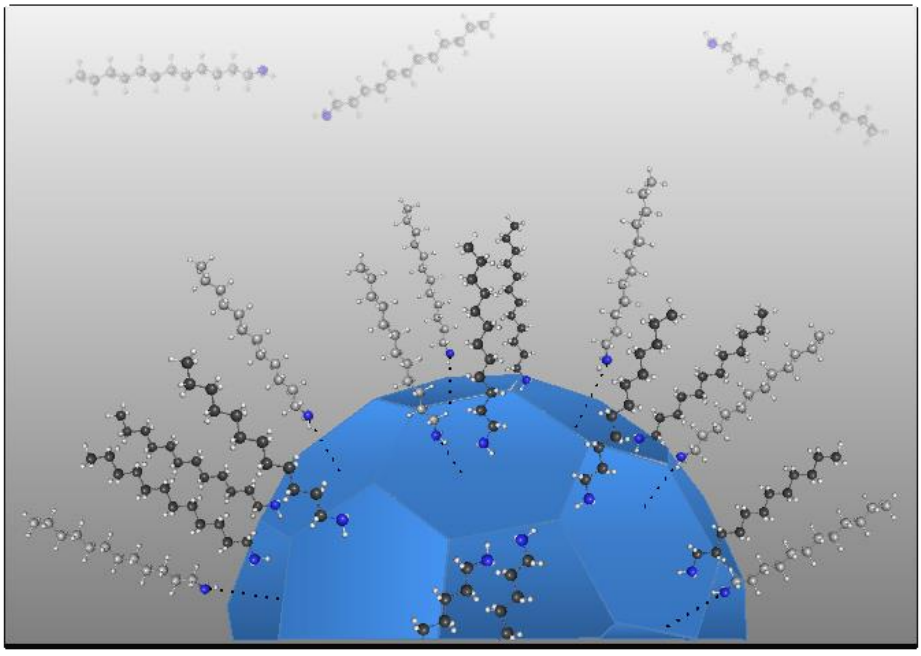

Figure 2.1. Illustration of one quadrant of a faceted NC (d = 3.8 nm) with DDA capping ligands. The proportion of strongly bound (black carbon atoms) and weakly bound DDA (grey

carbon atoms) are depicted in the proportions measured by NMR spectroscopies, showing the sparse surface coverage by DDA.

2.2 Results and Discussion

2.2.1 *Characterization of Dodecylamine Bound to ZnO Nanocrystals*

ZnO NCs with average diameters (*d*) between 3 and 7 nm were synthesized at room temperature in multigram batches by the wet chemical method described previously,[24] capped with dodecylamine (DDA), suspended in toluene and stored at -35 °C. The mean ZnO NC size was determined from the position of the first exciton peak[25,26] or by transmission electron microscopy (TEM). The total Zn concentration in the solution was measured by inductively coupled plasma optical emission spectrometry (ICP-OES).[17] These data give the concentration of NCs, which was on the order of 0.01-1 mM for the experiments described here. Figure 2.2 compares a typical ^{1}H NMR spectrum of capped ZnO NCs in toluene-d_8 versus DDA alone. For ZnO and similar systems, ^{1}H NMR resonances of ligands in the presence of NCs often appear downfield of the free ligand and are significantly broadened.[22,27] Broadening of the NMR ligand signals likely arises from multiple effects, including slow tumbling of the large NCs, decreased T_2, heterogeneity of the NCs in size, shape and surface properties, and the relatively high viscosity of the solutions.[13] In the presence of ZnO NCs, the signal at 0.4 ppm for the DDA NH_2 group disappears, the α-CH_2 peak is broadened and shifted downfield (to ~ 2.7 ppm), and the methyl and composite methylene peaks (–CH_3, 0.9 ppm; –$(CH_2)_{10}$–, 1.3 ppm) broaden and develop downfield shoulders (Figure 2.2, Figure 2.3).

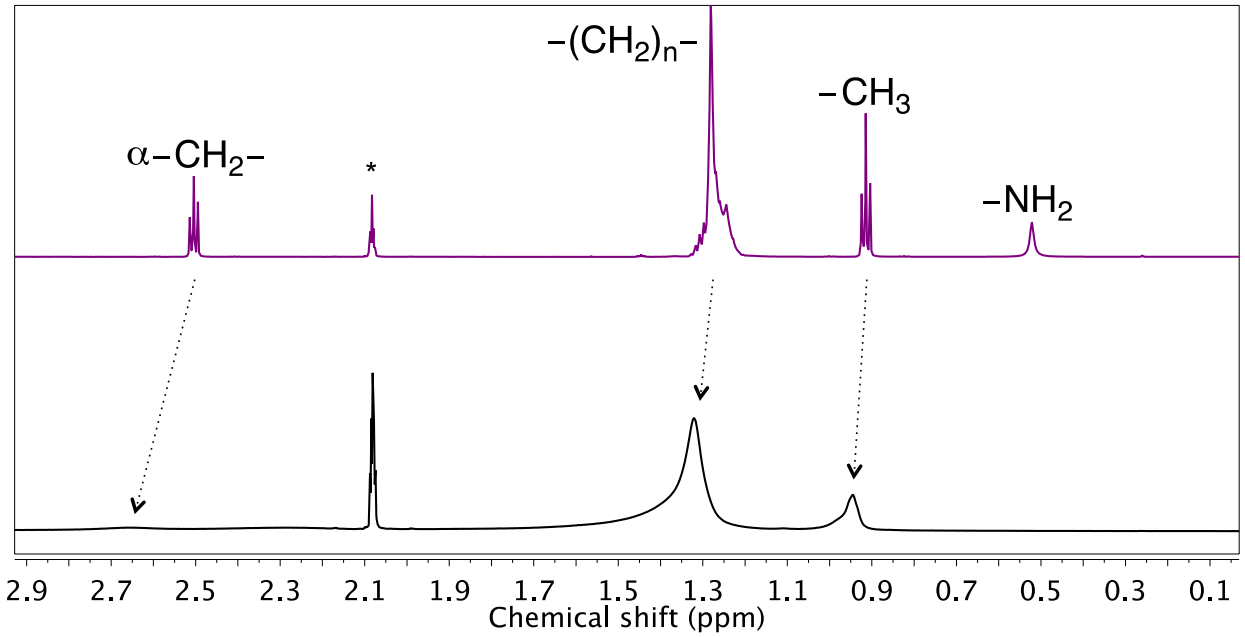

Figure 2.2. ^{1}H NMR spectra (700 MHz) of DDA only and capped ZnO NCs in toluene-d_8 (d = 4.3 nm, [NCs] = 6×10^{-4} M), top and bottom, respectively. The asterisk refers to the residual solvent signal. In the presence of NCs, the α-CH_2 signal is broadened and the amine peak is not observed. The ^{1}H NMR resonance for the internal methylene protons (–$(CH_2)_{10}$–) in ZnO/DDA solutions is well modeled as the sum of two peaks: one broad and more downfield (1.37 ppm), the other sharper and slightly upfield (1.31 ppm) (Figure 2.3). The –CH_3 resonances are also well modeled as two peaks, and essentially the same ratio of broad to sharper peaks is obtained. Based on the peak positions and widths, and the DOSY experiments described in detail below, the broad downfield signals are assigned to DDA strongly bound to the NCs. With larger NCs, the distinction between the broad and sharp signals is even more pronounced.

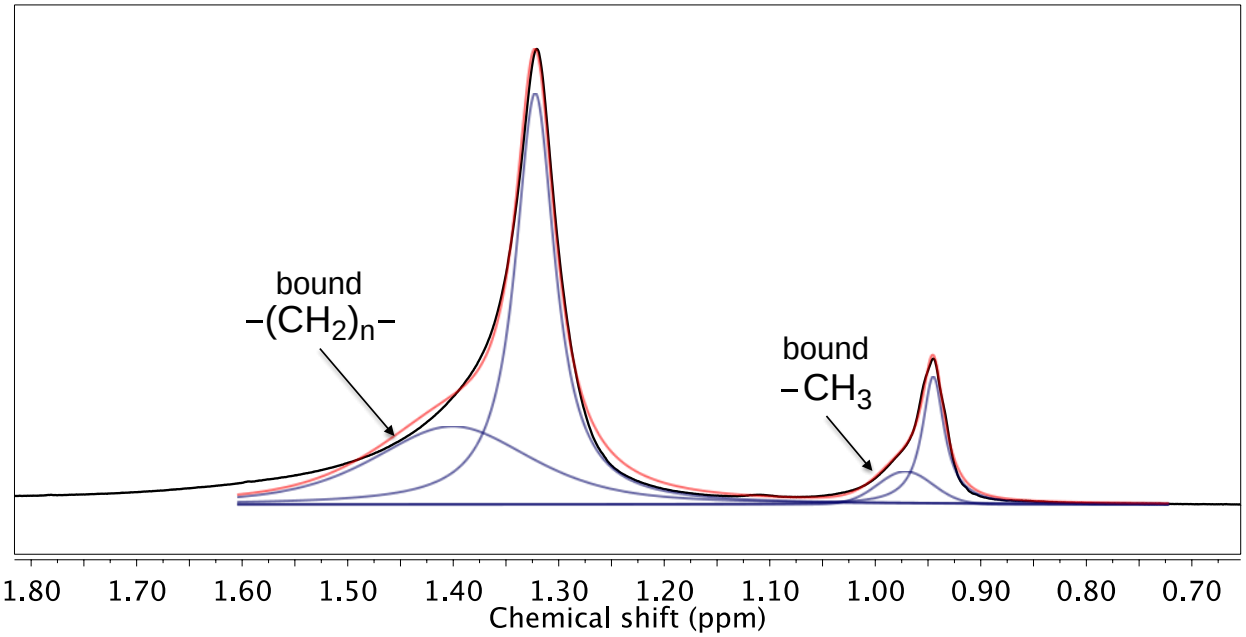

Figure 2.3. Fitting of the aliphatic signals in the ^{1}H NMR spectrum of ZnO/DDA solutions (the same data as in Figure 2.2) using the global spectral deconvolution (GSD) function in MestReNova.The experimental spectrum is shown in black, the blue traces are individual peak fits, and the red is the sum of the fits.

DOSY and Nuclear Overhauser Effect spectroscopy (NOESY) confirmed that the broad downfield peaks correspond to DDA bound to the NC. A ^{1}H DOSY NMR spectrum of the DDA only is displayed in Figure 2.4, and ZnO NCs in toluene-d_8 is shown in Figure 2.5. DOSY is a pseudo-two-dimensional technique, displayed with the one-dimensional ^{1}H NMR spectrum on the horizontal axis and diffusion coefficient (D) along the vertical axis. D can be related to the hydrodynamic radius R_H *via* the Stokes-Einstein relation (Equation (2.1)), where k_B is the Boltzmann constant, T is the absolute temperature, and η is the viscosity of the solution.[15,16] D is inversely proportional to R_H because larger species move more slowly in solution. Trimethoxybenzene (TMB) was added to the solution as an internal standard, and analysis of its resonances at 3.3 and 6.1 ppm gave a diffusion constant of 1.6×10^{-9} m^2s^{-1}, which is typical for a small molecule.[23]

$$D = \frac{k_B T}{6\pi\eta R_H} \tag{2.1}$$

Table 2.1. Values used for the DOSY data using the Stokes-Einstein relationship.

Variable	Value	Units	Source
η (viscosity)	5.56×10^{-4}	Pa•s ($kg \cdot m^{-1} \cdot s^{-1}$)	Fritzinger et. al[22]
T, (temperature)	298	K	-
k_B (Boltzmann constant)	1.38065×10^{-23}	$m^2 \cdot kg \cdot s^{-2} \cdot K^{-1}$	-
D (diffusion constant)	varies	$m^2 \cdot s^{-1}$	^{1}H DOSY data
R_H	varies	m	-

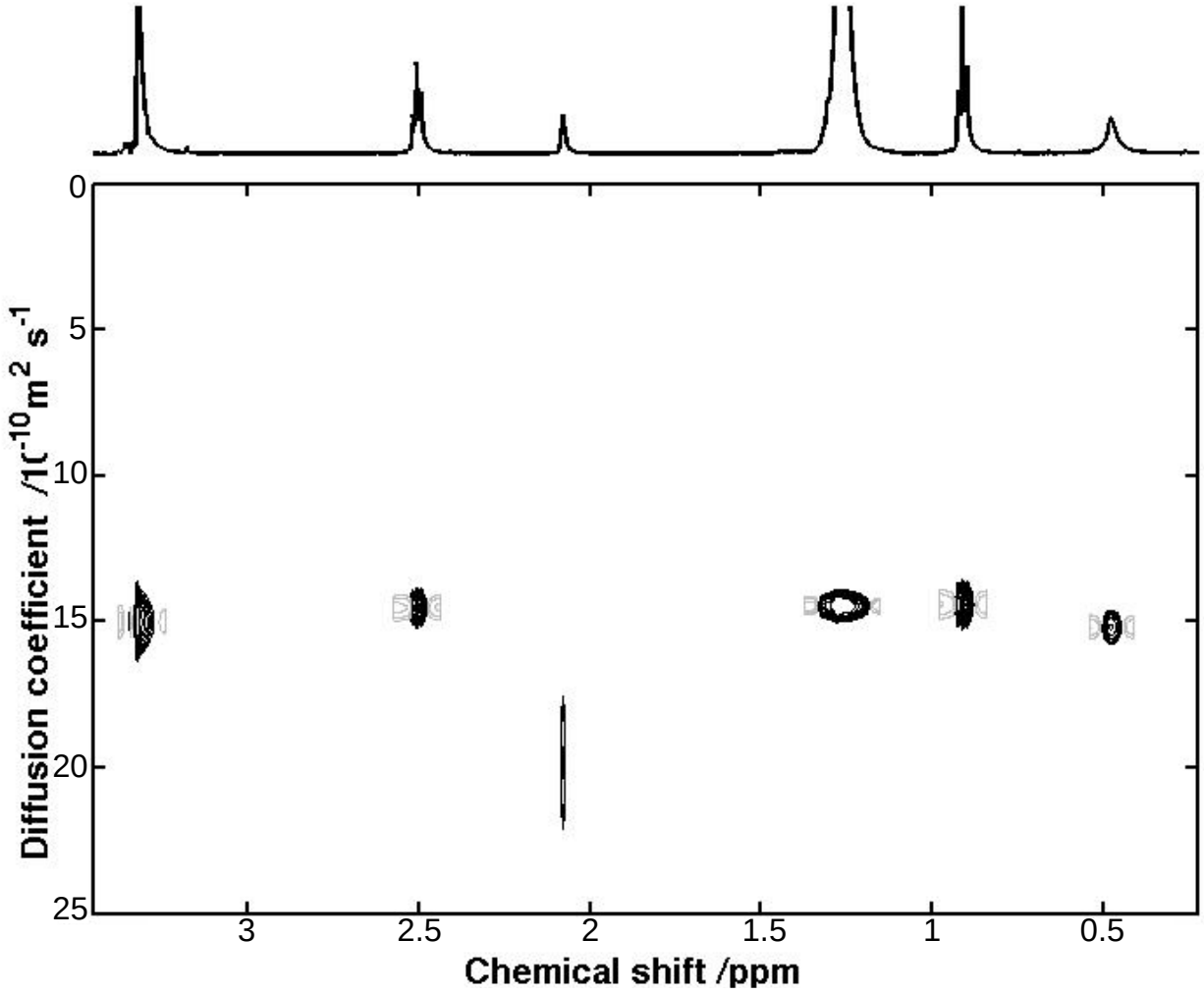

Figure 2.4. ^{1}H DOSY NMR spectrum of dodecylamine (DDA) in toluene-d_8.

In the DOSY spectrum of DDA only (Figure 2.4), all of the resonances corresponding to DDA diffuse at the same rate, 1.5×10^{-9} m^2s^{-1}. For ZnO NCs, the DDA signals between 0.5 and 2 ppm are split into two separate diffusion regimes (Figure 2.5). The *D* for the more slowly diffusing DDA peaks, $1.1(4) \times 10^{-10}$ m^2s^{-1} (errors reported in parentheses are twice the standard deviation from replicates), corresponds to the broad downfield resonance shown in Figure 2.3. The assignment of these slowly diffusing DDA molecules as strongly bound is consistent with literature precedent,[15] and is supported by a dilution experiment. Dilution of a sample of colloidal NCs by a factor of five led to no change in the strongly bound DDA groups per NC (*vide infra*). The diffusion peaks at $\sim 1 \times 10^{-10}$ m^2s^{-1} are thus assigned as strongly bound ligands, and this value is termed $D_{bound.}$ This apparent diffusion constant did not vary between batches of NCs that contain varying amounts of free DDA. These results indicate that strongly bound DDA do not exchange with free DDA on the NMR timescale (Table 2.2).

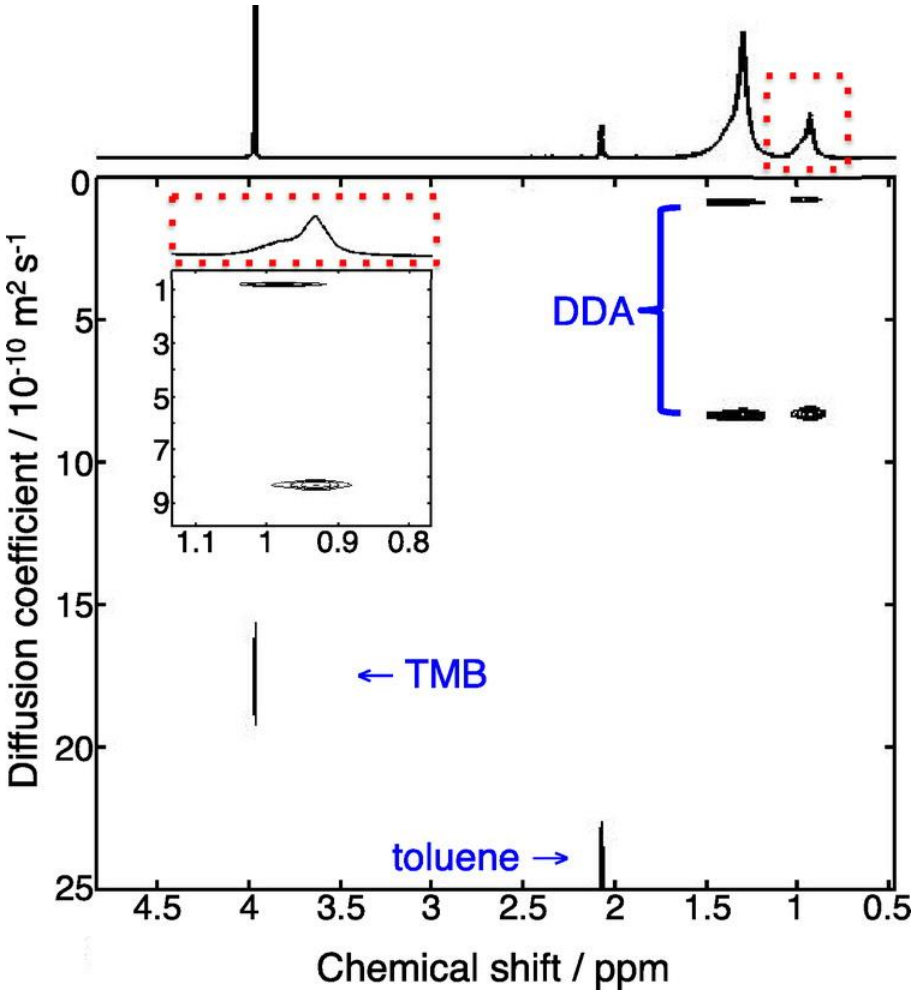

Figure 2.5. Typical ^{1}H DOSY NMR spectrum of ZnO NCs with DDA capping ligands in toluene-d_8. The data processing was done with DOSYToolbox 1.5, using Local Covariance Order Diffusion-Ordered Spectroscopy (LOCODOSY) for better resolution of the overlapping peaks.[28] Inset shows just the DDA methyl peak (dotted red box) to highlight the differences in chemical shift between the strongly bound DDA and the faster diffusing DDA.

The value of D_{bound} was used to estimate the hydrodynamic radius of the NCs using the Stokes-Einstein relation (eq 1.1). The hydrodynamic radius would include the diameter of the NC plus any DDA ligands bound to the surface. Indeed, the diameters obtained by the DOSY experiments are roughly the NC diameter determined from the optical spectra plus two ligands (Table 2.2), which also suggests that the NCs are not significantly aggregated. The value of D_{bound} was also confirmed in separate experiments by referencing to the D of ferrocene in the same solution ($R_H(Cp_2Fe)$ = 0.3 nm[23]). As reported previously,[10] the larger errors are unsurprising due to the high volume fraction of NCs and solution viscosity, giving rise to non-ideal diffusion due to nanoparticle/nanoparticle interaction, but the values are accurate within a few nanometers.

Table 2.2. Calculated hydrodynamic radius of ZnO NCs using the D_{bound} diffusion coefficient obtained from DOSY spectra.

NC batch	**NC size (d, nm)[a]**	**NC size plus two DDA ligands [1.5 nm (× 2)] [b]**	**D_{bound} (× 10^{-10} m^2s^{-1})**	**NC hydrodynamic size (nm) [c]**
A	3.6	6.6	0.9 ± 0.1	8 ± 3
B	3.8	6.8	0.9 ± 0.2	8 ± 2
C	4.3	7.3	1.3 ± 0.3	6 ± 3
D	4.7	7.7	1.1 ± 0.4	7 ± 4
E	6.5	9.5	0.9 ± 0.1	8 ± 2

[a] From the band edge energy. [b] DDA length rom Ref 9. [c] Calculated from Equation 2.1 using DOSY D_{bound}.

Table 2.3, NC batch B*). With excess DDA, the diffusion peak shifted to larger D values. This observation indicates that the second diffusion peak corresponds to species in a rapid equilibrium with free DDA, resulting in an averaged diffusion coefficient. Therefore this peak is termed Dmix, the diffusion peak corresponding to the concentration-dependent equilibrium between free DDA and weakly associated DDA.

^{1}H NMR spectra of as-prepared ZnO NCs with DDA added were recorded at 800 MHz for maximum sensitivity (Figure 2.6). To a sample of ZnO NCs, aliquots of a stock solution of DDA in toluene-d_8 were added by syringe (60 DDA per NC), followed by recording a spectrum. This was repeated for five additions, up to 300 extra DDA molecules per NC.

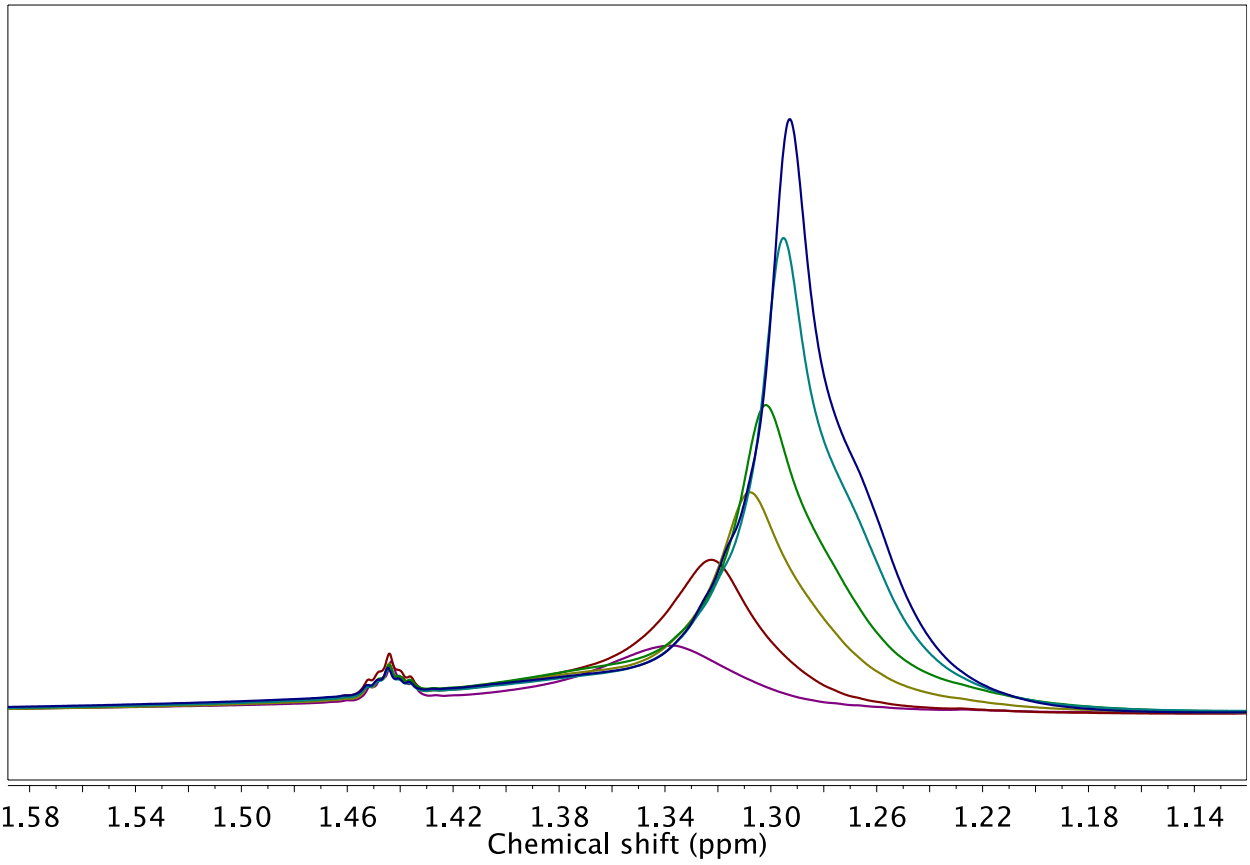

Figure 2.6. Overlay of ^{1}H NMR spectra of ZnO NCs (1.3×10^{-4} M) in toluene-d_8 with added DDA. DDA was added to the solution in 10 μL aliquots. Purple, red, yellow, green, light blue, and dark blue spectra correspond to 0, 60, 120, 180, 240, and 300 extra DDA molecules per NC, respectively. Residual THF appears at ~1.4 ppm, and the peak at ~1.3 ppm corresponds to the methylene signal of DDA.

For DOSY NMR spectroscopy, a smaller concentration of DDA was added (20 DDA extra per NC) to an analogous sample of ZnO nanocrystals, see Figure 2.7. The position of the faster DDA peak (1.39 ppm and 0.98 ppm) varies from to 4.6×10^{-10} to 5.4×10^{-10} m^2/s, whereas the peak corresponding to slower moving DDA remains at 0.9×10^{-10} m^2/s. With Figure 2.6, these results imply that the diffusion constant D_{mix} corresponds to more than one "type" of DDA, with one of the species interacting with the NCs.[29]

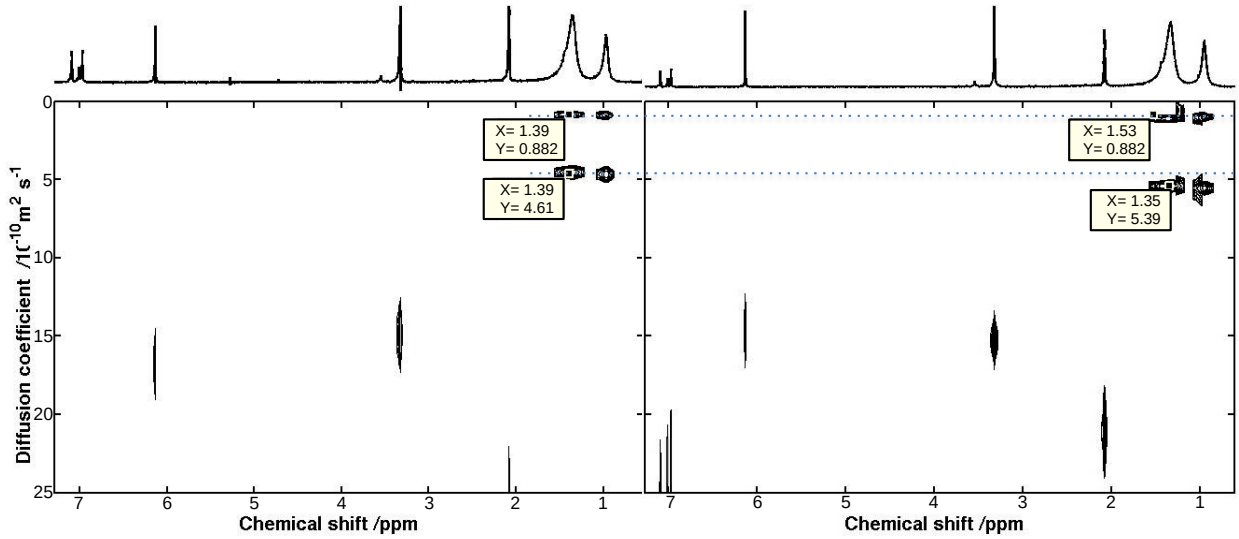

Figure 2.7. ^{1}H DOSY spectra of ZnO NCs. NCs as synthesized and NCs plus 20 equivalents of DDA per NC, left and right, respectively. The blue dotted lines were added to highlight the shift of the lower pair of DOSY peaks.

2.2.2 *Quantification of the Number of Dodecylamine Ligands in Each Regime*

The NMR data are well modeled using these three different classes of DDA binding to NCs: free, weakly associated, and strongly bound. A similar distinction between different levels of DDA association was presented in the study by Kahn *et al.*[15] They measured approximate rate constants of $k_{off\text{-}strong} = 13$ s^{-1} for dissociation of strongly associated DDA and $k_{off\text{-}weak} = 25 \times 10^5$ s^{-1} for dissociation of weakly associated amines.[15] This fast desorption rate of weakly associated amine from the NC surface is consistent with the rapid exchange with free DDA in the NMR spectra reported here. Here "weakly associated" encompasses all of the bound DDA molecules that exchange rapidly with free DDA and are not strongly bound to the NC surface like those

with D_{bound}. The nature of the bonding of the weakly associated DDA could involve Zn^{2+} sites that are less Lewis-acidic, Van der Waals interactions of the hydrocarbon chains with the strongly bound DDA (perhaps with the amine pointing out), and/or hydrogen bonding between the amine and the NC surface. Experiments with annealed nanocrystals discussed below favor a hydrogen bonding interaction with surface hydroxide groups.

One benefit of the averaged D_{mix} in this three-state model is the ability to determine the molar fractions of free and weakly associated DDA. For example, in a system with 100% free DDA (*i.e.* no weakly associated), D_{mix} would be equal to D_{free}. The two unknown mole fractions χ_{weak} and χ_{free} are determined from a set of two equations (Equation (2.2), Equation (2.3)), using the fraction of strongly bound DDA (χ_{bound}) calculated from integration of a 1D ^{1}H NMR spectrum (Figure 2.3), and assuming that when DDA molecules are bound to the NCs, they diffuse at the same rate. In other words, that the unknown D_{weak} is equal to D_{bound}.[22]

$$D_{mix} = \chi_{weak} D_{weak} + \chi_{free} D_{free} \tag{2.2}$$

$$\chi_{free} + \chi_{weak} + \chi_{bound} = 1 \tag{2.3}$$

Combining the data allows the calculation of the absolute number of bound DDA molecules per NC. The mole fractions and the NMR integrations *vs.* an internal standard give the concentration of each class of DDA. The concentration of NCs is given by the total Zn concentration (from ICP-OES) divided by the average number of Zn per NC.[11] Remarkably, 3.8 nm ZnO NCs have only 40-50 strongly bound DDA ligands.

The number of capping groups per nm^2 of NC surface area, also known as the ligand density, is given in Table 2.3. These calculations assume a spherical shape for the ZnO NCs, which is a good approximation based on TEM. The average ligand densities are remarkably constant across all as-prepared batches of NCs and sizes (Figure 2.8). The average ligand density of strongly bound DDA only is 1.0(3) per nm^2, and the density of both strongly bound and weakly associated DDA is 1.9(4) per nm^2. Different values are found for annealed NCs, as discussed below.

Table 2.3. Quantification of dodecylamine ligands on a variety ZnO NCs batches using ^{1}H and DOSY NMR data.

NC batch	NC diameter[a]	D_{bound}[b]	D_{mix}[c]	χ_{bound}[d]	χ_{weak}[e]	χ_{free}[e]	Surface area (nm^2)[f]	Total DDA/NC	DDA bound/ NC	DDA weak/ NC	DDA free/NC	Ligand/ nm^2 (bound +weak)	Ligand/ nm^2 (bound)
A	3.6(4)	0.9(1)	7.1(1.4)	0.43(6)	0.32(12)	0.26(10)	40	120(40)	50(20)	40(10)	30(10)	2.1(2)	1.2(2)
B	3.8(4)	0.9(2)	4.9(9)	0.47(5)	0.38(8)	0.15(8)	46	100(30)	40(15)	35(10)	25(15)	1.7(4)	0.9(3)
B*	3.8(4)	0.9(2)	9.3(14)	0.39(15)	0.23(2)	0.39(16)	46	140(40)	50(20)	30(10)	60(20)	1.8(3)	1.1(4)
B**	3.8(4)	0.9(1)	5.9(6)	0.47(5)	0.34(3)	0.20(2)	46	90(20)	40(15)	30(10)	20(5)	1.6(4)	0.9(3)
C	4.3(4)	1.3(3)	6.8(4)	0.34(6)	0.39(4)	0.27(2)	58	150(30)	55(10)	55(15)	40(10)	1.9(4)	0.9(2)
D	4.7(5)	1.1(4)	9.7(13)	0.39(4)	0.22(10)	0.40(14)	70	220(80)	85(40)	45(10)	90(40)	2.0(5)	1.2(4)
E	6.5(20)	0.9(1)	9.0(12)	0.59(4)	0.17(8)	0.24(6)	131	340(190)	200(100)	60(40)	70(50)	2.0(11)	1.6(8)
$F_{annealed}$	9.2(10)	1.1(10)	12(1)	0.51(8)	0.10(4)	0.39(6)	266	1870(100)	920(80)	200(100)	760(30)	4.2(3)	3.4(2)
$G_{annealed}$	9.5(10)	0.8(2)	7.1(14)	0.89(12)	0.06(4)	0.05(3)	284	1180(120)	1030(100)	90(70)	60(40)	4.0(2)	3.6(2)

[a] Average diameter of the NCs in the batch (values in nm), from the position of the first exciton peak (for $d < 7$ nm)[25] or TEM (for larger NCs), and the error is reported in parentheses as 10% or the standard deviation derived from TEM, respectively. [b] D values in units of 10^{-10} m^2/s and data are averaged using at least two of each 1D ^{1}H and DOSY experiments. Errors are calculated as two standard deviations from replicates or 10%, whichever was greater. [c] D_{mix} is the averaged diffusion coefficient between weakly bound and free DDA. [d] The mole fraction of strongly bound DDA (χ_{bound}) was calculated from fitting of a 1D NMR spectrum. [e] The mole fractions were calculated using Equations 2.2 and 2.3, assuming there are only three different classes of DDA in these solutions with ZnO NCs. $D_{free} = 1.45 \times 10^{-9}$ m^2/s for all of the calculations. [f] Diameter and surface area of the ZnO NCs without capping ligands, calculated assuming a spherical shape. * Batch labeled B* corresponds to batch B plus 65 equivalents of DDA per NC. ** Batch labeled B** corresponds to batch B diluted a factor of six to a final concentration of 1.3×10^{-4} M in NCs.

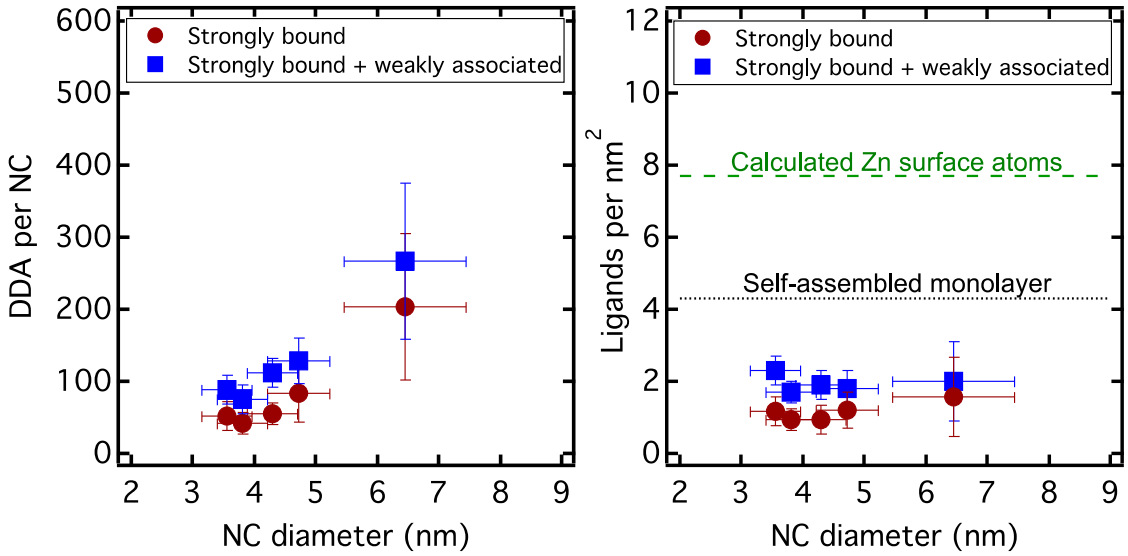

Figure 2.8. The number of DDA per NC versus NC diameter, and the number of ligands per nm^2 versus NC diameter, left and right, respectively.Errors are calculated as two standard deviations from replicates or 10%, whichever was greater. The black dotted line indicates SAM coverage for single crystal ZnO (4.2 per nm^2)[30] and the green dashed line indicates the coverage predicted with one DDA per calculated surface Zn (~7.7 per nm^2, average calculated from Table 2.5) .

2.2.3 *Comparison of Ligand Surface Density to SAMs and Surface Cation Estimates*

The significance of the observed surface ligand densities is revealed by comparison with the maximum surface coverage. To assess the maximum surface coverage, one can (1) estimate the number of available surface Zn binding sites or (2) compare to maximum coverage of similar ligands in the self-assembled monolayer (SAM) literature. There are a number of published methods to estimate the number of surface ions.

To estimate the number of surface Zn atoms per NC, we considered the approach used in several reported calculations with CdSe, as listed below in Table 2.4. Many authors have calculated the number of surface atoms.[3-8] Each method is explained with a pictorial representation for clarity, and the result of the calculation when applied to a ZnO NC with d = 3.55 nm. Calculations of ligand packing densities were also considered (bottom entry), based on sterics.

Table 2.4. Estimation of the number of surface atoms per nanocrystal. The average Zn-O bond length in wurtzite ZnO is 2.0 Å. The volume of a unit cell of ZnO is 0.04766 nm^3, with two ZnO units per unit cell. For wurtzite CdSe, the Cd-Se bond length is 0.262 nm.

Calculation	**Approach**	**Reference**	**Extended for ZnO (*d* = 3.55 nm)**
$n_{Cd}(surface) = n_{CdSe}(total) - n_{CdSe}(core^*)$ *core radius = [QD radius – one Cd-Se bond (0.262 nm)]	Core-shell: Shell thickness of one Cd-Se bond length.	Ref 19‡	296 surface Zn atoms
$n_{Cd}(surface) = n_{CdSe}(total) - n_{CdSe}(core^*)$ *core radius = [QD radius – two Cd-Se bonds (0.524 nm)]	Core-shell: Shell thickness of Cd-Se-Cd bond length.	Ref 18	526 surface Zn atoms
$n_{Cd}(surface) = n_{CdSe}(total) - n_{CdSe}(core^*)$ *core radius = [QD radius – 1.5 × one Cd-Se bond (0.393 nm)]	Core-shell: Shell thickness of 1.5 × one Cd-Se bond length.	Ref 31	418 surface Zn atoms
$n_{Cd}(surface) = 4N^{\frac{2}{3}}$ N = the total number of atoms	Calculated surface atoms: Weighted by the total number of atoms.	Ref 32	314 surface Zn atoms (628 total atoms, assuming 1:1 Zn:O)
$n_{Cd}(surface) = \left(\frac{\pi}{4}\right)\left(\frac{4\pi r_{QD}^2}{\pi r_{S^{2-}}^2}\right)$	Surface packing: 2D circles (radius of a S atom) onto the surface of a sphere (radius of QD).	Ref 33	247 Zn atoms (assuming Zn radius of 2 Å)
$n_{ligands}(surface) = \left(\frac{\pi}{2\sqrt{3}}\right)\left(\frac{4\pi r_{QD}^2}{\pi r_{ligand-cone}^2}\right)$	Surface packing: ligands represented as cones on the surface of a sphere (radius of QD).	Ref 34	623 DDA ligands

‡By our calculations, the number of Cd atoms was underestimated by half in ref 19 (173 Cd atoms, not 86), because the unit cell of wurtzite CdSe contains two Cd atoms.

Table 2.5 uses the method of the first entry in Table 2.4, one of the more conservative estimates of surface Zn atoms, to calculate the fraction of surface atoms bound to a surface DDA ligand (as determined by our NMR measurements). The number of Zn atoms in the outer shell (the grey shaded area) is calculated by determining the number of ZnO unit cells in that volume, and the number of Zn atoms will be double this value. We find that the number of uncapped surface atoms is between 15% and 30% of the total Zn atoms of the NC.

Table 2.5. Calculation of Zn surface atoms for spherical ZnO NCs. Using the method of Kuno *et al,*[19] the number of surface Zn atoms was calculated for the NCs studied here.

NC batch	**NC diameter (rounded to nearest 0.1 nm)**	**ZnO cells/NC**	**Zn atoms/NC**	**Inner sphere (two Zn-O bonds)**	**Surface Zn (rounded to nearest ten)**
A	3.6(4)	492	984	3.15	300
B	3.8(4)	607	1215	3.41	340
C	4.3(4)	874	1748	3.90	440
D	4.7(5)	1163	2326	4.33	540
E	6.5(20)	2948	5896	6.05	1030
$F_{annealed}$	9.2(10)	8555	17110	8.80	2140
$G_{annealed}$	9.5(10)	9419	18839	9.10	2280

Table 2.6 incorporates the NMR data presented above. Including *both* the weakly associated and strongly bound ligands, the surface Zn sites are 25(6)% covered, independent of NC size and concentration. Considering only strongly bound DDA ligands gives 15(5)% coverage of surface Zn. Thus a quarter or less of the calculated Zn surface atoms are bound to DDA according to surface cation calculations.

Table 2.6. Calculation of surface coverage using the number of Zn unit cells per NC.[a]

NC batch	NC diameter	Surface Zn atoms[a]	% surface Zn with strong +	% surface Zn with strong DDA	Zn surface atoms without DDA[b]
A	3.6(4)	300	30%	18%	210(30)
B	3.8(4)	340	22%	12%	270(30)
C	4.3(4)	440	25%	12%	330(20)
D	4.7(5)	540	24%	15%	410(60)
E	6.5(20)	1030	26%	20%	760(100)
$F_{annealed}$	9.2(10)	2140	58%	48%	900(200)
$G_{anneale}$	9.5(10)	2280	49%	45%	1160(50)

[a] Calculated assuming that all Zn atoms within 2 Å of the surface (one Zn-O bond) can be considered a surface Zn, following Kuno *et al.*[19] [b] This estimate is conservative because it assumes both strongly bound and weakly associated DDA occupy Zn sites, and assumes fewer surface atoms than most estimates in the literature (Table 2.4).

It is also informative to compare capping densities to maximum coverages achieved in SAMs. In this literature, the maximum coverage or saturation is often defined as "the highest possible packing of molecules", which generally does not correspond to one ligand per surface Zn atom.[35] For single crystal ZnO($10\bar{1}0$) surfaces, Chen *et al.* found that although DDA did not form a stable monolayer, similarly sized or larger thiols and phosphonic acids formed monolayers with surface coverages of 4.2 and 4.4 molecules per nm^2, respectively.[30] In the gold nanoparticle literature, Hinterwirth *et al.* observed higher ligand densities on nanoparticles than on a flat surface, up to 6.3 per nm^2, versus the theoretical 4.6 per nm^2 maximum coverage for a flat surface.[35] These authors suggest the higher coverage arises from the existence of edges and corners in a spherical nanoparticle, versus a flat surface. Thus, taking the non-polar ZnO($10\bar{1}0$) surface as representative of the various nanocrystal surfaces, the small DDA capping group should provide a maximum surface coverage of >4.2 per nm^2 on ZnO, and likely higher due to the small footprint of DDA and the edges and corners inherent to a quasi-spherical NC. Considering strongly bound DDA ligands only, the ligand density of ZnO NCs reported here, 1.0(3) per nm^2, is less than 25(8)% of the 4.2 per nm^2 lower estimate anticipated for a ZnO SAM.

If the weakly associated DDA molecules are also counted, the total ligand density of 1.9(4) per nm^2 rises to only 45(10)% of that anticipated for a SAM on a flat ZnO surface.

Reported surface densities for *anionic* ligands such as oleate and TOPO-derived anions, on chalcogenide and phosphide NCs, span values from 5 to 0.57 per nm^2.[13,36-40] These have been determined using ^1H NMR spectroscopy, thermogravimetric analysis (TGA), or X-ray photoelectron spectroscopy (XPS). It is important to distinguish neutral ("L-type") capping ligands, like DDA, from anionic ligands such as carboxylates or phosphonates ("X-type"). Dissociation of X-type ligands should require stoichiometric protons to form HX, and the activity and concentration of these protons may be a key factor for ligand coverage.[41] Comparisons between ZnO and chalcogenide NCs are complicated not only by the different ligand types but also by different unit cell sizes (unit cell volumes: CdSe, 112.2 $Å^3$; ZnO, 47.6 $Å^3$)[42] which imply different cation surface densities.

In sum, the surface coverages of as-prepared ZnO nanocrystals by strongly bound and weakly associated DDA are quite low compared to the typical image of a fully covered NC, by comparison to both surface cation estimates and the maximum coverage estimated for SAMs.

2.2.4 *Reasons for Low Capping Ligand Coverage*

The low surface coverage could have a number of origins: sterics, inaccessibility of Zn sites, or blockage by other species. Each of these possibilities is discussed in turn.

The density of capping ligands on NCs has been examined theoretically, as in Bullen and Mulvaney's modeling of a spherical NC with ligands represented by cones.[34] They estimated maximum surface coverage for large ligands such as trioctylphosphine oxide (TOPO) to be limited by steric bulk to only 30% of Cd+Se surface atoms for a 3.4 nm NC. Katari *et al.* found these estimates to agree with experimental X-ray photoelectron spectroscopy (XPS) coverage estimates of TOPO on CdSe.[20] However, terminal, linear aliphatic amines such as DDA have a much smaller "swept-out" cone radius,[34] which should allow binding to all surface metal atoms even on a flat surface. X-ray structures of small-molecule μ-oxo bridged Zn clusters with amine ligands also suggest that sterics should not limit DDA binding density.[43] Therefore sterics are unlikely to play a part in the low surface coverage.

The low observed DDA coverage may also be caused by blockage of Zn sites by other surface species or "ligands" for Zn. The likely candidates are DMSO, hydroxide, or ethoxide, since the NCs are formed in a hydrolytic process that involves ethanol and DMSO.[24] Unfortunately, such surface species are not directly observable by ^{1}H NMR spectroscopy, and DMSO has never been observed in any of the NMR spectra. Some have suggested that "residual water" is associated with ZnO and CdTe,[15,22] but released water was not observed in the NMR spectra for the samples described here. Annealing to remove associated water/hydroxide is discussed below. Alcohols are known to dissociate on the polar ZnO(000$\bar{1}$) face to form stable alkoxide intermediates.[44] In support of this hypothesis, added ethanol does reversibly interact with the NCs as judged by a change in the ^{1}H NMR chemical shift of the added ethanol. Treating NCs with ethanol-d_6 produced some CH_3CH_2OD, by ^{1}H NMR spectroscopy, but only a very small amount, < 10 per NC (*vide infra*). Thus, there is a small concentration of exchangeable ethanol/ethoxide on the surface, but not enough to account for the low DDA coverage observed here.

To coarsely investigate residual surface ligands, solutions of ZnO NCs in toluene were dried in vacuo and weighed before and after calcining (to remove all organics) using a microbalance (Table 2.7). The samples were calcined at 500 °C for 2 hours. As a control, an empty vial was similarly treated. The mass difference of the empty vial was < 0.2 mg, indicating that the observed weight loss in the other vials originates from the NCs, not from the glass itself or something about the procedure. In most cases the loss of mass is approximately the amount of DDA calculated from NMR integration.

Table 2.7. Calcination of NCs to investigate organic materials.

Sample	**NC diameter (nm)**	**Mol NCs**	**Vial before calcining (g)**	**Vial after calcining (g)**	**Mass difference (g)**	**DDA per NC[a]**	**DDA found per NC[b]**	**ΔDDA per NC[c]**
A	3.6	1.35×10^{-7}	4.6680 ± 0.0002	4.6642 ± 0.0001	0.0038 ± 0.0002	150 ± 10	120 ± 30	30 ± 30
A	3.6	1.35×10^{-7}	4.6541 ± 0.0002	4.6497 ± 0.0001	0.0044 ± 0.0002	175 ± 10	120 ± 30	50 ± 30
B	3.8	4.6×10^{-8}	4.6804 ± 0.0002	4.6788 ± 0.0002	0.00165 ± 0.0002	190 ± 10	90 ± 15	100 ± 30
B	3.8	9.2×10^{-8}	4.6563 ± 0.0002	4.6535 ± 0.0002	0.0028 ± 0.0002	170 ± 10	90 ± 15	80 ± 30
D	4.7	4.86×10^{-8}	4.5836 ± 0.0002	4.5809 ± 0.0002	0.0027 ± 0.0003	290 ± 35	220 ± 70	70 ± 70
Vial only (control)	-	-	4.6498 ± 0.0001	4.6495 ± 0.0002	0.0002 ± 0.0002	-	-	-

[a] Attributes all of the mass to DDA. [b] Calculated from ^{1}H NMR spectra. [c] Difference between the calculated DDA molecules per NC and the calculated number of DDA molecules from calcination.

To probe ethanol binding to the ZnO NCs, aliquots of a stock solution of ethanol (CH_3CH_2OH) in toluene-d_8 were added to a solution of NCs (8.5×10^{-4} M) in toluene-d_8 and ^{1}H NMR spectra were obtained (Figure 2.9). Each 5 µL aliquot of ethanol in toluene-d_8 was approximately one equivalent of ethanol per NC. The methyl peak of ethanol at low concentrations is downfield of the reported chemical shift of ethanol in toluene (0.97 ppm), but as more ethanol is added, shifts upfield. This shift with extra ethanol indicates an exchange process between free and bound ethanol. To test this theory, Nuclear Overhauser Effect Spectroscopy (NOESY) was performed, with a 100 ms mixing time (Figure 2.10). The existence of cross peaks at (3.4 ppm, 1.03 ppm) and (3.4 ppm, 1.1 ppm) indicate that ethanol spends time on the surface of the NC, either exchanging or nearby the bound ligands.[2]

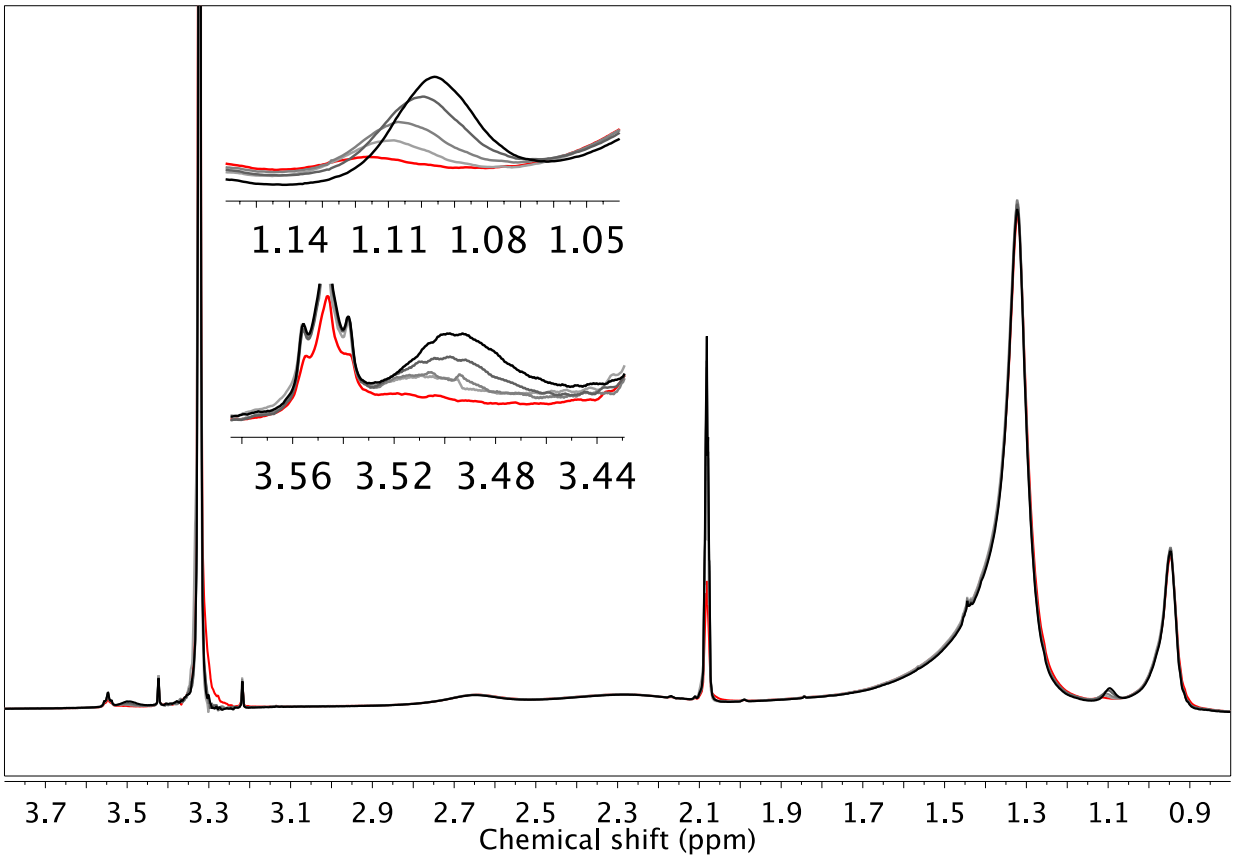

Figure 2.9. Overlay of ^{1}H NMR spectra of ZnO NCs in toluene-d_8 plus ethanol, each addition monitored after 10 minutes of equilibration. Each aliquot is approximately one equivalent per NC (grayscale), where darker gray indicates increasing equivalents of ethanol (1 equiv, 2 equiv, 3 equiv, and 4 equiv), and the NCs alone are shown in red. Insets are the two regions for ethanol.

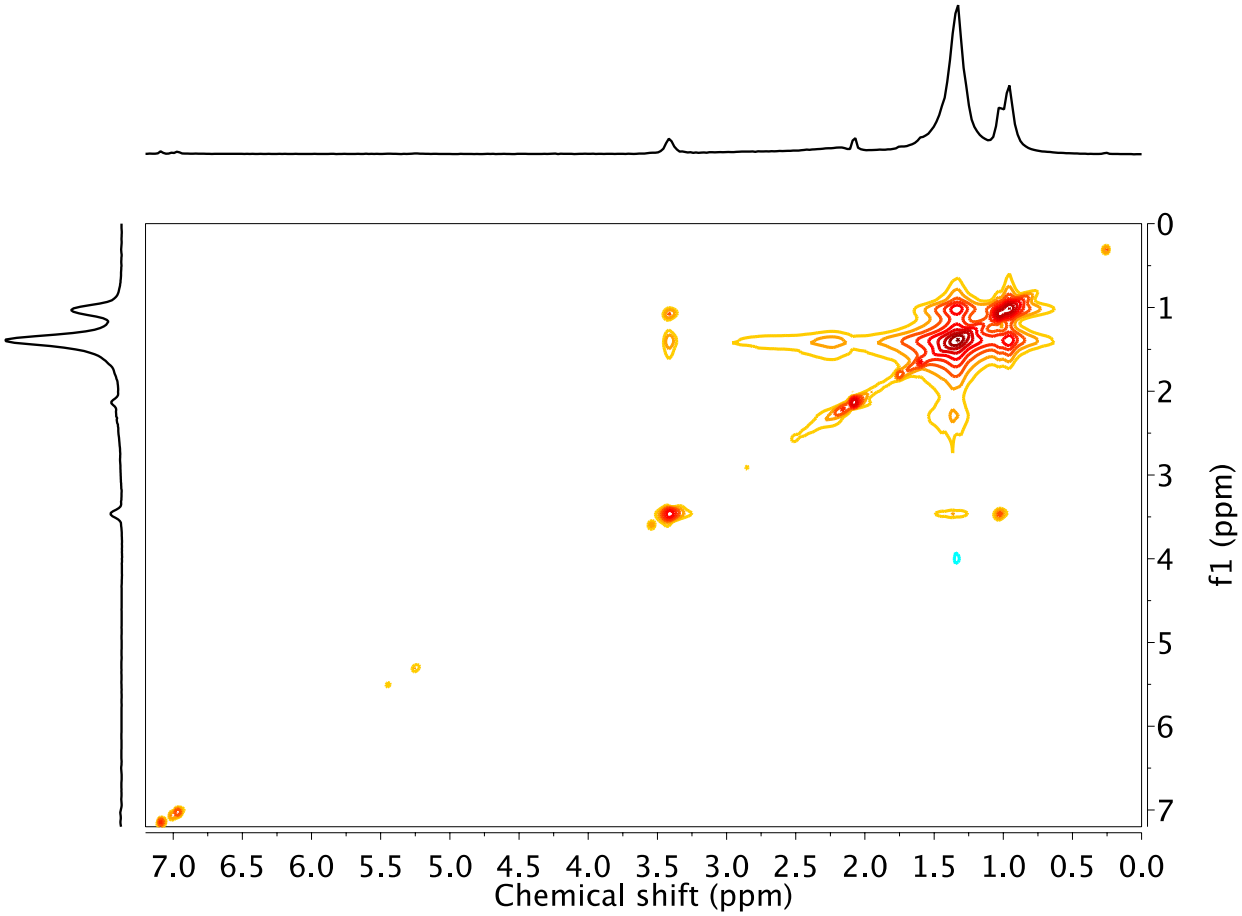

Figure 2.10. NOESY spectrum of ZnO NCs (2.4×10^{-4} M) in toluene-d_8 with a mixing time of 100 ms. Cross peaks (3.4 ppm, 1.03 ppm) and (3.4 ppm, 1.1 ppm) between ethanol and DDA suggest that ethanol spends time on the surface of the NC.

To probe the amount of any exchangeable ethanol molecules on the surface, ethanol-d_6 (300 equiv) was added to a solution of ZnO NCs (6.8×10^{-4} M). We anticipated that residual ethanol (CH_3CH_2OH) bound to the surface will exchange with the added ethanol-d_6, and signals for ethanol at ~ 1 ppm should appear. Instead, there is no apparent change in the ^{1}H NMR spectrum, indicating the absence of a significant concentration of exchangeable ethanol on the NC surface. This result, coupled with Figure 2.9, suggests that there are only trace residual ethanol molecules on the NC surface (< ~10 per NC), with an equilibrium between bound and unbound ethanol.

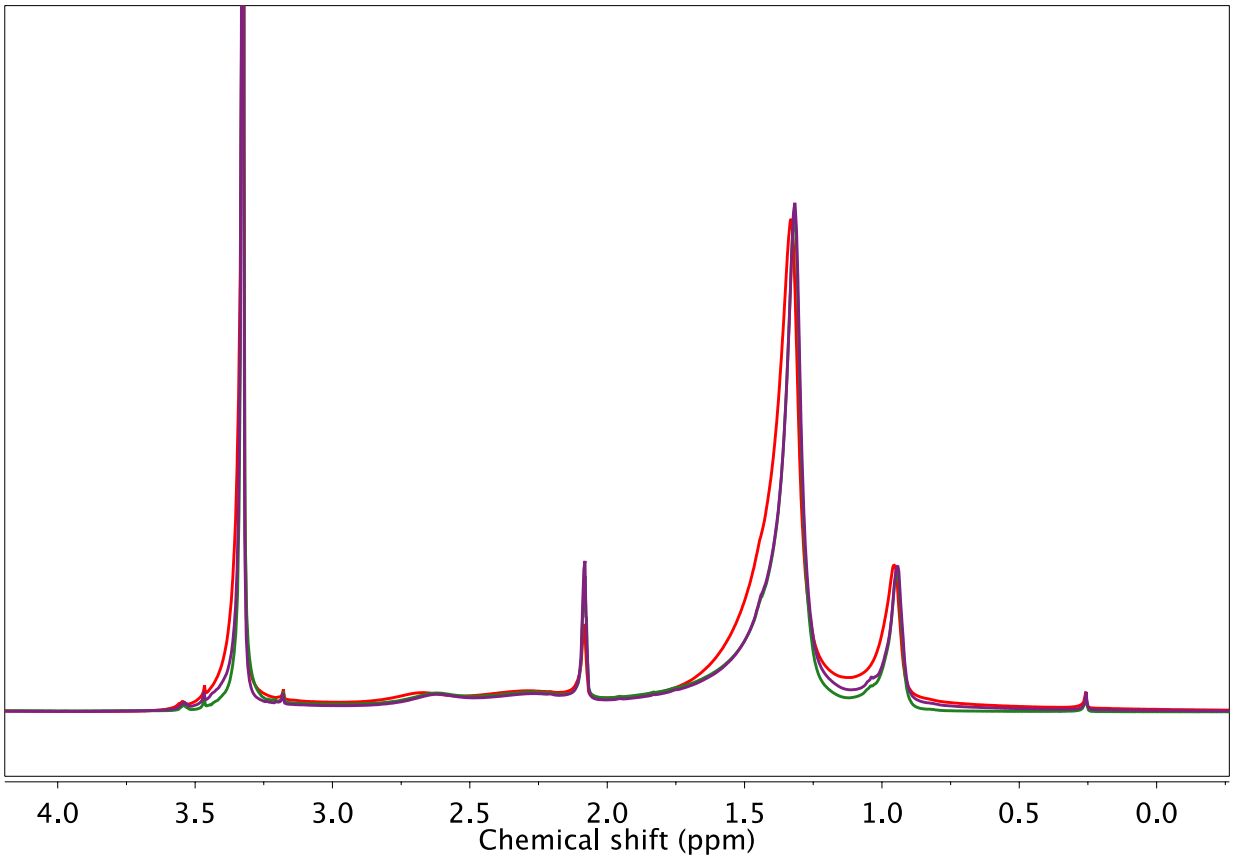

Figure 2.11. Overlay of ^{1}H NMR spectra of toluene-d_8 solutions of ZnO NCs plus ethanol-d_6 (NCs: 6.75×10^{-4} M): (red); (purple): 20 min after addition of 600 equiv of ethanol-d_6; (green): 24 hours later.

Another possible origin of the low DDA coverage is that the exposed NC surfaces are oxide rich. Of the four most common surfaces of wurtzite ZnO, $(10\bar{1}0)$ and $(11\bar{2}0)$ are nonpolar and therefore balanced in Zn and O atoms, $(000\bar{1})$ is primarily Zn terminated and $(000\bar{1})$ is primarily O-terminated.[45,46] Annealing is suggested to increase the fraction of the low energy $(10\bar{1}0)$ surfaces,[17] but little to no faceting is observed in the TEM images of our annealed samples (*vide infra*). Overall, the spherical nature of the NCs and the lack of faceting in the TEM images suggest that surface faceting is unlikely the origin of the low coverage of strongly bound DDA.

It is most likely that the low DDA coverage is due to the presence of surface hydroxide ligands, which reduce the number of sites available for DDA binding. Indeed, ZnO NCs prepared

by this method show OH stretches in their IR spectra. Heating in molten DDA causes these stretches to disappear, suggesting loss of H_2O.[17] The hypothesis that surface hydroxide ligands block DDA binding was tested by performing a similar annealing experiment, in which the present ZnO NCs were heated in molten DDA at 160 °C for 12 hours. TEM images show that the initial NCs (d = 3.8(4) nm) grow upon annealing, in this case to d = 9.2(10) nm (Figure 2.12). Efforts to make annealed NCs of the same size as room temperature as-prepared NCs (d < 7 nm) were unsuccessful, as observed in previous reports of DDA annealed NCs.[17] Previous studies have indicated that the annealed NCs are more predominantly hexagonal and therefore likely enriched in the lowest energy ZnO($10\bar{1}0$) surfaces,[17,46] although such hexagonal faceting is not evident in our images. ^{1}H and DOSY NMR analysis was performed to quantify the number of DDA ligands on the surface. The annealed NCs showed dramatic changes in the associated DDA, with a decrease in the density of weakly bound ligands and an increase in strongly bound ligands. The density of strongly bound DDA increases by a factor of three or more, to 3.5(3) per nm^2. This corresponds to ca. 45% of the estimated surface Zn atoms covered with strongly bound DDA, and is ~80% of the estimated coverage for a SAM on single crystal ZnO.

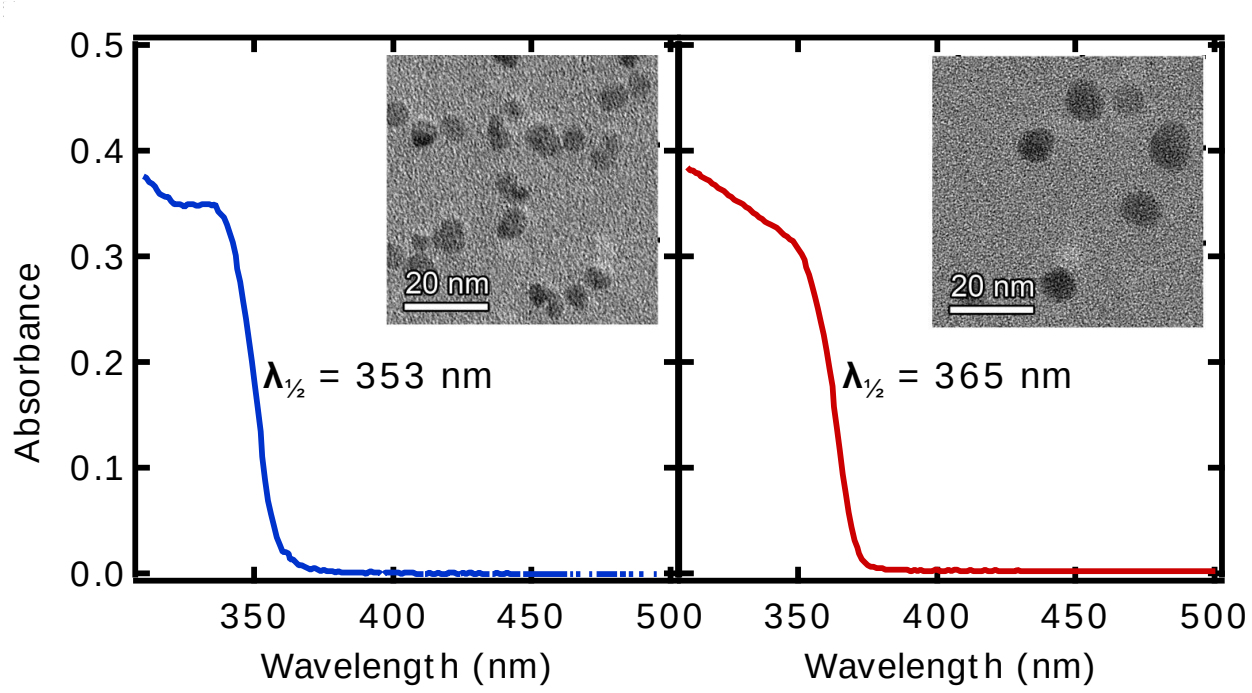

Figure 2.12. Optical absorption spectra in toluene and TEM images of batches B ZnO NCs (left, d = 3.8(4) nm) and annealed $F_{annealed}$ (right, d = 9.2(10) nm). We note that sample B had

aged for several months before the TEM analysis, and the particles grew slightly, so a more accurate determination of the size was accomplished using $\lambda_{½}$ according to reference.[25]

Annealing reduces the number of weakly associated ligands to 0.6(3) nm^{-2}, reduces the number of surface hydroxides,[17] and increases the number of strongly bound DDA molecules. One comprehensive explanation for these observations is that surface hydroxides can be considered "ligands" for Zn atoms at the surface, thereby blocking those cations from DDA. As annealing removes the hydroxides, the Zn sites are now open for a strong bond between Zn and the N of DDA. The robust binding is surprising because neutral monodentate alkylamines are not particularly strong ligands for Zn^{2+} in molecular coordination chemistry.[47,48] A roughly equivalent description is that the NCs are proton-terminated ZnO, and the strongly bound DDA binds to zinc atoms exposed by surface oxygen vacancies. Annealing with loss of H_2O forms more surface oxygen vacancies and therefore strongly binds more DDA. The weakly associated DDA ligands likely form hydrogen bonds to the hydroxides in the non-annealed NCs. This is more likely than purely Van der Waals forces between the long aliphatic chains because of the decrease of the weakly associated DDA upon removal of hydroxide.

2.3 Conclusions and Outlook

The surface coverage of neutral dodecylamine (DDA) capping ligands on ZnO NCs suspended in toluene solvent was investigated using a variety of NMR spectroscopies. Rather than a picture of a densely packed shell of ligands, our results implicate sparse or patchy coverage of amine capping ligands. 1D and DOSY ^{1}H NMR spectroscopies indicate that the DDA molecules in NC solutions can be divided into three categories: strongly bound, weakly associated, and free DDA. There are only ca. 15(5)% strongly bound DDA ligands per estimated surface zinc atom, which is less than 25(8)% of the coverage for a self-assembled monolayer. Figure 2.1 above is a fairly dramatic illustration of the low density found. NCs annealed at 160 °C for 12 h in molten DDA, which are thought to have fewer surface hydroxyl groups,[17] have more than three times the surface coverage of strongly bound DDA (1.0(3) per nm^2 to 3.5(3) per nm^2, respectively). This suggests that annealing causes the replacement of surface hydroxide ligands by DDA. Equivalently, the NCs could be described as proton-terminated ZnO, and annealing causes loss of H_2O to form surface oxygen vacancies, or bare Zn atoms, that strongly bind DDA.

The as-synthesized NCs have a substantial amount of weakly associated DDA, from 30-100% of the strongly bound ligands. These DDA ligands are much less abundant for the annealed NCs, suggesting that their weak interaction involves hydrogen bonding to surface hydroxides. These results paint a picture of ZnO NC surfaces lightly populated with a dynamic and complex shell of DDA ligands. This provides one explanation for the facile charge transfer reactions of these ZnO NCs,[11,33,49] especially proton-coupled electron transfer (PCET) reactions in which the e^-/H^+ abstractor likely has to come to the surface to remove the proton.[9]

2.4 EXPERIMENTAL

2.4.1 *General Considerations*

Tetramethylammonium hydroxide (TMAOH), zinc acetate dihydrate, trimethoxybenzene (TMB), and dodecylamine (DDA, 98%) were purchased from Aldrich and used as received. Toluene-d_8 and THF-d_8 were purchased from Cambridge Isotope, degassed by three freeze-pump-thaw cycles and (in the case of THF) dried by storage over sieves for two days. All other solvents were purchased from Fischer Scientific and were dried using a Seca Solvent System installed by Glass Contour. Fluka TraceCERT® High Purity brand Zn standard (1000 μg/L in 2% HCl) was used as the standard for ICP-OES which was carried out using a Perkin Elmer Optima 8300. ZnO NCs were prepared by base hydrolysis from $Zn(OAc)_2 \bullet 2H_2O$.[24] The annealed NCs were heated in molten DDA for 12 h at 160 °C.[17]

2.4.2 *Microscopy and Spectroscopy*

TEM images were collected using a FEI Tecnai G2 F20. Average diameter of the NCs in the batch (values in nm) were determined from the position of the first exciton peak ($d < 7$ nm)[25] or from statistical analysis of TEM images using ImageJ ($d > 7$ nm). The error is reported as 10% or as the standard deviation derived from a Gaussian fit to the histogrammed TEM, respectively. Optical spectra were acquired using a Hewlett Packard 8453 diode array spectrophotometer.

Samples for NMR spectroscopy were prepared under N_2 in a glovebox. 1D ^{1}H NMR spectra were obtained on Bruker AV300, AV301, DRX499, AV500, AV700 or AV800 (with a cryogenically cooled probehead) spectrometers, and the data were processed using MestReNova© version 7.1.2. DOSY data were collected on the DRX499, AV700, and AV800

spectrometers equipped with TBI Z gradient probe heads. The DOSY data were processed with "DOSY Toolbox" version 1.5 using Local Covariance Order Diffusion-Ordered Spectroscopy (LOCODOSY) to more effectively resolve overlapping peaks[28] and the results were superior to those obtained from DOSY processing with MestReNova or TopSpin. Chemical shifts are reported relative to TMS by referencing the residual solvent. ^{1}H NMR spectra were recorded with a 15 s delay between scans to allow full relaxation of the DDA and methyl signals of trimethoxybenzene (TMB), which was added to the NMR samples as a concentration standard. The T_1 was measured for the methyl signals of TMB and were found to be approximately 2 seconds. In the DOSY experiments, the pulse program used was ledbpgp2s, and the gradient shape SINE.100 or SMSQ10.100. The gradient duration δ and the diffusion delay Δ were optimized for each sample by comparing one slice of signals at 95% gradient strength and 5% strength (using 1D pulse program ledbpgp2s1d). Values were chosen which led to approximately 90% loss of the initial intensity of the peaks of interest at highest gradient, and were typically δ = 1 - 3 ms and Δ = 100 - 200 ms. The eddy current compensation was set at 5 ms. In the full DOSY experiment, the amplitude of the sinusoidal gradient pulses was varied exponentially in strength from 5 to 95% of the maximum strength in 16 or 32 steps.

2.4.3 *Fitting of NMR Spectra*

MestReNova was used to deconvolve the overlapping peaks using the Line Fitting and Global Spectral Deconvolution (GSD) tools. The number of peaks was fixed, but the peak heights, widths, and areas were allowed to vary based on minimizing the residual. In addition, the ratios of Gaussian to Lorentzian lineshapes were allowed to float, given that the NMR spectra are complicated by heterogeneous broadening of NC sizes. Empirically, the upfield peaks assigned in the main text to D_{mix} were always Lorentzian, whereas the upfield broadened peaks assigned to bound DDA were generally Gaussian.

2.4.4 *Calcination of NC Samples*

ZnO samples were dried to a solid in 3 mL scintillation vials, being very careful to avoid placing fingerprints on the vial. Using a microbalance, the vials containing the solid NCs were weighed three times each, alternating between samples, and the standard deviation was calculated between the three trials. The vials were then calcined at 500 °C for 2 hours until the solid

appeared completely yellow, indicating that all of the organic compounds had been removed. After calcination, the vials were again weighed using the microbalance.

2.5 NOTES TO CHAPTER 2

(1) Tian, J.; Cao, G. *Nano Rev* **2013**, *4*, 22578.

(2) Bruchez, M.; Moronne, M.; Gin, P.; Weiss, S.; Alivisatos, A. P. *Science* **1998**, *281*, 2013.

(3) Weiss, E. A. *Acc. Chem. Res.* **2013**, *46*, 2607.

(4) El-Sayed, M. A. *Acc. Chem. Res.* **2004**, *37*, 326.

(5) Smith, A. M.; Nie, S. *Acc. Chem. Res.* **2009**, *43*, 190.

(6) Munro, A. M.; Jen-La Plante, I.; Ng, M. S.; Ginger, D. S. *J. Phys. Chem. C* **2007**, *111*, 6220.

(7) Majetich, S. A.; Carter, A. C.; Belot, J.; McCullough, R. D. *J. Phys. Chem.* **1994**, *98*, 13705.

(8) Knowles, K. E.; Tagliazucchi, M.; Malicki, M.; Swenson, N. K.; Weiss, E. A. *J. Phys. Chem. C* **2013**, *117*, 15849.

(9) Schrauben, J. N.; Hayoun, R.; Valdez, C. N.; Braten, M.; Fridley, L.; Mayer, J. M. *Science* **2012**, *336*, 1298.

(10) Valdez, C. N.; Braten, M.; Soria, A.; Gamelin, D. R.; Mayer, J. M. *J. Am. Chem. Soc.* **2013**, *135*, 8492.

(11) Hayoun, R.; Whitaker, K. M.; Gamelin, D. R.; Mayer, J. M. *J. Am. Chem. Soc.* **2011**, *133*, 4228.

(12) Yin, Y.; Alivisatos, A. P. *Nature* **2005**, *437*, 664.

(13) Morris-Cohen, A. J.; Malicki, M.; Peterson, M. D.; Slavin, J. W. J.; Weiss, E. A. *Chem. Mater.* **2012**, 1155.

(14) Anderson, N. C.; Hendricks, M. P.; Choi, J. J.; Owen, J. S. *J. Am. Chem. Soc.* **2013**, *135*, 18536.

(15) Coppel, Y.; Spataro, G.; Pagès, C.; Chaudret, B.; Maisonnat, A.; Kahn, M. L. *Chem. Eur. J.* **2012**, *18*, 5384.

(16) Hens, Z.; Martins, J. C. *Chem. Mater.* **2013**, *25*, 1211.

(17) Norberg, N. S.; Gamelin, D. R. *J. Phys. Chem. B* **2005**, *109*, 20810.

(18) Kalyuzhny, G.; Murray, R. W. *J. Phys. Chem. B* **2005**, *109*, 7012.

(19) Kuno, M.; Lee, J. K.; Dabbousi, B. O.; Mikulec, F. V.; Bawendi, M. G. *J. Chem. Phys.* **1997**, *106*, 9869.

(20) Katari, J. E. B.; Colvin, V. L.; Alivisatos, A. P. *J. Phys. Chem.* **1994**, *98*, 4109.

(21) Evans, C. M.; Cass, L. C.; Knowles, K. E.; Tice, D. B.; Chang, R. P. H.; Weiss, E. A. *J. Coord. Chem.* **2012**, *65*, 2391.

(22) Fritzinger, B.; Moreels, I.; Lommens, P.; Koole, R.; Hens, Z.; Martins, J. C. *J. Am. Chem. Soc.* **2009**, *131*, 3024.

(23) Canzi, G.; Mrse, A. A.; Kubiak, C. P. *J. Phys. Chem. C* **2011**, *115*, 7972.

(24) Schwartz, D. A.; Norberg, N. S.; Nguyen, Q. P.; Parker, J. M.; Gamelin, D. R. *J. Am. Chem. Soc.* **2003**, *125*, 13205.

(25) Meulenkamp, E. A. *J. Phys. Chem. B* **1998**, *102*, 5566.

(26) Wood, A.; Giersig, M.; Hilgendorff, M.; Vilas-Campos, A.; Liz-Marzán, L. M.; Mulvaney, P. *Aust. J. Chem.* **2003**, *56*, 1051.

(27) Hens, Z.; Moreels, I.; Martins, J. C. *ChemPhysChem* **2005**, *6*, 2578.

(28) Nilsson, M. *J. Magn. Reson.* **2009**, *200*, 296.

(29) Sandström, J. *Dynamic NMR Spectroscopy*; Academic Press Inc.: New York, 1982.

(30) Chen, J.; Ruther, R. E.; Tan, Y.; Bishop, L. M.; Hamers, R. J. *Langmuir* **2012**, *28*, 10437.

(31) Morris-Cohen, A. J.; Donakowski, M. D.; Knowles, K. E.; Weiss, E. A. *J. Phys. Chem. C* **2010**, *114*, 897.

(32) Hamann, T. W.; Gstrein, F.; Brunschwig, B. S.; Lewis, N. S. *Chem. Phys.* **2006**, *326*, 15.

(33) Morris-Cohen, A. J.; Frederick, M. T.; Cass, L. C.; Weiss, E. A. *J. Am. Chem. Soc.* **2011**, *133*, 10146.

(34) Bullen, C.; Mulvaney, P. *Langmuir* **2006**, *22*, 3007.

(35) Hinterwirth, H.; Kappel, S.; Waitz, T.; Prohaska, T.; Lindner, W.; Lämmerhofer, M. *ACS Nano* **2013**, *7*, 1129.

(36) Anderson, N. C.; Owen, J. S. *Chem. Mater.* **2012**, *25*, 69.

(37) Moreels, I.; Martins, J. C.; Hens, Z. *ChemPhysChem* **2006**, *7*, 1028.

(38) Hassinen, A.; Gomes, R.; De Nolf, K.; Zhao, Q.; Vantomme, A.; Martins, J. C.; Hens, Z. *J. Phys. Chem. C* **2013**, *117*, 13936.

(39) Hassinen, A.; Moreels, I.; De Nolf, K.; Smet, P. F.; Martins, J. C.; Hens, Z. *J. Am. Chem. Soc.* **2012**, *134*, 20705.

(40) Gomes, R.; Hassinen, A.; Szczygiel, A.; Zhao, Q.; Vantomme, A.; Martins, J. C.; Hens, Z. *J. Phys. Chem. Lett.* **2011**, *2*, 145.

(41) De Roo, J.; Van den Broeck, F.; De Keukeleere, K.; Martins, J. C.; Van Driessche, I.; Hens, Z. *J. Am. Chem. Soc.* **2014**.

(42) Madelung, O. *Semiconductors: Data Handbook*; 3rd ed.; Springer: New York, 2004.

(43) Song, B.; Reuber, J.; Ochs, C.; Hahn, F. E.; Lügger, T.; Orvig, C. *Inorg. Chem.* **2001**, *40*, 1527.

(44) Vohs, J. M. *Chem. Rev.* **2012**, *113*, 4136.

(45) Jagadish, C.; Pearton, S. J. *Zinc Oxide Bulk, Thin Films and Nanostructures*; Elsevier Ltd.: Amsterdam, 2006.

(46) Henrich, V. E.; Cox, P. A. *The Surface Science of Metal Oxides*; Press Syndicate of the University of Cambridge: Cambridge, 1994.

(47) Wilkinson, G.; Gillard, R. D.; McCleverty, J. A. *Comprehensive Coordination Chemistry*; Pergamon Books Ltd.: Great Britain, 1987; Vol. 5.

(48) McCleverty, J. A.; Meyer, T. J. *Comprehensive Coordination Chemistry II*; Elsevier Ltd.: Oxford, UK, 2004; Vol. 6.

(49) Morris-Cohen, A. J.; Aruda, K. O.; Rasmussen, A. M.; Canzi, G.; Seideman, T.; Kubiak, C. P.; Weiss, E. A. *Phys. Chem. Chem. Phys.* **2012**, *14*, 13794.

Chapter 3. PROTONS GENERATED FROM PHOTOCHEMICAL REDUCTION OF ZNO NANOCRYSTALS

Much of the chemistry explored in this thesis will explore reactions that move electrons and protons in or out of ZnO nanocrystals (NCs). The methods used to achieved reduced NCs were photochemical (absorption of light followed by hole quenching) or chemical, by the addition of reductants with or without acid. A subsequent chapter will explore in great detail chemical reductions with ZnO NCs. The focus of this chapter is to describe and explain studies that were conducted with photochemically reduced ZnO NCs.

3.1 Introduction to Photoreduced Zinc Oxide Nanocrystals

The photochemical reduction of metal oxides has been studied from many perspectives, ranging from photocatalysis[1,2] to charge injection in dye-sensitized solar cells. The mechanism of photochemical reduction of metal oxides occurs through the initial formation of an exciton (electron/hole pair) through the absorption of visible light of higher energy than the bandgap of the material. The hole can be quenched either when the excited electron relaxes back into the valence band, or the hole can be "trapped" by reaction with an organic molecule, often an alcohol. The transient hole is exceptionally oxidizing; generally from +1.0 to +3.5 V vs. NHE.[1] The position of the valence band of titanium dioxide (TiO_2) and zinc oxide (ZnO) is approximately 3 V vs. NHE,[3] sufficiently oxidizing to react with many organics. Indeed, this highly oxidizing process is used for a wide variety of applications, from driving water splitting to self-cleaning surfaces and air and water purification.[1] While this mechanism is very well understood, the hole quenching by an alcohol is complicated and the location of protons generated in this process is unknown.

TiO_2 and ZnO are well suited models for studying this photoreduction process because they are easy to prepare, nontoxic, and widely available. Zinc oxide (ZnO), in both bulk and nanocrystalline forms, has long attracted interest for these and other applications,[4,5] and has been used to develop fundamental understanding of interfacial ET.[6,7]

Specifically for ZnO, photoreduction was first studied in the quantum confinement regime in 1985.[8,9] Since the initial observation of photoreduction of ZnO NCs, extra electrons in ZnO

NCs have been extensively studied with a variety of techniques including optical spectroscopy, electron paramagnetic resonance (EPR) spectroscopy to monitor the unpaired conduction band electrons, the increase of band gap emission and decrease of trap emission, magnetism, and much more.[10-17] As described above, ZnO nanocrystals are irradiated with light of a higher energy than the bandgap, generating an exciton.[11,12] The hole migrates to the surface and is quenched by an organic molecule in solution, probably residual alcohol from the synthesis, leaving behind an unpaired electron in the conduction band of ZnO NCs (ZnO/e^-).[10] ZnO/e^- can be observed by eye (blue color) or monitored with optical (Figure 3.1) and EPR spectroscopies.[14] The photoreduction reaches a maximum value that depends on the volume of the nanocrystals.[18]

As a result of the photoreduction process, the hole of the exciton should generate one proton per electron as ethanol is oxidized (Equation (3.1)). By stoichiometry, each ethanol molecule that is oxidized generates two electrons and two protons. Although the mechanism of multiple electron accumulation in ZnO NCs is not the emphasis of this research, it is being actively explored in many research groups.[16,19-22] ZnO band energies (as well as those of many other materials) shift with pH or proton activity of contacting solutions, with a linear "Nernstian" decline of ~60 meV per pH unit.[23,24] ZnO NC films have higher differential capacitances when exposed to protic (aqueous) vs. aprotic solutions, also indicating that protons play an important role.[25] We are very interested in investigating the coupling of electrons to protons in ZnO NCs.

$$\mathrm{ZnO} + h\nu + \frac{1}{2}\mathrm{EtOH} + \frac{1}{2}\mathrm{H_2NR} \rightarrow \mathrm{ZnO}:e^-/\mathrm{H}^+ + \frac{1}{2}\mathrm{CH_3CH{=}NR} + \frac{1}{2}\mathrm{H_2O} \qquad (3.1)$$

The product of ethanol oxidation by photoreduced ZnO NCs should be acetaldehyde. Acetaldehyde and other minor products have been observed at a variety of ZnO surfaces,[26] but to our knowledge was not been observed for these NCs before Miles Braten's work. He analyzed GC and GC-MS spectra of photolyzed solutions and found that an imine (eq 1; R = $C_{12}H_{25}$) was produced. The likely mechanism for formation of the imine is condensation of acetaldehyde with one of the many dodecylamine (DDA) ligands in the NC solution.[27,28] This observation explains the fate of acetaldehyde from the photooxidation of ethanol, but the protons have to our knowledge, never been observed or quantified. There is no simple spectroscopic tool to measure the formation of these extra acidic protons, so a more indirect measure was investigated.

3.2 RESULTS AND DISCUSSION

3.2.1 *Oxidation of Photoreduced ZnO Nanocrystals with ET Reagents*

ZnO NCs with average diameters (*d*) between 3 and 5 nm were synthesized by a wet chemical method described previously,[29] washed with ethanol, capped with dodecylamine (DDA) or trioctylphosphine oxide (TOPO*) and stored in toluene (*ca*. 10^{-4} M in NCs).[30] UV irradiation of ZnO NCs in the absence of oxygen generates reduced NCs[10,12,13,31,32] that are stable for weeks and are blue in color.[14,15] Extended photolysis generates reduced NCs with an average of more than one electron per NC ($n_{e^-} > 1$), as determined spectroscopically or by titration.[14,32] Photoreduction is followed by the appearance of the characteristic EPR signal[14] at g ~ 1.96 and the broad IR absorption band[12,13] that tails deep into the visible[14] (the high energy portion of which is shown in Figure 1.1). The extra electrons generated by photochemical reduction are stable in anaerobic solutions and can be treated like molecular electron transfer reagents.[33]

The reduced NCs are easily oxidized with either oxygen,[10] non-reduced ZnO NCs,[33] or outer sphere electron acceptors. A key challenge for using small molecule oxidants is compatibility with the NC solutions, as the NCs can easily precipitate with highly charged species or polar solvents. Aprotic solvents were used so that protons could be easily tracked (as opposed to reactions in water, where protons are ubiquitous). Nonpolar solvents were necessary to disperse the NCs, given the alkane tail of the capping ligands. Ferrocenium salts ($[FeCp_2][X]$; X = PF_6, BF_4) and triarylaminium radicals ($Ar_3N^{+\bullet}$) were initially used, but the salts were insoluble or caused the NCs to precipitate, respectively. Instead, a salt of the lipophilic decamethylferrocenium ($FeCp^*_2{}^+$) was prepared with the large, noncoordinating anion $BAr^F_4{}^-$ ($BAr^F_4{}^-$ = $(3,5(CF_3)_2C_6H_3)_4B^-$).[34] The oxidant $[FeCp^*_2][BAr^F_4]$ is insoluble in toluene (which was used to suspend the NCs for many of the ZnO NC experiments) but is soluble and stable in THF. Toluene and THF are both aprotic and miscible, and the introduction of THF into a toluene solution of NCs had no observable impact on photoreduction. Therefore solvent mixtures of toluene and THF were used for many of the experiments described here. Other electron deficient metallocenes were considered for use as oxidants, and cobaltocenium ($CoCp_2^+$) and decamethylcobaltcinium ($CoCp^*_2{}^+$) were prepared and used, sometimes requiring small amounts of DCM in addition to THF for solubility.

Oxidation of photoreduced NCs was performed optically in a N_2 glove-box by monitoring the decrease of the broad optical absorption of ZnO/e^- in toluene with each 10 μL aliquot of oxidant (in THF) added. After the equivalence point, optical bands associated with excess oxidant grew in with each aliquot added (Figure 3.1). The reaction was monitored at 850 nm, where neither $FeCp^*_2^+$ nor $FeCp^*_2$ absorb.

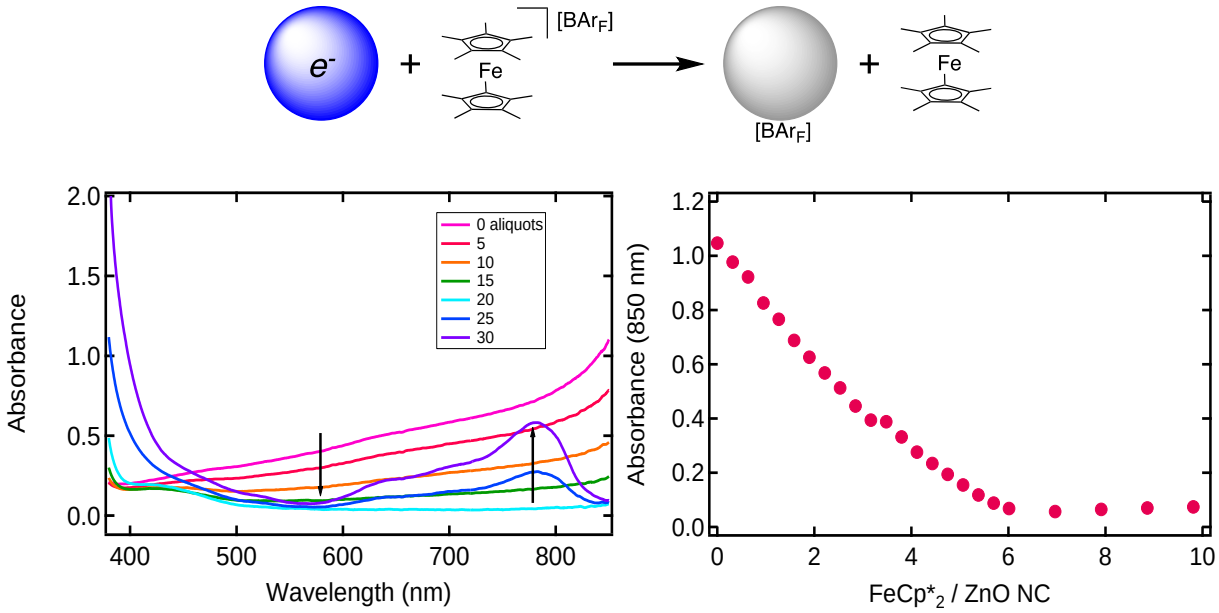

Figure 3.1. Optical titration of ZnO/e^- in toluene (d = 3.8 nm, 1.9 × 10^{-4} M) with $[FeCp^*_2][BAr^F_4]$(10 μL aliquots of 1.1 × 10^{-2} M THF solution), left. The equivalence point was at ~25 aliquots, which were later converted to oxidizing equivalents, and the dotted line is the growth of excess $[FeCp^*_2][BAr^F_4]$. Right: Titration monitored as the absorbance at 850 nm (ZnO/e^-) versus the ratio of moles of $[FeCp^*_2][BAr^F_4]$ per mole of ZnO NCs, the equivalence point at $\langle n_{e^-} \rangle$ = 6.4 ± 1.1.

By using optical titrations with chemical oxidants, electrons in the photoreduced ZnO NCs can be quantified based on the number of oxidizing equivalents used. An additional piece of information that comes from these experiments is the linearity of the titrations. Each electron contributes the same absorbance at 850 nm, following the Beer-Lambert law, regardless if it is the first electron in the NCs or the sixth. For every electron, the molar absorption coefficient at 850 nm was found to be 1000 ± 200 M^{-1} cm^{-1}/e^- for NCs with d = 3 to 4 nm. This makes

following the electrons at the arbitrarily chosen 850 nm convenient for optical monitoring of the reactions. We note that this is true only at very high energies, well off of the peak maximum, and is not true in the near IR (see Chapter 5 for more information). Using optical spectroscopy as a tool, we are now able to count the electrons in the NCs. We will now turn our attention to the protons on the NCs that should be generated concomitantly with the electrons in the photoreduction process.

3.2.2 *Investigating the Proton Generated from Photoreduction: Reaction with PCET Reagents*

One way to test that the photoreduction process generates protons is to react the NCs with hydrogen atom transfer (HAT) reagents. Previous work showed that ZnO/e^- reacts with the oxyl radicals 2,4,6-tri-*t*-butylphenoxyl radical (^{t}Bu$_3$ArO$^\bullet$) and 2,2,6,6-tetramethyl-piperidin-1-yl-oxyl radical (TEMPO),[35] which are classic hydrogen atom abstracting reagents.[36] These reactions can be monitored by optical (Figure 3.2), EPR, or ^{1}H NMR spectroscopy (Figure 3.3). ZnO/e^- in toluene can be oxidized by ^{t}Bu$_3$ArO$^\bullet$, and the disappearance of the electrons is linear, indicating that the reaction is fast and goes to completion (Figure 1.2). The reaction was monitored at 626 nm (absorption for loss of ZnO/e^- and then appearance of any excess ^{t}Bu$_3$ArO$^\bullet$), well-separated from the ZnO band gap absorbance, and at 850 nm (absorption for only ZnO/e^-).

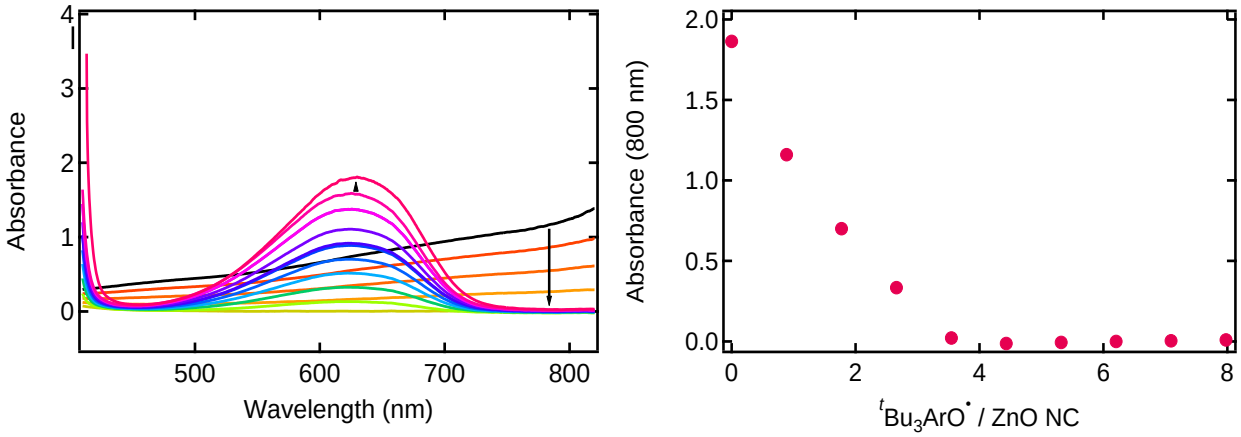

Figure 3.2. Optical titration of ZnO/e^- in toluene (d = 3.9 nm, 4.6 × 10^{-4} M) with ^{t}Bu$_3$ArO$^\bullet$ (10 μL aliquots of 1.14 × 10^{-1} M toluene solution), left. The equivalence point was at ~5 aliquots, which were later converted to oxidizing equivalents. Right: Titration monitored as the absorbance at 850 nm (ZnO/e^-) and 626 nm (^{t}Bu$_3$ArO$^\bullet$) versus the ratio of moles of ^{t}Bu$_3$ArO$^\bullet$ per mole of ZnO NCs, the equivalence point was found to be $\langle n_{e^-} \rangle$ = 3.8 ± 0.6.

The reaction with $^{t}Bu_3ArO^{\bullet}$ was characterized by GC-FID with the assistance of Dr. Joel Schrauben.[28] The yield of $^{t}Bu_3ArOH$ is essentially quantitative (100 ± 5%) versus the reducing equivalents in the NCs determined by titration. By NMR spectroscopy, both $^{t}Bu_3ArOH$ and TEMPOH products were observed from reactions of their radical precursors with ZnO/e^{-} and TiO_2/ e^{-} (not shown). Figure 3.3 shows a ^{1}H NMR spectrum of photoreduced ZnO NCs reacted with TEMPO, forming TEMPOH. The ^{1}H NMR spectra of photoreduced NCs are slightly broadened from non-reduced NCs, presumably from the paramagnetism of extra electrons in the NCs.

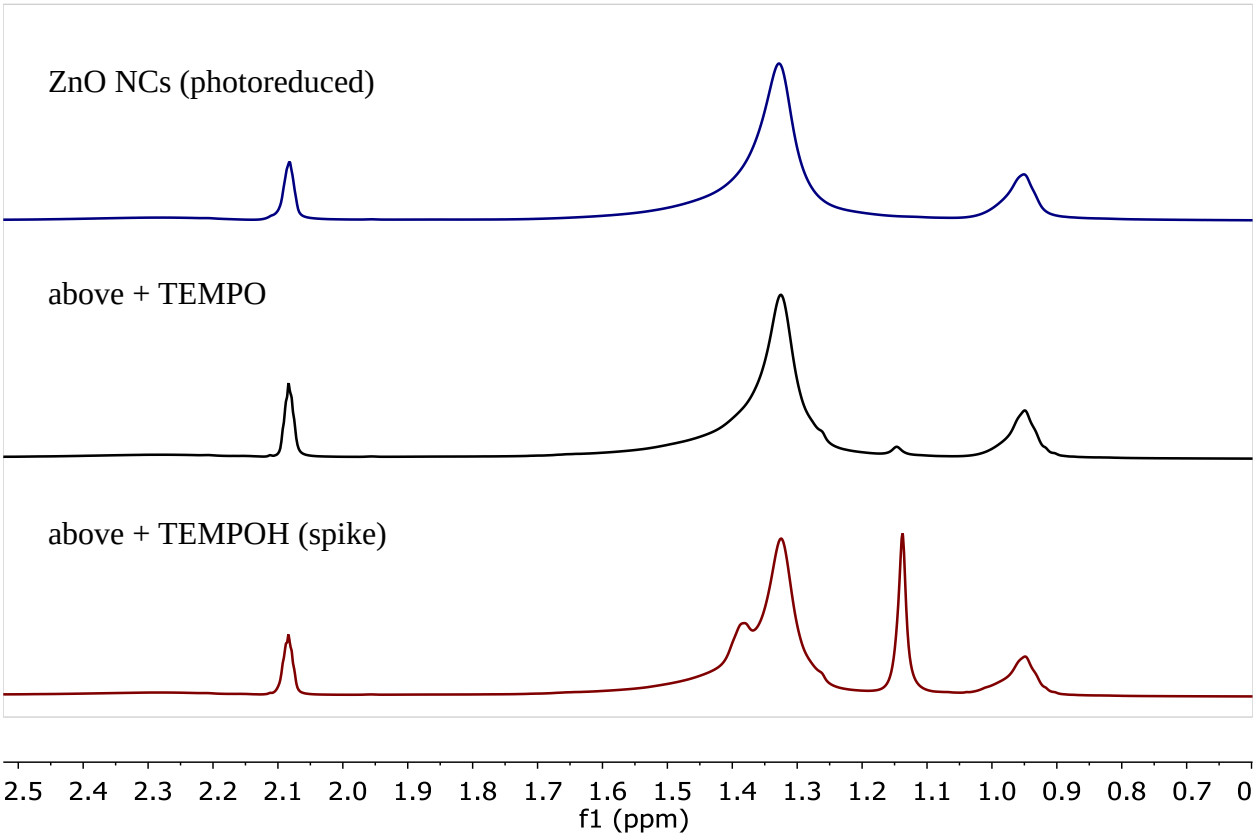

Figure 3.3. ^{1}H NMR spectra of photoreduced ZnO NCs (d = 3.9, [NCs] = 4.3×10^{-4} M), plus TEMPO (10 equiv), top and middle, respectively. The assignment of TEMPOH was confirmed by spiking (~2 mg) (bottom). The peak at 1.15 corresponds to the methyl peaks of TEMPOH.

The observation that photoreduced ZnO NCs react with HAT acceptors shows that the photoreduced ZnO NCs can transfer electrons *and protons*. Experiments to track the rate of

reaction between ZnO/e^- and the HAT acceptors show that the bimolecular rate constants vary with the bond dissociation free energy (BDFE) according to the Marcus cross relation,[37] which suggests that the process may be concerted.[28] However, these experiments do not address the source of the protons that are transferred to the HAT reagents. Protons may originate from the synthesis, residual water on the surface, or the photooxidation of ethanol. A more deliberate attempt to track the source of the protons is necessary.

3.2.3 *Adding/Removing Protons on Photoreduced ZnO NCs*

Locating the proton from photochemical reduction is not straightforward because of the extremely oxidizing nature of the hole and because protons are already present on the surface of the particle leftover from the synthesis. Instead, several methods to probe the effect of a few extra protons per NC (derived from photoreduction) were investigated.

The base P4-^{t}Bu phosphazene is strong enough to deprotonate the ZnO NCs, based on ^{31}P NMR spectra showing the formation of the protonated base (see Chapter 5). This base is bulky, noncoordinating, and its conjugate acid in soluble in toluene/THF mixtures. We hypothesized that removing protons using a base might affect the properties of ZnO NCs. However, addition of the base to a solution of photoreduced ZnO NCs shows no obvious changes by optical (Figure 3.4) or EPR spectroscopy.

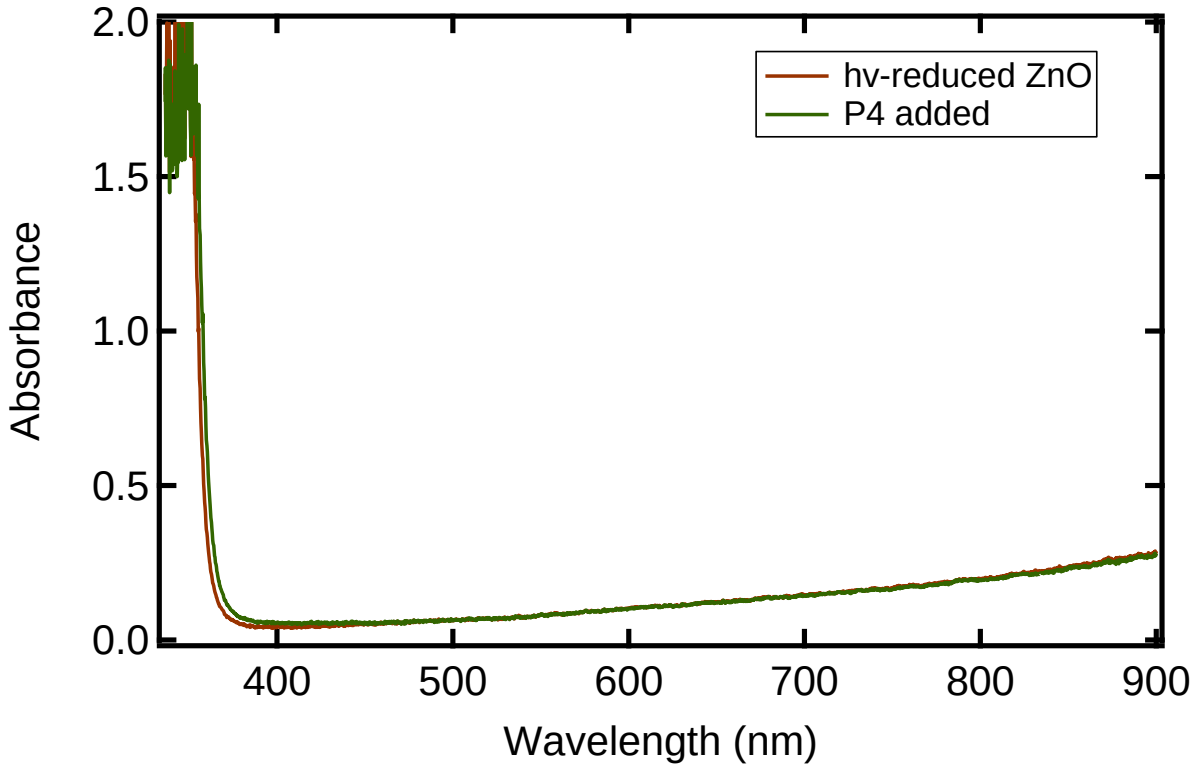

Figure 3.4. Optical absorption spectrum of photoreduced ZnO NCs (d = 4.4 nm, 3.9 × 10^{-4} M, $\langle n_{e^-} \rangle$ = 3.7), followed by the addition of P4-^{t}Bu phosphazene base (160 equiv). There appear to be no optical changes from the addition of P4 base.

Although the optical spectra of the NCs is unchanged with removal of protons, addition/removal of protons might change their redox chemistry. As described in the introduction to this chapter, according to the Nernst equation an increase in pH should render the NCs more reducing. However, pH is a log scale and describing the protons generated from photoreduction as a pH change is not helpful because of the non-aqueous solvent. By stoichiometry (see Equation (3.1)) , the photoreduction of the NCs would add a *few* protons per NC, and we set out to determine if these extra protons are quantifiable, and if they changed the redox chemistry of the NCs.

Electrochemical experiments with colloidal suspensions of the NCs were unsuccessful (see Chapter 5), so methods to indirectly measure the redox potential of the NCs were devised. The following experiment was conducted with an electron acceptor, decamethylcobaltocenium ($CoCp^*_2^+$). Cobaltocenes and other metallocene reductants are explored in more detail in

Chapter 4, but we highlight this experiment here because it involves photoreduced NCs. To a solution of photoreduced NCs was added [$CoCp^*_2$][PF_6] (Figure 1.5). There is very little electron transfer to $CoCp^*_2^+$, as the reduction potential of $CoCp^*_2$ is higher than the NC conduction band edge. As P4 base is added to the solution, all of the electrons in the NCs are transferred to the $CoCp^*_2^+$. This result shows that the chemical potential of the photoreduced NCs is greatly increased by removing residual protons. This result supports those discussed in Chapter 4, where we show the inverse - the *addition* of protons *decreases* the redox potential of the NCs, as predicted by the Nernst equation.

For the reactivity depicted in Figure 3.5, the P4-^{t}Bu base removes protons from the NCs, likely more than just the protons generated from photoreduction. This result also indicates that all the protons affect the reducing power of the NCs – even the residual protons leftover from the synthesis. Addition of P4-^{t}Bu base to a solution of as-prepared NCs makes them more difficult to reduce, as discussed more in Chapter 4.

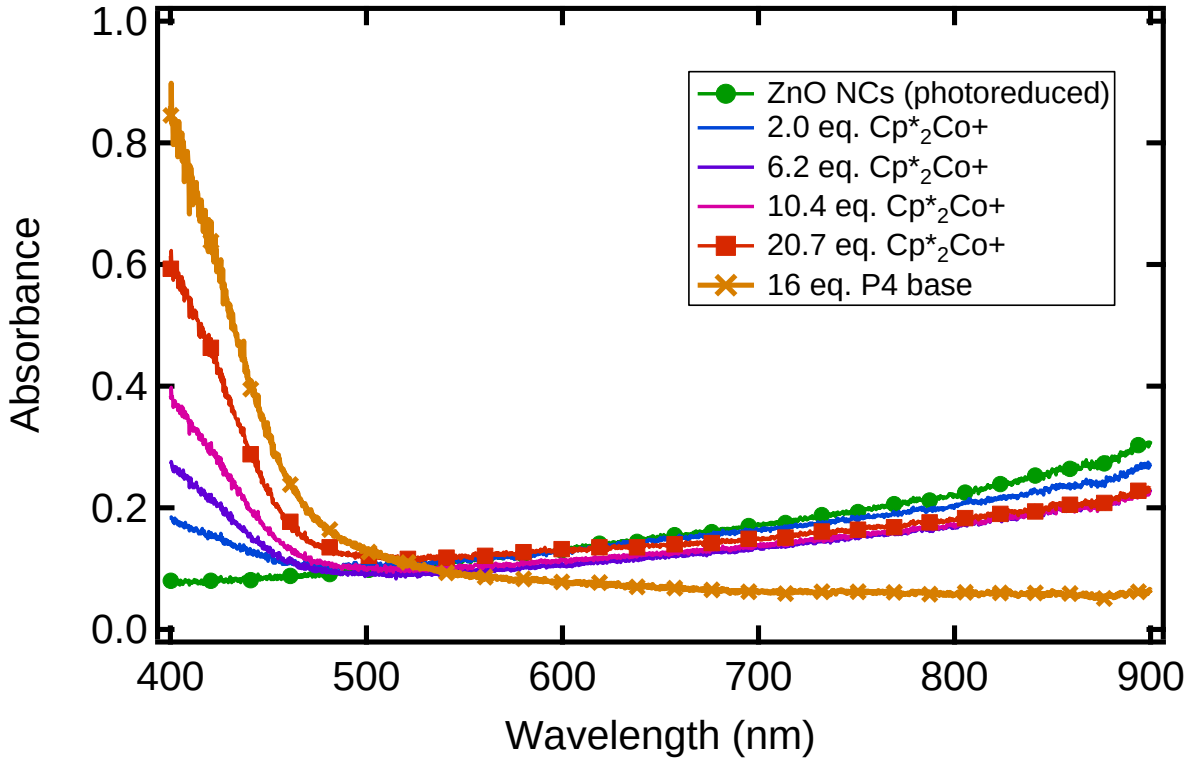

Figure 3.5. Optical spectra of ZnO NCs (d = 4.4 nm, 3.9 × 10^{-4} M, $\langle n_{e^-} \rangle$ = 4.2) plus [$CoCp^*_2$][PF_6] (from 2.0 to 20.7 equiv, added in 10 μL aliquots of a 2.4 × 10^{-2} M solution in

1:5 THF:DMF). The sample was allowed to stir between each addition. Then P4-^{t}Bu phosphazene base was added as a solution in toluene (16 equiv, 30 μL of 6.3×10^{-2} M solution).

Similarly, we hypothesized that removal of extra protons prior to photoreduction (or addition of protons) might affect the photoreduction processes and increase/decrease the amount of reduction. A solution of NCs was split into three parts (Figure 3.6). P4 base was added to one, an acid (Brookhart's acid, $HBAr^{F}_{4}(Et_2O)_2$) was added to another, and the third was a control with NCs only. All three samples were irradiated for 45 minutes and reached their maximum values within that time. All three samples gave approximately the same absorbance spectrum. Extra/fewer protons did not result in any less (or more) absorbance due to electrons in the NCs (Figure 1.6 below). This result is similar to what was found in an analogous study on photoreduction of ZnO NCs with different hole quenchers.[18] This indicates that extra or fewer protons do not affect the mechanism of electron trapping in the conduction band of ZnO NCs. Because protons change the thermodynamics of the NCs, this experiment also indicates that the initial band edge energy does not influence the mechanism by which reduction stops in photoreduced NCs.

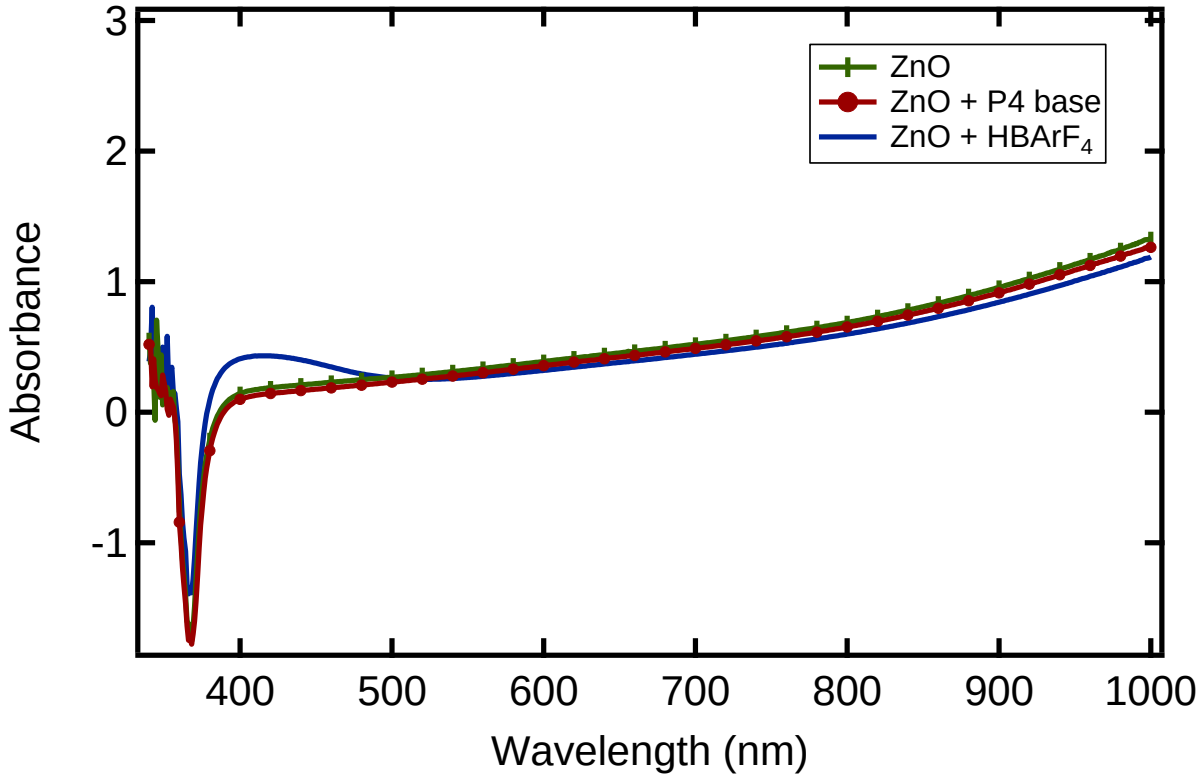

Figure 3.6. Optical spectra of ZnO NCs photoreduced with and without the presence of acid and base. The NCs alone (d = 4.3 nm, 1.8 × 10^{-4} M, 50/50 toluene/THF) are shown in green, P4-^{t}Bu base added prior in red (10 equiv), and $HBAr^{F}_{4}$ added prior in blue (3 equiv). No obvious change in the absorbance due to ZnO/e^{-} is observed, other than the growth of a peak at ~410 nm and green color observed with acid, likely a photodecomposition product of the acid.

Another experiment to probe the source of the protons was to photoreduce/oxidize with HAT reagents repeatedly. If the reactive protons come solely from photoreduction, they should be replenished every phtooreduction cycle. If the protons come from the synthesis only, they should eventually be depleted. A solution of NCs was photoreduced and fully oxidized with TEMPO. Then, the NCs were precipitated from solution using acetonitrile and resuspended in toluene. The NCs were again photolyzed, but the solutions were very unstable, either due to removal of capping ligands or charge unbalance. In the ^{1}H NMR spectrum, there are several unidentified products that were attributed to photodegradation of TEMPO and TEMPOH (Figure 3.7). This photoreduction/oxidation sequence was inconclusive because of solubility issues and instability of TEMPO/H derivatives to light from the arc lamp.

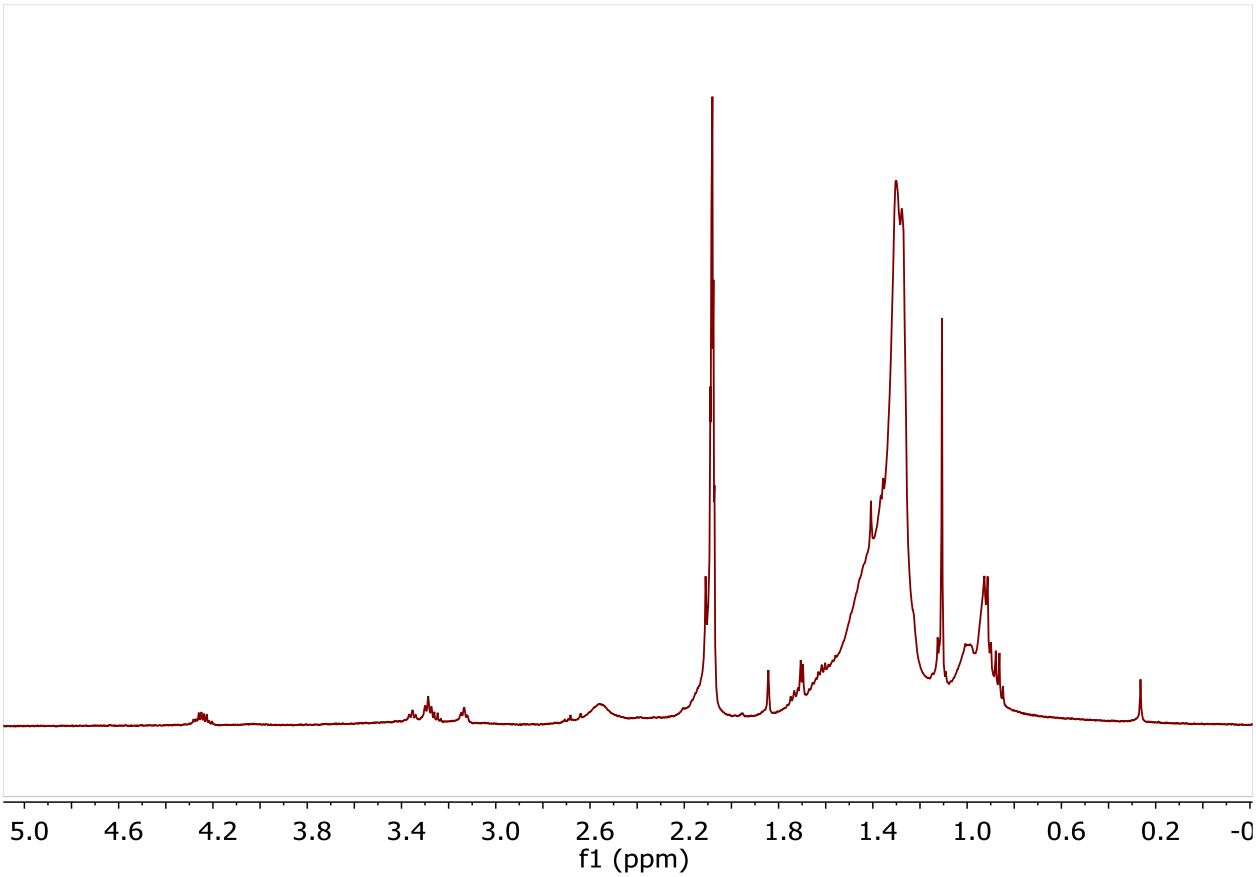

Figure 3.7. ^{1}H NMR of one sequence of photoreduction/oxidation with TEMPO/photoreduction of ZnO NCs (d = 4.3 nm, 1.8 × 10^{-4} M) and TEMPO (7 equiv) in toluene-d_8. The NCs were photoreduced in the NMR tube (A_{850} = 0.6 through the NMR tube), titrated with TEMPO, precipitated with MeCN, suspended in toluene-d_8, and photolyzed again (A_{850} = 0.45 through the NMR tube) prior to acquisition of this spectrum. The peaks are assigned mostly to TEMPO decomposition products and DDA ligands from the NCs.

3.2.4 *Stoichiometry of Photoreduced NCs*

Another way to investigate if extra protons are generated during photoreduction was devised. Mixing solutions of the reduced NCs with the e^- acceptor [FeCp*$_2$][BAr$^F{}_4$] should generate NCs with extra protons. By stoichiometry, the average number of electrons per NC (<n_{e^-}>) should be equal to the number of protons generated from the oxidation of ethanol in the photoreduction

process (Equation (3.1)). After the electrons in the NCs are removed, there should therefore be $<n_{e^-}>$ more protons than the original ZnO NCs (Equation (3.2)). In contrast, oxidation by the $1e^-/1H^+$ acceptor ^{t}Bu$_3$ArO$^\bullet$ regenerates the original ZnO NCs and ^{t}Bu$_3$ArOH (Equation (3.3)).[28] One batch of photoreduced NCs that is split in half and oxidized by HAT vs. ET oxidants should give NCs that are very similar, except for a difference in $<n_{e^-}>$ more protons (Figure 3.8).

$$\mathrm{ZnO}:e^-/\mathrm{H}^+ + [\mathrm{FeCp}^*_2][\mathrm{BAr}^\mathrm{F}_4] \rightarrow [\mathrm{ZnO\text{-}H}^+][\mathrm{BAr}^\mathrm{F}_4] + \mathrm{FeCp}^*_2 \qquad (3.2)$$

$$\mathrm{ZnO}:e^-/\mathrm{H}^+ + {}^t\mathrm{BuArO}^\bullet \rightarrow \mathrm{ZnO} + {}^t\mathrm{BuArOH} \qquad (3.3)$$

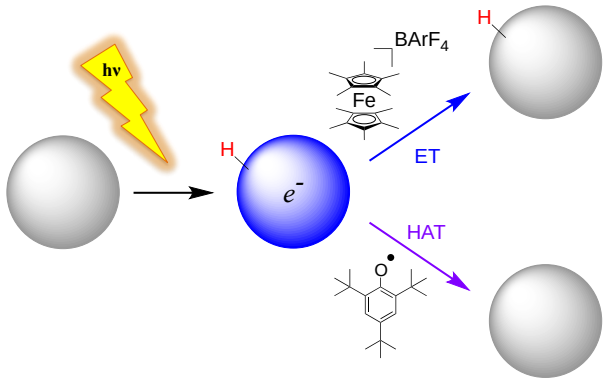

Figure 3.8. Photoreduction of ZnO NCs followed by oxidation with $[FeCp^*_2][BAr^F_4]$ or ^{t}Bu$_3$ArO$^\bullet$, top and bottom, respectively. A single proton is drawn for clarity, but there should be $<n_{e^-}>$ protons remaining on the NCs oxidized with $[FeCp^*_2][BAr^F_4]$.

A solution of photoreduced NCs was split in half, and each portion was completely oxidized using $[FeCp^*_2][BAr^F_4]$ or ^{t}Bu$_3$ArO$^\bullet$ to yield ZnO-H$^+$[BAr$^F_4$] (Equation (3.2)) or ZnO NCs (Equation (3.3)). The two different products have identical optical spectra and are both EPR silent.[38] However, they have different redox properties.

The reductant decamethylchromocene ($CrCp^*_2$, -1.56 V *vs.* Fc/Fc$^+$)[38] cannot reduce as-prepared NCs. However, addition of $CrCp^*_2$ to ZnO-H$^+$ (photoreduced NCs oxidized by $[FeCp^*_2][BAr^F_4]$) yields reduced NCs (Figure 3.9). In contrast, addition of $CrCp^*_2$ to the NCs oxidized by ^{t}Bu$_3$ArO$^\bullet$ shows no reaction. This is as expected because the phenoxyl removes both the proton and the electron, generating samples that react exactly like as-prepared NCs.

Similarly, addition of the strong base P4-^{t}Bu phosphazene to a mixture of [ZnO-H^{+}][BAr^{F}_{4}] and $CrCp^{*}_{2}$ deprotonated the NCs, as observed by $^{31}P(^{1}H)$ NMR spectroscopy, and shifted the equilibrium completely back to the starting reagents ZnO and $CrCp^{*}_{2}$ (Figure 3.10). No reduction of the NCs by $CrCp^{*}_{2}$ has been observed in the presence of the base alone, confirming the role of the extra proton. We note that the base and the oxidant likely do not discriminate between protons leftover from the synthesis and protons generated from photoreduction. Experiments with isotopically labeled ethanol were not pursued because we anticipate that the protons exchange. Even with these caveats, the experiments above indicate that photoreduction adds protons to the ZnO NCs that drastically affect their redox activity.

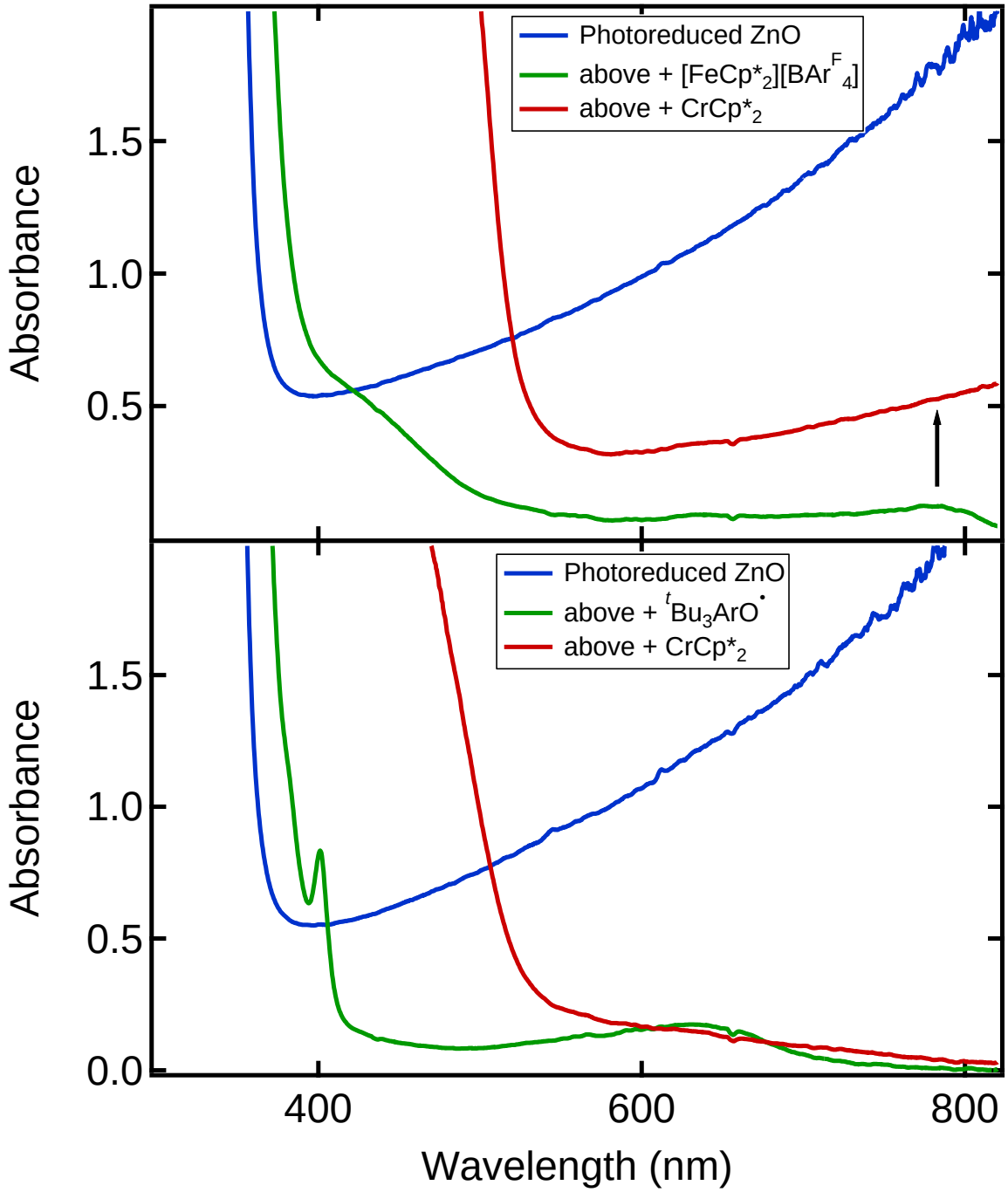

Figure 3.9. Optical spectra of photoreduced ZnO NCs (d = 3.5 nm, 6.4 × 10^{-4} M, $\langle n_{e^-} \rangle$ = 3) in 50/50 toluene/THF mixture. (Top) A solution of [FeCp*$_2$][BAr$^F_4$] in THF (4 equiv) or (bottom) a toluene solution of ^{t}Bu$_3$ArO$^\bullet$ is added (4 equiv), to fully oxidize the reduced NCs. To each solution was then added CrCp*$_2$ as a solution in toluene (4 equiv).

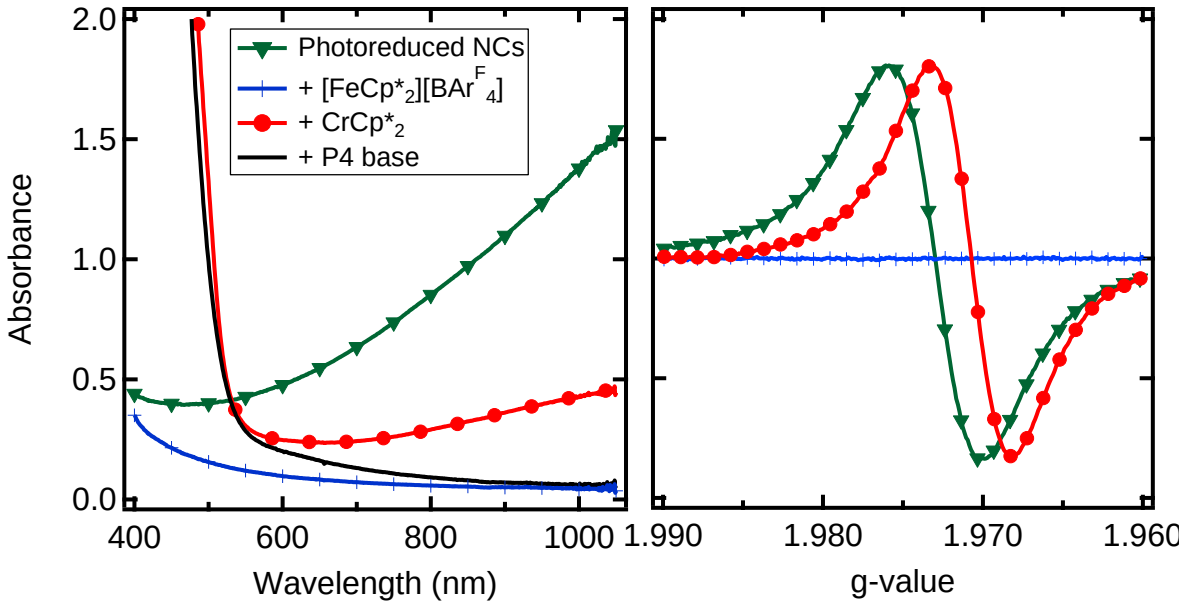

Figure 3.10. Optical spectra of photoreduced ZnO NCs with $<n_{e^-}>$ = 3.7 (d = 3.7 nm, 3×10^{-4} M, green), oxidized with [FeCp*$_2$][BAr$^F_4$] (blue, 4.5 equiv), then reduced again by CrCp*$_2$ (red, 31 equiv), $<n_{e^-}>$ = 1.2. Subsequent addition of P4-^{t}Bu base (black) forms unreduced NCs and CrCp*$_2$ (left). EPR spectra of ZnO NCs (d = 3.9 nm, 3×10^{-4} M) after photoreduction (green) then oxidation with [FeCp*$_2$][BAr$^F_4$] (blue), and recharging with CrCp*$_2$ (red, normalized to the peak height of green), (right).

These observations indicate that the presence of only a few extra protons per NC substantially affects their redox properties. They also suggest that the extra protons are generated from the photoreduction process and remain on the NC to affect their reactivity. However, there are several alternative explanations that must be eliminated. (1) Excess ions in solution (FeCp*$_2^+$/FeCp*$_2$/BAr$^F_4$/etc.) allow the NCs to be reduced further and (2) the reduced NCs are easier to reduce a second time because something about them has changed after photoreduction (other than the protons).

NCs that have never been reduced were treated in the same manner (addition of oxidant followed by CrCp*$_2$, Figure 3.11). There is no "re-reduction" as was observed with the photoreduced NCs. This results suggests that the photoreduction process is necessary for the re-

reduction to occur, and that the presence of $FeCp^*_2^+/FeCp^*_2/BAr^F_4$ does not measurably affect their redox chemistry.

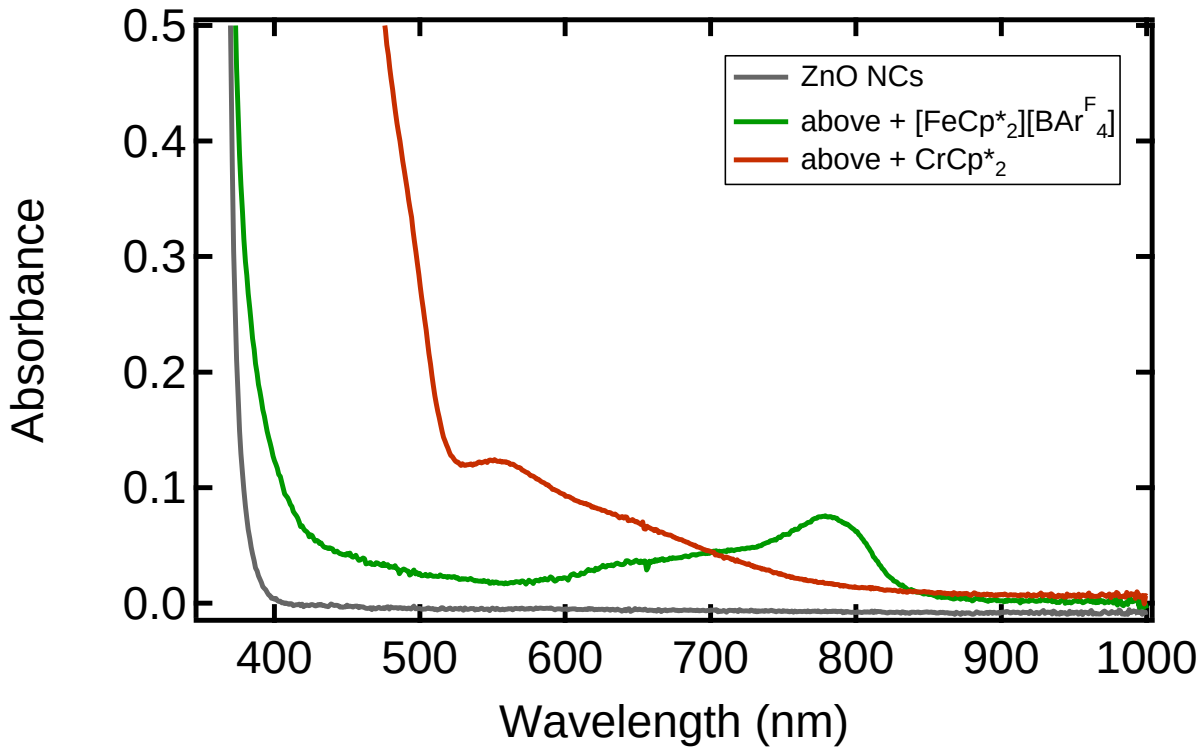

Figure 3.11. Optical spectra of as-prepared ZnO NCs, not photoreduced(d = 3.5 nm, 4.3×10^{-4} M) in 50/50 toluene/THF (grey). Addition of $[FeCp^*_2][BAr^F_4]$ to the NCs results in the appearance of peak at ~780 nm corresponding to $[FeCp^*_2][BAr^F_4]$ (green). Addition of $CrCp^*_2$ (17 equiv) to the resulting mixture resulting in only formation of $FeCp^*_2$, and no reduction of the NCs (red).

Nanocrystals were also reduced using chemical methods ($CoCp^*_2$, see Chapter 4) and treated in the same fashion (oxidation with $[FeCp^*_2][BAr^F_4]$ followed by reduction with $CrCp^*_2$). These NCs also did not become re-reduced (Figure 3.12), indicating that the re-reduction is due specifically to the photoreduction process. The explanation here is that the hole generated from photoreduction oxidizes ethanol, leaving residual extra protons in solution that affect the redox activity of the NCs. Therefore reduction does not irreversibly change the NCs and make them easier to reduce.

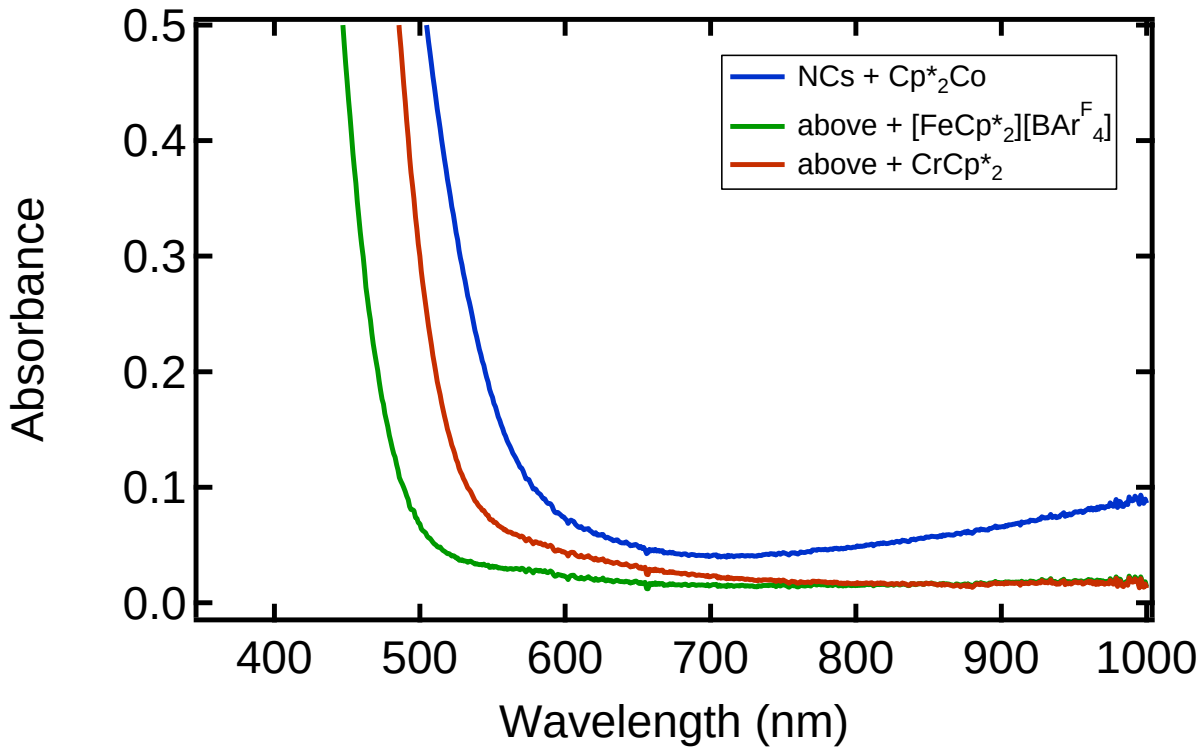

Figure 3.12. Optical spectra of ZnO NCs (d = 3.5 nm, 4.3 × 10^{-4} M) in 50/50 toluene/THF reduced with the chemical reductant $CoCp^*_2$ (39 equiv)(blue). Addition of $[FeCp^*_2][BAr^F_4]$ (9 equiv) results in a decrease of the signal corresponding to reduced ZnO NCs, and a signal at ~600 nm corresponding to the resulting $FeCp^*_2$. Addition of $CrCp^*_2$ to this solution (34 equiv) did not result in any ZnO NC reduction (red).

3.3 Conclusions and Outlook

The photoreduction of metal oxides is widely studied, and generates both a highly-reducing electron in the conduction band and an oxidizing hole in the valence band. The hole oxidizes organics, in the case of these ZnO NCs, ethanol into acetaldehyde. The stoichiometry of this reaction dictates that every electron should come with an accompanying proton. Following the proton in protic media is difficult, but by dispersing the ZnO NCs in nonpolar solvents the proton can be more easily studied. A base of sufficient strength to deprotonate the NCs was used, and we find that removing protons makes the photoreduced NCs more reducing, but otherwise does

not alter their optical spectra. To investigate whether protons are generated from the photoreduction process, the NC redox potential was indirectly probed by addition of an outer sphere molecular reductant. We find that the photoreduction process generates (a few) protons that strongly affect the reactivity of dodecylamine-capped ZnO nanocrystals in toluene/THF solutions.

Future experiments should explore whether the proton that is accepted by the HAT reagents comes from photoreduction. Although proton exchange will be an issue, photoreduction using deuterated ethanol may generate TEMPOD/^{t}Bu$_3$ArOD. Exchange may be minimized by initially reacting the NCs with a sufficient amount of P4 base to remove residual protons, or using annealed NCs, and using TOPO (rather than DDA) as the capping ligand.

3.4 EXPERIMENTAL

3.4.1 *General Considerations*

Tetramethylammonium hydroxide (TMAOH), zinc acetate dihydrate, dodecylamine (DDA), isopropylmagnesium chloride, and 1,3-bis(trifluoromethyl)-5-bromobenzene were purchased from Aldrich and used as received. The base 1-*tert*-butyl-4,4,4-tris(dimethylamino)-2,2-bis[tris(dimethylamino)-phos-phoranylidenamino]-2λ^5,4λ^5-catenadi(phosphazene) (P4 phosphazene base, 1.0 M in hexanes) was obtained from Aldrich, dried to a solid in a N_2 glovebox, and recrystallized from pentane before use. Sodium tetrafluoroborate, bis(pentamethylcyclopentadienyl) cobalt (decamethylcobaltocene, CoCp*$_2$) and 2,4,6-tri-*tert*-butylphenol (^{t}Bu$_3$ArOH) were obtained from Aldrich and were dried in a vacuum oven, recrystallized from pentane or ethanol, respectively, before use. The corresponding phenoxyl radical ^{t}Bu$_3$ArO$^{\bullet}$ was prepared according to the literature procedure.[39] [H(Et$_2$O)$_2$][BAr$^{F}_4$] was synthesized using reported literature procedures[40] from [Na][BAr$^{F}_4$][41] (dried in a vacuum oven for at least 24 hours) and anhydrous HCl in Et$_2$O. Bis(pentamethylcyclopentadienyl)iron (FeCp*$_2$), bis(cyclopentadienyl)cobalticinium hexafluoro-phosphate ([CoCp$_2$][PF$_6$]), and bis(pentamethylcyclopentadienyl)chromium (CrCp*$_2$) were purchased from Strem and used as received, except for CrCp*$_2$ which was purified by sublimation or recrystallization from pentane before use. The oxidized product [FeCp*$_2$][BAr$^{F}_4$] (BAr$^{F}_4$$^{-}$ = [B(C$_6$H$_3$(CF$_3$)$_4$)]$^{-}$) was prepared by

adapting literature procedures.[42] Toluene-d_8 and THF-d_8 were purchased from Cambridge Isotope and degassed by three freeze-pump-thaw cycles and (in the case of THF) drying via storage over sieves for two days. All other solvents were purchased from Fischer Scientific and were dried using a Seca Solvent System installed by Glass Contour. Fluka TraceCERT® High Purity brand Zn standard (1000 μg/L in 2% HCl) was used as the standard for ICP-OES (inductively coupled plasma-optical emission spectrometry).

3.4.2 *ZnO Nanocrystal Preparation*

Nanocrystals (NCs) were prepared following reported procedures with minor modifications.[17] For small NCs, at room temperature under air, a solution of $Me_4NOH•5H_2O$ (TMAOH, 13.3 g, 7.3 mmol) in 140 mL of ethanol was added to a stirring solution of zinc acetate ($Zn(OAc)_2•2H_2O$, 10.0 g, 4.6 mmol) in 300 mL DMSO and 150 mL ethanol, at a rate of ~5 mL/minute. After 60 minutes of stirring, NCs were precipitated from the clear solution with the addition of ~800 mL ethyl acetate until the solution was cloudy and white. The NCs were isolated from the solution by centrifugation in six separate tubes followed by decantation. The resulting white pellets were washed twice to remove excess starting material by iterative dissolution of each pellet in 2 mL of ethanol and precipitation with 10 mL *n*-heptane. The NCs were then capped by dissolving each of the six pellets in 1 mL molten DDA (120 - 160 °C), consolidated in one test tube, and allowed to rest for 5 – 10 minutes. For larger NCs, the DDA solution was heated for longer (10 – 60 minutes). After cooling, NCs were precipitated from solution with the addition of ~5 mL ethanol. The white solid was collected by centrifugation and decantation and dried under vacuum. The white solid was brought into an N_2 glovebox, dissolved in ~20 mL of toluene to give a colorless solution and stored in the freezer (-35 ^oC). The average NC diameter was calculated from the UV-visible absorption spectrum using the experimentally derived relationship between diameter and the energy of the band gap absorbance (for d = 3 – 6 nm).[43]

3.4.3 *Calculation of Nanocrystal Concentration*

An aliquot (0.5 mL) of room temperature ZnO NCs in toluene was dried under vacuum, and the sample was calcined at 500 ^{o}C for at least 2 hours to remove residual organic matter. After calcination, samples were digested in EMD Omni*Trace*® HNO_3 and diluted to a volume of 5 mL with deionized water in a volumetric flask. Five samples were then prepared for ICP analysis and the concentration determined by the method of standard additions. Each of the five samples contained a 100 μL aliquot of the 5 mL calcined ZnO sample and 0, 50, 150, 300, and 500 μL of Zn standard (1000 μg/mL in 2% HCl), and were diluted with deionized water in 10 mL volumetric flasks. The intensity of the atomic emission spectrum for Zn was recorded by ICP for each sample and used to extrapolate the concentration of Zn in the original sample, using the x-intercept for the linear fit of a plot of Zn intensity *vs.* [Zn added]. The average volume of each ZnO NC was calculated assuming a spherical NC with $^{4}/_{3}\pi r^{3}$, where r is the radius determined from the optical spectra (see above). Crystalline Wurtzite ZnO has a unit cell volume of 47.66 $Å^{3}$ with two formula units per unit cell. Thus the average number of Zn atoms per NC is $(2 \times {}^{4}/_{3}\pi r^{3}) \div 47.66\ Å^{3}$. The concentration of NCs is given by dividing the total Zn concentration (determined by ICP) by the number of Zn atoms per NC.

3.4.4 *Photochemical Reduction of ZnO Nanocrystals*

Photochemical reduction was carried out by photoexcitation of anaerobic ZnO NC solutions using an Oriel 200 W Hg/Xe lamp. We note that the NCs must have residual ethanol on the surface in order for proper photoreduction, but to my knowledge, we have never had a sample in which there is insufficient ethanol. In a typical titration or photoreduction experiment, an anaerobic solution of NCs (10^{-3}-10^{-5} M) was prepared in a quartz Kontes cuvette equipped with a stir bar, and irradiated while stirring for 1-60 minutes, approximately 10 cm from the lamp aperture. In other experiments, NC solutions were stirred in a Unisoku sample holder to prevent large concentration gradients, and irradiation of the solutions was carried out orthogonally to UV-vis detection. The reduced solutions were taken into a N_2 glovebox where titrations were carried out using an Ocean Optics spectrometer. In a typical titration, twenty 10 μL aliquots of reagent (e.g. ~0.1 M solution of $^{t}Bu_3ArO^{\bullet}$ in toluene) were added to 2 mL of a 5×10^{-4} M

solution of reduced ZnO NCs in a cuvette, while stirring. The optical spectra were recorded 30 seconds after each addition.

3.4.5 *Spectroscopy*

All samples were prepared under N_2. UV-vis spectra were recorded in an N_2-filled glovebox using an Ocean Optics USB4000 spectrometer configured with an XR1 grating for extended range, and a DT-Mini-2-GS lightsource. The data were processed using Ocean Optics SpectraSuite© and Igor Pro Version 6.22A. Other UV-vis spectra were obtained on a Hewlett Packard 8453 diode array spectrophotometer. Continuous wave EPR spectra were obtained at room temperature on a Bruker E580 X-band spectrometer (perpendicular mode detection). Electrochemical data were obtained using a CH Instruments 600D potentiostat.

^{1}H NMR spectra were obtained on Bruker AV300, AV301, DRX499, or AV500 spectrometers and data were processed using MestReNova©. Chemical shifts were reported relative to TMS by referencing the residual solvent. Inductively-coupled plasma optical-emission spectroscopy (ICP-OES) was carried out using a Perkin Elmer Optima 8300.

3.5 NOTES TO CHAPTER 3

(1) Hoffmann, M. R.; Martin, S. T.; Choi, W.; Bahnemann, D. W. *Chem. Rev.* **1995**, *95*, 69.

(2) Khan, M. M.; Adil, S. F.; Al-Mayouf, A. *J. Saudi Chem. Soc.* **2015**, *19*, 462.

(3) Gratzel, M. *Nature* **2001**, *414*, 338.

(4) Chennupati Jagadish, S. J. P. *Zinc Oxide Bulk, Thin Films and Nanostructures*; Elsevier Ltd.: Amsterdam, 2006.

(5) Anderson, J.; Van de Walle, C. G. *Rep. Prog. Phys.* **2009**, *72*, 126501.

(6) Hamann, T. W.; Gstrein, F.; Brunschwig, B. S.; Lewis, N. S. *Chem. Phys.* **2006**, *326*, 15.

(7) Schimpf, A. M.; Ochsenbein, S. T.; Buonsanti, R.; Milliron, D. J.; Gamelin, D. R. *Chem. Commun.* **2012**, *48*, 9352.

(8) Koch, U.; Fojtik, A.; Weller, H.; Henglein, A. *Chem. Phys. Lett.* **1985**, *122*, 507.

(9) Bahnemann, D. W.; Kormann, C.; Hoffmann, M. R. *J. Phys. Chem.* **1987**, *91*, 3789.

(10) Haase, M.; Weller, H.; Henglein, A. *J. Phys. Chem.* **1988**, *92*, 482.

(11) Shim, M.; Guyot-Sionnest, P. *Nature* **2000**, *407*, 981.

(12) Shim, M.; Guyot-Sionnest, P. *J. Am. Chem. Soc.* **2001**, *123*, 11651.

(13) Germeau, A.; Roest, A.; Vanmaekelbergh, D.; Allan, G.; Delerue, C.; Meulenkamp, E. *Phys. Rev. Lett.* **2003**, *90*, 097401.

(14) Liu, W. K.; Whitaker, K. M.; Smith, A. L.; Kittilstved, K. R.; Robinson, B. H.; Gamelin, D. R. *Phys. Rev. Lett.* **2007**, *98*, 186804.

(15) Liu, W. K.; Whitaker, K. M.; Kittilstved, K. R.; Gamelin, D. R. *J. Am. Chem. Soc.* **2006**, *128*, 3910.

(16) Whitaker, K. M.; Ochsenbein, S. T.; Polinger, V. Z.; Gamelin, D. R. *J. Phys. Chem. C* **2008**, *112*, 14331.

(17) Schwartz, D. A.; Norberg, N. S.; Nguyen, Q. P.; Parker, J. M.; Gamelin, D. R. *J. Am. Chem. Soc.* **2003**, *125*, 13205.

(18) Schimpf, A. M.; Gunthardt, C. E.; Rinehart, J. D.; Mayer, J. M.; Gamelin, D. R. *J. Am. Chem. Soc.* **2013**, *135*, 16569.

(19) Klimov, V. I.; Mikhailovsky, A. A.; McBranch, D. W.; Leatherdale, C. A.; Bawendi, M. G. *Science* **2000**, *287*, 1011.

(20) Schaller, R. D.; Agranovich, V. M.; Klimov, V. I. *Nat Phys* **2005**, *1*, 189.

(21) Klimov, V. I.; McGuire, J. A.; Schaller, R. D.; Rupasov, V. I. *Phys. Rev. B* **2008**, *77*, 195324.

(22) Jha, P. P.; Guyot-Sionnest, P. *ACS Nano* **2009**, *3*, 1011.

(23) Bolts, J. M.; Wrighton, M. S. *J. Phys. Chem.* **1976**, *80*, 2641.

(24) Gerischer, H. *Electrochim. Acta* **1989**, *34*, 1005.

(25) Roest, A. L.; Germeau, A.; Kelly, J. J.; Vanmaekelbergh, D. l.; Allan, G.; Meulenkamp, E. A. *ChemPhysChem* **2003**, *4*, 959.

(26) Morales, M. V.; Asedegbega-Nieto, E.; Iglesias-Juez, A.; Rodríguez-Ramos, I.; Guerrero-Ruiz, A. *ChemSusChem* **2015**, *8*, 2223.

(27) Cohn, A. W.; Janßen, N.; Mayer, J. M.; Gamelin, D. R. *J. Phys. Chem. C* **2012**, *116*, 20633.

(28) Schrauben, J. N.; Hayoun, R.; Valdez, C. N.; Braten, M.; Fridley, L.; Mayer, J. M. *Science* **2012**, *336*, 1298.

(29) Schwartz, D. A.; Norberg, N. S.; Nguyen, Q. P.; Parker, J. M.; Gamelin, D. R. *J. Am. Chem. Soc.* **2003**, *125*, 13205.

(30) Norberg, N. S.; Gamelin, D. R. *J. Phys. Chem. B* **2005**, *109*, 20810.

(31) Hoyer, P.; Weller, H. *Chem. Phys. Lett.* **1994**, *221*, 379.

(32) Wood, A.; Giersig, M.; Mulvaney, P. *J. Phys. Chem. B* **2001**, *105*, 8810.

(33) Hayoun, R.; Whitaker, K. M.; Gamelin, D. R.; Mayer, J. M. *J. Am. Chem. Soc.* **2011**, *133*, 4228.

(34) Chávez, I.; Alvarez-Carena, A.; Molins, E.; Roig, A.; Maniukiewicz, W.; Arancibia, A.; Arancibia, V.; Brand, H.; Manuel Manríquez, J. *J. Organomet. Chem.* **2000**, *601*, 126.

(35) Hayoun, R., University of Washington, 2011.

(36) Warren, J. J.; Tronic, T. A.; Mayer, J. M. *Chem. Rev.* **2010**, *110*, 6961.

(37) Mayer, J. M. *Acc. Chem. Res.* **2011**, *44*, 36.

(38) Valdez, C. N.; Braten, M.; Soria, A.; Gamelin, D. R.; Mayer, J. M. *J. Am. Chem. Soc.* **2013**, *135*, 8492.

(39) Manner, V. W.; Markle, T. F.; Freudenthal, J. H.; Roth, J. P.; Mayer, J. M. *Chem. Commun.* **2008**, 256.

(40) Brookhart, M.; Grant, B.; Volpe, A. F. *Organometallics* **1992**, *11*, 3920.

(41) Yakelis, N. A.; Bergman, R. G. *Organometallics* **2005**, *24*, 3579.

(42) Le Bras, J.; Jiao, H.; Meyer, W. E.; Hampel, F.; Gladysz, J. A. *J. Organomet. Chem.* **2000**, *616*, 54.

(43) Meulenkamp, E. A. *J. Phys. Chem. B* **1998**, *102*, 5566.

Chapter 4. CHEMICAL REDUCTION OF ZNO NANOCRYSTALS

4.1 INTRODUCTION

The energy and density of charge carriers in semiconductor nanomaterials is a critical factor in their use in electronic, optoelectronic and plasmonic devices, energy technologies, and other applications. Extra carriers – more commonly electrons rather than holes – can be introduced into semiconductor materials by various procedures. The extra carriers affect the physical properties of the nanomaterials and are typically chemically reactive, which is critical to applications from artificial photosynthesis (solar fuels) and dye-sensitized solar cells (DSSCs) to self-cleaning coatings. For nanoscale zinc oxide (ZnO) and other oxides/chalcogenides, electrons have been added by photochemistry[1-5] or electrochemistry,[6] with dihydrogen (in bulk),[7,8] and by aliovalent-[9-16] vacancy-induced-[17-19] and remote doping.[20-26] Remote doping refers to the use of an external redox reagent, typically in solution, to add carriers. In many cases these treatments allow fine control of the density of carriers. This chemical reactivity is particularly important at the nanoscale because the majority of the material is at or near the surface. Nanocrystals (NCs) can be treated like molecular reductants,[27] with the additional advantages that they can store multiple electrons per NC and their electronic structure (band structure) can be easily tuned. Free carriers in ZnO nanocrystals have been investigated using optical, electron paramagnetic resonance (EPR), and magnetic circular dichroism spectroscopies.[1,4,5,28] The most common method of carrier generation is photoreduction, in which a photogenerated valence-band hole is quenched by a chemical reductant.[1-3,21,29] Early studies of remote doping of colloidal ZnO include those from Henglein[1] using donors prepared radiolytically, and from Guyot-Sionnest using sodium biphenyl.[20]

We use aprotic solvents so that the electron/proton/NC stoichiometry can be determined and the number of added charge balancing ions (protons) can be controlled. Given the many insights gained from studying the charge carriers, the role of charge-balancing ions is becoming recognized.[30] Charge balancing ions are necessary in steady-state conditions for many applications, but cannot be easily studied using the typical methods used to study carriers, *e.g.* short-timescale photoluminescence or transient absorption experiments. Achieving charge

balance is likely to be of particular importance in high surface area nanomaterials with substantial concentrations of charge carriers. Protons in particular are often involved because they are ubiquitous and originate from water or solvent, unless materials are at high temperature or vacuum. The general importance of protons has long been known, for instance the movement of oxide band energies with pH of the contacting aqueous solution.[31,32] One report followed the reduction of ZnO electrodes by molecular reductants in water and found that the observed rates were modulated by changes in the proton activity, using the Nernstian shift of ~60 mV/pH in the ZnO conduction band energy.[33] Hupp et al. measured this Nernstian shift for nanoscale ZnO and TiO_2 electrodes and found that the Nernstian relationship holds over a wide range of proton activities.[34] Although there are many studies such as these on protons in bulk materials, a detailed, atomic-level understanding is difficult because proton stoichiometry is difficult to control in oxide materials.

We have recently shown that protons influence the reactivity of nanoscale metal oxides, where the protons are generated in the photochemical reduction process.[35] Ethanol was used as the hole quencher, where the charge of the extra electrons in the conduction band are compensated by protons generated in the well-known oxidation of ethanol ($CH_3CH_2OH + h\nu \rightarrow CH_3CHO + 2e^- + 2H^+$). For ZnO NCs, multiple electrons per NC are accumulated[29,36,37] by this process, which was recently shown to reach a maximum that depends on the hole quencher.[5] The maximum number of electrons per NC ($<n_{e^-}>_{max}$) was also found to scale with NC volume. Therefore the maximum photochemically attainable carrier *density*, $<N_{e^-}>_{max}$, is independent of the size of the NC.[5] All of these reports are on photochemically reduced NCs. The previous chapter on reduced ZnO NCs focused exclusively on reactions with NCs that were reduced photochemically.

This chapter will focus on the equilibrium remote doping of ZnO nanocrystals, using external redox agents, suspended in an aprotic, low-polarity solvent (1:1 toluene:THF). The experiments reported here were published in an initial qualitative report where protons were added to shift the effective redox potential of ZnO NCs.[22]

4.2 Results and Discussion

4.2.1 *Reduction of ZnO NCs Using Outer Sphere Electron Transfer Agents*

The photochemical reduction of ZnO NCs introduces electrons into the conduction band *and* generates protons. In an attempt to study the electron only, chemical reductants were explored to directly reduce ZnO NCs. The ZnO NC solutions are soluble in toluene and THF, so chemical reducing agents that are soluble and compatible with the NCs are necessary. Sodium biphenyl has been shown to reduce CdSe nanoparticles by adding an electron directly to the conduction band.[20]

Initial attempts to reduce ZnO NCs were performed with sodium biphenyl, sodium metal, and sodium anthracene. These experiments were not successful, likely due to sodium binding to the surface of the NCs which resulted in NC precipitation (not shown). The reducing agents decamethylferrocene ($FeCp^*_2$), cobaltocene ($CoCp_2$), and decamethylchromocene ($CrCp^*_2$) are soluble in THF and were chosen based on their stability and ease of use. Addition of these reductants as solutions to ZnO NCs did not result in reduced NCs, as observed by optical spectroscopy (Figure 4.1, Figure 4.2, Figure 4.3).

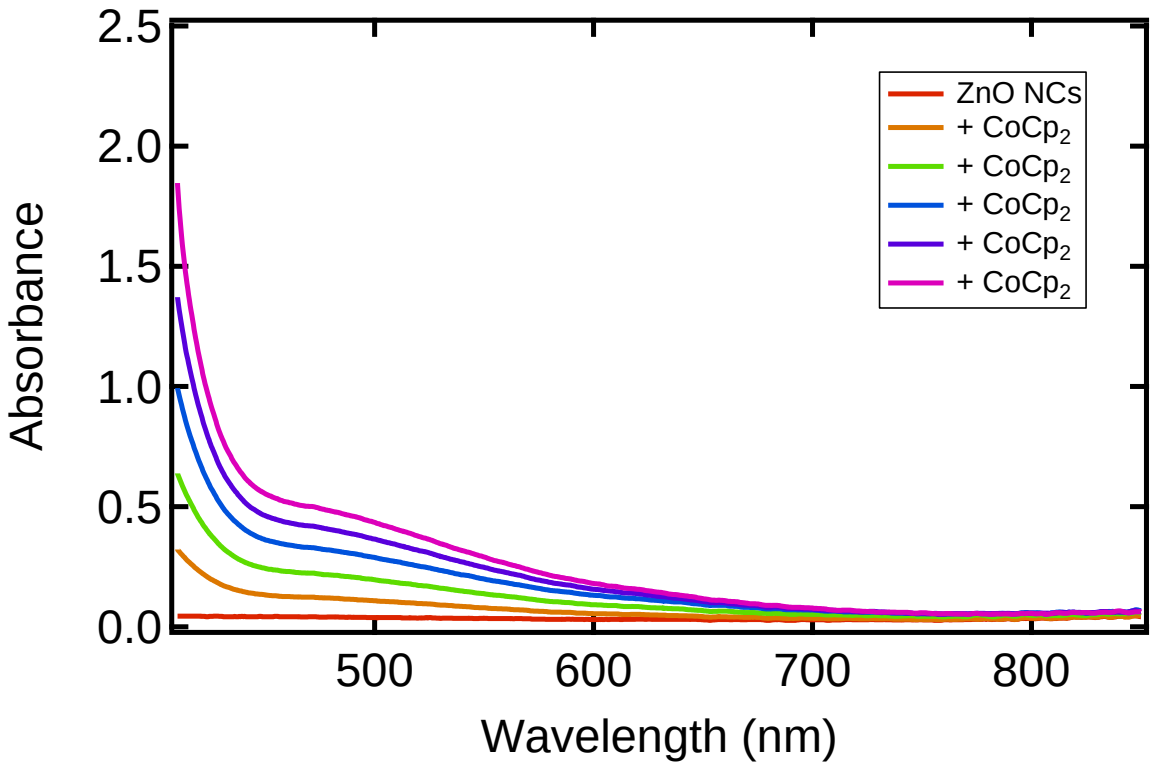

Figure 4.1. Optical spectra of ZnO NCs (d = 3.9 nm, 3.4 × 10^{-5} M) with added $CoCp_2$ (10 equiv per NC at the end).

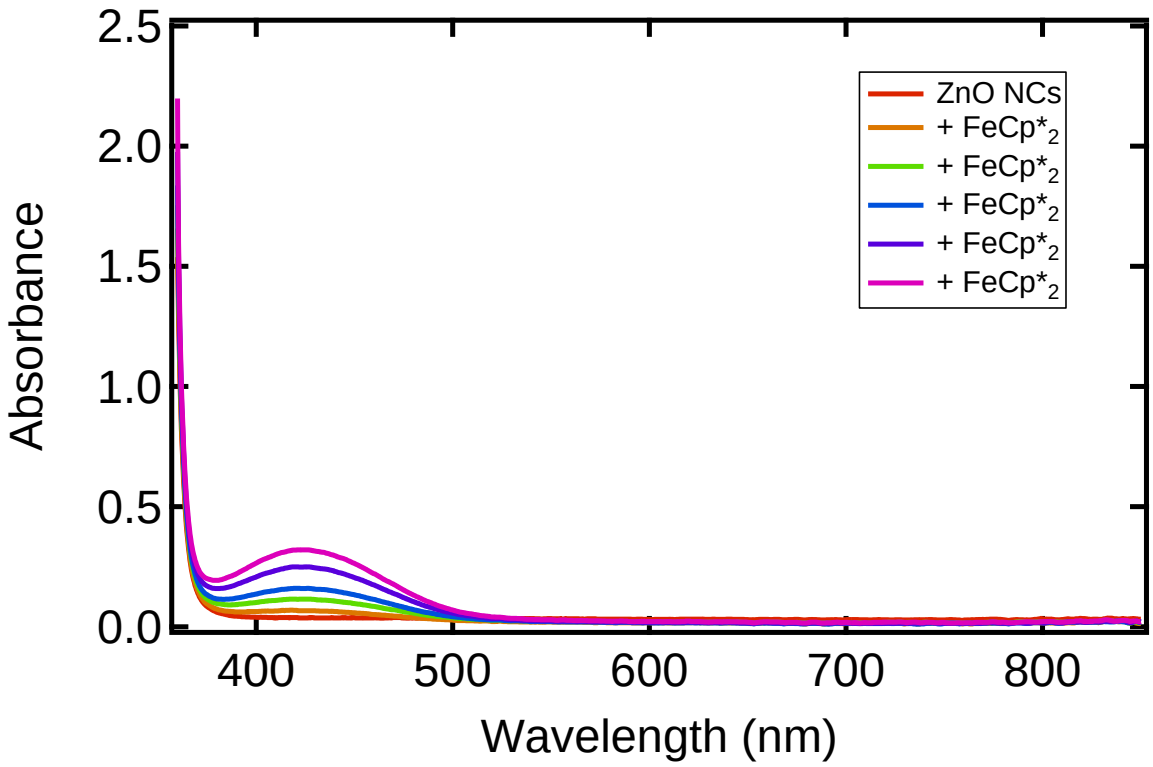

Figure 4.2. Optical spectra of ZnO NCs (d = 3.9 nm, 3.4 × 10^{-5} M) with added $FeCp^*_2$ (10 equiv per NC at the end).

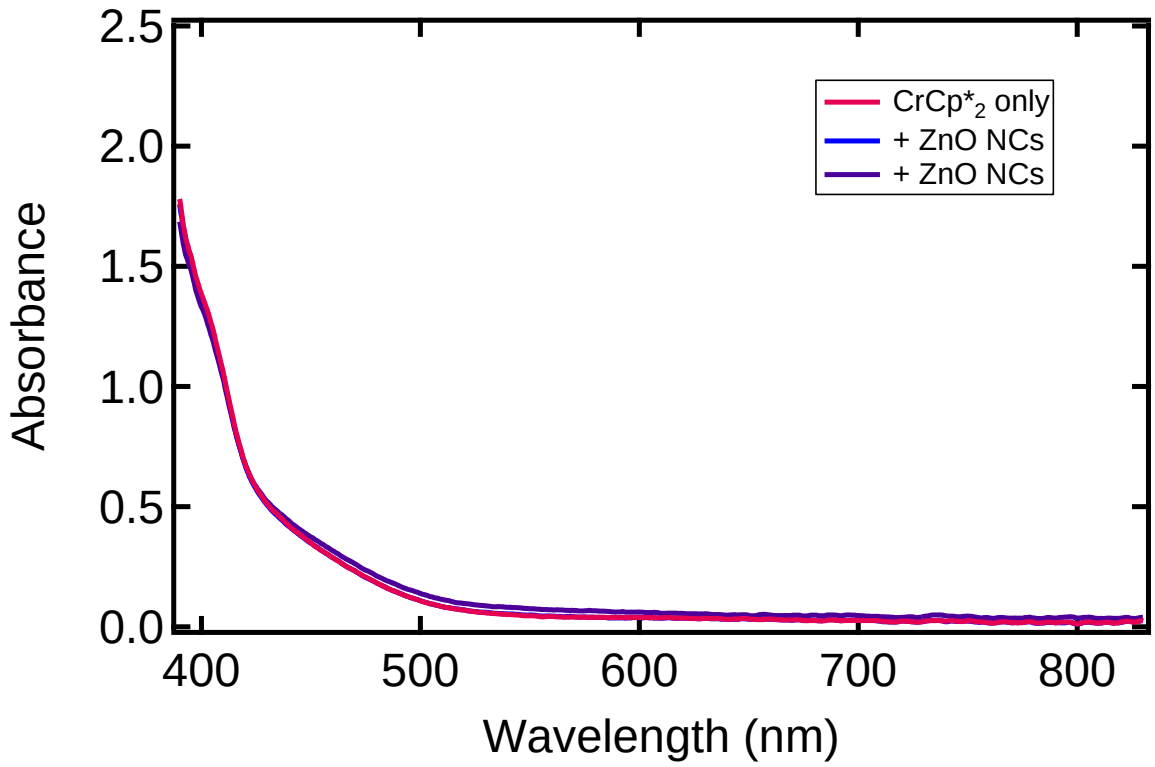

Figure 4.3. Optical spectra of $CrCp^*_2$ (1.7×10^{-2} M) plus aliquots of ZnO (final concentration of 1.82×10^{-5} M). With $\langle n_{e^-} \rangle = 5$ the absorbance change at 850 nm should be ~ 0.1.

Decamethylcobaltocene ($CoCp^*_2$) is a much more potent reducing agent (-1.94 V vs. Fc/Fc^+ in DCM)[38] and the neutral 19-electron complex is soluble in toluene. Addition of $CoCp^*_2$ to toluene/THF suspensions of ZnO NCs was monitored by optical spectra and showed rapid formation of the characteristic broad near-IR (NIR) spectrum of reduced ZnO and the presence of $CoCp^*_2{}^+$ (Figure 4.4).[22] The absorbance at 850 nm indicates an average number of electrons per NC $\langle n_{e^-} \rangle$ of ~2 for small NCs, and up to 10 for larger (r > 4 nm) NCs. The $\langle n_{e^-} \rangle$ with $CoCp^*_2$ is quantified using the molar absorption coefficient obtained for each size of NCs (discussed in Chapter 5). Addition of aliquots of $CoCp^*_2$ showed that $\langle n_{e^-} \rangle$ reaches its maximum when there is at least a five-fold excess of $CoCp^*_2$ relative to $CoCp^*_2{}^+$.[22,39] Attempts were made to fit this equilibrium-limited reduction of ZnO NCs by $CoCp^*_2$ to simple and Langmuir isotherms, but neither model fit well (Chapter 5).

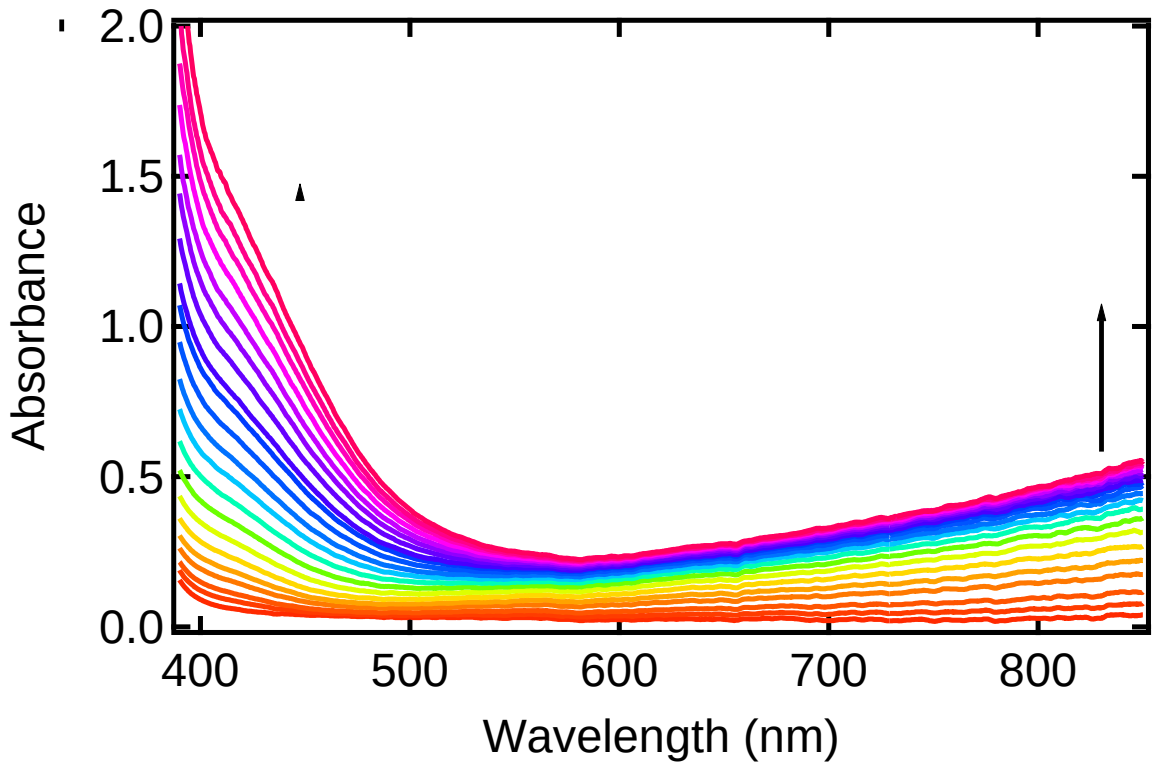

Figure 4.4. Optical spectra of ZnO NCs (d = 3.4, 9.3 × 10^{-4} M) in toluene with the addition of $CoCp^*_2$ (10 uL aliquots of 1.1 × 10^{-2} M in toluene, 03.2 equiv at the end of the additions). The reaction forms ZnO/e^- and $CoCp^*_2{}^+$, characterized by the tail of the intraband transition from 600 nm to lower energy.

The reduction of ZnO NCs by $CoCp^*_2$ was also monitored by ^{1}H NMR spectroscopy. The 19-electron metallocene is paramagnetic with a sharp singlet at 48 ppm corresponding to the ten methyl groups. The resulting product, $CoCp^*_2{}^+$, is characterized by a diamagnetic singlet at 1.8 ppm. Mixtures of the oxidized and reduced versions of $CoCp^*_2$ are the in fast-exchange regime, such that the two coalesce into a single signal at an averaged chemical shift. Addition of 11 equiv of $CoCp^*_2$ to a solution of ZnO NCs in toluene/THF gives, in addition to the resonances associated with the DDA capping ligands, a broad peak at 46.5 ppm corresponding to a mixture of $CoCp^*_2$/$CoCp^*_2{}^+$ (Figure 4.5). Addition of [TBA][$B(C_6F_5)_4$] to a solution of the NCs with $CoCp^*_2$ shifted the peak further upfield (Figure 4.6). This result suggests that either (1) TBA^+ causes further reduction of the NCs (no additional electrons were observed in the NCs by optical spectroscopy, ruling out this hypothesis), or that (2) $CoCp^*_2{}^+$ is tightly ion paired with the

reduced NCs. The latter hypothesis is intuitively reasonable because the electron in the ZnO NCs should be stabilized by a charge-balancing cation. In the NMR spectrum, this ion-paired $CoCp^*_2^+$ does not rapidly exchange with free $CoCp^*_2$, and therefore the position of the averaged peak for $CoCp^*_2$/$CoCp^*_2^+$ cannot be used to determine the number of electrons transferred to the NCs.

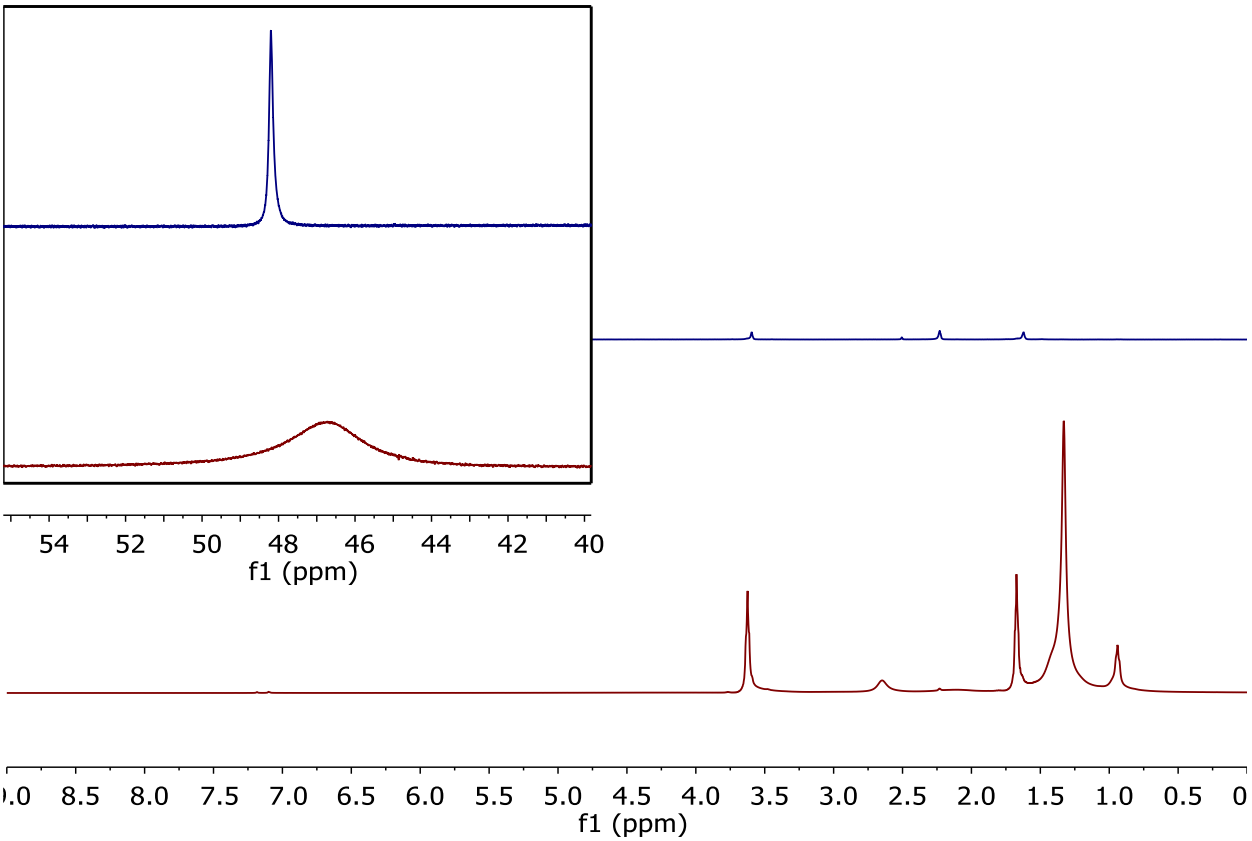

Figure 4.5. ^{1}H NMR spectra of $CoCp^*_2$ alone (3.7×10^{-3} M) and with ZnO NCs (d = 3.9 nm, 3.4×10^{-4} M, 11.2 equiv $CoCp^*_2$ per NC) in 50/50 v/v toluene-d_8/THF-d_8. The inset shows the peak corresponding to $CoCp^*_2$ and in the case of NCs, the mixture of $CoCp^*_2$/$CoCp^*_2^+$ in the fast exchange regime, shifted downfield from the purely paramagnetic $CoCp^*_2$.

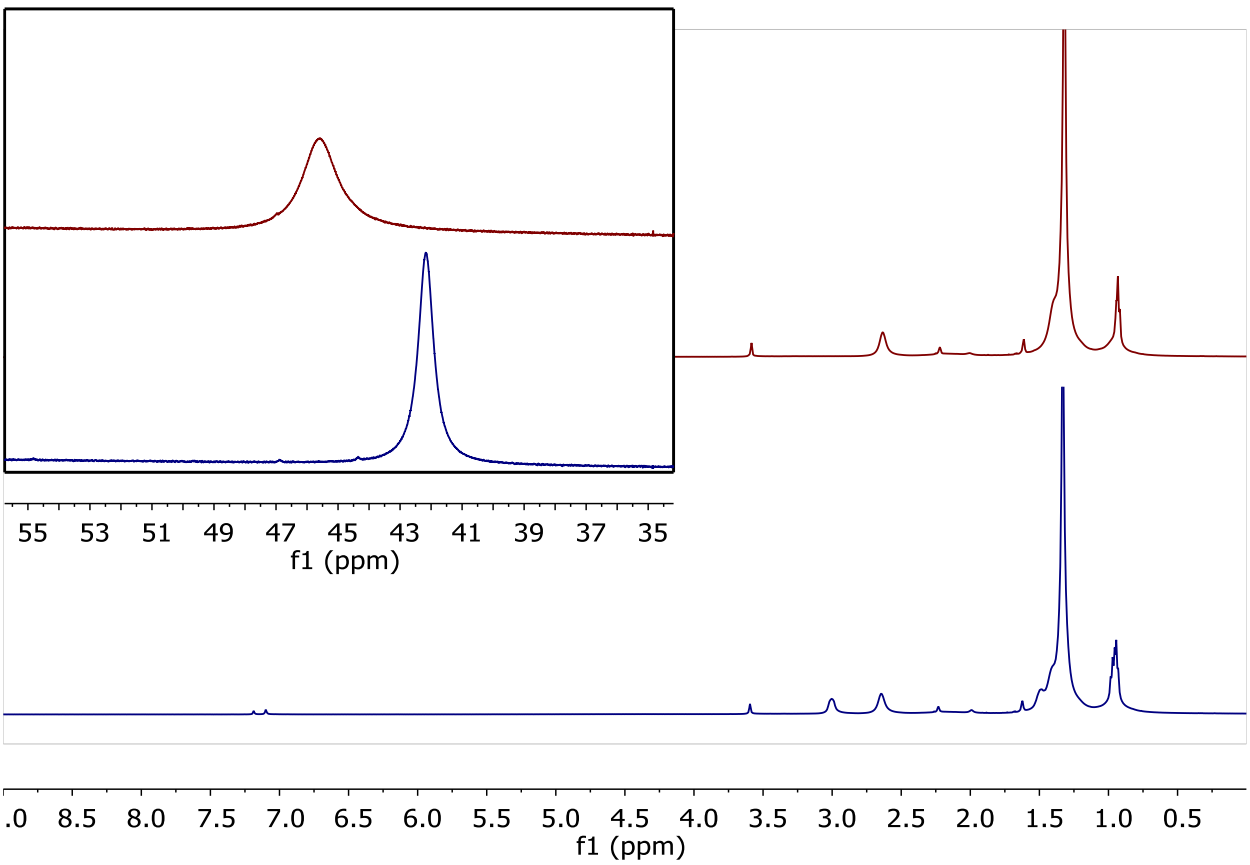

Figure 4.6. ^{1}H NMR spectra of ZnO NCs (d = 3.9 nm, 3.4 × 10^{-4} M) reduced with $CoCp^*_2$ (27 equiv per NC) (red), followed by the addition of [TBA][$B(C_6F_5)_4$] (22 equiv per NC, blue). The inset shows the peak corresponding to the mixture of $CoCp^*_2$/$CoCp^*_2^+$ in the fast exchange regime, and addition of TBA^+ shifts the equilibrium toward more $CoCp^*_2^+$.

Initial attempts to reduce the ZnO NCs with Na medal or Na anthracenide/naphthalenide were unsuccessful because of NC precipitation. We developed methods to make the NC solutions more stable (*vide infra*), and a wider range of alkali metal-based reductants were explored. A THF solution of [A][benzophenone] (A = K^+ or Na^+, -2.30 V vs. Fc/Fc^+ (THF))[38] was prepared and added to solutions of ZnO NCs in toluene/THF. Addition of the [Na][benzophenone] solution to ZnO NCs results in an increase in the near-IR band corresponding to ZnO/e^- without NC precipitation (Figure 4.7). In addition to reduced NCs, the products of this reaction are neutral benzophenone and Na^+, the latter of which is likely associated with ZnO/e^-. Similar experiments with [K][benzophenone] as the reductant resulted in some NC reduction, but the NCs stability was lower with each addition, finally resulting in

flocculation (Figure 4.8). This points to the difference in cation ability to stabilize the reduced NCs, which will be explored more in future experiments, and is discussed in Chapter 5.

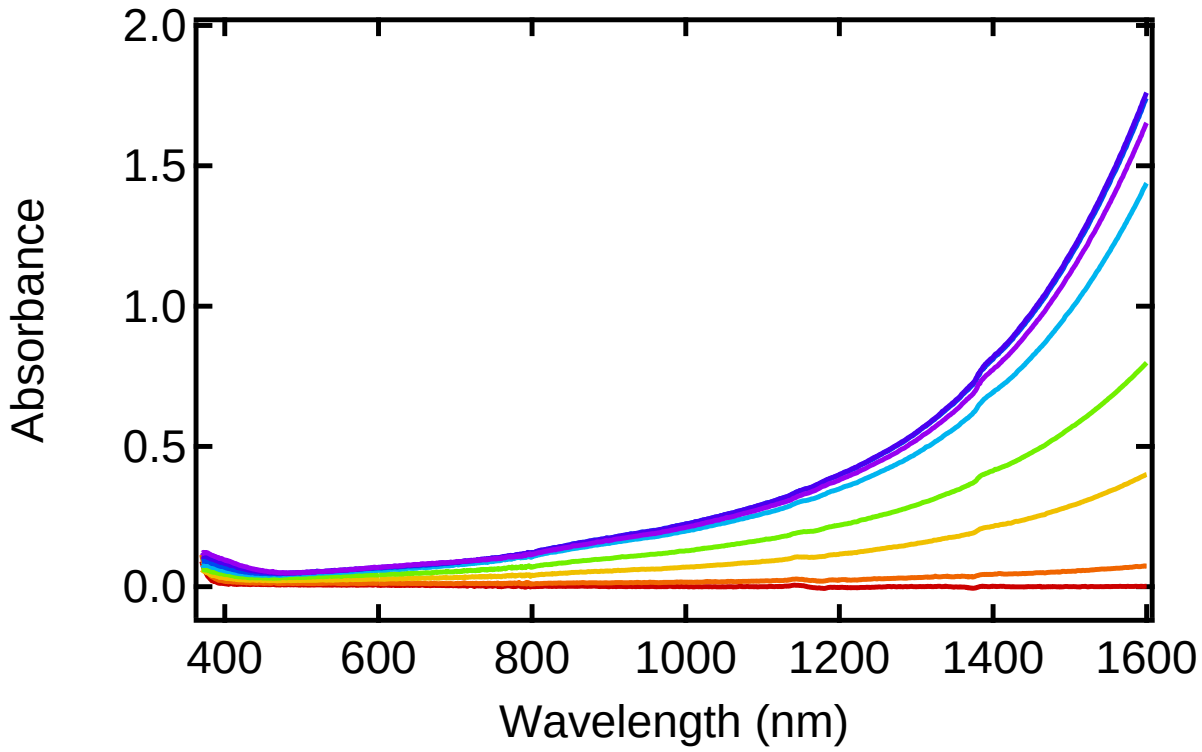

Figure 4.7. Optical spectra of ZnO NCs (d = 3.8 nm, 1.6 × 10^{-5} M, TOPO-capped, red) with the addition of [Na][benzophenone] as a solution in THF (2.8 × 10^{-2} M, 70 equiv per NC at the end of the additions).

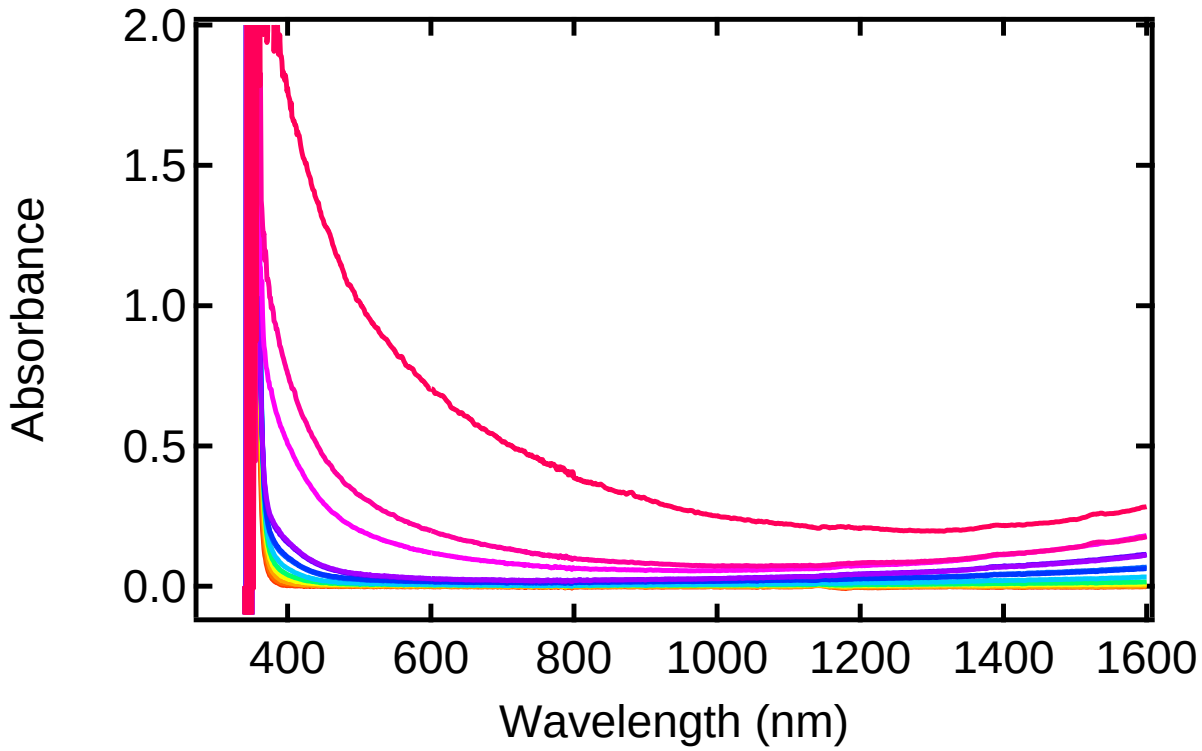

Figure 4.8. Optical spectra of ZnO NCs (d = 3.8 nm, 1.6 × 10^{-5} M, TOPO-capped, red) with the addition of [K][benzophenone] as a solution in THF (2.8 × 10^{-2} M, 75 equiv per NC at the end of the additions)

4.2.2 *Addition of Acid to Increase the Electrons Transferred to ZnO NCs: Monitored by Optical and NMR Spectroscopies*

As discussed in the chapter on photoreduced NCs (Chapter 3), the presence of a few extra protons can change the redox potential of the ZnO NCs dramatically. Based on this observation, we searched for a method to study the effect of stoichiometric extra *protons*, without the complex reactivity that arises from a highly oxidizing hole generated from the absorption of UV light.

Brookhart's acid, the diethyl ether oxonium ion with the anion tetrakis[3,5-bis(trifluoromethyl)phenylborate $[H(Et_2O)_2][BAr^F{}_4]$, is a stable white solid and a strong organic-soluble acid that was first reported by Brookhart in 1992.[40] Although this acid is exceptionally strong, it is stable in small amounts (equivalents varied) with the ZnO NCs and enabled a systematic study of the effect of each proton on the redox chemistry of the NCs. Initial

experiments used a concentrated solution of the $[H(Et_2O)_2][BAr^F{}_4]$ in THF, but we eventually noticed that this acid is capable of polymerizing THF. To avoid this issue, excess DDA was added in later experiments to form dodecylammonium [DDA-H]$[BAr^F{}_4]$ (the two ether molecules are omitted from the formula for clarity) which was used as the acid source in most experiments, except where otherwise noted. In addition to $[H(Et_2O)_2][BAr^F{}_4]$, other acids were prepared in an attempt to protonate the ZnO NCs, including pyridinium triflate [py-H][OTf], protonated DMF triflate [DMF-H][OTf], protonated DBU triflate [DBU-H][OTf] and [P1-^{t}Bu phosphazene][BF_4] prepared according to reported procedures.[41] However, these acids were insoluble in toluene and toluene/THF mixtures, and thus were unsuitable for protonating the NCs.

In one experiment, a solution of ZnO NCs was initially reduced with 20 equiv $CoCp^*_2$ to $\langle n_{e^-} \rangle$ ~1.4, followed by the addition of $[H(Et_2O)_2][BAr^F{}_4]$ which caused a roughly linear increase in $\langle n_{e^-} \rangle$ up to at least 15 e^-/NC (Figure 4.9). The $\langle n_{e^-} \rangle$ with $CoCp^*_2$ is quantified using the molar absorption coefficient at 850 nm (Chapter 5). This is substantially more reduction than can be achieved for the same NCs by the photochemical process of eq 1 ($\langle n_{e^-} \rangle_{(max)} \sim 6$[37]). The changes are rapid, within the time of mixing of the reagents. This is consistent with the previous observation of rapid NC-to-NC electron transfer.[27] The resulting electron distribution between ZnO NCs and $CoCp^*_2/CoCp^*_2{}^+$ is stable, indicating an equilibrium situation controlled by thermodynamic rather than kinetic factors (Scheme 4.1).

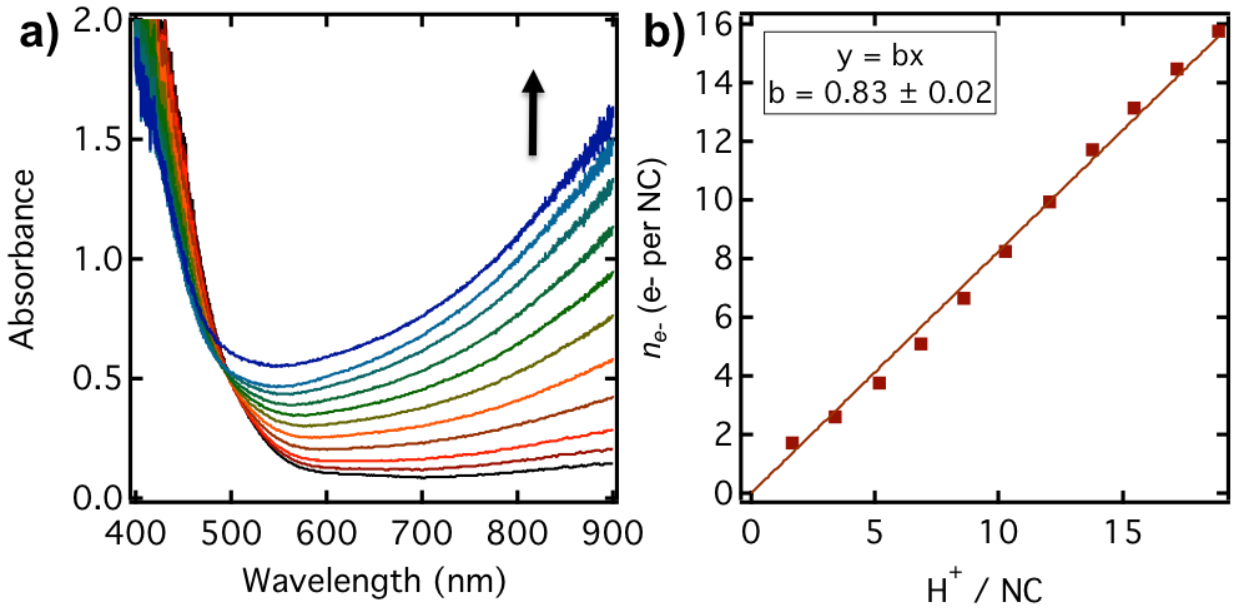

Figure 4.9. Reduction of ZnO NCs with $CoCp^*_2$ and $[H(Et_2O)_2][BAr^F_4]$. a) Absorption spectra of ZnO NCs (1×10^{-4} M, d = 4.3 nm) with 20 equiv $CoCp^*_2$ (bottom black trace), then with 10 µL (1.7 equiv each) aliquots of $[H(Et_2O)_2][BAr^F_4]$ in THF.After ~20 equiv of acid, the NCs precipitated. b) Plot of $<n_{e^-}>$ vs. equivalents of acid.

Scheme 4.1. Reduction of ZnO NCs with metallocenes with the addition of acid as [DDA-H][BAr^F_4].

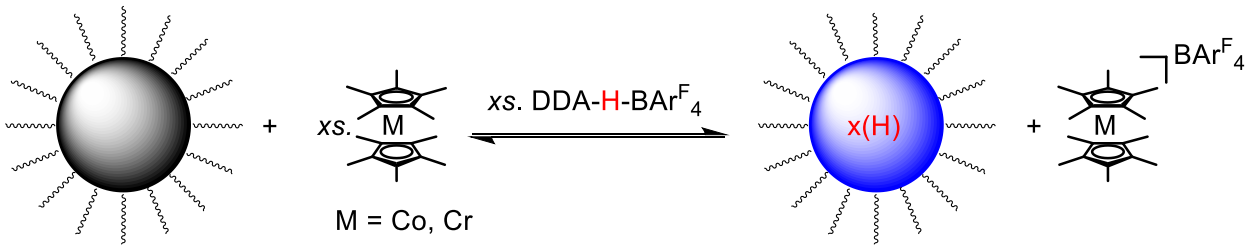

The reduction of the NCs with $CoCp^*_2$/$[H(Et_2O)_2][BAr^F_4]$ added can also be monitored by ^{1}H NMR spectroscopy, similar to the above experiments without acid. The averaged peak corresponding to $CoCp^*_2$ and $CoCp^*_2{}^+$ is shifted upfield as protons are added and electrons transferred to the NCs, resulting in a higher ratio of $CoCp^*_2{}^+$ (Figure 4.10). Traditionally, the position of this peak provides information about the amount of each species in solution, but as we demonstrated above, some of the $CoCp^*_2{}^+$ is ion-paired to the NCs.

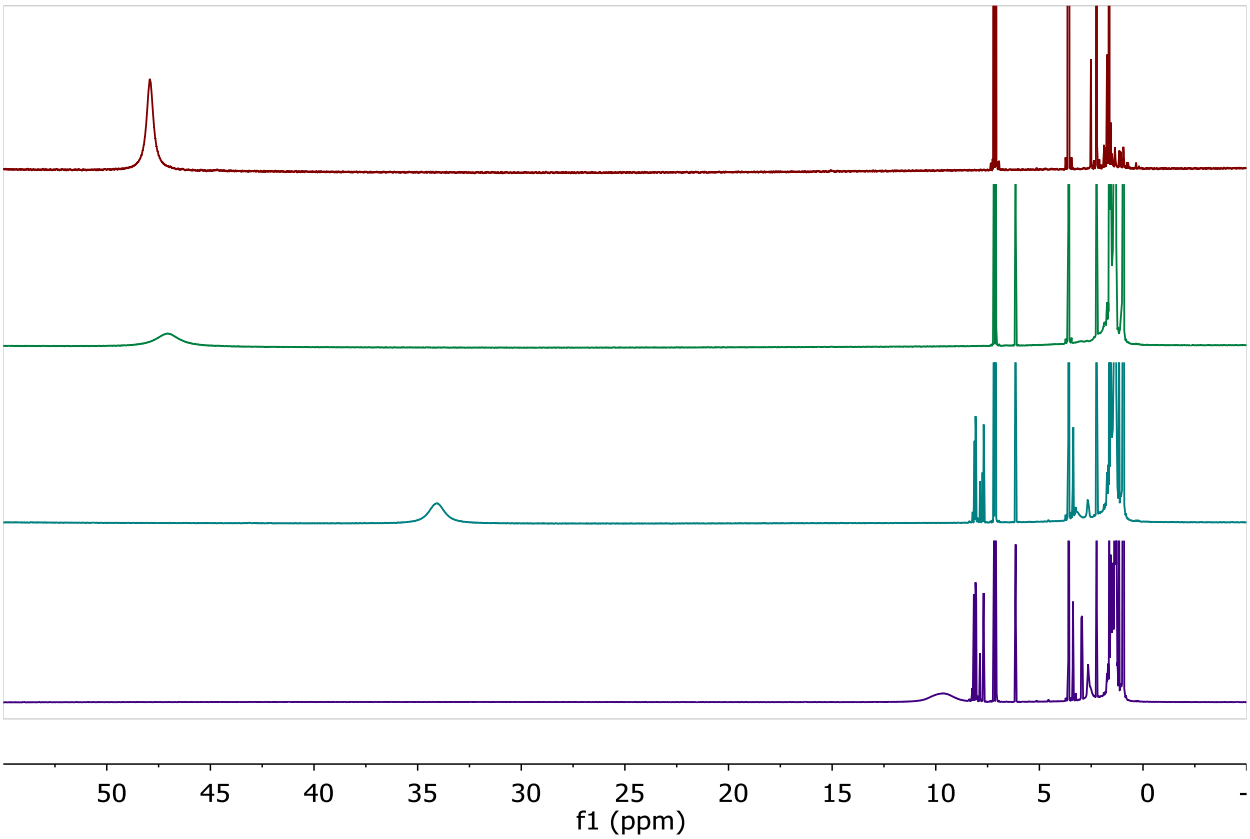

Figure 4.10. ^{1}H NMR spectrum of $CoCp^*_2$ (12 mM, 51 per NC, red) with ZnO NCs (d = 3.8 nm, 2.3 × 10^{-4} M, green) in 50/50 toluene-d_8/THF-d_8 plus addition of acid as [DDA-H][BAr^F_4] (blue and purple, 4 equiv and 8 equiv total, respectively).

That the reduction with $CoCp^*_2$ and DDA-H^+ is an equilibrium process is further indicated by the reversibility with addition of base, as shown in Figure 4.11. Addition of the P4-*t*-Bu-phosphazene base to a solution of NCs with excess $CoCp^*_2$ and DDA-H^+ shows a decrease in the NIR absorbance from conduction band electrons. Therefore, addition of base shifts the equilibrium such that electrons are transferred from the NCs back to $CoCp^*_2{}^+$ (Figure 4.11, right). Addition of acid or base alone does not introduce electrons to the NCs.

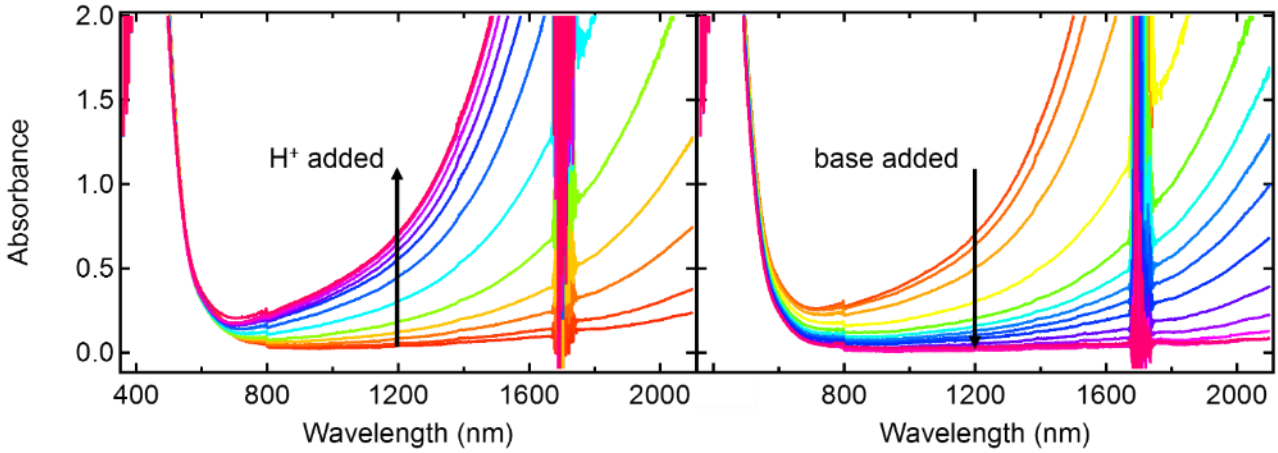

Figure 4.11. Reversible reduction of NCs with $CoCp^*_2$ using acid and base. *Left:* Absorption spectra of ZnO NCs (r = 3.0 nm, 5.2 × 10^{-6} M, TOPO−capped) and $CoCp^*_2$ (6.4 × 10^{-3} M) in toluene/THF plus acid, added as a toluene/THF solution of DDA-H^+ (20 μL additions of 8.5 × 10^{-3} M, 15 equiv per NC per addition). The increase of absorbance at 510 nm and longer wavelengths are due to the tail of the NIR absorbance associated with extra electrons in ZnO NCs, the noise from 1680-1740 nm is from solvent absorbance and the artifact at 800 nm is from the detector switchover. *Right:* To the sample on the left, P4-*t*-Bu-phosphazene base was added as a toluene/THF solution (20 μL additions of 8.5 × 10^{-3} M).

The reduction of the NCs can also be followed at the band edge (~350 nm) at very low concentrations (10^{-7} M) because the excitonic absorption is strongly absorbing (>10^5 cm^{-1})[42]. As reductant and acid are added, the conduction band is filled with electrons and the first excitonic absorption is bleached, consistent with the Burstein-Moss effect (Figure 4.12).

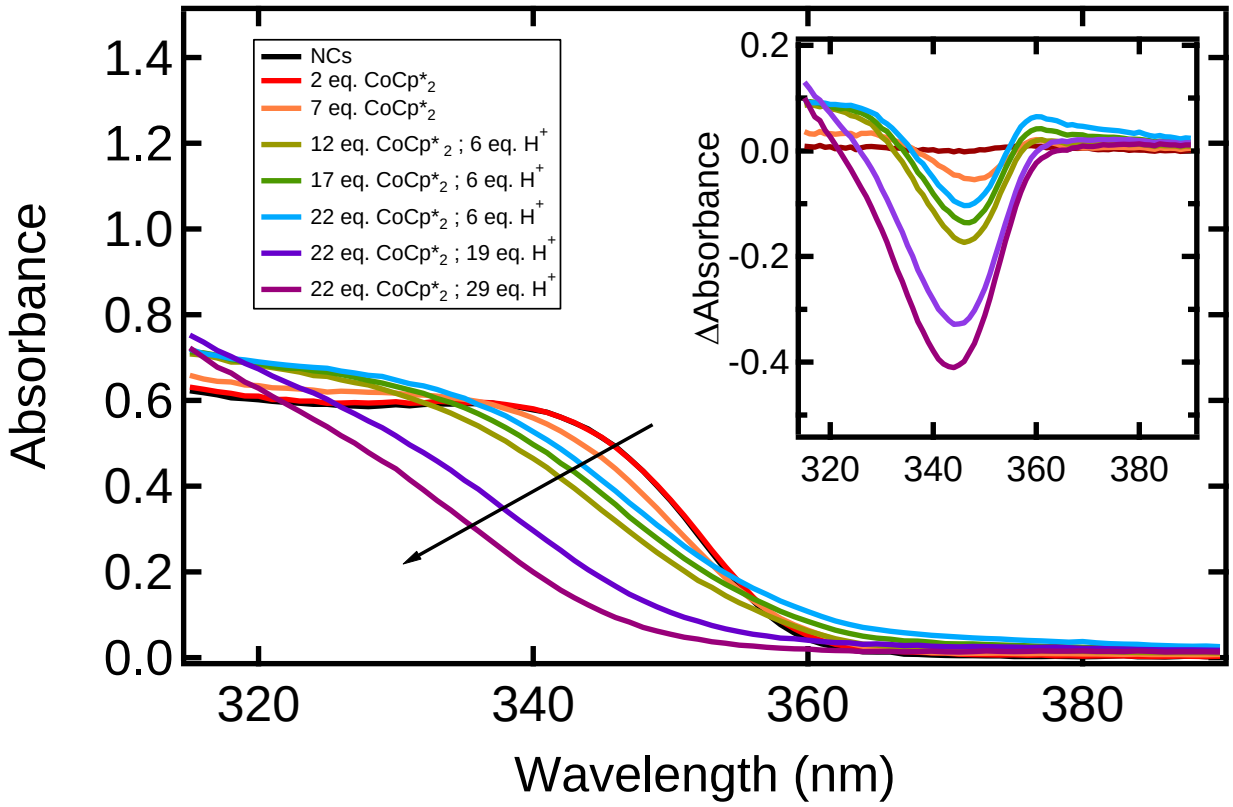

Figure 4.12. Observation of Burstein-Moss shift. Absorption spectrum of ZnO NCs (r = 1.9 nm, 6.5 ×10^{-7} M) in 50/50 toluene/THF, as $CoCp^*_2$ and DDA-H^+ is added. The inset shows the change in absorbance relative to the initial spectrum (no acid or reductant added). All are volume-corrected.

4.2.3 *Correlation of EPR Spectra and Absorbance at 850 nm.*

Previous studies of photoreduced ZnO:e^--H^+ NCs by EPR spectroscopy gives singlets near g = 1.96 for electrons in ZnO NCs.[4,43] The electrons are believed to occupy the conduction band because the peaks are unchanged even at very low temperature. Liu et al. also reported that the signal for ZnO:e^- is sensitive to NC radius as well as $\langle n_{e^-} \rangle$.[37] To the best of our knowledge, chemically reduced ZnO NCs have not yet been studied by EPR spectroscopy. It was our goal to compare the room temperature EPR spectra of electrons in photoreduced ZnO NCs with electrons that were introduced via $CoCp^*_2$ with and without added protons. Examples of the absorption data and EPR data are shown below in Figure 4.13 and Figure 4.14.

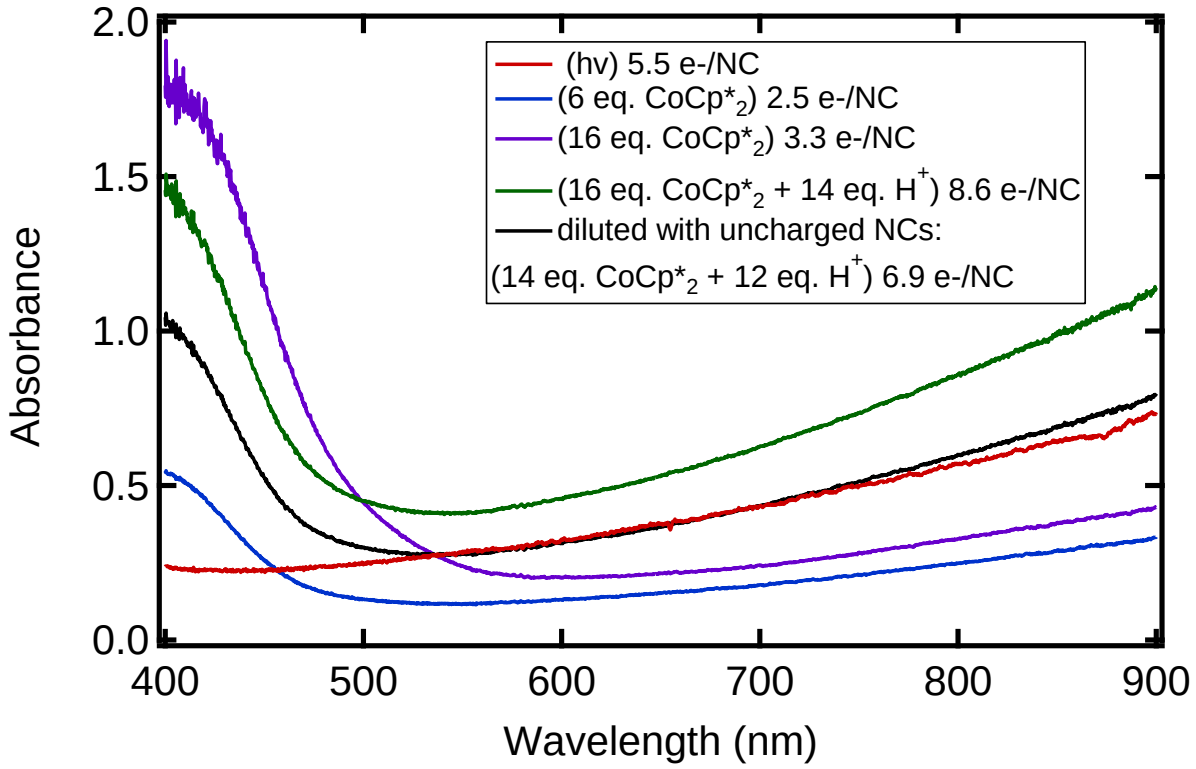

Figure 4.13. Optical absorption spectra of photoreduced, $CoCp^*_2$-reduced, $CoCp^*_2$/acid-reduced ZnO NCs(2.3×10^{-4} M, d = 5.6 nm), and a sample that was diluted with as-prepared NCs. The acid is added as [DDA-H][BAr^F_4].

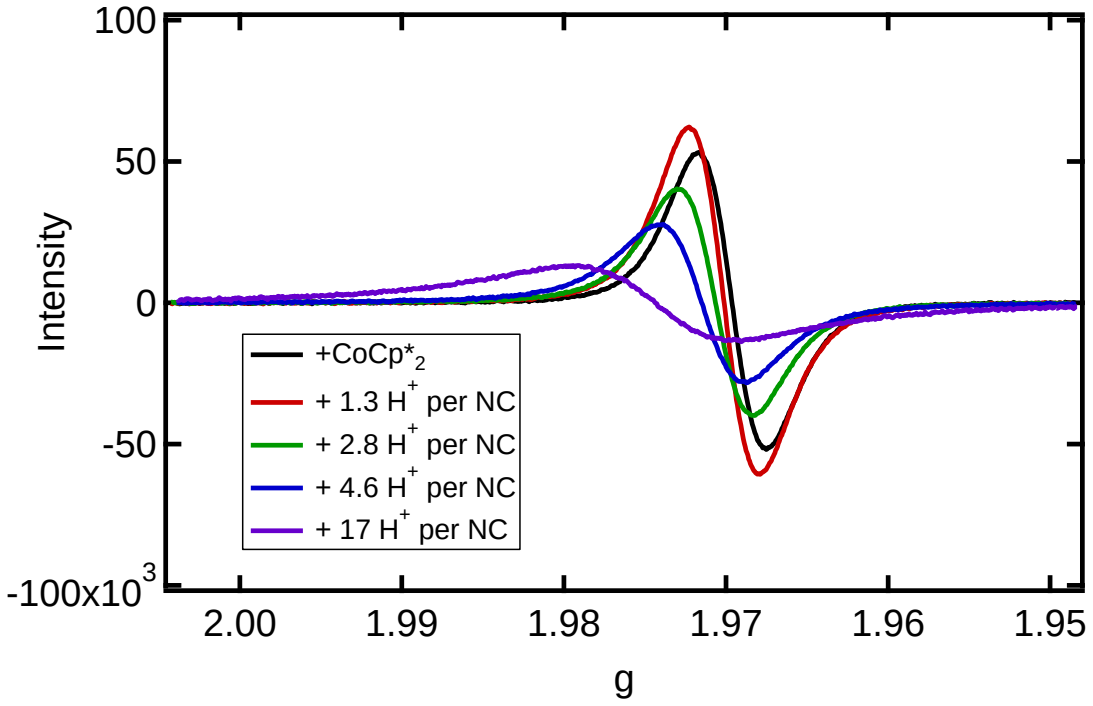

Figure 4.14. EPR spectra of Cp^*_2Co-reduced and Cp^*_2Co/acid-reduced ZnO NCsconverted from field to g with DPPH as an external reference (4.5×10^{-4} M, d = 3.6 nm), in 50/50 toluene/THF, and the acid is added as $[DDA\text{-}H][BAr^F{}_4]$.

For photoreduced NCs, there is a characteristic relationship between g and A(850), plotted as blue diamonds in Figure 4.15. The g and A(850) values for seven different solutions of chemically reduced and protonated NCs are also plotted in Figure 4.15, as red circles. Within the scatter of the data, the g/A(850) relationship is the same for the two reduction methods. Therefore it is likely, that the underlying g/$\langle n_{e^-} \rangle$ and A(850)/$\langle n_{e^-} \rangle$ relationships are also independent of reduction method. This supports the use of the same ε(850 nm) for photochemically and chemically reduced NCs. Absorbance at 850 nm (11,765 cm^{-1}) is the very high energy tail of the peak maximum (centered between 1500 – 3500 cm^{-1} depending on NC size and $\langle n_{e^-} \rangle$), and this tail does not appear to be dramatically affected (within error) by reduction method, NC size, or $\langle n_{e^-} \rangle$. In sum, electrons/protons that are added to the ZnO NCs using stoichiometric reductants/acids appear the same by EPR spectroscopy as photoreduced NCs.

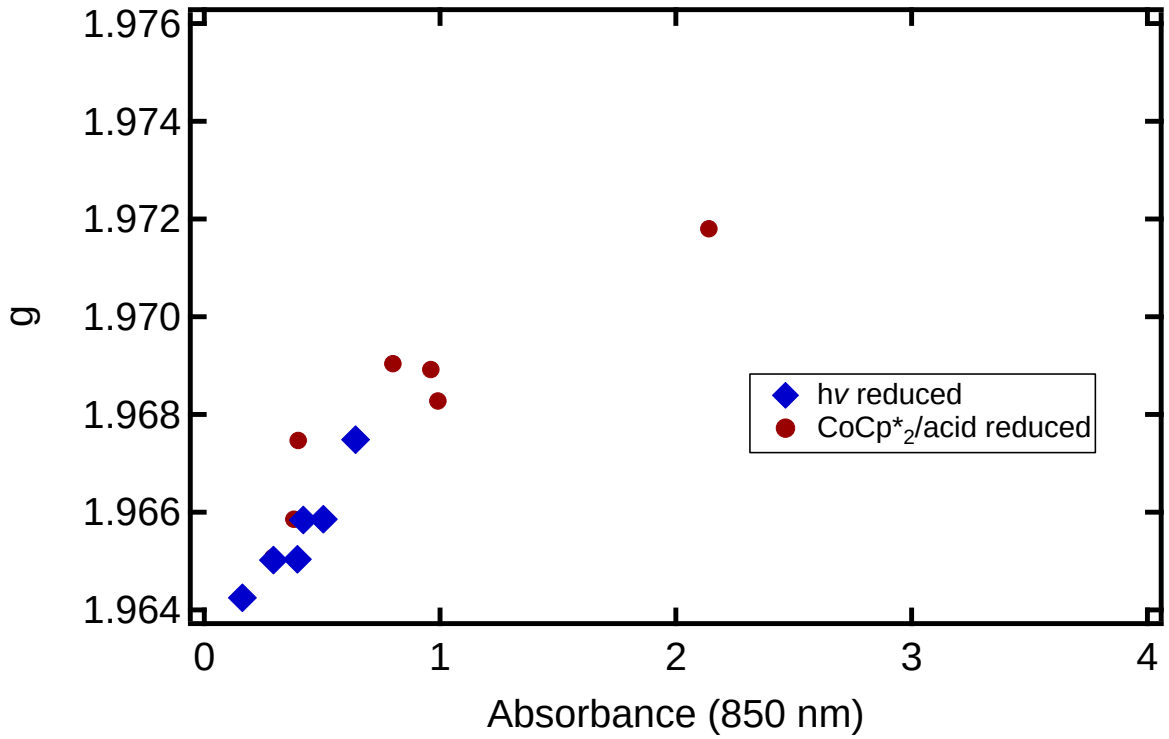

Figure 4.15. The g value of reduced ZnO NCs (d = 5.6 nm) as a function of the normalized absorbance at 850 nm of reduced NCs.Photochemically reduced and chemically reduced ZnO NCs follow the same trend of higher g value with more electrons per NC.

4.2.4 *Square Scheme for Zinc Oxide Nanocrystals*

The above reactions are summarized in a proton-coupled electron transfer (PCET) square scheme (Scheme 4.2). Protonation steps are depicted along the horizontal axis and electron transfers along the vertical axis. Using metallocenes as reductants and small amounts of acid, protons and electrons have been individually added to ZnO NCs in a stoichiometric fashion. The diagonal reactions describe photoreduction, where ethanol is oxidized to acetaldehyde, leaving behind protons and electrons on the NCs. The reverse reaction along the diagonal is hydrogen atom transfer from photoreduced ZnO to the oxyl radicals (TEMPO and $^{t}Bu_3ArO^{\bullet}$).

The facilitation of reduction by stoichiometric protons is qualitatively consistent with the effect of pH on metal-oxide band-edge energies. The traditional ~60 meV/pH linear relationship for band-edge energies would predict a 1:1 e^{-}/H^{+} stoichiometry via the Nernst equation,[44-46] which is observed for the reductions studied here.

Scheme 4.2. Reactions interconverting reduced and protonated ZnO NCs.

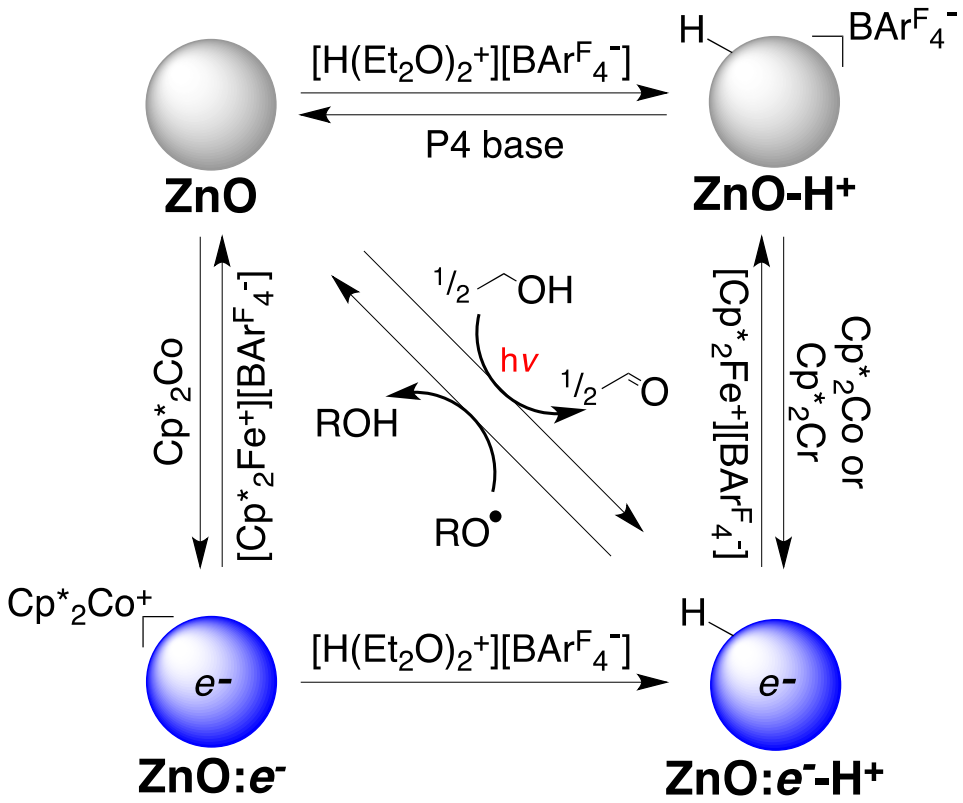

4.2.5 *Addition of More Electrons to ZnO NCs*

The studies above of proton and electron addition to dodecylamine (DDA)-capped ZnO NCs were limited to small amounts of acid because precipitation occurred with excess acid.[22] We have found two ways to overcome this precipitation issue. NCs capped with trioctylphosphine oxide-derived ligands (TOPO, 90%) have a higher solution stability, most likely because TOPO (90%) contains ligands that are anions (X-type) such as di-*n*-octylphosphonate,[47] which bind more strongly than neutral DDA (L-type ligand). NC solution stability was also substantially increased by preparation of a THF solution of $[H(Et_2O)_2][BAr^F_4]$ that contains excess DDA as the proton source $[DDA\text{-}H][BAr^F_4]$. As described above, addition of this strong acid to a THF solution of DDA immediately forms the dodecylammonium salt of the inert fluorinated anion, $[DDA\text{-}H][BAr^F_4]$. Protonating of the NCs with $[DDA\text{-}H][BAr^F_4]$ + excess DDA presumably increases the number of surface ligands and helps to maintain the NC suspension. Direct

measurement of the surface ligands and [DDA-H][BAr^F_4] by ^{1}H NMR spectroscopy[48] was not possible because the changes are obscured by the large increase in free DDA.

With a large excess of both $CoCp^*_2$ and [DDA-H][BAr^F_4], the NCs were further reduced until a maximum was reached, $\langle n_{e^-} \rangle_{max}$. Additional equivalents of reductant and/or acid did not result in any increase of electrons transferred to the NCs (Figure 4.16). This maximum value for saturation of electrons per NC is fairly consistent for NCs of the same average size, from one batch to another. However, this $\langle n_{e^-} \rangle_{max}$ does vary considerably with NC size. For example, a solution of NCs with an average radius (r) of 1.7 nm achieves a maximum of eight electrons per NC, whereas a NC with r = 3.5 nm saturates at about 120 electrons per NC (Figure 4.16).

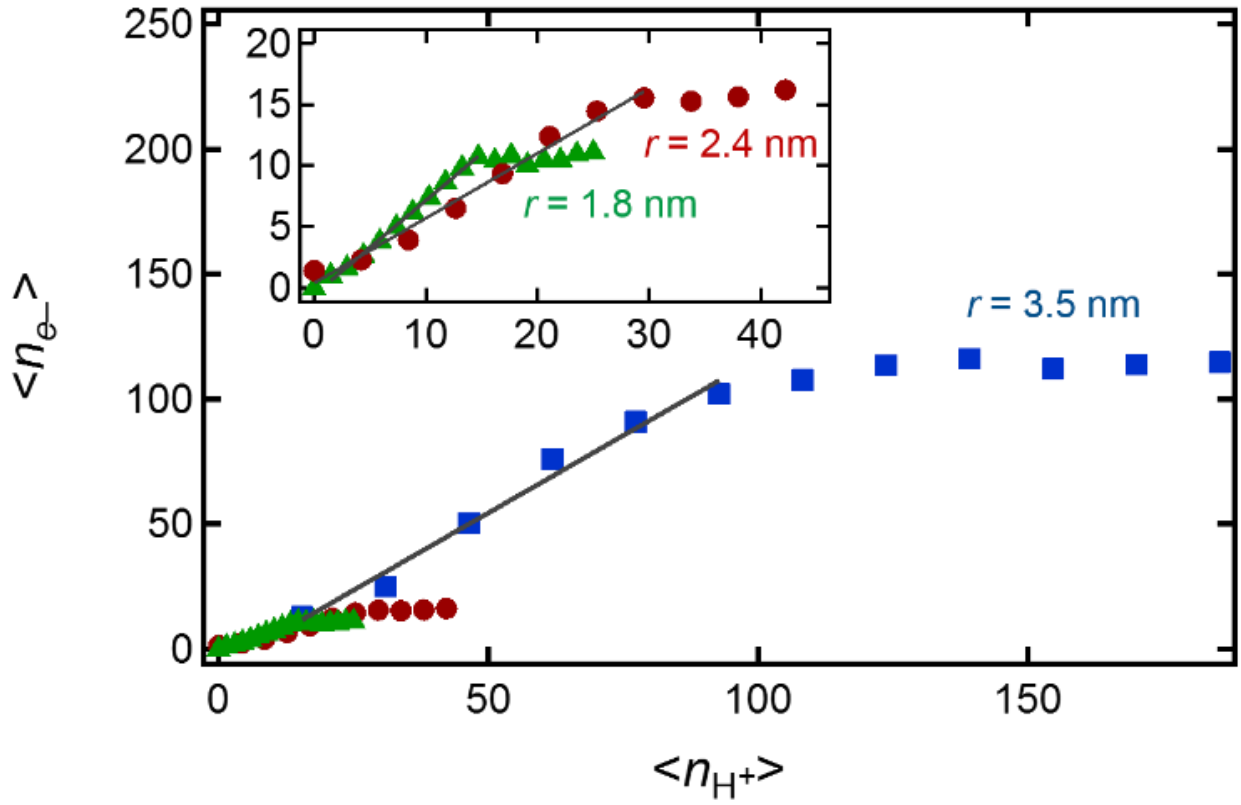

Figure 4.16. Dependence of NC reduction on NC size.Average number of electrons per NC ($\langle n_{e^-} \rangle$) versus added H^+ per NC for three representative sizes of NCs: r = 1.8 nm (green triangles), 2.4 nm (red circles), and 3.5 nm (blue squares). The corresponding slopes are about 1 e^- per added H^+ (0.8 ± 0.3, 0.7 ± 0.2, 1.4 ± 0.2, respectively). Analogous traces at different NC sizes are shown in the supporting information.

4.2.6 *Coupling Electron and Proton Transfers: The Importance of Charge Balance.*

The average number of carriers per NC ($<n_{e^-}>$) is plotted as a function of H^+ per NC ($<n_{H^+}>$) for $CoCp^*_2$ and [DDA-H][BAr^F_4] with ZnO NCs (Figure 4.17). The growth of $<n_{e^-}>$ is linear with respect to added protons over a wide range, reaching a maximum ($<n_{e^-}>_{max}$) that is unchanged with further addition of acid. Over a large number of experiments and NC batches and sizes, the slope of this line before saturation ($<n_{e^-}>/<n_{H^+}>$) is near one for all samples (0.9 ± 0.3, Figure 4.18). In some of the traces there is a small deviation from linearity at very low amounts of acid. The small variation in slopes and occasional low-acid deviations likely result in part from the difficulty of precise measurements of small amounts of strong acid in the glove box. There are also likely small variations in the NC suspensions from sample to sample, as some may have trace acid or base (perhaps surface hydroxide) and it is difficult to avoid trace impurities in solvents at the sub-10^{-5} M level. Consistent with this concern, the slopes are more likely to be < 1.0 for the smaller particles, where the amounts of added materials are less (Figure S4). We also notice that larger NCs typically deviate on the end of >1, which might arise from differences in the NC synthesis. Larger NCs are heated which may remove trace acid. In addition, at larger amounts of $CoCp^*_2$, a trace impurity consumes the first additions of acid, which is only relevant for the larger NCs because the $CoCp^*_2$ must be at a much higher concentration (see 4.4.3). Although there are many experimental reasons to explain the deviation from one, the average $<n_{e^-}>/<n_{H^+}>$ is very close to one, at 0.9 ± 0.3 (Figure 4.18). In sum, within uncertainty, each added proton results in one electron being transferred to the ZnO NCs from the excess $CoCp^*_2$ reductant present in solution.

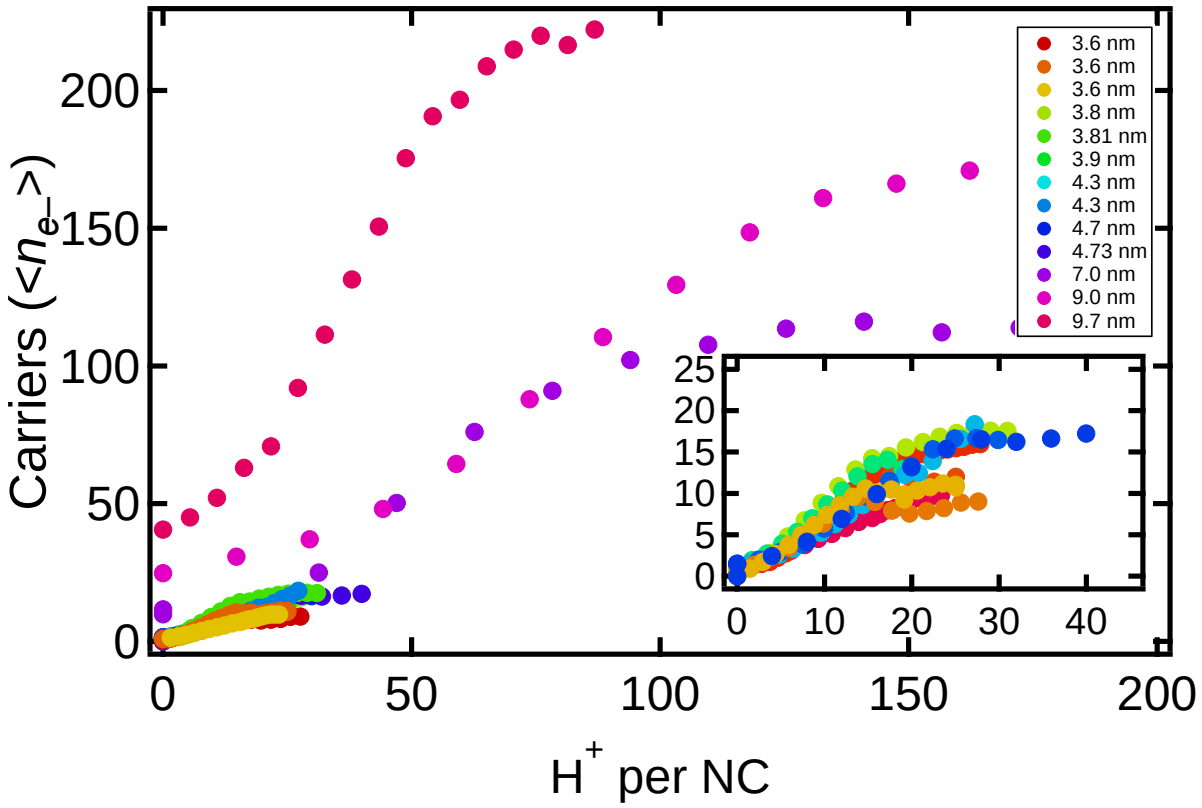

Figure 4.17. Plot of <n_{e^-}> versus <n_{H^+}>.The average number of carriers per NC (<n_{e^-}>) plotted as a function of <n_{H^+}>, for a variety of NC sizes. The legend gives the NC diameter, from 3.6 nm to 9.7 nm. The inset shows the smaller NCs.

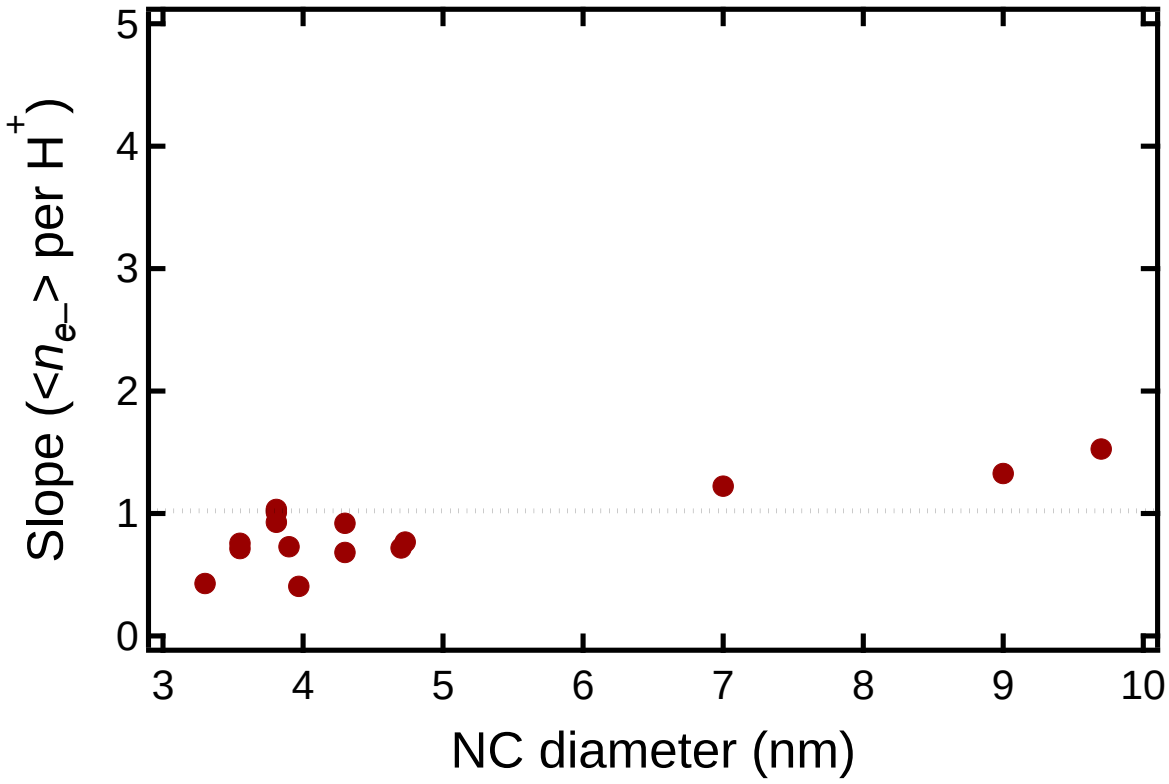

Figure 4.18. The slope from Figure 4.17 is plotted as a function of NC diameter.The dotted line represents $\langle n_{e^-} \rangle / \langle n_{H^+} \rangle = 1$.

4.2.7 *Discussion of Charge Balance in ZnO NCs*

The experiments reported here show that the addition of electrons to ZnO NCs is tightly coupled to the addition of protons under our conditions. These conditions involve the addition of acid, as [DDA-H][$BAr^F{}_4$], to toluene/THF suspensions of ZnO NCs with excess reductant, $MCp^*{}_2$. In all cases, the number of electrons added to the NCs rises linearly with the number of protons added, then reaches a maximum. All indications are that the electron and proton transfer processes examined here are at chemical equilibrium, since the reduction occurs rapidly, the final solutions are stable, the same reduction is obtained independent of the order of addition, and the electron transfer is reversed upon addition of base. The observation of a maximum charging density is very similar to the prior observation that $\langle n_{e^-} \rangle_{max}$ in photodoped ZnO NCs scales with nanocrystal volume, yielding constant maximum electron densities over all nanocrystal sizes.[5]

The reason that electron and proton transfers are coupled is likely for charge balance. The thermochemical preference for charge balance has long been discussed in molecular proton-coupled electron transfer (PCET) processes.[49-52] As another example, charge balance has long been known to be critical to electron transfer in and out of polymer films on electrodes.[53] In the ZnO NC system discussed here, the key role of charge balance is implicated by the observation that roughly one electron is added for each proton added to the solution. The linear and roughly 1:1 e^-:H^+ behavior is perhaps surprising from an orbital perspective, as discussed below, but it is required if charge balance dictates the NC reactivity.

We anticipate that charge balance and PCET play key roles in many processes that involve redox reactions of nanoscale semiconductors. It could be argued that the experiments here differ from most applications in that acidic protons have intentionally been added, but protons will be present at any material/solution interface given the ubiquity of water. In addition, any added electron must have a charge-balancing cation that likely plays a role in the overall energetics of e^- addition, for example, before the addition of acid the charge-balancing cation is $MCp^*_2{}^+$. The 1:1 e^-:H^+ equilibrium stoichiometry from charge balance provides a rationalization of the well-known dependence of band edge energies on the pH of contacting aqueous solutions.[31,32] As emphasized by Hupp, the 60 mV shift per pH unit is the Nernstian shift expected for a 1:1 e^-:H^+ process such as $TiO_2 + e^- + H^+ \rightarrow TiOOH$.[34,45,54-56] Charge balance is likely to be especially important when there are many electrons per nanoparticle and high carrier densities, as is often the case in the steady-state condition of many devices. In TiO_2 dye-sensitized solar cells, for instance, the steady-state concentration of conduction band/trap state electrons is on the order of 10^{18} cm^{-3}, which corresponds to one extra electron per ~3,000 titanium atoms.[57] The maximum charging density of $4.4(1.0)\times10^{20}$ cm^{-3} for protonated ZnO and $CoCp^*_2$ corresponds to one electron for every 100(20) Zn atoms (a unit cell volume of 47.66 $Å^3$ and two ZnO units per unit cell, gives 4.2×10^{22} Zn atoms cm^{-3}).

The linear dependence of $<n_{e^-}>$ on the number of added protons (Figure 4.18) is surprising from an electronic structure perspective. Theory predicts that spherical quantum-confined NCs should have well-separated–hydrogen atom-like orbitals in their "conduction band."[3,58] After filling the s-type orbital with two electrons, there should be a break in the linearity before the next six electrons fill p-type orbitals, *etc*. Our data show no evidence for such a discontinuity, even with small numbers of electrons where shell filling should be most evident. The observed

$\langle n_{e^-}\rangle/\langle n_{H^+}\rangle$ linearity could be due to the effects of surface trap states, inhomogeneous broadening due to NC size heterogeneity or surface dipole effects. While the merits of these various explanations could be debated, it is not evident why any of them would lead to linearity and the roughly 1:1 stoichiometry. Thus we favor the simple explanation that charge balance governs the NC reduction.

4.2.8 *Carrier Density of Chemically Reduced ZnO Nanocrystals*

The $\langle n_{e^-}\rangle_{max}$ values can also be analyzed as added electrons per unit volume, *i.e.* carrier density. Here the free carriers are electrons in the conduction band introduced via the molecular reductant. For $CoCp^*_2$ and added acid, there is a nearly constant maximum carrier density $\langle N_{e^-}\rangle_{max}$ of 4.4 (± 1.0)×10^{20} cm^{-3} over NC sizes ranging from 1.5 to 5 nm in radius (Figure 4.19). This density is constant over more than an order of magnitude in $\langle n_{e^-}\rangle_{max}$ and corresponds to approximately one reduced Zn atom for every 100, where the electron is delocalized over the NC. This result is very similar to the prior photochemical reductions, which for EtOH as the hole quencher gave $\langle N_{e^-}\rangle_{max}$ of 1.4(± 0.4)×10^{20} cm^{-3}. A plot of charge carriers as a function of NC radius can be fit to $\langle n_{e^-}\rangle_{max} = ar^p$, where $p = 3$ fits well, and the best fit gives $p = 3.3 \pm 0.4$. We define maximum carrier density as $\langle N_{e^-}\rangle_{max} = \langle n_{e^-}\rangle_{max}[(4/3)\pi r^3]^{-1}$. Then by substitution we can show that the maximum carrier density can be related to the fit constant a: where $\langle N_{e^-}\rangle_{max} = ar^3[(4/3)\pi r^3]^{-1} = 3a[4\pi]^{-1}$. The fit in Figure 4.19 for a fixed $p = 3$ gives $a = 1.6 \pm 2$. The fit constant a is empirically derived, similar to the values of a which depend on the hole quencher ($a = 0.5 – 2.1$),[5] and in this report a is dependent on the strength of the reductant (*vide infra*).

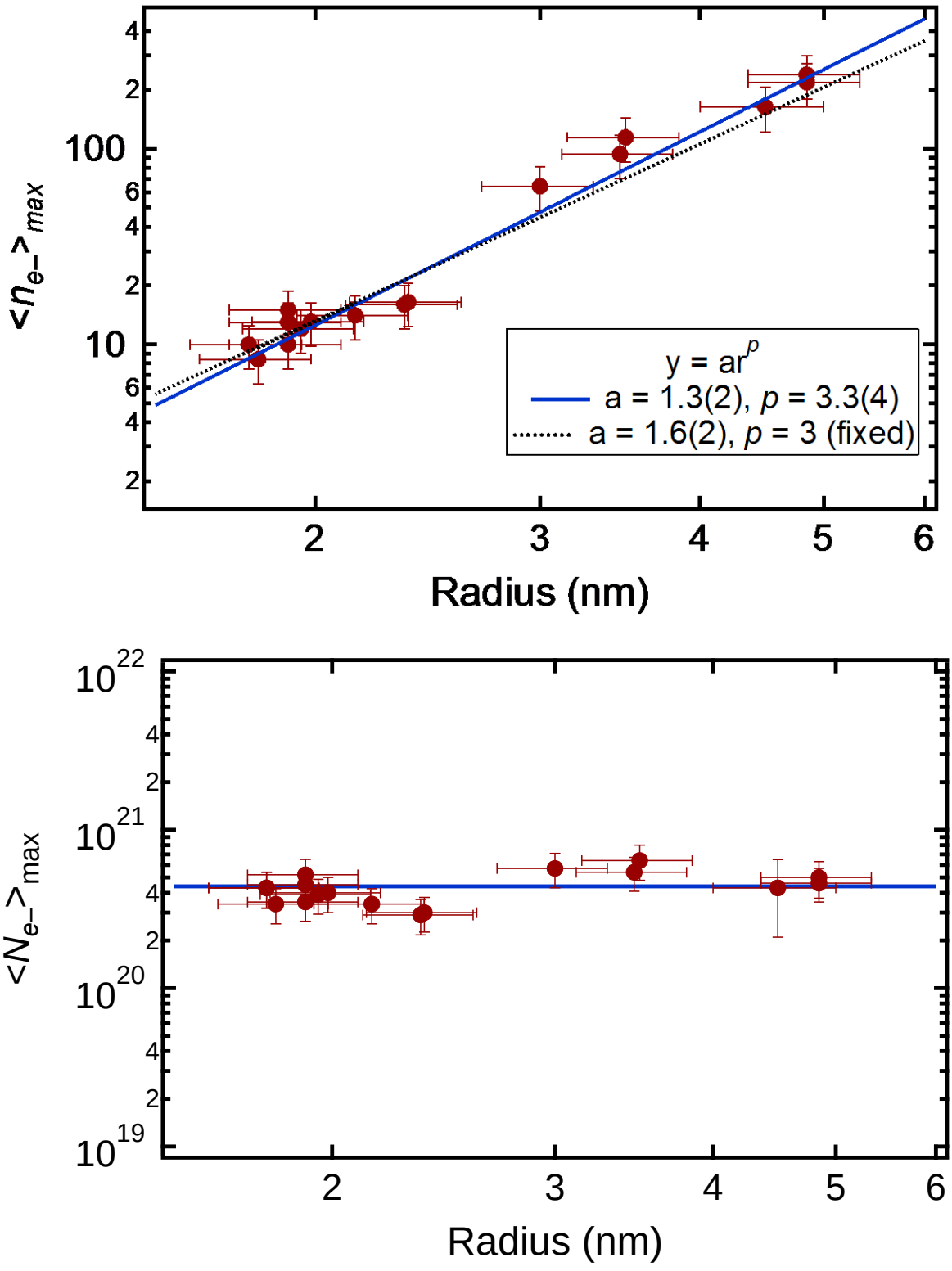

Figure 4.19. NC size-independent carrier density of ZnO NCs reduced with $CoCp^*_2$ and protons. *Top:* The maximum average number of carriers per NC, $<n_{e-}>_{max}$, attained in ZnO NCs

using $CoCp^*_2$ and acid, *versus* the NC radius. Both axes use logarithmic scales. The data are fit using the polynomial function $\langle n_{e^-}\rangle_{max} = ar^p$, where a phenomenological fit weighted by the error gives $p = 3.3 \pm 0.4$ (blue line), and $p = 3$ (dotted black line) also fits well. NC sizes are calculated using the optical absorbance[59] ($r < 3.5$ nm) or from TEM ($r > 3.5$ nm). Uncertainties on the NC size are the standard deviation from TEM measurements or 10%, whichever was greater. *Right:* Maximum carrier density $\langle N_{e^-}\rangle_{max}$, *vs.* the NC radius. The uncertainties were estimated at 25%, and the line represents the average of all NC sizes, $4.4(1.0)\times10^{20}$ cm^{-3}.

4.2.9 *Estimating the NC Chemical Potential*

The number of electrons per NC reaches a saturation point, $\langle n_{e^-}\rangle_{max}$, which is independent of the amount of excess of both the reductant and the acid. $\langle n_{e^-}\rangle_{max}$ varies with the volume of the NCs (r^3), so the same maximum carrier density $\langle N_{e^-}\rangle_{max}$ is reached with a given reductant, independent of NC size. The marginal, *i.e.* highest energy, electron in the NCs has a chemical potential equal to the Fermi energy of the material (E_F) in these nanocrystals.[60] At equilibrium, the chemical potential of the NCs is equal to the solution potential of the molecular redox couple. To a first approximation, the solution potential is given by the formal potential of the reductant and the ratio of $MCp^*_2{}^+$ to MCp^*_2 in solution via the Nernst equation (Equation (4.1)).[61] This method to determine E_F independently of electron counting in the semiconductor has been adapted from that used by Kamat for TiO_2 and CdSe.[62,63] We note that this analysis is only an approximation as it depends on the absolute concentration of reductant in solution initially, but is useful as a method to convert between stoichiometry ($\langle N_{e^-}\rangle_{max}$) and a chemical potential (energy) scale.

As acid is added to solutions containing NCs and $CoCp^*_2$, the $[CoCp^*_2{}^+]_{eq}/[CoCp^*_2]_{eq}$ ratio increases. Thus addition of acid causes the E_F of the system to decrease as electrons flow from the $CoCp^*_2$ to the NCs (Figure 4.20). The drop in E_F reflects the less reducing conditions, and stabilization of the added electrons by the positive charge of the protons.

$$E_F = -1.95 + 0.059 \log\left[\frac{MCp^{*+}_{2\ eq}}{MCp^{*}_{2eq}}\right] \text{ (V } \textit{vs}\text{ Fc/Fc}^+\text{)} \qquad (4.1)$$

Plots of E_F *vs.* H^+ added per NC added have a linear portion before saturation is reached (Figure 4.20). We note that these data are obtained from the optical spectra of electrons in the

ZnO NCs, as in Figure 4.9, but the data are analyzed according to Equation (4.1). The slope of the linear portion, the change in E_F per H^+ ($\partial E_F/\partial \langle n_{H^+} \rangle$), is plotted in Figure 5C. This slope is slightly affected by the amount of MCp^*_2 initially present, but the general trend is that the $\partial E_F/\partial \langle n_{H^+} \rangle$ is greater for smaller NCs than for larger NCs. In other words, the Fermi level is more sensitive to each added proton for smaller NCs. This is reasonable, as a single proton will be a greater perturbation to a small NC than a larger one.

After no additional carriers can be added to the NCs, the Fermi level reaches a minimum value ($E_{F(lim)}$, linear portion of Figure 4.20 near -2.0 V). Essentially the same $E_{F(lim)}$ is found for all sizes of NCs (Figure 5D), because roughly the same $[MCp^*_2{}^+]_{eq}/[MCp^*_2]_{eq}$ ratio is obtained at maximum reduction. However, the absolute value of $E_{F(lim)}$ is approximate, and changes slightly with the equivalents of MCp^*_2 used, for example by doubling the $[MCp^*_2]$ gives a difference in $E_{F(lim)}$ of about 20 mV. Even with these small changes, the constancy of $E_{F(lim)}$ with NC radius (Figure 4.21) is closely related to the constant carrier density $\langle N_{e^-} \rangle_{max}$.

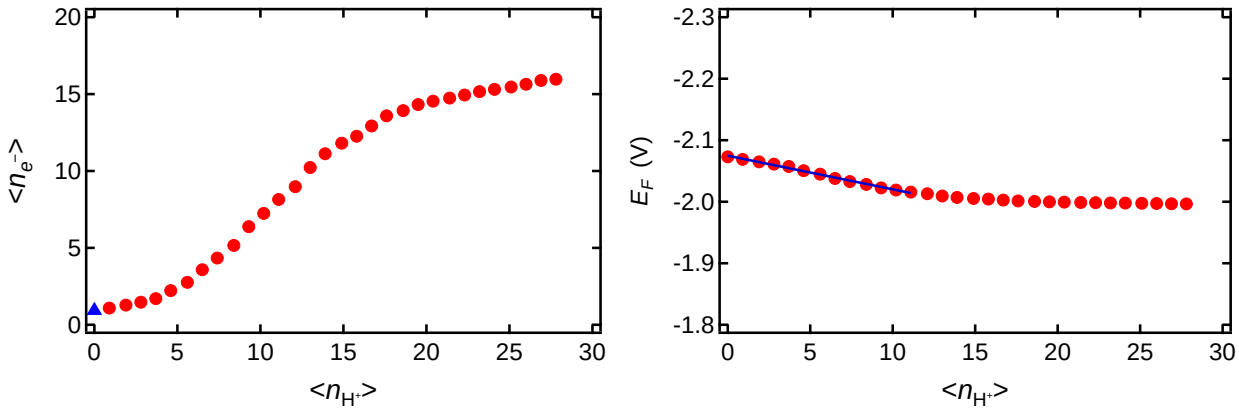

Figure 4.20. Estimation of NC Fermi level. Left: Plot of $\langle n_{e^-} \rangle$ of ZnO NCs (r = 1.9 nm) with $CoCp^*_2$ as the reductant as a function of $\langle n_{H^+} \rangle$ (H^+ per NC), where the triangle represents $\langle n_{e^-} \rangle$ before addition of acid. Right: The Fermi level of the reduction of ZnO NCs is calculated with Equation (4.1), using the same data plotted in panel A. The ratio of $CoCp^*_2$ to $CoCp^*_2{}^+$ is modified by the Fermi level before reaching $E_{F(lim)}$; the slope of this relationship (blue line) is plotted in panel C. At the maximum carrier density, E_F saturates, represented in panel D as $E_{F(lim)}$.

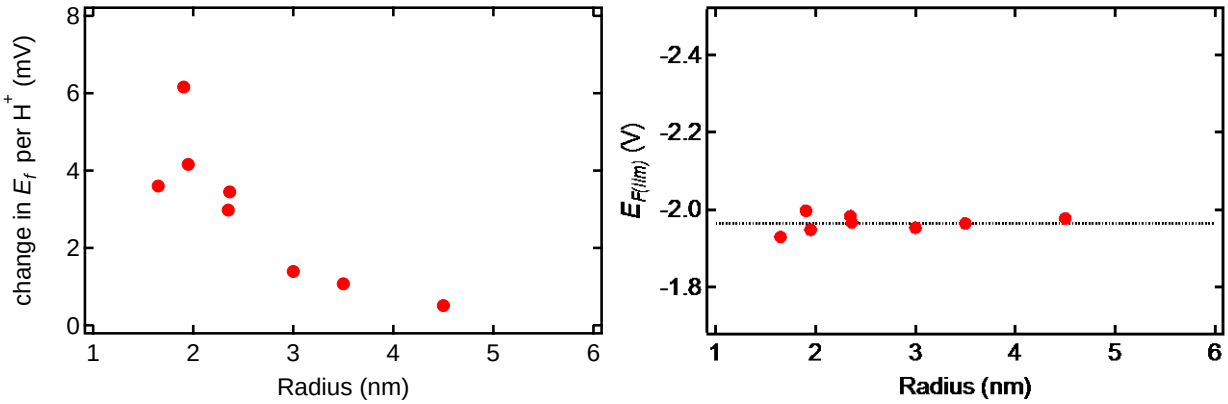

Figure 4.21. Fermi level changes as a function of NC size. *Left*: The slope of E_F change per H^+ added is plotted as a function of NC size. *Right*: Calculated $E_{F(lim)}$ for various NC sizes, where the dashed line shows the average $E_{F(lim)}$ as -1.97 V.

4.2.10 *Surface Protonation vs. Proton Intercalation.*

What is the behavior of the charge-balancing protons in this system at the atomic level? Are they at the surface of the NCs, as hydrogen-bonded DDA-H^+ cations or surface hydroxide groups? Or do they intercalate into the lattice of the NCs? While we have no direct evidence, the intercalation interpretation most simply explains the data.

For carriers in ZnO, we and others have shown that electrons are confined within the NCs. EPR spectra of photocharged ZnO NCs suggest that the added electrons occupy orbitals that are delocalized over the whole NC. This is indicated by the dependence of g* on the NC radius and the line broadening observed with ^{67}Zn-doped NCs.[37] Proton intercalation has been suggested to occur with reduced TiO_2, ZnO, and other metal oxides.[34] It is well known that metal oxides are porous materials for cations, a key feature of their use in lithium batteries.[64] Most notably, Hupp suggested the "deep" intercalation of protons occurs upon electrochemical reduction of nanoparticulate TiO_2 and ZnO electrodes.[34,45,54-56] Intercalation explained both the observed pH dependence of conduction band energies and the electrode weight gain of oxides measured by a quartz crystal microbalance upon reduction in the presence of H^+ versus D^+.[45,54] Calculations by Van de Walle and others,[65] as well as various experimental studies,[66] indicate that hydrogen atoms ($H^+ + e^-$) are likely common n-type dopants in bulk ZnO. The calculations indicate that the intercalated protons bind strongly to a single lattice oxide, forming a hydroxide ion. Measured rates of H diffusion in bulk ZnO, if extrapolated to ambient temperatures and to the

nanoscale, would predict that H should move fast enough to reach its thermodynamically most favorable position on the timescale of our experiments (seconds).[67-69] We have shown here that $<n_{e^-}>_{max}$ is limited by the volume of the NC. This volume-dependence of the electrons does not provide any direct evidence for intercalation. However, there is a 1:1 relationship of electrons and protons in this system, and it is likely that the electrons and protons are both distributed within the volume of the NC.

Perhaps the strongest argument for intercalation over surface protonation is the very large difference in electron addition between H^+ and $MCp^*_2{}^+$ cations. From a continuum electrostatics point of view, the difference in size between these two cations is quite small for a r = 4.9 nm NC. Yet $CoCp^*_2$ adds over 200 electrons to r = 4.9 nm NCs when protons balance the charge *vs*. 40 electrons when $CoCp^*_2{}^+$ is the cation. An alternative scenario to explain the differences between the cations could invoke protonated surface creating a trap state, generating an electron distribution that is substantially different than a surface with an ion-paired $CoCp^*_2{}^+$. However, this is not evident from the EPR spectra or broad plasmonic absorbance. Very similar EPR spectra are seen for the conduction band electrons in Al^{3+}-doped ZnO (AZO) NCs,[14] where the charge balance is achieved by the aliovalent dopant inside the NC, not on the surface. In our view, these arguments together are strongly suggestive of proton intercalation throughout the NC upon charging.

4.2.11 *Extension to Weaker Reductants: Comparison of $CrCp^*_2$ and $CoCp^*_2$*

Another benefit of using redox couples to add carriers, versus photoreduction as a dopant method, is the ability to precisely tune the applied potential by varying the reductant. Remote doping experiments were performed using a weaker reducing agent, decamethylchromocene ($CrCp^*_2$). As reported earlier, $CrCp^*_2$ is not sufficiently reducing to donate electrons to the as-prepared ZnO NCs.

The reduction potentials of $CoCp^*_2$ (-1.94 V vs. Fc/Fc^+ in CH_2Cl_2)[38] and $CrCp^*_2$ (-1.46 V vs. Fc/Fc^+ in MeCN)[70] are reported in solvents typical for electrochemistry, but the experiments described here are in 100% toluene or 50/50 toluene/THF. To determine the reduction potentials under these specific conditions, cyclic voltammetry (CV) was performed in a N_2 glovebox with THF and toluene mixtures. Figure 4.22 shows the CV of a THF solution of $CoCp^*_2$ and $CrCp^*_2$ (~5 mM each) with 0.4 M $^n Bu_4NPF_6$ supporting electrolyte. The figure also shows CVs of the

same solution after the addition of solid DDA (~50 mM), and then after the addition of 1 mL toluene (to 25% by volume), to make the solution more similar to the conditions used for all other experiments. When more than ~25% toluene was added, the electrolyte precipitated. The measured reduction potentials, $E_{1/2}$[CoCp*$_2$]= -1.95 V vs. Fc/Fc$^+$ and $E_{1/2}$[CrCp*$_2$]= -1.56 V vs. Fc/Fc$^+$), and the $\Delta E_{1/2}$ = ~400 mV are the same in all three cases (Figure 4.22).

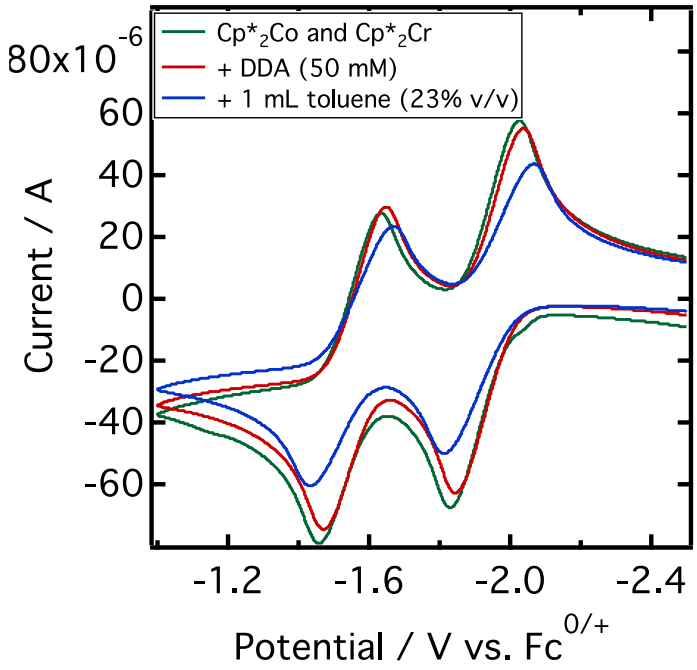

Figure 4.22. Overlaid CVs of CoCp*$_2$ and CrCp*$_2$ in THF (green), with added DDA (red), and with added toluene (blue).

Without acid, CrCp*$_2$ is not sufficiently reducing to add electrons to the ZnO NCs (Figure 4.3). In contrast, addition of aliquots of CrCp*$_2$ to a solution of ZnO NCs already containing 10 equivalents of [DDA-H][BAr$^F{}_4$] resulted in an equilibrium-determined reduction of the NCs (Figure 4.23, left). This result is similar to the chemical reduction with CoCp*$_2$. The opposite experiment involving addition of [DDA-H][BAr$^F{}_4$] to a ZnO NC solution with 10 equivalents CrCp*$_2$ previously added gave a roughly linearly increasing $\langle n_{e^-} \rangle$ (Figure 4.23, right). For a given solution composition, the same $\langle n_{e^-} \rangle$ was obtained independent of the order of addition of acid and reductant, but the paths to that point are not identical. In sum, each addition of protons allows for reduction of the NCs by CrCp*$_2$.

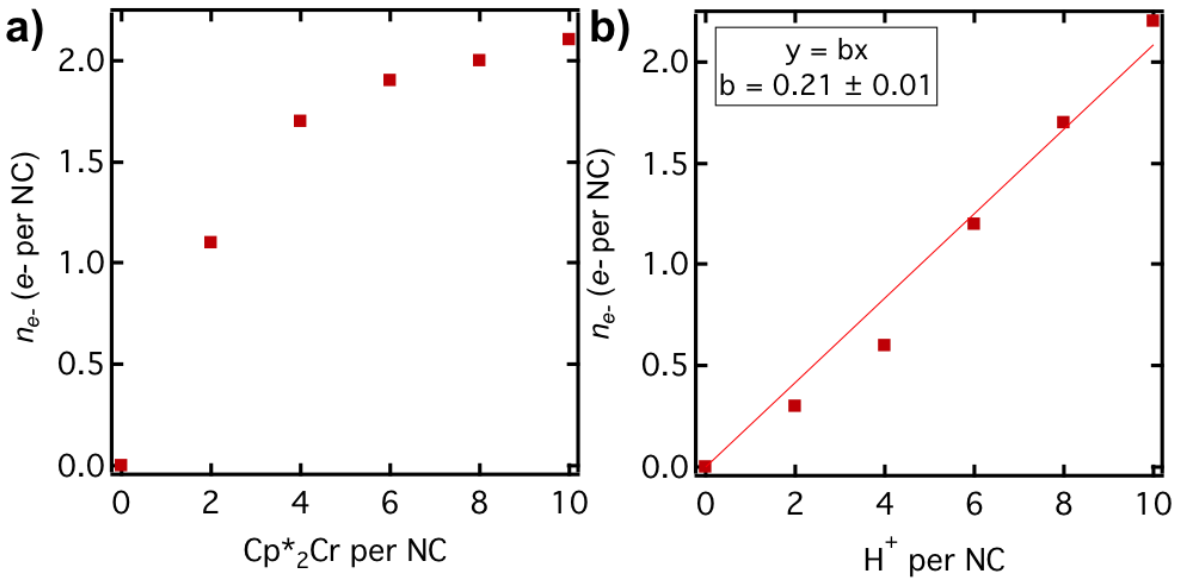

Figure 4.23. Chemical reduction of ZnO NCs (d = 3.7 nm, 2.5 × 10^{-4} M) using $CrCp^*_2$ and the acid $[H(Et_2O)_2][BAr^F_4]$. a) Addition of 5 × 10 µL aliquots of $CrCp^*_2$ (~2 equiv each) into a solution of ZnO NCs with 10 equiv acid. b) Addition of 5 × 10 µL aliquots of acid (~2 equiv each) into a solution of ZnO NCs with 10 equiv $CrCp^*_2$.

While many of the experiments explored here varied NC batches, sizes, concentrations, etc. we wanted to more directly the reduction of the same solution of NCs with the two metallocenes (MCp^*_2, M = Co, Cr). One sample of NCs was protonated with 10 equivalents $[H(Et_2O)_2][BAr^F_4]$ per NC, and split in half. Each half was reduced with aliquots of MCp^*_2 (0.5 equiv to 10 equiv per NC, Figure 4.24). As metallocene is added to the NC solution the optical spectra show the characteristic growth of a band rising into the near-IR corresponding to ZnO/e-. The $\langle n_{e^-} \rangle$ was calculated using the molar extinction coefficient for electrons at 850 nm, and we find that electrons are transferred into the NCs in a sigmoidal-like fashion (Figure 4.25) for both metallocenes, with a linear portion followed by a maximum. For $CrCp^*_2$, a maximum is reached at approximately five equivalents of metallocene with $\langle n_{e^-} \rangle \sim 1$. For $CoCp^*_2$ the maximum is reached around seven equivalents of metallocene with $\langle n_{e^-} \rangle \sim 4$.

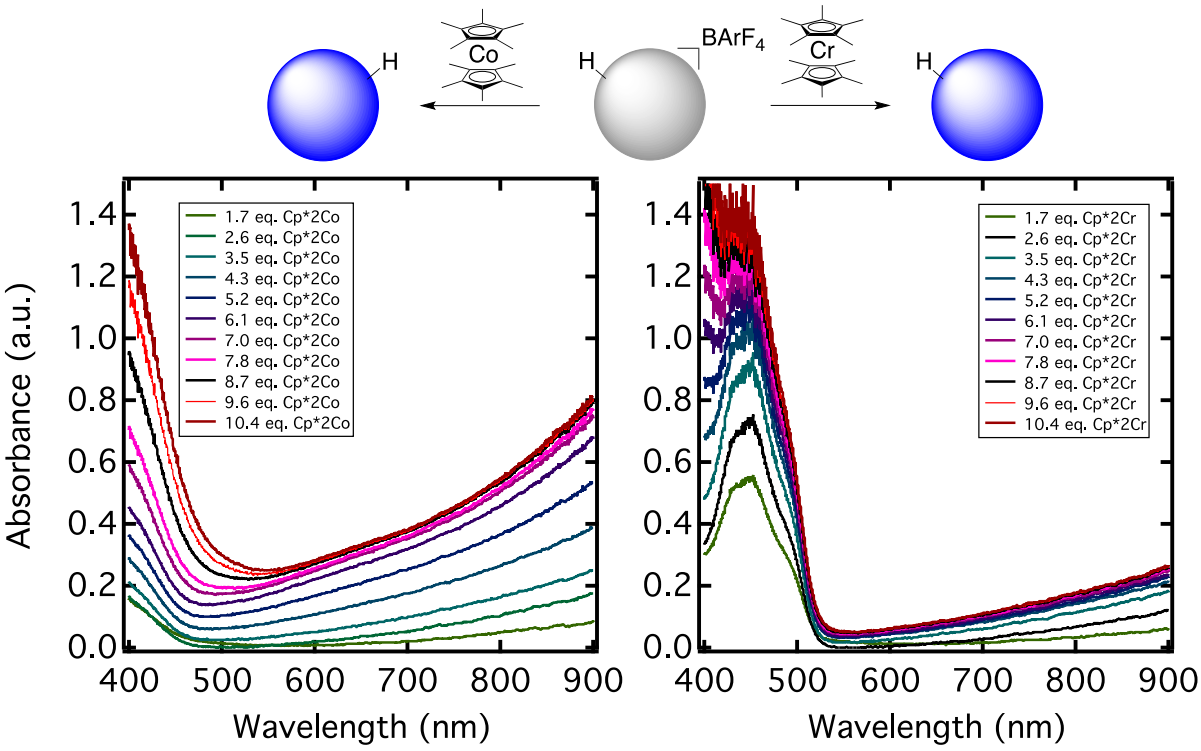

Figure 4.24. Comparison of NC reduction with $CoCp^*_2$ versus $CrCp^*_2$ with a fixed number of protons. A solution of ZnO NCs (d = 4.3 nm, 1.6×10^{-4} M) in 50/50 toluene and THF was acidified with solid $[H(Et_2O)_2][BAr^F_4]$ to make a solution with 10 equiv of acid per NC. $CoCp^*_2$ (left) and $CrCp^*_2$ (right) were added in 10 μL aliquots (stock solutions of 3×10^{-2} M in toluene) with stirring, until the $\langle n_{e^-} \rangle_{max}$ was reached (1.4 e^- per NC for $CrCp^*_2$; 4.4 e^- per NC for $CoCp^*_2$).

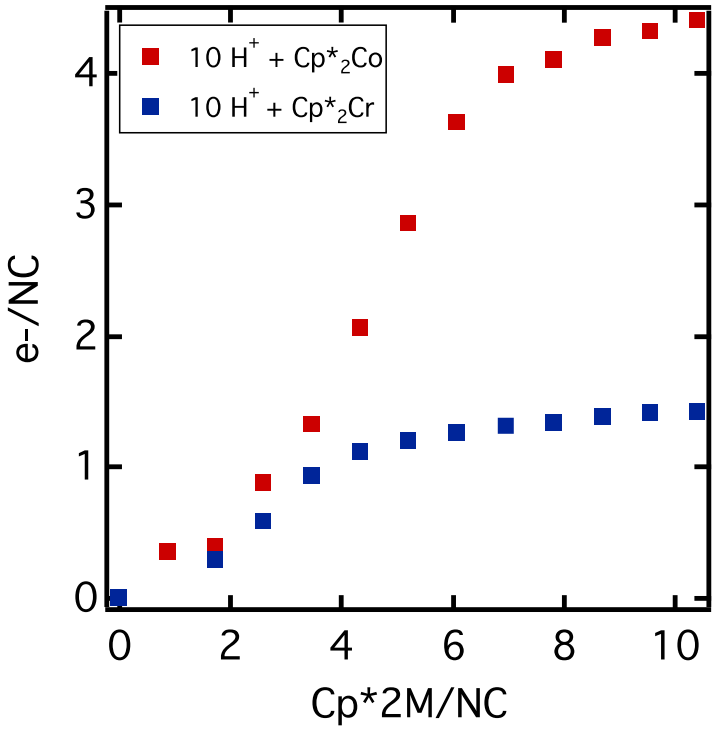

Figure 4.25. Plot of equivalents of of metallocene per ZnO NC (d = 4.3 nm, 1.6 × 10^{-4} M) versus $<n_{e^-}>$, for the experiment shown in Figure 4.24. $CrCp^*_2$ and $CoCp^*_2$ (stock solutions of 3 × 10^{-2} M in toluene) were added by 10 μL aliquots to NC solutions (1.6 × 10^{-4} M) with 10 equiv $[H(Et_2O)_2][BAr^F_4]$ per NC, until the $<n_{e^-}>$ was reached (4.4 e^- per NC for $CoCp^*_2$ and 1.4 e^- per NC for $CrCp^*_2$).

For both metallocenes, $<n_{e^-}>$ rises linearly with added acid. The slopes of the $<n_{e^-}>/H^+$ plots for $CrCp^*_2$ are however, generally less than one. Each size of NC can again be charged only to a maximum number of electrons even in the presence of excess acid and reductant. The $<n_{e^-}>_{max}$ with $CrCp^*_2$ shows a similar dependence on size (Figure 4.26). The maximum carrier density of 1.3(± 0.5)×10^{20} cm^{-3} is again independent of size (Figure 4.26). This carrier density is *ca*. 3 times smaller than the maximum attained with $CoCp^*_2$.

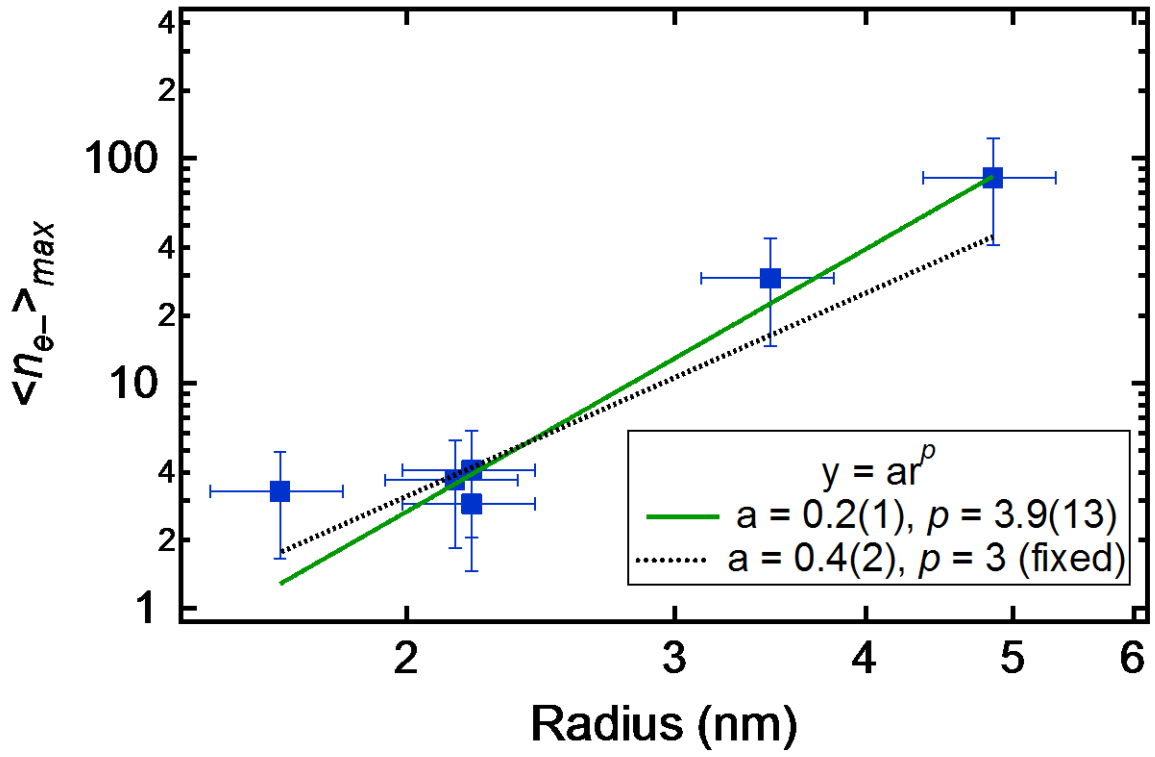
$<n_{e-}>_{max}$
100
10
1
2
3
4
5
6
Radius (nm)
y = ar^p
a = 0.2(1), p = 3.9(13)
a = 0.4(2), p = 3 (fixed)

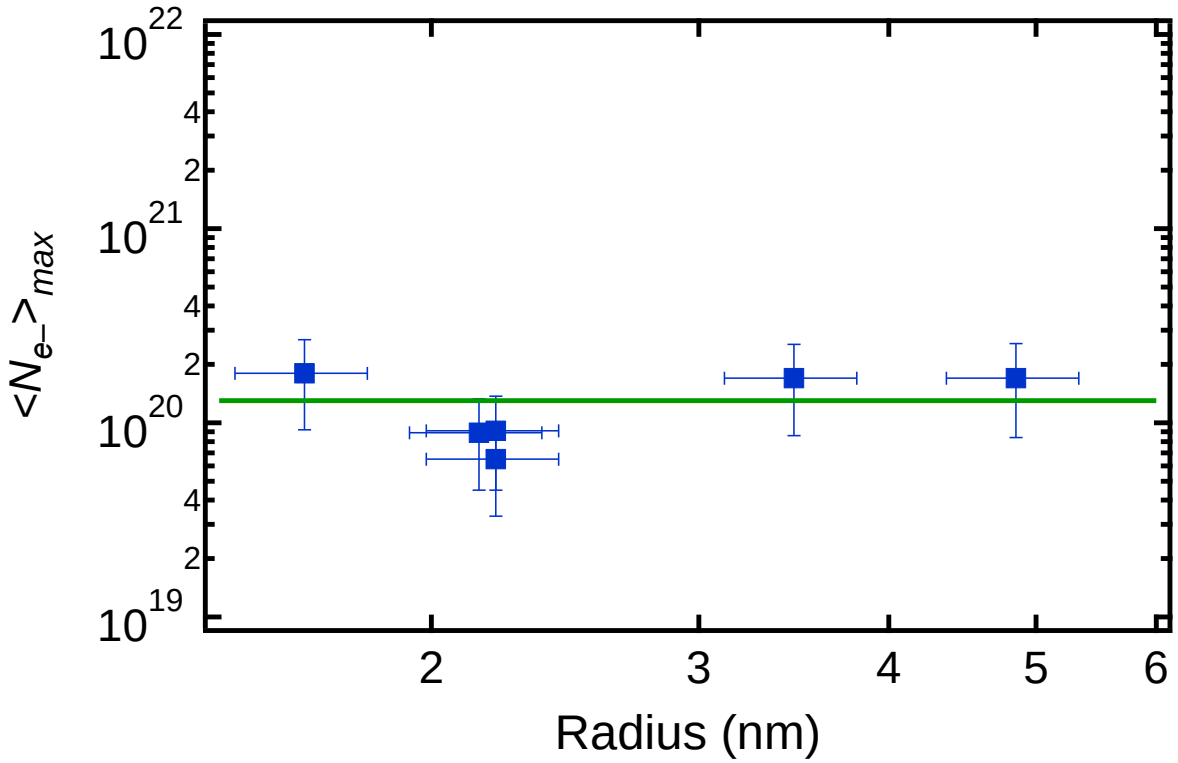
$<N_{e-}>_{max}$
10^{22}
10^{21}
10^{20}
10^{19}
2
3
4
5
6
Radius (nm)

Figure 4.26. NC size-independent carrier density of ZnO NCs reduced with $CrCp^*_2$ and protons. *Left:* The maximum average number of carriers per NC $<n_{e^-}>_{max}$ attained in ZnO NCs using $CrCp^*_2$ and acid, *versus* the NC radius. Both axes use logarithmic scales. The data are fit using the polynomial function $<n_{e^-}>_{max} = ar^p$, where a phenomenological fit weighted by the error gives $p = 3.9 \pm 1.3$ (green line), and $p = 3$ (dotted black line) fits well. NC sizes are calculated using the optical absorbance[59] ($r < 3.5$ nm) or from TEM ($r > 3.5$ nm). Uncertainties on the NC size are from the standard deviation from TEM or 10%, whichever was greater. *Right:* Maximum carrier density $<N_{e^-}>_{max}$, *versus* the NC radius. The value of $<n_{e^-}>_{max}$ was calculated from titration with excess $CrCp^*_2$ and acid, and uncertainties were estimated at 50%. The line represents the average of all NC sizes, $1.3(\pm 0.5) \times 10^{20}$ cm^{-3}.

According to the reported reduction potentials and the electrochemical experiments described above, there is a 0.39 V difference in reduction potential between $CoCp^*_2$ and $CrCp^*_2$. However, the ratio of electrons transferred to the NCs under fixed-acid conditions is three (Figure 4.25), and the ratio of maximum carrier densities is three (Figure 4.19 vs. Figure 4.26). In other words, under equivalent conditions of NC, proton, and reductant concentrations, $CoCp^*_2$ transfers only *ca.* three times more electrons than $CrCp^*_2$. This is a surprisingly small value. If these were simple molecular electron transfer equilibria governed by the Gibbs free energy relationship $K_{eq} = e^{-\Delta G^{\circ\prime}/RT}$ and $-\Delta G^{\circ} = -nFE^{\circ\prime}$, the 400 mV difference in reduction potentials ($E^{\circ\prime}$) in the reductants would predict the ratio of equilibrium constants ($K_{eq}^{CoCp^*_2}/K_{eq}^{CoCr^*_2}$) to be $10^{6.7}$. In other words, the difference in driving force between the reactions ($\Delta\Delta G^{\circ}$) is not a simple predictor of the extent of reduction. At a carrier density of $4.4(1.0) \times 10^{20}$ cm^{-3}, the last electron has an E_F, an effective reduction potential, that is 400 mV higher than the marginal electron at $1.3(0.5) \times 10^{20}$ cm^{-3}. The $\Delta(<N_{e^-}>_{max})/\Delta E^{\circ\prime}$ for the two reductants gives $\sim 8 \times 10^{20}$ carriers cm^{-3} per V of applied potential. This analysis shows that the electrons become progressively more difficult to add to the NCs as the carrier densities increase. This is a direct measure of how the Fermi energy changes with increased carrier density in a colloidal nanocrystal system.

4.2.12 *A Working Model of the Effect of Added Protons*

The increase in $<n_{e^-}>$ with added protons and the considerations above suggest a simple band interpretation (Figure 4.27). The electrons transferred from $CoCp^*_2$ occupy orbitals that behave like a band, so that the key parameter is the carrier density and not the number of electrons. As acid is added the energies of the bands decrease, creating a new equilibrium state with higher $<N_{e^-}>$. Experiments at lower NC concentrations, due to the large extinction coefficient of the band edge absorption, suggest that there is a Burstein-Moss shift of the absorption band edge, as predicted by this model (Figure 4.12). A similar scheme describes the change in In_2O_3 NC band positions with aliovalent Sn^{4+} doping to make *n*-type ITO NCs.[28]

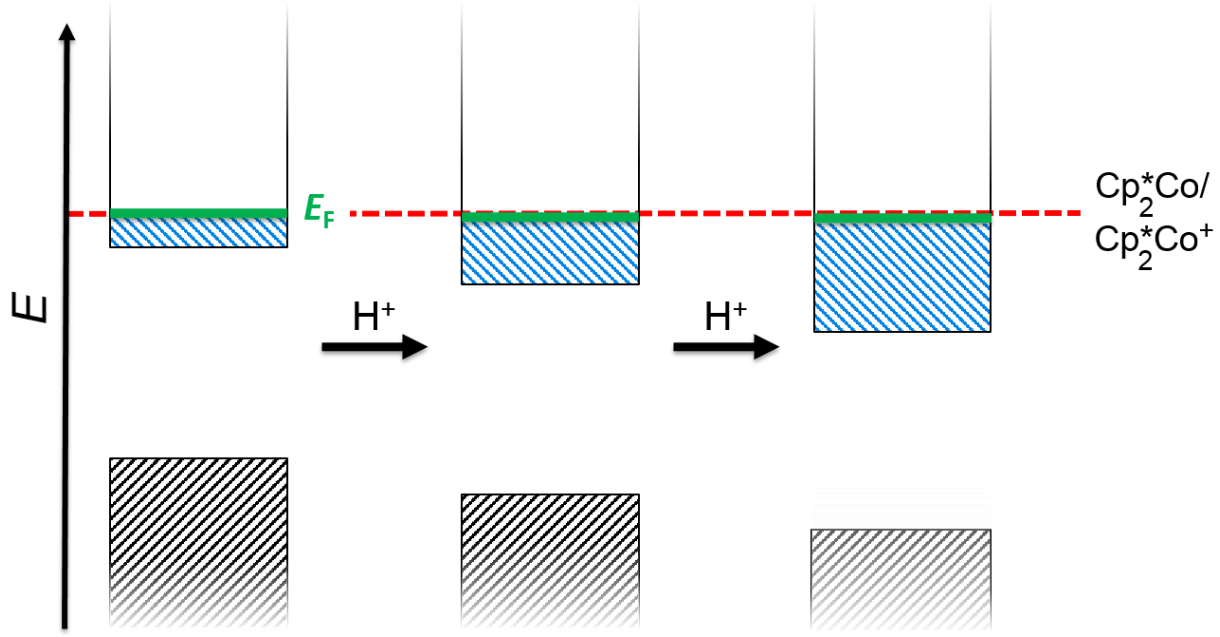

Figure 4.27. Schematic depiction of the effect of protons on the energetics of ZnO NCs with excess reductant.Under these conditions the Fermi energy of the solution (E_F), indicated by the green dashed line, is roughly constant (see 4.2.9), with a slight decrease that relates to Figure 4.20. The hatched areas indicate energy ranges where the orbitals are occupied by electrons, the lower black hatching being the filled valence band, and the upper blue hatched area represents the added conduction band electrons. The leftmost band diagram represents an equilibrium mixture of NCs and excess $CoCp^*_2$, and the arrows indicate the equilibrium changes as acid is added.

This scheme fails to explain why $<N_{e^-}>_{max}$ is reached with excess acid. Some other feature is preventing further stabilization of the NC orbitals beyond a certain amount of protons. Two suggestions are: reduction of something in the reaction mixture that occurs at a fixed value of $<N_{e^-}>$, or there is electron-electron repulsion in the NCs that becomes proton-independent at high carrier densities. From the latter, it follows that a weaker reductant will become isoergic with the electron-electron repulsion energy of the NCs at a lower potential than the more potent reductant, which is observed for $CoCp^*_2$ versus $CrCp^*_2$. Alternatively, the energetic cost of forming interstitial H^+ could become too large beyond the critical density. Since this is a PCET process, the energetics involve both protons and electrons, and the scheme depicted above does not fully explain both. Studies are underway to analyze the effects of other cations on the remote doping of ZnO NCs, which should shed additional light on this issue.

4.3 CONCLUSIONS

Charge carriers (electrons) were added to ZnO nanocrystals (NCs) using molecular reductants. The driving force for electron transfer from the reductant to the NCs was varied systematically by the addition of acid, which lowers the energy of the NC orbitals. Since these are thermal rather than photochemical studies, they directly address the thermodynamics of the charge carriers. We report quantitative analysis of the electron/proton stoichiometry and the density of the electron charge carriers as a function of protons added. Optical monitoring and stoichiometric addition of acid allows for determination of the amount and potential (energy) of added electrons as a function of the number of protons.

In the presence of excess reductant, the number of electrons per NC ($<n_{e^-}>$) reaches a maximum, beyond which the addition of more acid has no effect. This $<n_{e^-}>_{max}$ varies with the NC radius with an r^3 dependence, so the density of electrons ($<N_{e^-}>_{max}$) is constant over a range of NC sizes, to give $<N_{e^-}>_{max} = 4.4(1.0)\times10^{20}$ cm^{-3} (for $CoCp^*_2$). The same trend is observed for the weaker reducing agent $CrCp^*_2$, with $<N_{e^-}>_{max} = 1.3(0.5)\times10^{20}$ cm^{-3}. Up until the saturation point, the addition of electrons is linear with respect to protons added. This linearity contrasts with the typical description of hydrogen atom-like states (S, P, etc.) in the conduction band. The 1:1 relationship of $<n_{e^-}>$ with protons per NC, and the dramatic dependence of $<N_{e^-}>_{max}$ on the

nature of the cation (H^+ *vs.* $MCp^*_2{}^+$) suggest that the protons intercalate into the NCs under these conditions. A ZnO:e^--H^+ NC with an intercalated H^+ would be related to the much-discussed hydrogen (atom)-doped bulk ZnO.[65,71]

The maximum carrier density in chemically reduced ZnO NCs is reached when the Fermi level of the NCs matches the potential of the reductant in solution, a limit that is thermodynamically controlled. Initially we anticipated multiple slopes, after the filling of an *S*-like orbital, and then *P*-etc. The linear addition of electrons into the conduction band with the addition of protons suggests that the proton-electron coupling and charge balance is more important than the suggested discrete spacing of so-called "atom-like" orbitals within the conduction band of the NC. The simple model in Figure 4.27 provides a reasonable rationalization of most of the results presented here, including the linear increase in the number of electrons with added protons, the small difference in maximum carrier density with $CoCp^*_2$ *vs*. $CrCp^*_2$ despite their large difference in reducing power, the decrease in the Fermi energy with added protons, and the maximum carrier density being the same for different size NCs.

The differences between the reductants, the volume dependence, calculations of the Fermi level using the redox couple, and a proposed model encompassing these effects were explored. This study illustrates the strong coupling between protons and electrons in ZnO NCs and shows that proton activity is a key parameter in nanomaterial energetics.

4.4 EXPERIMENTAL

4.4.1 *General Considerations.*

ZnO nanocrystals (NCs) were prepared as reported previously (r = 1.5 to 2 nm),[72,73] and capped with either dodecylamine (DDA) or trioctylphosphine oxide-based ligands (TOPO, 90%). Larger NCs (r = 2 to 5 nm) were prepared by heating in DDA (170 ^{o}C) prior to suspension in toluene or capping with TOPO.[73] All reactions with the NCs after synthesis were done under inert atmosphere, either in a N_2-filled glove box or in quartz cuvettes with a Kontes™ Teflon valve. Using a molar absorption coefficient derived for each size of NCs, the optical spectra were used to determine the number of electrons. At each size of NC, the absorption coefficient at 850 nm and 1200 nm was determined using the previously reported method,[35] via titration of photoreduced NCs with $[FeCp^*_2][BAr^F_4]$ [$BAr^F_4{}^-$ = $B(C_6H_3\text{-}3,5\text{-}(CF_3)_2)_4{}^-$] or 2,4,6-tri-*tert*-butyl-

phenoxyl radical ($^{t}Bu_3ArO^{\bullet}$) as the oxidant (see Chapter 5for more detail). The oxidants were synthesized as reported previously.[35,74] All starting materials and reagents were purchased from Aldrich or Strem and used as received unless otherwise indicated. Brookhart's acid $[H(Et_2O)_2][BAr^F{}_4]$ was used as the proton source, and was synthesized from $[Na][BAr^F{}_4]$ and HCl.[40] $CoCp^*{}_2$[75] and $CrCp^*{}_2$ were purchased from Aldrich and purified by filtration from pentane before use. The base 1-*tert*-butyl-4,4,4-tris(dimethylamino)-2,2-bis[tris(dimethylamino)-phosphoranylidenamino]-2λ5,4λ5-catenadi(phosphazene) **(**P4-*t*-Bu-phosphazene) was purchased from Aldrich as a solution in hexanes and was dried and recrystallized from pentane before use. The solvent mixture for all experiments was kept at 50/50 v/v of toluene and THF for solubility of the reagents.

4.4.2 *Spectroscopy and Microscopy*

Continuous wave EPR spectra were obtained at room temperature on a Bruker E580 X-band spectrometer (perpendicular mode detection). Samples were prepared in an N2-filled glovebox, prepared in 4 mm quartz tubes, and referenced to the external standard DPPH (g = 2.0036). EPR and absorption spectra of d = 5.6 nm ZnO NCs capped with DDA and suspended in toluene were recorded at room temperature. The NCs were either photoreduced (10-30 minutes) in Kontes quartz cuvettes, chemically reduced with $CoCp^*{}_2$ alone or with $[H(Et_2O)_2][BAr^F{}_4]$, or chemically reduced with $CoCp^*{}_2$/acid and diluted with as-prepared NCs. The data were collected on three separate days using the same batch of NCs, but with freshly prepared reductant and acid. Absorption spectra were recorded in cuvettes, and samples were then transferred to quartz EPR tubes. The absorbance at 850 nm was normalized to the same concentration of NCs (1.1×10^{-4} M), and the ε(850 nm) was used to calculate the number of electrons per NC.

Optical absorption spectra were collected in an N_2-filled glovebox using an Ocean Optics USB4000 spectrometer configured with an XR1 grating for extended range, and a DT-Mini-2-GS lightsource. Other UV-vis spectra were obtained on a Hewlett Packard 8453 diode array spectrophotometer or an Agilent Cary 5000 spectrometer (for all spectra with wavelengths longer than 1000 nm) in an N_2-filled glovebox, with fiber optic cables coupled through the wall of the glovebox. The data were processed using Ocean Optics SpectraSuite© and Igor Pro Version 6.22A.

Electrochemical experiments were performed with a glassy carbon working electrode, Ag wire pseudo-reference, a platinum wire counter electrode, and a scan rate of 0.1 V/s. CVs were internally referenced to Fc/Fc^+ (0 V) by addition of Fc to the solution of analyte.

^1H and ^{31}P NMR spectra were obtained on Bruker AV300, AV301, DRX499, or AV500 spectrometers and the data were processed using MestReNova©. All samples were prepared inside an N_2-filled glovebox in standard 5 mm NMR tubes. Chemicals shifts were reported relative to TMS by referencing the residual solvent (^1H), or externally to phosphoric acid (^{31}P).

TEM measurements were acquired on an FEI Tecnai G2 F20 or or an FEI Tecnai Osiris 200kV microscope. The average diameter of the NCs in the batch (values in nm) were determined from the position of the first exciton peak ($d < 7$ nm) or from statistical analysis of TEM images using ImageJ ($d > 7$ nm). The error is reported as 10% or as the standard deviation derived from a Gaussian fit to the histogrammed TEM, respectively.

4.4.3 *Trace Impurity in CoCp**$_2$*

A trace impurity is occasionally present in $CoCp^*_2$ with a λ_{max} at 640 nm. Repeated filtering or recrystallizations in pentane did not remove this impurity, but it was not present in all samples. The impurity is consumed by the first additions of acid (Figure S6), which explains the sigmoidal shape at very small amounts of acid. There is more impurity present in the case with 600 $CoCp^*_2$ versus 60 equivalents per NC. It's consumed by the acid at 10 equivalents of H^+ per NC, which suggests that the impurity is present in <2%, which explains why the curved shape is mainly observed with large NCs, at high concentrations of $CoCp^*_2$.

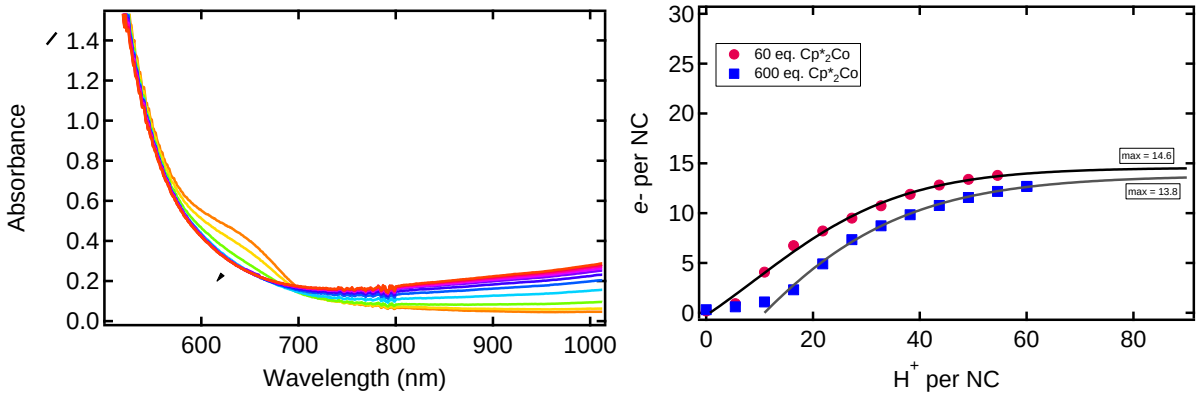

Figure 4.28. Trace impurity in $CoCp^*_2$.NCs (r = 1.9 nm, 1.8×10^{-5} M, TOPO-capped) reduced with $CoCp^*_2$, 60 equivalents (red circles) and 600 equivalents (blue squares). Electrons per NC monitored at 1600 nm as a function of acid added as a toluene/THF solution of [DDA-H][BAr^F_4] (10 μL, 1.8×10^{-2} M stock). Data are fit to a sigmoid curve, and approximately the same $\langle n_{e-} \rangle_{max}$ is reached at 13.8 and 14.6 electrons per NC, respectively.

4.5 Notes to Chapter 4

(1) Haase, M.; Weller, H.; Henglein, A. *J. Phys. Chem.* **1988**, *92*, 482.

(2) Hoyer, P.; Weller, H. *Chem. Phys. Lett.* **1994**, *221*, 379.

(3) Germeau, A.; Roest, A.; Vanmaekelbergh, D.; Allan, G.; Delerue, C.; Meulenkamp, E. *Phys. Rev. Lett.* **2003**, *90*, 097401.

(4) Liu, W. K.; Whitaker, K. M.; Kittilstved, K. R.; Gamelin, D. R. *J. Am. Chem. Soc.* **2006**, *128*, 3910.

(5) Schimpf, A. M.; Gunthardt, C. E.; Rinehart, J. D.; Mayer, J. M.; Gamelin, D. R. *J. Am. Chem. Soc.* **2013**, *135*, 16569.

(6) Roest, A. L.; Houtepen, A. J.; Kelly, J. J.; Vanmaekelbergh, D. *Faraday Discuss.* **2004**, *125*, 55.

(7) Theys, B.; Sallet, V.; Jomard, F.; Lusson, A.; Rommeluère, J.-F.; Teukam, Z. *J. Appl. Phys.* **2002**, *91*, 3922.

(8) Strzhemechny, Y. M.; Mosbacker, H. L.; Look, D. C.; Reynolds, D. C.; Litton, C. W.; Garces, N. Y.; Giles, N. C.; Halliburton, L. E.; Niki, S.; Brillson, L. J. *Appl. Phys. Lett.* **2004**, *84*, 2545.

(9) Buonsanti, R.; Llordes, A.; Aloni, S.; Helms, B.; Milliron, D. *Nano Lett.* **2011**, *11*, 4706.

(10) De Trizio, L.; Buonsanti, R.; Schimpf, A. M.; Llordes, A.; Gamelin, D. R.; Simonutti, R.; Milliron, D. J. *Chem. Mater.* **2013**, *25*, 3383.

(11) Diroll, B. T.; Gordon, T. R.; Gaulding, E. A.; Klein, D. R.; Paik, T.; Yun, H. J.; Goodwin, E. D.; Damodhar, D.; Kagan, C. R.; Murray, C. B. *Chem. Mater.* **2014**, *26*, 4579.

(12) Kanehara, M.; Koike, H.; Yoshinaga, T.; Teranishi, T. *J. Am. Chem. Soc.* **2009**, *131*, 17736.

(13) Liang, X.; Ren, Y.; Bai, S.; Zhang, N.; Dai, X.; Wang, X.; He, H.; Jin, C.; Ye, Z.; Chen, Q.; Chen, L.; Wang, J.; Jin, Y. *Chem. Mater.* **2014**.

(14) Schimpf, A. M.; Ochsenbein, S. T.; Buonsanti, R.; Milliron, D. J.; Gamelin, D. R. *Chem. Commun.* **2012**, *48*, 9352.

(15) Wang, T.; Radovanovic, P. V. *J. Phys. Chem. C* **2011**, *115*, 406.

(16) Ye, X.; Fei, J.; Diroll, B. T.; Paik, T.; Murray, C. B. *J. Am. Chem. Soc.* **2014**, *136*, 11680.

(17) Dorfs, D.; Härtling, T.; Miszta, K.; Bigall, N. C.; Kim, M. R.; Genovese, A.; Falqui, A.; Povia, M.; Manna, L. *J. Am. Chem. Soc.* **2011**, *133*, 11175.

(18) Manthiram, K.; Alivisatos, A. *J. Am. Chem. Soc.* **2012**, *134*, 3995.

(19) Zhao, Y.; Pan, H.; Lou, Y.; Qiu, X.; Zhu, J.; Burda, C. *J. Am. Chem. Soc.* **2009**, *131*, 4253.

(20) Shim, M.; Guyot-Sionnest, P. *Nature* **2000**, *407*, 981.

(21) Shim, M.; Guyot-Sionnest, P. *J. Am. Chem. Soc.* **2001**, *123*, 11651.

(22) Valdez, C. N.; Braten, M.; Soria, A.; Gamelin, D. R.; Mayer, J. M. *J. Am. Chem. Soc.* **2013**, *135*, 8492.

(23) Palomaki, P. K. B.; Miller, E. M.; Neale, N. R. *J. Am. Chem. Soc.* **2013**, *135*, 14142.

(24) Koh, W.-k.; Koposov, A. Y.; Stewart, J. T.; Pal, B. N.; Robel, I.; Pietryga, J. M.; Klimov, V. I. *Sci. Rep.* **2013**, *3*, 2004.

(25) Jeong, K. S.; Deng, Z.; Keuleyan, S.; Liu, H.; Guyot-Sionnest, P. *J. Phys. Chem. Lett.* **2014**, *5*, 1139.

(26) Wheeler, L. M.; Neale, N. R.; Chen, T.; Kortshagen, U. R. *Nat. Commun.* **2013**, *4*, 2197.

(27) Hayoun, R.; Whitaker, K. M.; Gamelin, D. R.; Mayer, J. M. *J. Am. Chem. Soc.* **2011**, *133*, 4228.

(28) Schimpf, A. M.; Thakkar, N.; Gunthardt, C. E.; Masiello, D. J.; Gamelin, D. R. *ACS Nano* **2013**, *8*, 1065.

(29) Wood, A.; Giersig, M.; Mulvaney, P. *J. Phys. Chem. B* **2001**, *105*, 8810.

(30) Kambe, S.; Nakade, S.; Kitamura, T.; Wada, Y.; Yanagida, S. *J. Phys. Chem. B* **2002**, *106*, 2967.

(31) Morrison, S. R. *Electrochemistry at Semiconductor and Oxidized Metal Electrodes*; Plenum Press: New York, 1980.

(32) *Semiconductor Electrodes*; Finklea, H. O., Ed.; Elsevier: New York, NY, 1988; Vol. 55.

(33) Hamann, T. W.; Gstrein, F.; Brunschwig, B. S.; Lewis, N. S. *Chem. Phys.* **2006**, *326*, 15.

(34) Lyon, L. A.; Hupp, J. T. *J. Phys. Chem. B* **1999**, *103*, 4623.

(35) Schrauben, J. N.; Hayoun, R.; Valdez, C. N.; Braten, M.; Fridley, L.; Mayer, J. M. *Science* **2012**, *336*, 1298.

(36) Cohn, A. W.; Janßen, N.; Mayer, J. M.; Gamelin, D. R. *J. Phys. Chem. C* **2012**, *116*, 20633.

(37) Liu, W. K.; Whitaker, K. M.; Smith, A. L.; Kittilstved, K. R.; Robinson, B. H.; Gamelin, D. R. *Phys. Rev. Lett.* **2007**, *98*, 186804.

(38) Connelly, N. G.; Geiger, W. E. *Chem. Rev.* **1996**, *96*, 877.

(39) Attempts to fit the equilibrium between ZnO NCs and $CoCp^*_2$ using a Langmuir isotherm were unsuccessful, likely because the potential of adding an additional electron increases with electron occupancy.

(40) Brookhart, M.; Grant, B.; Volpe, A. F. *Organometallics* **1992**, *11*, 3920.

(41) Saouma, C. T.; Kaminsky, W.; Mayer, J. M. *J. Am. Chem. Soc.* **2012**, *134*, 7293.

(42) Lommens, P.; Lambert, K.; Loncke, F.; De Muynck, D.; Balkan, T.; Vanhaecke, F.; Vrielinck, H.; Callens, F.; Hens, Z. *ChemPhysChem* **2008**, *9*, 484.

(43) Whitaker, K. M.; Ochsenbein, S. T.; Polinger, V. Z.; Gamelin, D. R. *J. Phys. Chem. C* **2008**, *112*, 14331.

(44) Bolts, J. M.; Wrighton, M. S. *J. Phys. Chem.* **1976**, *80*, 2641.

(45) Lemon, B. I.; Hupp, J. T. *J. Phys. Chem. B* **1997**, *101*, 2426.

(46) Gerischer, H. *Electrochim. Acta* **1989**, *34*, 1005.

(47) Green, M. *J. Mater. Chem.* **2010**, *20*, 5797.

(48) Valdez, C. N.; Schimpf, A. M.; Gamelin, D. R.; Mayer, J. M. *ACS Nano* **2014**, *8*, 9463.

(49) Stiefel, E. I. *Proc. Natl. Acad. Sci. USA* **1973**, *70*, 988.

(50) Binstead, R. A.; Moyer, B. A.; Samuels, G. J.; Meyer, T. J. *J. Am. Chem. Soc.* **1981**, *103*, 2897.

(51) Hammes-Schiffer, S. *Chem. Rev.* **2010**, *110*, 6937.

(52) *Proton-coupled Electron Transfer: A Carrefour For Chemical Reactivity Traditions*; Formosinho, S.; Barroso, M., Eds.; Royal Society of Chemistry: Cambridge, U.K., 2012.

(53) Murray, R. W. *Acc. Chem. Res.* **1980**, *13*, 135.

(54) Lemon, B. I.; Hupp, J. T. *J. Phys. Chem.* **1996**, *100*, 14578.

(55) Yan, S. G.; Lyon, L. A.; Lemon, B. I.; Preiskorn, J. S.; Hupp, J. T. *J. Chem. Educ.* **1997**, *74*, 657.

(56) Lemon, B. I.; Lyon, L. A.; Hupp, J. T. *In Nanoparticles and Nanostructured Films: Preparation, Characterization, and Applications*; Wiley–VCH: New York, 1998.

(57) O'Regan, B. C.; Durrant, J. R. *Acc. Chem. Res.* **2009**, *42*, 1799.

(58) Roest, A. L.; Kelly, J. J.; Vanmaekelbergh, D.; Meulenkamp, E. A. *Phys. Rev. Lett.* **2002**, *89*, 036801.

(59) Meulenkamp, E. A. *J. Phys. Chem. B* **1998**, *102*, 5566.

(60) For a bulk material, E_F is defined as the energy at which the probability of finding an electron is 0.5. Since this definition is less valuable for molecular species, and NCs are intermediate between molecular and bulk scales, we prefer the equivalent definition in the text.

(61) Equation 1 is an approximation first because the –1.95 V value is for THF, not for the 50/50 toluene/THF solutions used for NC measurements. Second, using the nominal concentration of $CoCp^*_2^+$ is an approximation because it does not take into account the tight ion pairing occurring in this low-polarity medium.

(62) Jakob, M.; Levanon, H.; Kamat, P. V. *Nano Lett.* **2003**, *3*, 353.

(63) Harris, C.; Kamat, P. V. *ACS Nano* **2010**, *4*, 7321.

(64) Goodenough, J. B.; Kim, Y. *Chem. Mater.* **2010**, *22*, 587.

(65) Van de Walle, C. G. *Phys. Rev. Lett.* **2000**, *85*, 1012.

(66) Anderson, J.; Van de Walle, C. G. *Rep. Prog. Phys.* **2009**, *72*, 126501.

(67) Thomas, D. G.; Lander, J. J. *J. Chem. Phys.* **1956**, *25*, 1136.

(68) Ip, K.; Overberg, M. E.; Heo, Y. W.; Norton, D. P.; Pearton, S. J.; Stutz, C. E.; Luo, B.; Ren, F.; Look, D. C.; Zavada, J. M. *Appl. Phys. Lett.* **2003**, *82*, 385.

(69) Nickel, N. H. *Phys. Rev. B* **2006**, *73*, 195204.

(70) Astruc, D. *Electron Transfer and Radical Processes in Transition-Metal Chemistry*; John Wiley & Sons, Inc.: New York, 1995.

(71) Wang, L.-Q.; Zhou, X.-D.; Exarhos, G. J.; Pederson, L. R.; Wang, C.; Windisch, J. C. F.; Yao, C. *Appl. Phys. Lett.* **2007**, *91*, 173107.

(72) Schwartz, D. A.; Norberg, N. S.; Nguyen, Q. P.; Parker, J. M.; Gamelin, D. R. *J. Am. Chem. Soc.* **2003**, *125*, 13205.

(73) Norberg, N. S.; Gamelin, D. R. *J. Phys. Chem. B* **2005**, *109*, 20810.

(74) Manner, V. W.; Markle, T. F.; Freudenthal, J. H.; Roth, J. P.; Mayer, J. M. *Chem. Commun.* **2008**, 256.

(75) There is occasionally a small amount (<1%) of an impurity in the $CoCp^*_2$ (max = 630 nm) that has proven difficult to remove, but it did not affect the values of $<n_{e^-}>$ max (see Experimental).

Chapter 5. INSIGHTS GAINED FROM WORKING WITH ZINC OXIDE NANOCRYSTALS

5.1 INTRODUCTION

The aim of this chapter is not to tell one cohesive story. It is an attempt to communicate the intuition that we have gained working with ZnO nanocrystals, through some experiments that worked as expected and some that did not. It will describe and attempt to explain the experiments that were performed, including some that were abandoned because the results were unclear, and some "back of the envelope" calculations that we have found to be helpful in developing our (constantly evolving) conceptual understanding. I hope that this chapter is useful to someone working on this project, working with colloidal nanocrystals in general, or just as a fun perusal of the random walk that my graduate research occasionally took.

5.2 EPSILON CALCULATION OF ZNO NANOCRYSTALS

One of the keys to a majority of the data presented in this thesis is calculating the absolute number of electrons in solution, which leads to the average number of electrons per nanocrystal (NC), $\langle n_{e^-} \rangle$. Determining $\langle n_{e^-} \rangle$ is important for characterizing the reduction process and subsequent reactions of ZnO NCs. Optical spectroscopy is a convenient handle to probe the electrons in metal oxides, and reduced oxides (especially TiO_2 and ZnO) have a characteristic blue color attributed to intraband transitions in ZnO (or at very high $\langle n_{e^-} \rangle$, a plasmonic absorption).[1]

To our knowledge, the first known report of calculating the concentration of electrons in a reduced nanocrystal solution was published by Koelle et al. in 1985.[2] In their study, they calculated the absorption coefficient of each electron in photoreduced TiO_2 at 780 nm using cobaltoceniumdicarboxylate as a titrant. Using the known concentration of nanoparticles, they calculated an average of 309 electrons per nanoparticle (d = 10 nm) and a carrier density of $\langle N_{e^-} \rangle = 5.9 \times 10^{20}$ cm^{-3}, which they report uses 1/10th of the density of states in the conduction band of TiO_2.

5.2.1 *Quantification of Electrons in ZnO NCs Using Optical Spectroscopy*

For ZnO, Liu et al. calculated $\langle n_{e^-} \rangle$ by adding methyl viologen dichloride in ethanol to photoreduced ZnO NCs (ZnO/e^-) and observed the characteristic IR tail of ZnO/e^- disappear.[3] We developed a similar approach for calculating $\langle n_{e^-} \rangle$ for the ZnO NCs in nonpolar solutions. For PCET reactions especially, it is necessary to avoid the introduction of protic solvents so that tracking of the protons is more facile. The NCs were therefore dissolved in toluene and oxidants soluble in nonpolar solvents were desired. Initially, ferrocenium salts ([$FeCp_2$][X]; X = PF_6, BF_4) were used, but owing to the insufficient solubility of the salts, the calculated concentration of electrons was not reproducible. Instead, a salt of the lipophilic decamethylferrocenium ($FeCp^*_2{}^+$) was prepared, with the large, noncoordinating anion $BAr^F_4{}^-$ ($BAr^F_4{}^-$ = (3,5-$(CF_3)_2C_6H_3)_4B^-$).[4] Although the new oxidant [$FeCp^*_2$][BAr^F_4] is insoluble in toluene, it is soluble in THF. Toluene and THF are both aprotic and miscible, and the introduction of 100 μL of THF into a 2 mL toluene solution had no observable impact on photoreduction. With this oxidant, a straightforward determination of $\langle n_{e^-} \rangle$ was possible.

As described in the photoreduction chapter (Chapter 3), "titrations" were carried out with photoreduced NCs to calculate the concentration of electrons. In a typical experiment, an anaerobic solution of ZnO NCs in toluene or 50/50 v/v toluene/THF (10^{-3}-10^{-5} M) was placed in a quartz Kontes cuvette equipped with a stir bar, and irradiated while stirring for 1-60 minutes approximately 10 cm from the lamp aperture with a Newport 100 W Hg or Hg/Xe arc lamp. The reduced solutions were then taken into a N_2 glovebox where titrations were carried out using an Ocean Optics (earlier experiments) or Cary 5000 (later experiments) spectrometer. In a typical titration, twenty 10 μL aliquots of reagent (*e.g.* ~0.1 M solution of [$FeCp^*_2$][BAr^F_4] in THF) were added to 2 mL of a 5×10^{-4} M solution of reduced ZnO NCs in a cuvette, while stirring. The optical spectra were recorded 30 seconds to 2 minutes after each addition, and the reaction is much faster than this timescale. After the equivalence point, optical bands associated with excess oxidant grew in with each aliquot added. The reaction was monitored at 850 nm, where neither $FeCp^*_2{}^+$ nor $FeCp^*_2$ absorb, to determine the moles of oxidant added per particle, or $\langle n_{e^-} \rangle$, equal to 6.4 ± 1.1 in the example shown below. $\langle n_{e^-} \rangle$ for photoreduced NCs varies with irradiation time, distance from the irradiation lamp, and concentration of NCs, but is always in the range of

zero to six for as-prepared NCs that have not been treated specially to grow larger (additional reaction time, heat above RT, etc.).

Other oxidants were also used to calculate $<n_{e^-}>$. A cobaltocenium salt $[CoCp_2][BAr^F{}_4]$ was prepared and used to titrate the nanocrystals and gave the same $<n_{e^-}>$ as $[FeCp^*{}_2][BAr^F{}_4]$, but requires a small amount of DCM. Previous work also showed that ZnO/e^- also reacts with the oxyl radicals 2,4,6-tri-*t*-butylphenoxyl radical (^{t}Bu$_3$ArO$^\bullet$) and 2,2,6,6-tetramethyl-piperidin-1-yl-oxyl radical (TEMPO),[5] which are classic hydrogen atom abstracting reagents.[6] ZnO/e^- in toluene can also be titrated with ^{t}Bu$_3$ArO$^\bullet$ to determine $<n_{e^-}>$. The reaction is conveniently monitored at 626 nm (absorption for loss of ZnO/e^- and then appearance of any excess ^{t}Bu$_3$ArO$^\bullet$), well separated from the ZnO band gap absorbance, and 850–2200 nm (absorption for only ZnO/e^-) (Figure 5.2). As a practical matter, the calculated molar absorption coefficient per electron is very sensitive to errors in [^{t}Bu$_3$ArO$^\bullet$]. For each and every titration, the concentration of the ^{t}Bu$_3$ArO$^\bullet$ solution was determined using its known absorption coefficient at 630 nm (400 $M^{-1}cm^{-1}$)[7]. Such a calibration has the added benefit of correcting for small systematic errors in the pipettor volume per addition of titrant, therefore this oxidant was the most frequently used calculating $<n_{e^-}>$.

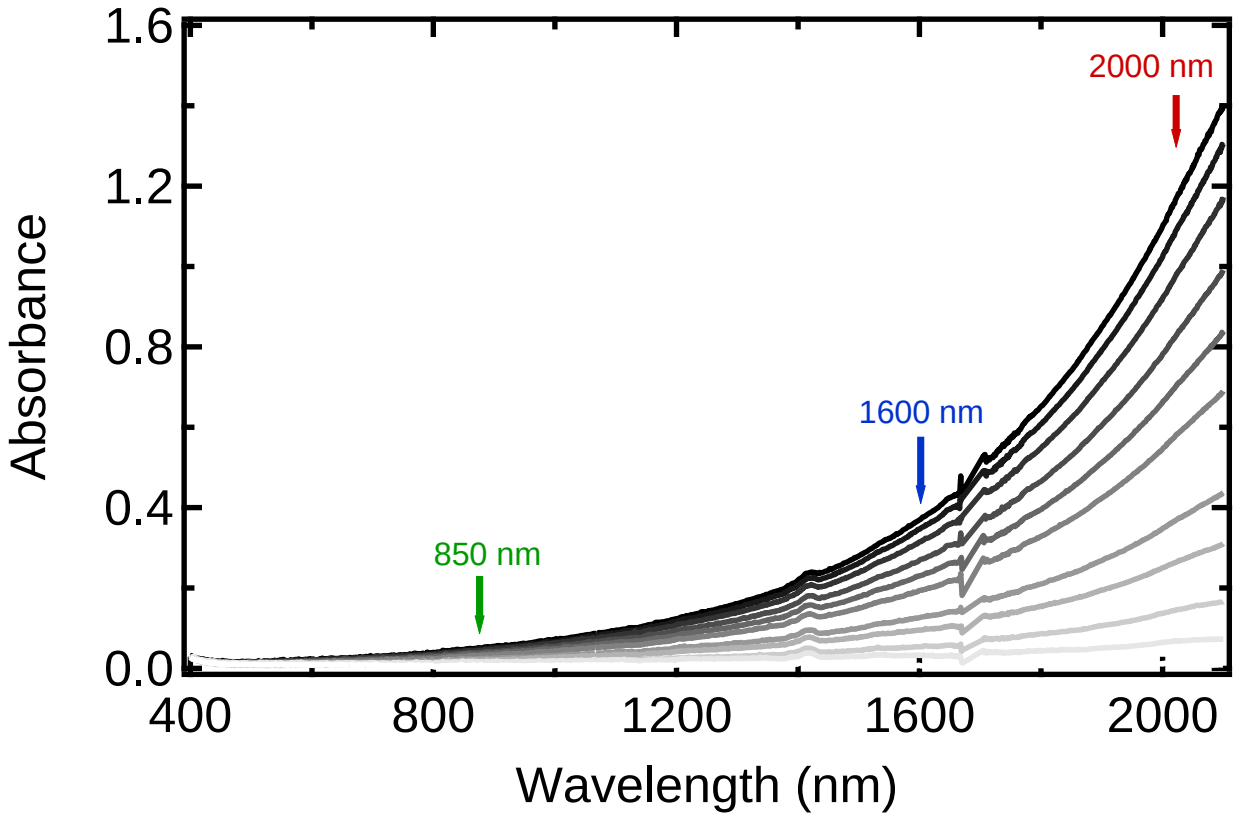

Figure 5.1. Calculation of absorption coefficient by titration of photoreduced NCs with $^{t}Bu_3ArO^{\bullet}$. An example experiment for the oxidation of photoreduced ZnO NCs (d = 6.0 nm, 5.2 × 10^{-6} M, TOPO*-capped) with $^{t}Bu_3ArO^{\bullet}$. The optical absorbance is monitored as aliquots of $^{t}Bu_3ArO^{\bullet}$ in toluene is added (not linear additions, as aliquots were removed for other analysis).

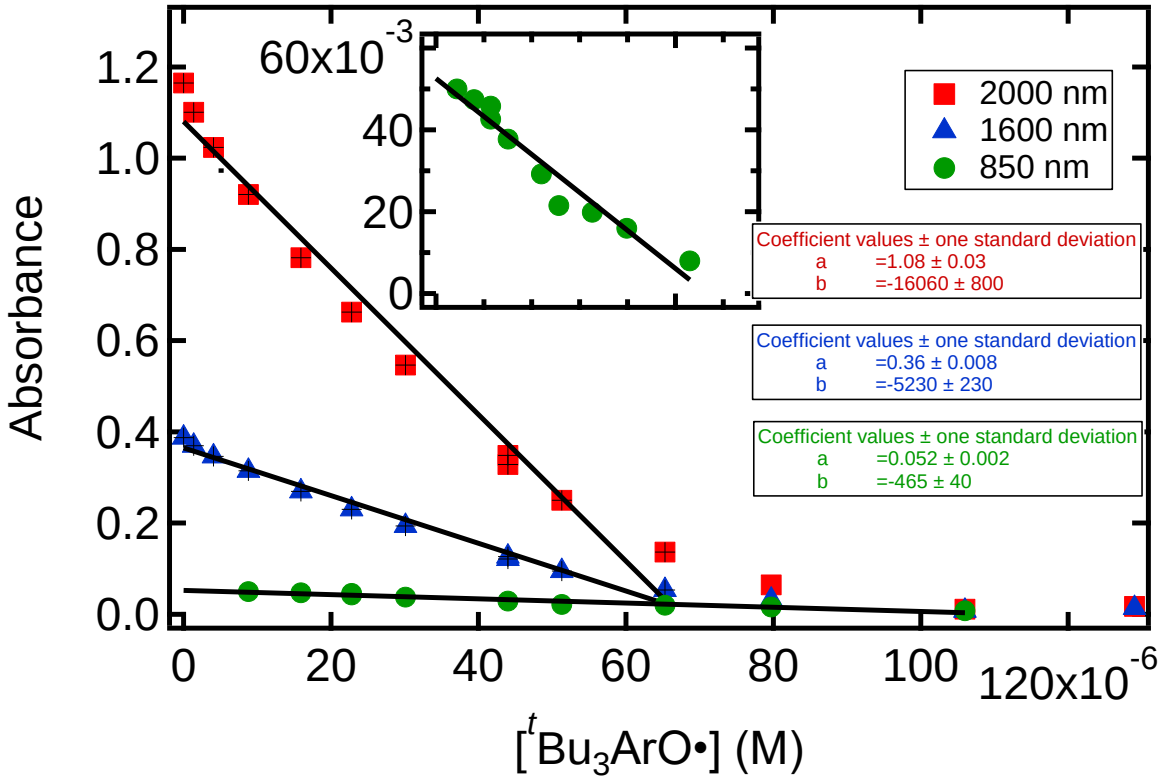

Figure 5.2. Calculation of absorption coefficient via optical spectroscopy. An example experiment for the oxidation of photoreduced ZnO NCs (r = 3.0 nm, 5.2 × 10^{-6} M, TOPO*−capped) with $^{t}Bu_3ArO^{\bullet}$. The absorbance is plotted as a function of [$^{t}Bu_3ArO^{\bullet}$], monitored at 850 nm (green circles), 1600 nm (blue triangles), and 2000 nm (red squares), and corrected for volume. Closer to the peak maximum at long wavelengths, the absorbance as phenoxyl is added is nonlinear, indicating that a linear absorption coefficient does not hold at 2000 nm or 1600 nm. At 850 nm (inset), the absorbance changes are linear with respect to [$^{t}Bu_3ArO^{\bullet}$], indicating that using a molar absorption coefficient at this wavelength is appropriate.

5.2.2 *Calculating a Molar Absorption Coefficient (ε) per Electron*

Compiling the data from titrations with ET and PCET oxidants gives a linear relationship between the concentration of electrons in solution and the absorbance of the intraband transition, much like a molecular species.[5] The concentration of electrons in solution was calculated using the amount of oxidant added, using several batches of NCs and three different oxidants ($FeCp^{*}_2{}^{+}$, $^{t}Bu_3ArO^{\bullet}$, and $CoCp_2{}^{+}$) (Figure 5.3). The extinction coefficient per electron at 850 nm

was found to be remarkably constant over all the batches of as-prepared NCs (ε = 1000 ± 100 $M^{-1}cm^{-1}$ for small NCs).[5] Just like in the Beer-Lambert law, the molar absorption coefficient is independent of how many electrons are in the NCs conduction band as well as the oxidant used. All wavelengths between 400 and 2100 nm could be monitored, but the absorption coefficient does not follow Beer's law closer to the peak maximum (longer wavelengths). Due to spectrometer limits, 850 nm was chosen and used with viable molar absorption coefficients (according to Figure 5.2), which was surprisingly linear. A linear relationship was unexpected given our understanding of the NCs' discrete electronic states, for example, from tight-binding calculations that predict the lowest conduction energy levels of ZnO quantum dots as having *S*, *P*, and *D* symmetries with orbital degeneracies of 2, 6, and 10.[8] We believe the constant extinction coefficient can be explained by the relatively high energy at which we are monitoring. At 850 nm (~12,000 cm^{-1}), the transition is well above the energies for the electric dipole allowed *S*-to-*P* or *P*-to-*D* transitions, and hence we are likely monitoring the transition to states much higher in the conduction band.[9] Whether an electron originates from the *S* or the *P* level cannot be probed at this energy. However, we have found this extinction coefficient to be useful in quantifying $<n_{e^-}>$ without requiring a titration (Figure 5.3).

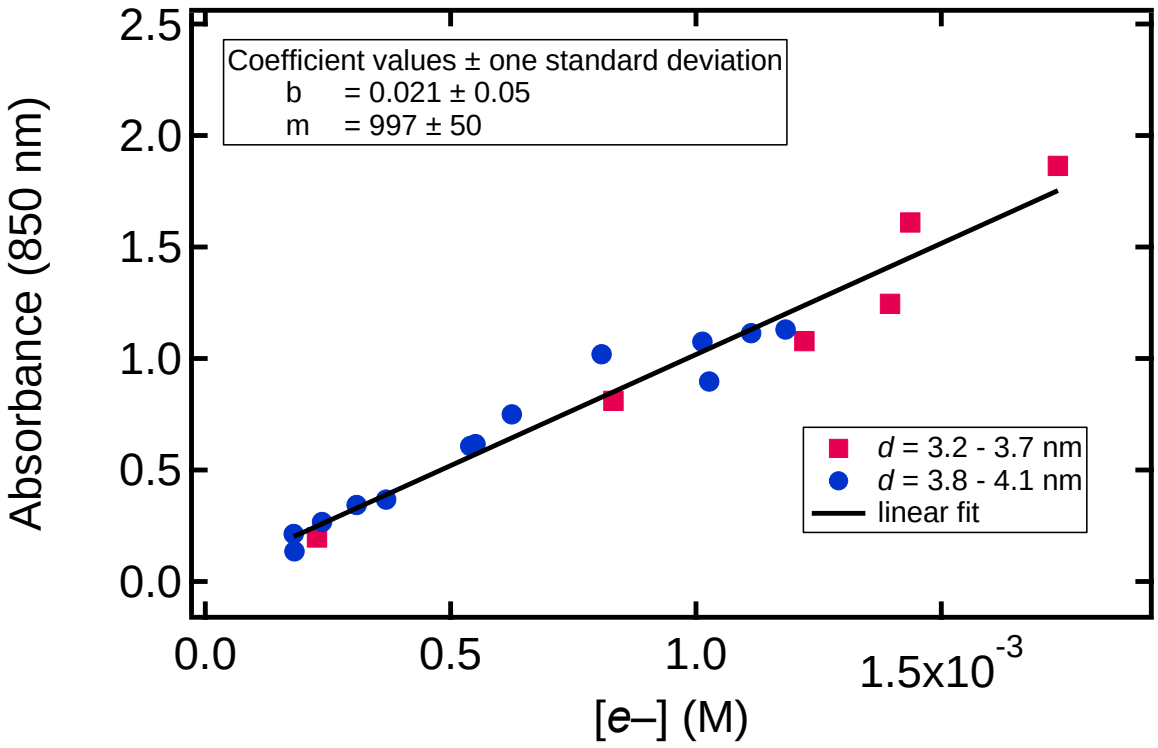

Figure 5.3. A Beer's law plot for ZnO/e^- of various diameters in toluene. Titrations with ^{t}Bu$_3$ArO$^\bullet$, [FeCp*$_2$][BAr$^F_4$], or [Cp$_2$Co][BAr$^F_4$] were performed to determine $\langle n_{e^-} \rangle$, where [e^-'s] is simply $\langle n_{e^-} \rangle$ times the particle concentration. The slope of a linear fit is the extinction coefficient, giving ε = 1000 ± 100 M^{-1}cm^{-1}. The uncertainty is estimated as twice the standard deviation from the fit.

5.2.3 *Size Dependence of ε per Electron*

For larger NCs that were intentionally treated for increased growth (more time, heat, etc), the extinction coefficient was not the same as the as-prepared NCs. This is related to the size-dependent shift of the peak maximum, as reported by Schimpf et al.[10] Another way to analyze electron filling in the NCs is to integrate under the peaks, or use the optical density, however we did not use this method. The absorbance per electron at 850 nm was more convenient for the experiments here. In practical terms, we find that the absorbance per electron in photoreduced ZnO NCs varies with the NC size in a roughly-linear fashion (Figure 5.4). As a convenient aside, this plot can be used to quickly approximate the NC size using the epsilon value, if one does not have access to a TEM, for example.

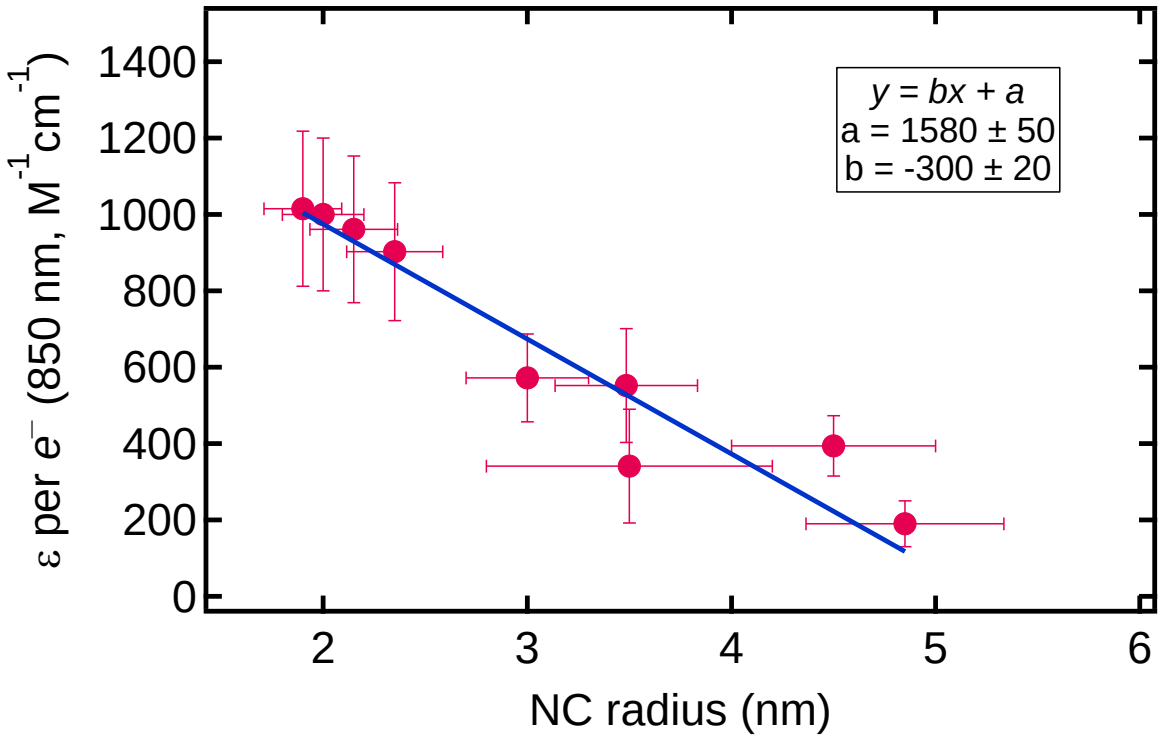

Figure 5.4. Absorption coefficient (ε, $M^{-1}cm^{-1}$) versus NC radius (nm) at 850 nm. NC sizes are calculated using the optical absorbance[11] (r < 3.5 nm) or from TEM (r > 3.5 nm). Uncertainties on the NC size are from the standard deviation from TEM or 10%, whichever was greater and uncertainties on the epsilon were calculated at 10%, following Figure 5.3. Although the data do not necessarily need to follow a trend, they fit well to $y = bx + a$ with a slope of 300 $M^{-1}cm^{-1}$ per nm in radius.

5.2.4 *Verifying the ε per Electron for Chemically Reduced NCs*

The titrations described here to determine an epsilon for electrons in ZnO were performed with photoreduced NCs. We set out to test if the epsilon calculated for photoreduced NCs is also valid for chemically reduced NCs. Unfortunately, the molar absorption coefficient cannot be calculated using the method described above, because of the excess reductant ($CoCp^*_2$ etc.) that is always present will react with the oxidant. Instead, we optimized conditions in order to use the $CrCp^*_2/CrCp^*_2{}^+$ couple as a measure of the electrons in two ways. Using $CrCp^*_2$ and acid to add electrons (and protons) to ZnO, and either base or $[FeCp^*_2][BAr^F_4]$ to remove the elections, the

epsilon at 850 nm was compared to the known electrons in the $CrCp^*_2/CrCp^*_2^+$ couple in the UV region. We calculated the molar absorption coefficient for $CrCp^*_2$, ε(380nm) = 2150 (± 100) $M^{-1}cm^{-1}$. As acid is added, the equilibrium shifts such that $CrCp^*_2$ (absorbance at 380 nm) reduces the NCs and $CrCp^*_2^+$ is formed (absorbance at 450 nm) (Figure 5.5). The equilibrium can also be observed in reverse, as P4-^{t}Bu base is added, the electrons shift from the NCs back to $CrCp^*_2$. The $<n_{e^-}>$ is plotted using two methods, Abs(850) for NCs, and Abs(380) for $CrCp^*_2$ (Figure 5.6). The analogous experiment using $[FeCp^*_2][BAr^F_4]$ to remove electrons gives the same result (Figure 5.7). Thus we find that for small NCs ε = 1000 ± 100 $M^{-1}cm^{-1}$ is valid for calculating electrons in ZnO NCs, photoreduced or chemically reduced.

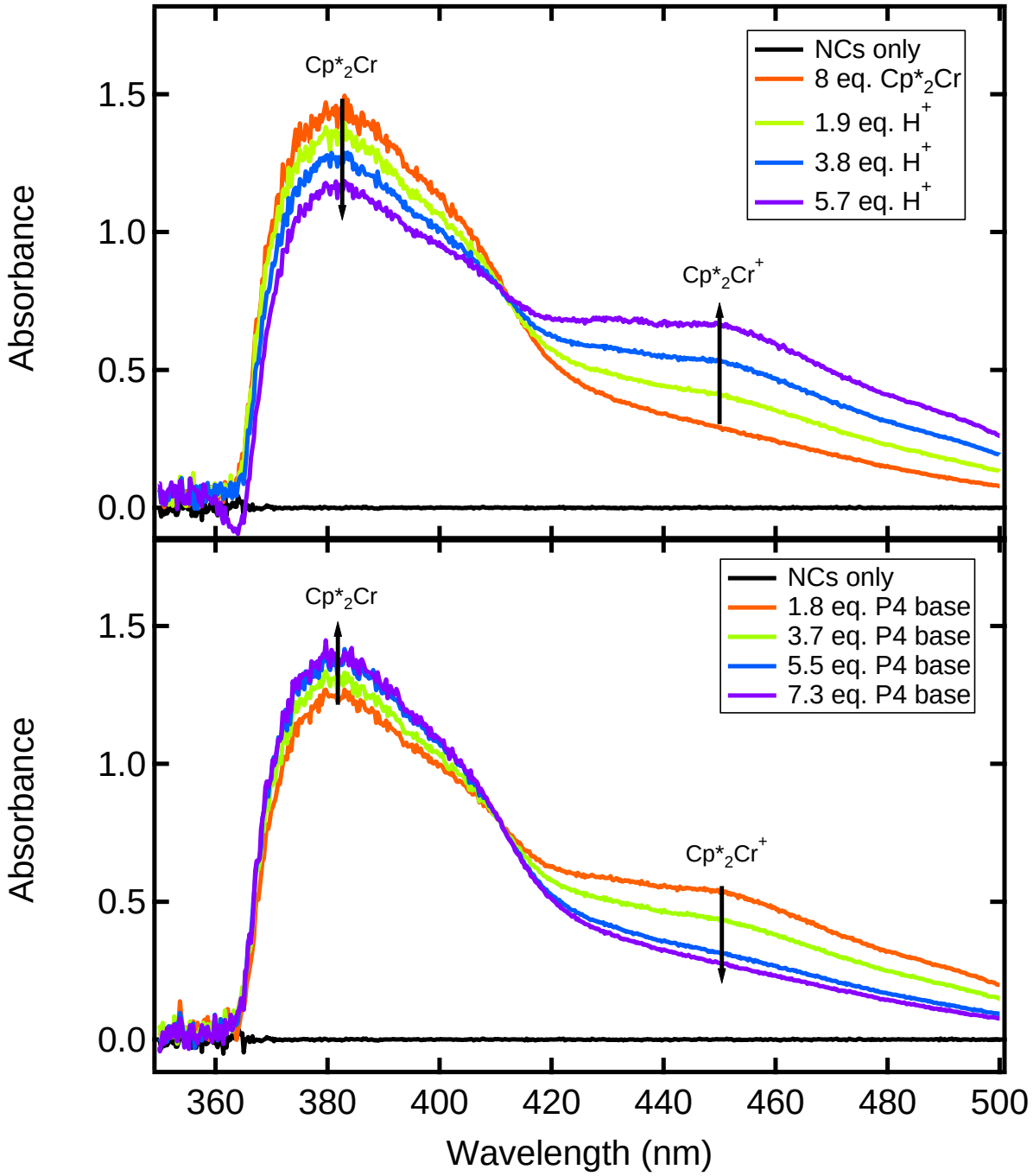

Figure 5.5. Optical absorption spectra to verify the absorption coefficient per electron using $CrCp^*_2$. The optical absorption spectra for ZnO NCs (d = 4.4 nm, 9.1 × 10^{-5} M) reduced with $CrCp^*_2$ (8 equiv) and acid as 10 µL additions of a THF solution of [DDA-H][BAr^F_4] (top), followed by the addition of 10 µL aliquots of a toluene solution of P4-^{t}Bu base (bottom). The absorbance of $CrCp^*_2$ is monitored at 380 nm, and $CrCp^*_2{}^+$ at 450 nm.

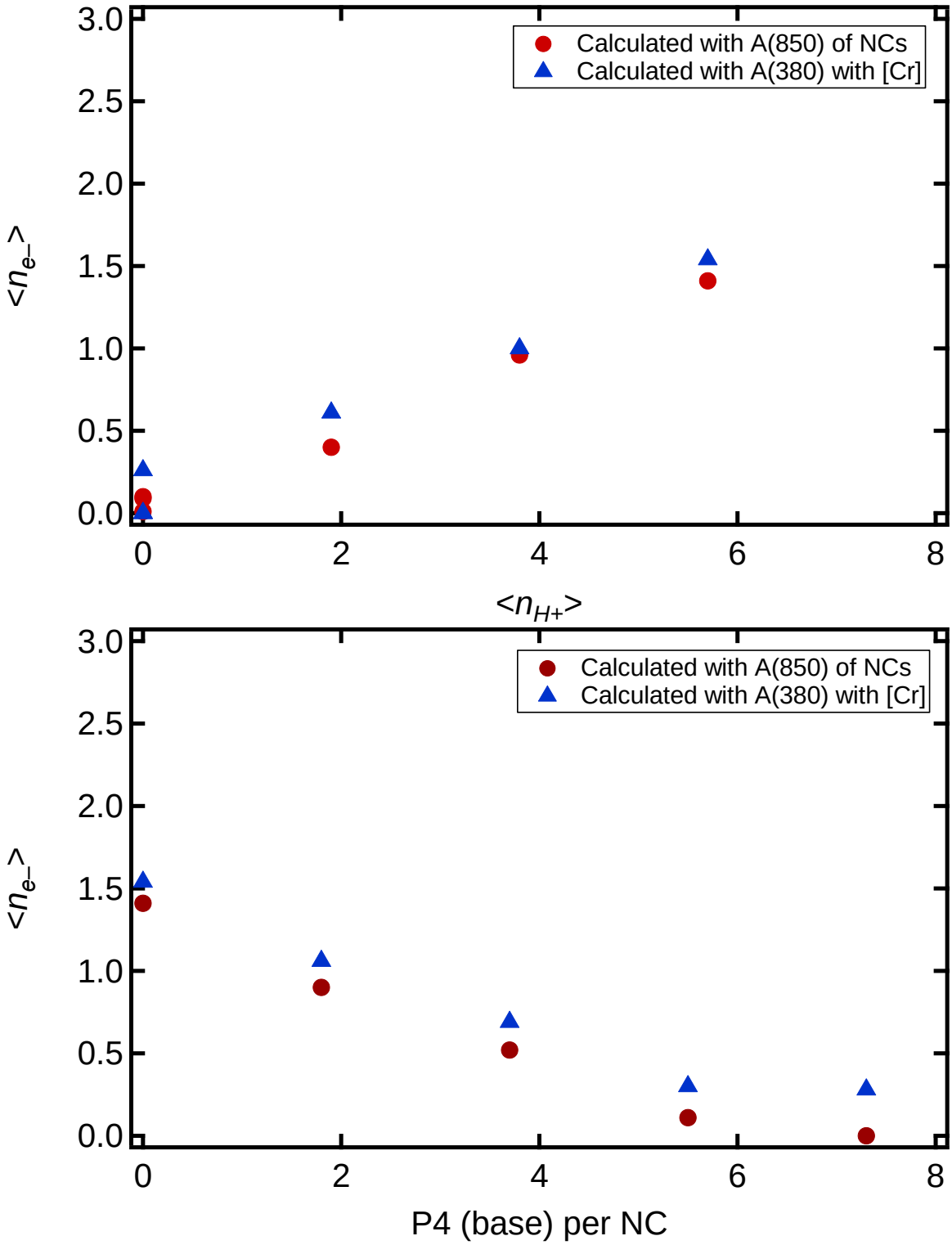

Figure 5.6. Verifying the absorption coefficient per electron using $CrCp^*_2$. The calculated $\langle n_{e^-} \rangle$ for ZnO NCs (d = 4.4 nm, 9.1 × 10^{-5} M) reduced with $CrCp^*_2$ and acid as [DDA-H][BAr^F_4], followed by P4 base (data shown above).

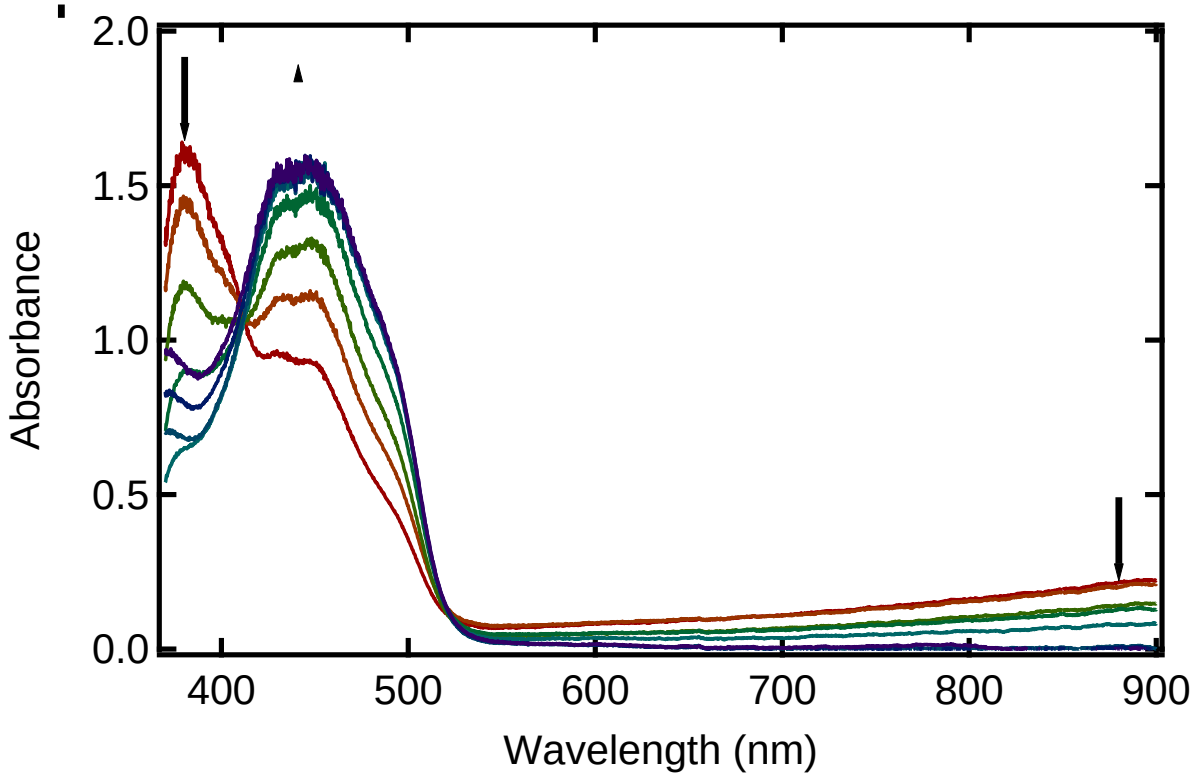

Figure 5.7. Verifying the absorption coefficient per electron using $[FeCp^*_2][BAr^F_4]$. The optical absorption spectra for ZnO NCs (d = 3.8 nm, 1.2×10^{-4} M) reduced with $CrCp^*_2$ and acid (9 equiv $CrCp^*_2$, 7 equiv $[DDA\text{-}H][BAr^F_4]$, initial spectrum in red), followed by the addition of a solution of $[FeCp^*_2][BAr^F_4]$ (1.1 equiv per addition) to form $FeCp^*_2$.

5.3 Fitting The Reduction of Nanocrystals to an Equilibrium Expression

We attempted to fit the addition of electrons to ZnO NCs (using $CoCp^*_2$ with and without acid) to simple equilibria expressions and more complicated Langmuir isotherms. We were unable to find a model that fit all of the data well, as the value of the equilibrium constant varied sample to sample, and Langmuir isotherms gave only curvature, but a few simple methods were explored as discussed below. Additionally, we did not utilize a model that took into account the ladder filling of electrons into the NCs; *i.e.* each successive addition of electrons into the NCs is harder than the previous.

The simplest case was a molecular equilibrium expression, where $CoCp^*_2$ is in excess and mass balance is assumed such that every electron in the NCs generates one equivalent of $CoCp^*_2{}^+$, shown in Equation (5.1) below.

$$ZnO + CoCp^*_2 \rightarrow ZnO/e^- + CoCp^{*+}_2 \quad (5.1)$$

$$K = \frac{[ZnO/e^-][CoCp^{*+}_2]}{[ZnO][CoCp^*_2]} \quad (5.2)$$

This first issue with the simple expression in Equation (5.2) is that there is more than one e^- transferred to each NC. So what should be used for the term [ZnO]? We chose to define "empty sites" on the NCs where the conduction band can be occupied by electrons. We initially fixed the number at 2 (filling of the S-shell), but this value did not work with some experiments, as $<n_{e^-}>$ was sometimes > 2. We finally settled on calculating a "maximum number of empty sites", by using the number of electrons transferred at the end of the reaction, and assuming this was the highest possible value of $<n_{e^-}>$ for that particular sample with $CoCp^*_2$ (Scheme 5.1). Using this max number of sites (which varied from 0.9 to 3), we calculated a unitless K for many reduction experiments of NCs. The K varied from 0.3 to 2, and was independent of the concentration of NCs and NC diameter.

Scheme 5.1 K_{EQ} for the reduction of NCs by $CoCp^*_2$.

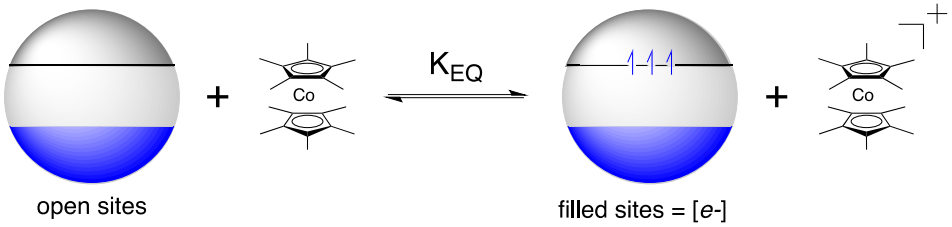

One example experiment is represented below in Figure 5.8 and Figure 5.9. As $CoCp^*_2$ is added to a solution of NCs, the number of electrons increases until it saturates at $<n_{e^-}> \sim 2$. The equilibrium expression is rearranged to plot [filled sites][$CoCp^*_2{}^+$][empty sites]$^{-1}$ versus [$CoCp^*_2$] (Figure 5.9). The maximum number of sites per NC was calculated to be 2.1 for this example, and all of the values vary with each addition of $CoCp^*_2$. The slope of the line of best fit gives K = 1.6.

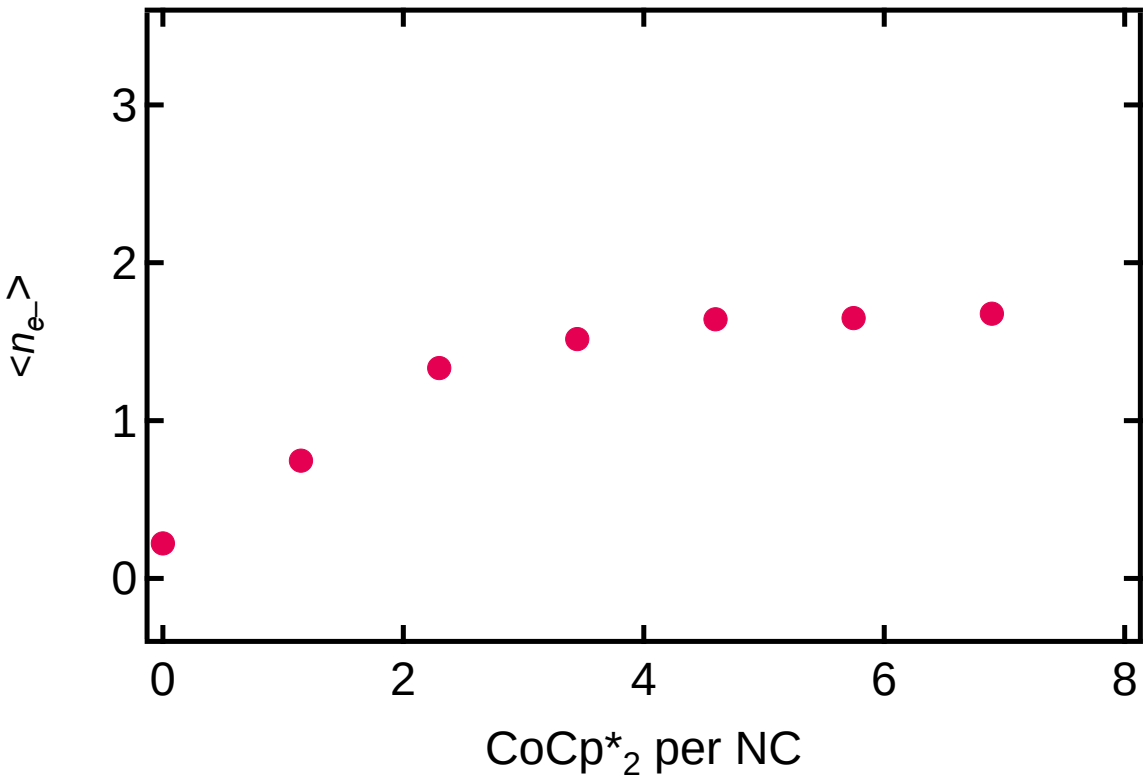

Figure 5.8. <n_{e^-}> for ZnO NCs (d = 4.1 nm, 1.0 × 10^{-4} M) as a function of equivalents of CoCp*$_2$ added, where <n_{e^-}> is calculated using the absorbance at 850 nm.

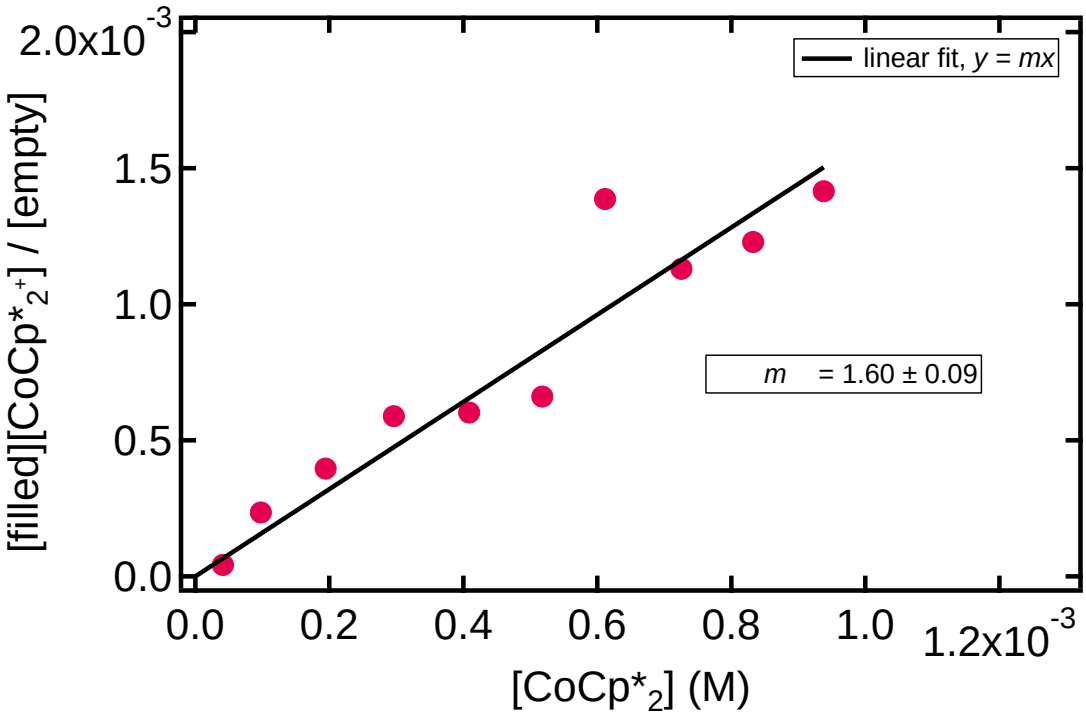

Figure 5.9. Fitting the reduction of ZnO NCs (d = 4.1 nm, 1.01 × 10^{-4} M) to an equilibrium expression. The horizontal axis represents the amount of $CoCp^*_2$ remaining, and the vertical axis is the expression following Scheme 5.1, where $\langle n_{e^-} \rangle$ is calculated using the absorbance at 850 nm.

Another issue with fitting these data to the equilibrium expression in Equation (5.2) is that we discovered from NMR experiments (see Chapter 4) that $CoCp^*_2{}^+$ is tightly bound to the NC surface. Thereby a more accurate equilibrium expression should be one in which the $CoCp^*_2{}^+$ is tightly bound to the NCs, to generate one species, Equations (5.3) and (5.4). This gives a K that is in units of M^{-1}.

$$\mathrm{ZnO} + \mathrm{CoCp}_2^* \rightarrow \left[\mathrm{ZnO}/e^-\right]\left[\mathrm{CoCp}_2^{*+}\right] \tag{5.3}$$

$$K = \frac{[\mathrm{CoCp}_2^{*+}]}{[\mathrm{ZnO}][\mathrm{CoCp}_2^*]} \tag{5.4}$$

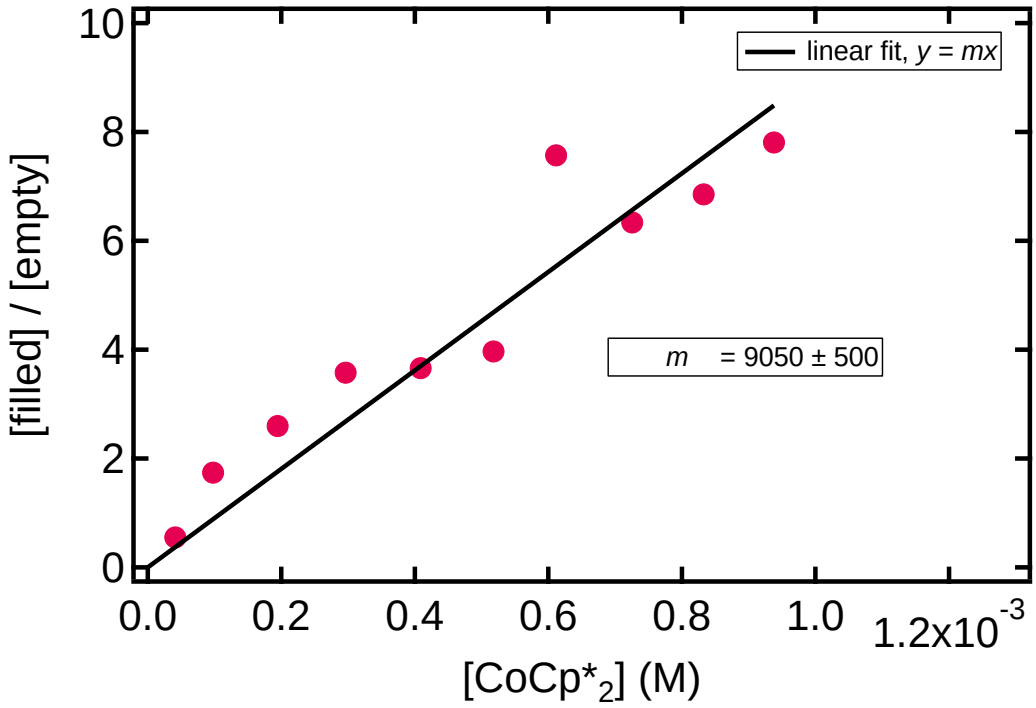

Figure 5.10. Fitting the reduction of ZnO NCs (d = 4.1 nm, 1.01 × 10^{-4} M) to an equilibrium expression (following Equation (5.4)) versus equivalents of $CoCp^*_2$ remaining, where $\langle n_{e^-} \rangle$ is calculated using the absorbance at 850 nm.

The other variable that we wanted to test for the equilibrium expression was addition of excess ligand, dodecylamine (DDA). A sample of ZnO NCs in toluene was split into thirds. To each sample was added 0, 300, or 1000 equivalents of DDA per NC. The reduction was $CoCp^*_2$ was performed as indicated above. The equilibrium expression following Scheme 5.2 was used to find the equilibrium constant K (Figure 5.11). We find that K decreases with more DDA, indicating that the ligand affects the equilibrium with $CoCp^*_2$, perhaps by blocking access to the surface (we could not accurately quantify the number of surface ligands by ^{1}H NMR spectroscopy because the free DDA signal was too large).

Scheme 5.2. Reduction of ZnO NCs with added DDA.

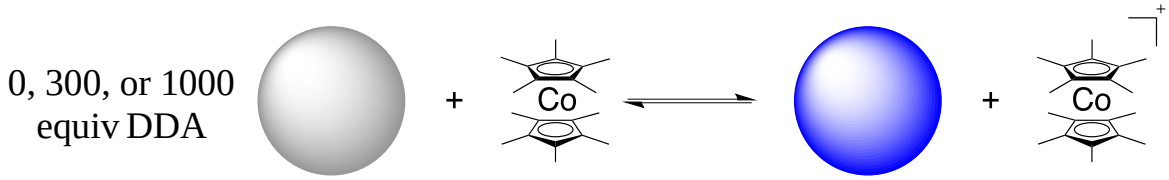

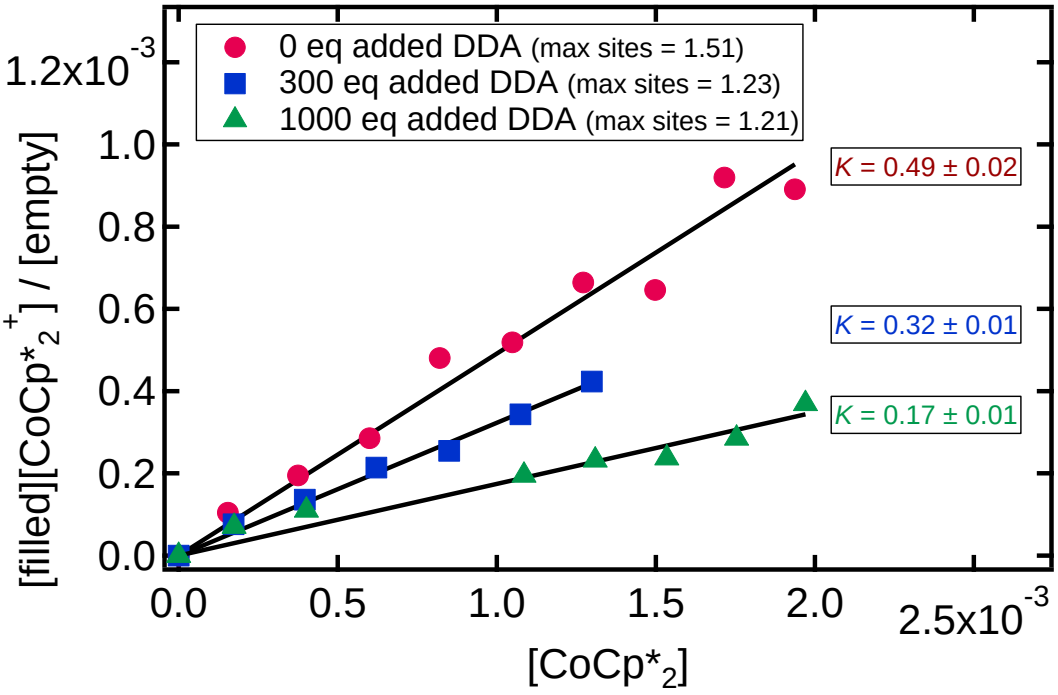

Figure 5.11. Fitting the reduction of ZnO NCs (d = 3.9 nm, 1.01 × 10^{-4} M) to an equilibrium expression (following Scheme 5.2) versus equivalents of $CoCp^*_2$ added, where $\langle n_{e^-} \rangle$ is calculated using the absorbance at 850 nm (red). Excess DDA was added to the NCs prior to reduction with $CoCp^*_2$, 300 equivalents (blue) and 1000 equivalents (green). The K (slope of the line of best fit) decreases with more DDA added.

Although these experiments give some insight into the equilibrium with ZnO NCs, we believe that they are unable to function as an accurate model of the reduction with $CoCp^*_2$ for the following reasons: (1) Addition of excess DDA affects the K, and based on our NMR studies, there is always a variable amount of excess free DDA present. (2) There is likely some $CoCp^*_2{}^+$ bound to the NCs and a small amount free in solution, where each scenario gives a different equilibrium expression (Equation (5.2) versus Equation (5.4)). (3) The $\langle n_{e^-} \rangle$ varies batch to batch, and this number must be used in the equilibrium expression as max "sites", which varies from sample to sample, perhaps because of a small amount of residual protons from the synthesis. (4) The model does not factor in the higher chemical potential of each additional electron added to the NCs.

5.4 QUANTIFYING RESIDUAL PROTONS USING PHOSPHAZENE BASES

5.4.1 *The Phosphazene Bases*

We hypothesized that there are residual protons on the ZnO NCs' surface or in the lattice that affected their reactivity with reductants. We set out to quantify protons on the NCs, both residual from the synthesis on as-prepared ZnO NCs and protons generated using photoreduction and oxidation with $[FeCp^*_2][BAr^F_4]$ ($ZnO\text{-}H^+$). Phosphazene bases were selected based on their high pK_{BH+}, their solubility in nonpolar solvents, the ability to track protonated/unprotonated versions of the base by ^{31}P NMR, and most importantly, their reputation as non-coordinating bases. The bases used were P1-^{t}Bu [*tert*-butylimino-tri(pyrrolidino)phosphorane] pK_{BH} = 28.35 in MeCN,[12] P2-^{t}Bu [1-*tert*-butyl-2,2,4,4,4-pentakis(dimethylamino)-2λ^5,4λ^5-catenadi(phosphazene)] pK_{BH} = 33.5 in MeCN,[13] and P4-^{t}Bu [1-*tert*-butyl-4,4,4-tris(dimethylamino)-2,2-bis[tris(dimethylamino)-phosphoranylidenamino]-2λ^5,4λ^5-catenadi(phosphazene)] pK_{BH} = 42.7 in MeCN (Scheme 5.3).[12]

Scheme 5.3. Phosphazene bases used in this study.

P1-^{t}Bu **P2-^{t}Bu** **P4-^{t}Bu**

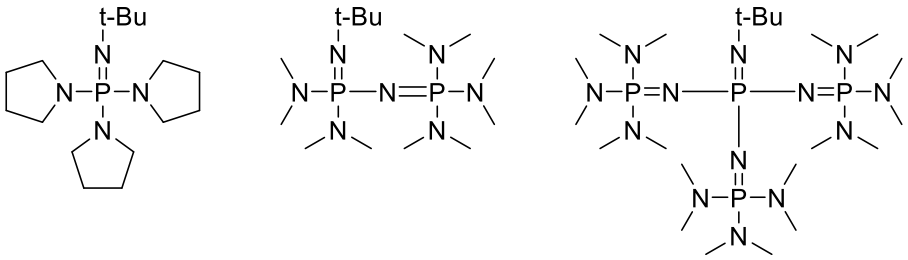

5.4.2 *P1-^{t}Bu and Nanocrystals*

To a solution of NCs (as-prepared and photoreduced) in toluene-d_8, 49 equiv of the P1-^{t}Bu was added and ^{31}P NMR spectra were acquired (Figure 5.12). The spectra showed only one peak at δ = -11 ppm, which corresponds to the P1-^{t}Bu base only. Another batch of NCs was tested, and the same lack of reactivity was observed. While no evidence of the protonated P1-^{t}Bu was observed, we were unsure about the chemical shift for the protonated base in toluene-d_8 and wanted to confirm that no protonated base was generated. The protonated P1-^{t}Bu base was generated

independently by addition of 0.5 equiv of pyridinium triflate [py-H][OTf], and a signal for the protonated base appears at δ = 22 ppm. The two separate signals for P1-^{t}Bu and its conjugate acid indicate that exchange is slow on the NMR timescale. Therefore we conclude that P1-^{t}Bu does not deprotonate as-prepared or photoreduced NCs. We note that it would be interesting to test this base on a sample of ZnO-H^+ (without the corresponding electron in the conduction band) that was generated from photoreduced NCs followed by oxidation with $[FeCp^*_2][BAr^F_4]$, although the quantity would be very small and the experiment was not attempted here.

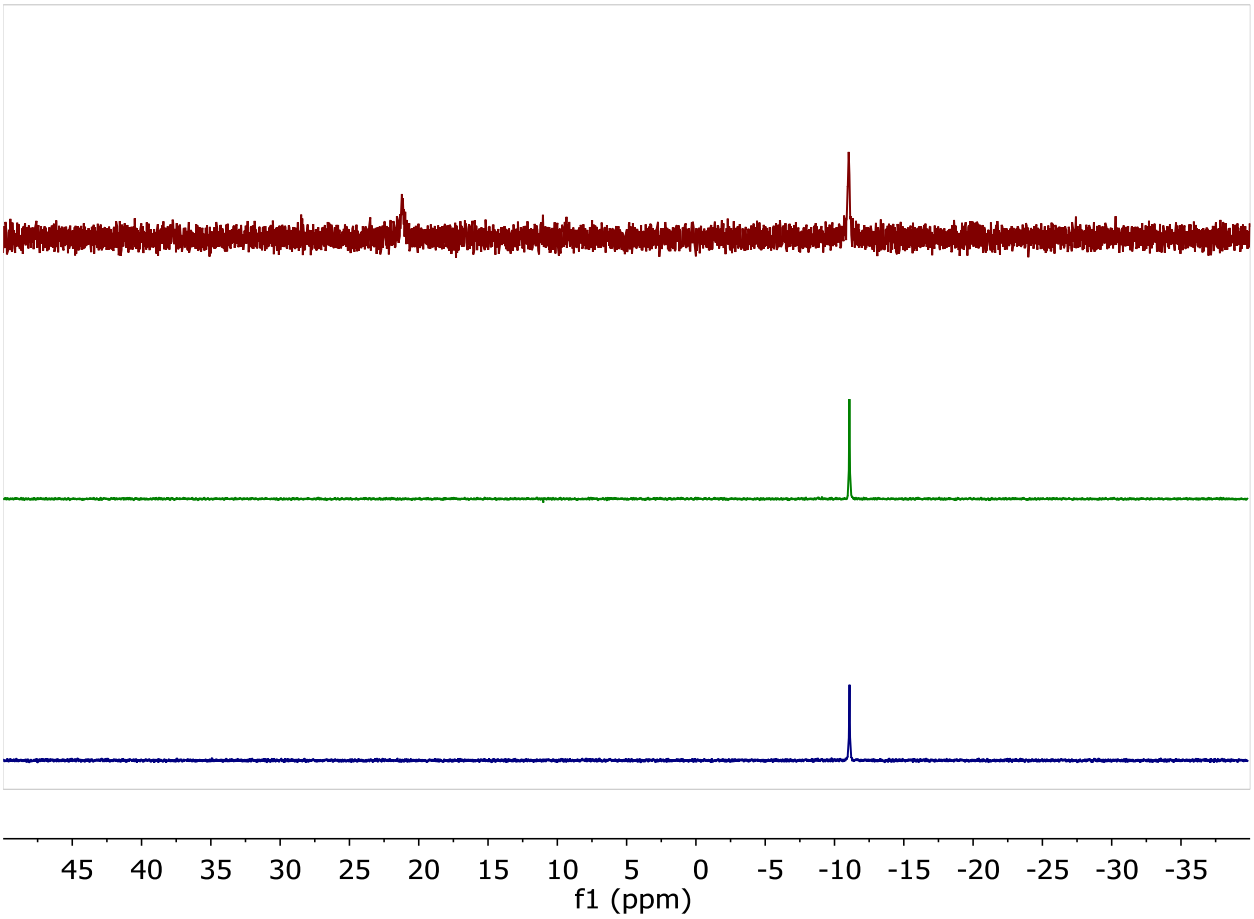

Figure 5.12. Reactions of ZnO NCs and P1-^{t}Bu.^{31}P NMR (202 MHz) spectra of P1-^{t}Bu (δ = -11 ppm) in toluene-d_8 with the following added (top, red): pyridinium triflate (0.5 equiv), to generate 0.5 equiv of the protonated P1-^{t}Bu-H^+ (δ = 21 ppm), (middle, green): as-prepared ZnO NCs (d = 3.4 nm, 0.15 mM, 49 equiv base per NC) and (bottom, blue): the same batch of ZnO NCs, photoreduced. Both samples of ZnO NCs did not protonate the P1-^{t}Bu base.

Based on the above results with P1-^{t}Bu, the following analogous experiments were conducted: (1) Based on our hypothesis that the photoreduced NCs transfer protons to HAT acceptors (Chapter 3), we wanted to investigate the relative pK_a's of ^{t}Bu$_3$ArOH and the P1-^{t}Bu phosphazene base. Addition of ^{t}Bu$_3$ArOH to a solution of P1-^{t}Bu in toluene-d_8 gives no change in the P1-^{t}Bu ^{31}P NMR spectrum (Figure 5.13, top); P1-^{t}Bu does not deprotonate ^{t}Bu$_3$ArOH. This is intuitively reasonable, as formation of ^{t}Bu$_3$ArO$^-$ in toluene should be extremely difficult. (2) To investigate if protons would be transferred *to* the ZnO NCs from the protonated base, a solution of the conjugate acid (P1-^{t}Bu-H$^+$, Figure 5.13) was added to a solution of NCs (d = 6.4 nm, Figure 5.13, bottom). We find that the signal for P1-^{t}Bu-H$^+$ remains at the same chemical shift, but broadens. This could be due to some reversible binding to the NC surface, but no evidence for formation of the parent P1-^{t}Bu base was observed (at -11 ppm). Therefore the weak acid P1-^{t}Bu-H$^+$ does not appear to protonate the ZnO NCs. The lack of proton transfer in either direction with P1-^{t}Bu base suggests that either there is a kinetic barrier, or I believe it more likely that there are a fixed number of basic sites at the NC surface that are saturated with protons, but P1-^{t}Bu base is not strong enough to remove them.

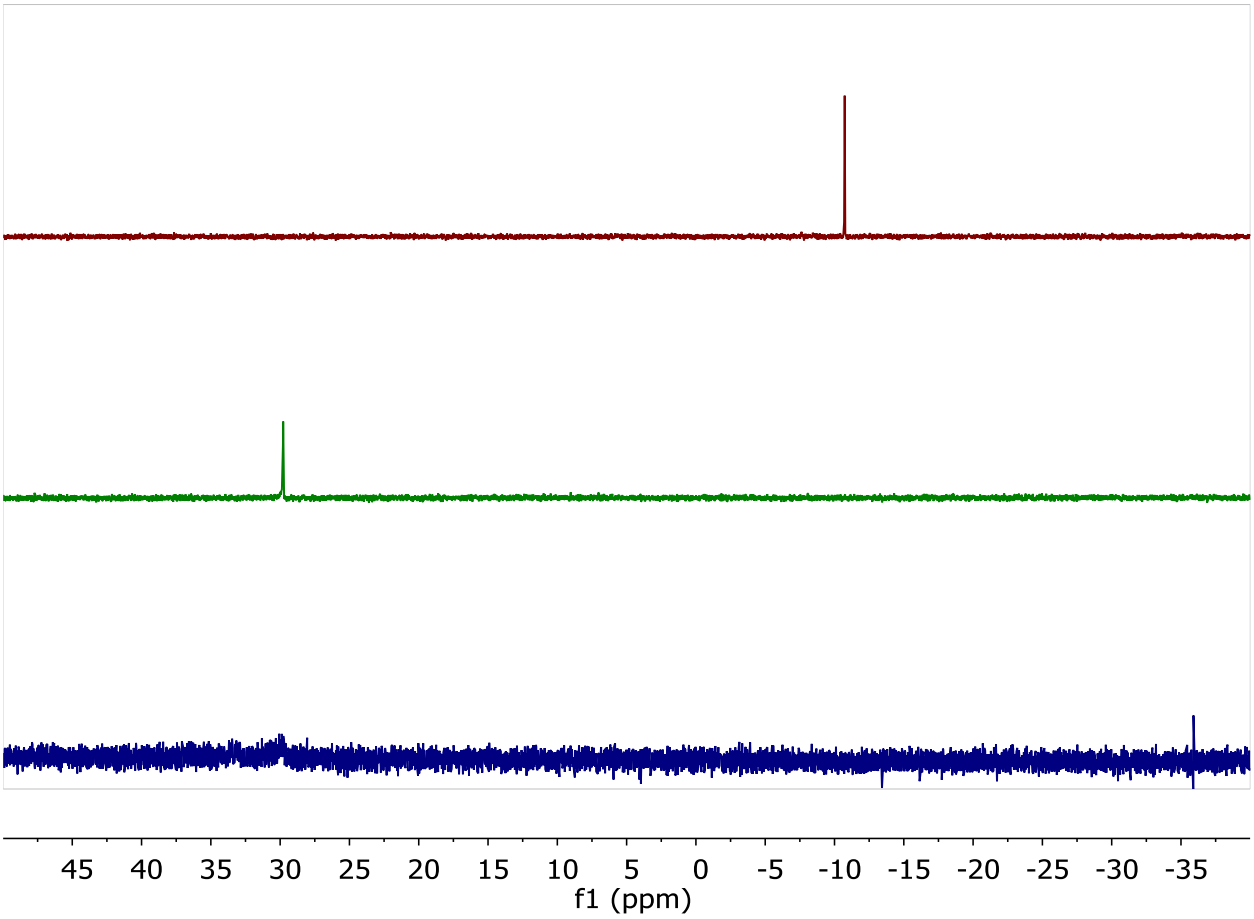

Figure 5.13. Additional reactions using P1-^{t}Bu.^{31}P NMR spectra (202 MHz) of (top, red): a solution of P1-^{t}Bu (36 mM) and phenol (26 mM) in toluene-d_8. The peak at (δ = -11 ppm) corresponds to P1-^{t}Bu only, so the phenol is not deprotonated. (Middle, green): A solution of [P1-^{t}Bu-H][BF_4] in THF, and (bottom, blue): [P1-^{t}Bu-H][BF_4] plus ZnO NCs (130 equiv P1-^{t}Bu-H^+ per NC) in toluene:THF (5:1).

5.4.3 *P2-^{t}Bu and Nanocrystals*

The more basic P2-^{t}Bu was also investigated to deprotonate the NCs. The P2-^{t}Bu base (Figure 5.14, red) and the protonated version P2-^{t}Bu-H^+ (generated using [DBU-H][OTf]) (Figure 5.14, yellow) give ^{31}P resonances for each P nucleus that are well-separated. The base is named P2 because it contains two non-identical P atoms that have distinct ^{31}P resonances (Scheme 5.3). Addition of 21 equiv of P2-^{t}Bu base to a solution of NCs in toluene-d_8, as-prepared (green) and

photoreduced (blue) thus gives four signals. The signals are assigned to P2-^{t}Bu (~70%) and very broad resonances for P2-^{t}Bu-H^{+} (~30%). However, the peaks are broad and a quantitative analysis is tenuous. The broadness complicates our ability to determine if the protonated base is formed, and a subsequent experiment with a different batch of NCs used ~500 equivalents of base and the P2-^{t}Bu-H^{+} (Figure 5.14, bottom, purple) was not observed. This could be explained by heating in DDA (which may remove residual protons), but was only performed once, or due to signal to noise issues based on the large quantity of P2-^{t}Bu base used. Due to the broadness, this base was not pursued further to quantify the number of protons per NC, but it would be interesting to perform a more thorough study across many NC batches to look for trace protons with this relatively mild base.

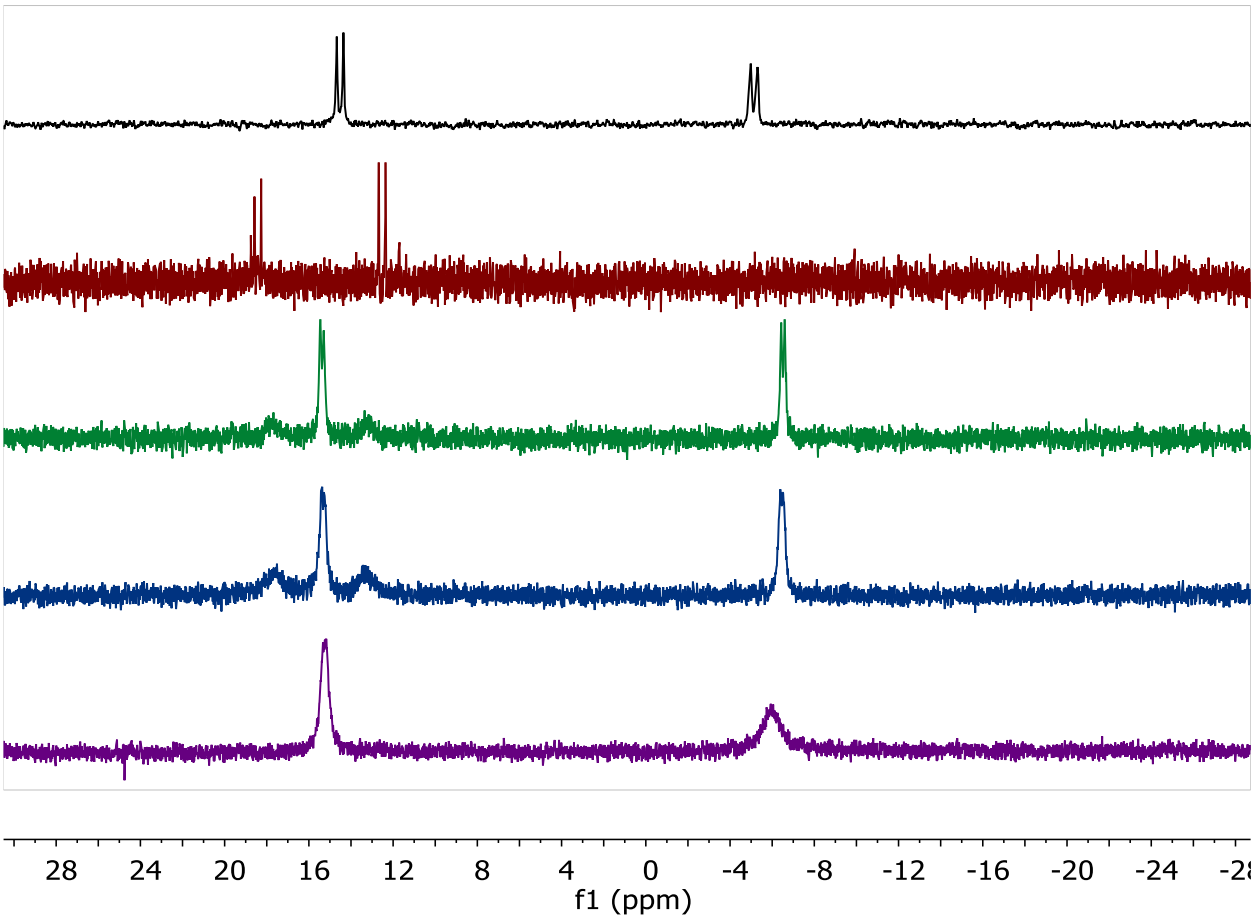

Figure 5.14. Reactions of ZnO NCs and P2-^{t}Bu. ^{31}P NMR spectra (202 MHz) of (black): P2-^{t}Bu base in toluene-d_8, and (red): protonated P2-^{t}Bu-H^{+} generated with [DBU-H][OTf]. The P2-^{t}Bu base was also added to ZnO NCs, (green): as-prepared NCs (d = 3.4 nm, 1.5 mM) and (blue):

photoreduced NCs. The broad peaks at δ = 17 ppm and δ = 13 ppm correspond to the protonated P2-^{t}Bu-H$^+$, where between 5-6 protons were removed per NC. (Purple): Another batch of ZnO NCs (*d* = 6.5, 0.11 mM) was prepared in and mixed with P2-^{t}Bu (61 mM), but no P2-^{t}Bu-H$^+$ was observed.

5.4.4 *P4-^{t}Bu and Nanocrystals*

Similar to the other experiments with phosphazene bases, the P4-^{t}Bu base was added to a solution of ZnO NCs in toluene-d_8. The ^{31}P NMR spectrum for both the protonated and unprotonated forms of the base are easily observed (Figure 5.15). The protonated chemical shifts at −22.7 (q, 1P) and 12.6 ppm (d, 3P) are similar to the reported values. Several methods of addition of P4-^{t}Bu to the NCs were explored. The first was the addition of increasing amounts of P4-^{t}Bu and monitoring the amount of protonation by ^{31}P NMR spectroscopy. We found that the number of protons that came off the NCs was fixed (not an equilibrium) and did not change with the addition of more base.

Over a range of NC sizes, the P4-^{t}Bu base was used to quantify the number of protons that can be removed (Figure 5.16). The number of protons present on as-prepared NCs roughly varies with NC size, suggesting that the protons are on the surface and inherent to the synthesis. It is possible that residual water acts as an acid source, but we believe that the concentration of water is very low in these solutions as they are all prepared in dry, degassed solvents in the glovebox. Another possibility is that this very strong base could deprotonate the DDA ligands bound to the NC to form Zn-NHR, but we have not observed any evidence of this by ^{1}H NMR spectroscopy. It would be beneficial to do a more thorough study coupled with IR spectroscopy to further investigate these protons and their source. For our experiments with reductants and added acid, it was sufficient that we know the base is sufficiently strong to deprotonate the NCs and that the amount could be quantified by ^{31}P NMR spectroscopy.

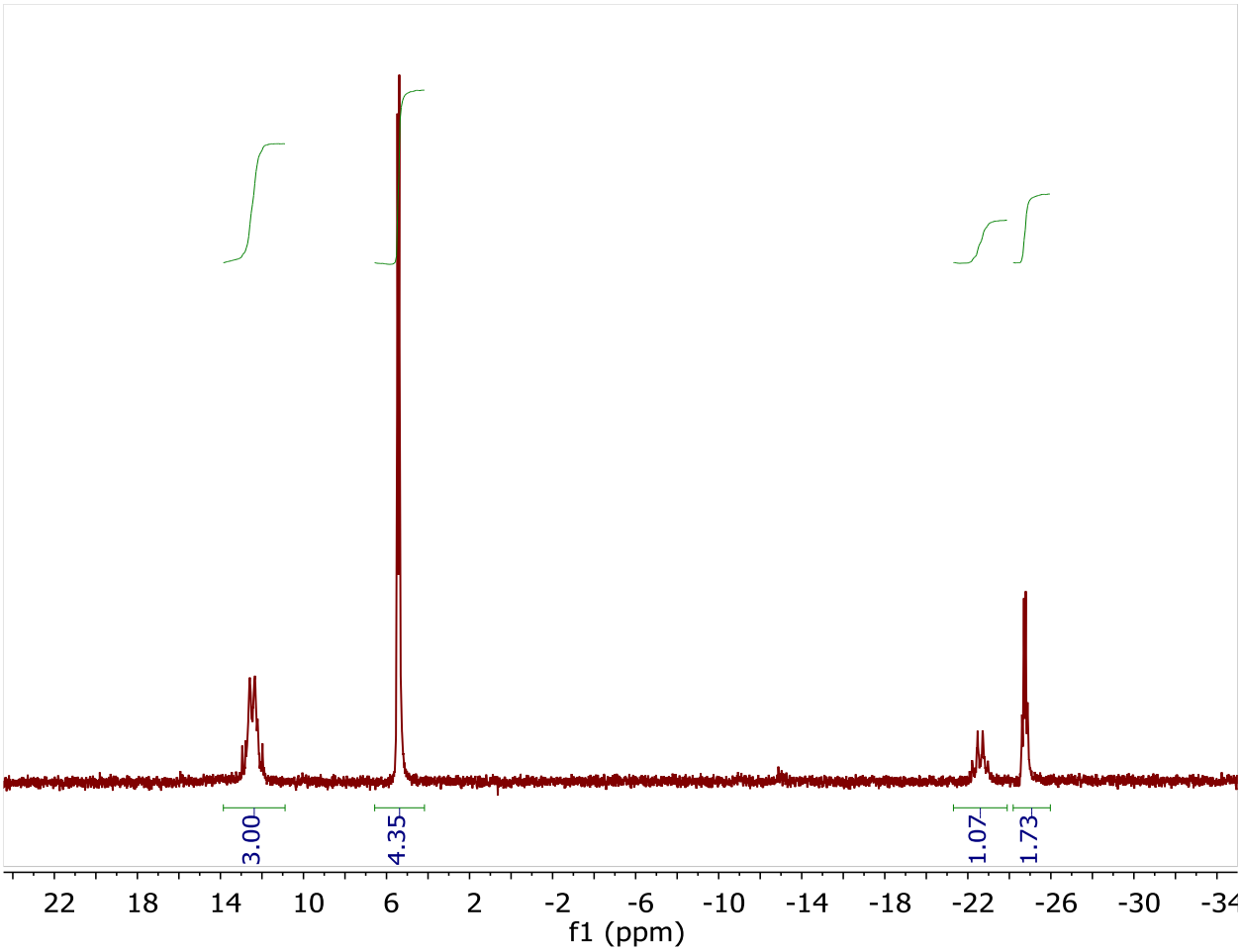

Figure 5.15. Reaction of ZnO NCs and P4-^{t}Bu.^{31}P NMR (202 MHz) spectrum of ZnO NCs (d = 6.5 nm, 1.1 × 10^{-4} M) and P4-^{t}Bu base (50 mM) in toluene-d_8. The signals at −22.7 (q, 1P) and 12.6 ppm (d, 3P) correspond to protonated P4 (P4-H^{+}), and -24.7 (q, 1P) and 5.4 (d, 3P) ppm correspond to the unprotonated P4-^{t}Bu base.

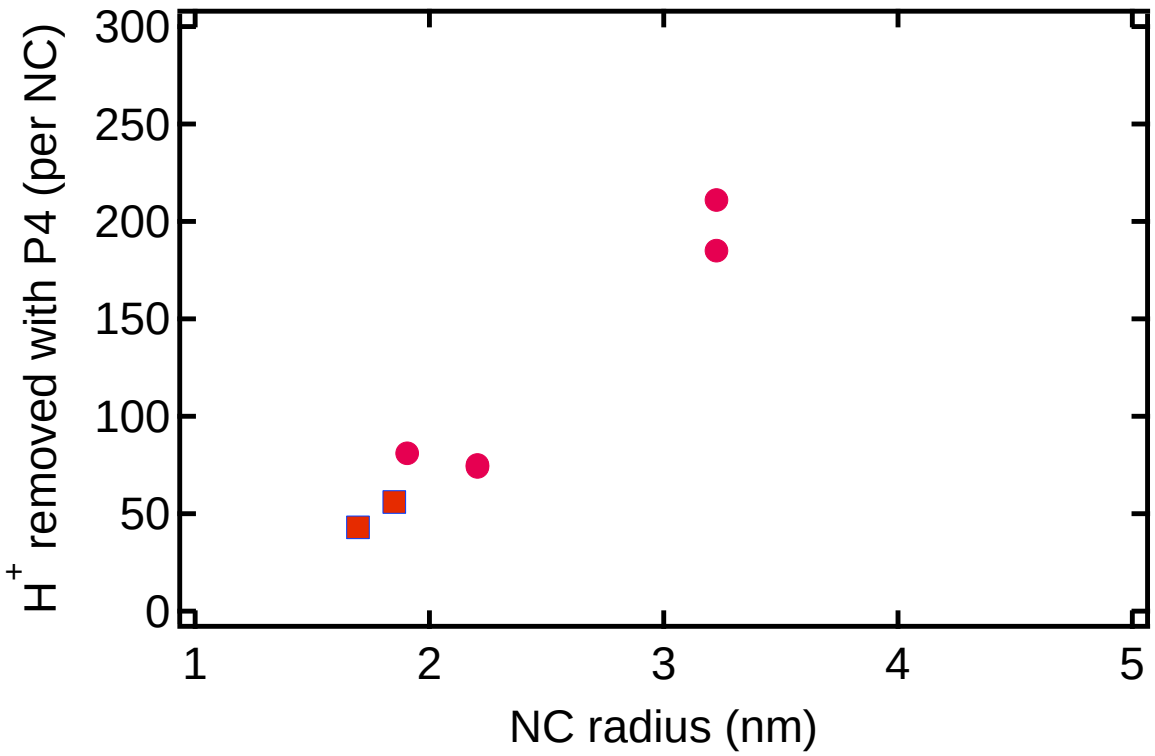

Figure 5.16. Preliminary experiments using ^{31}P NMR spectroscopy and the P4-^{t}Bu base to quantify the number of protons per NC. Shown here is a general trend of the residual protons per NC versus NC radius. The data points with square were only performed once and all of the P4-^{t}Bu base was consumed. Errors were not reported on this plot, but are assumed to be large.

5.5 Hysteretic Behavior: Reversibility with Base

In addition to quantifying the number of protons per NC, the P4-^{t}Bu base is also a useful tool for other spectroscopies. It is a white solid that is easily measured out on a balance and added to NC solutions to change the number of protons (residual or otherwise). In a chapter on chemical reductants (Chapter 4), we described the addition of P4-^{t}Bu to reverse the effects of the acid [DDA-H][HBAr$^{F}_{4}$] addition. Excess reductant (CoCp*$_2$) is added to the ZnO NCs in 50/50 toluene/THF in a quartz cuvette, followed by the addition of acid ([DDA-H][HBAr$^{F}_{4}$]) as a solution. After the reduced NCs reach $<n_{e^-}>_{max}$, the reduction is reversed by the addition of a solution of P4-^{t}Bu phosphazene base. When monitored carefully, we noticed a hysteretic effect in the process, where the base-addition path to return to un-reduced NCs did not overlay on the

acid-addition path (Figure 5.17). This was repeated with two separate batches of NCs, and the same effect was observed. This was also performed via cycling (Figure 5.18), *i.e.* adding additional acid after the first addition of base. We find in preliminary experiments that the path is slightly different than the initial acid-added path. We believe that the hysteresis may be due to proton movement through the NCs lattice, an impurity in the $CoCp^*_2$, or removal of surface protons vs. a different place for protons. This should be investigated more in the future.

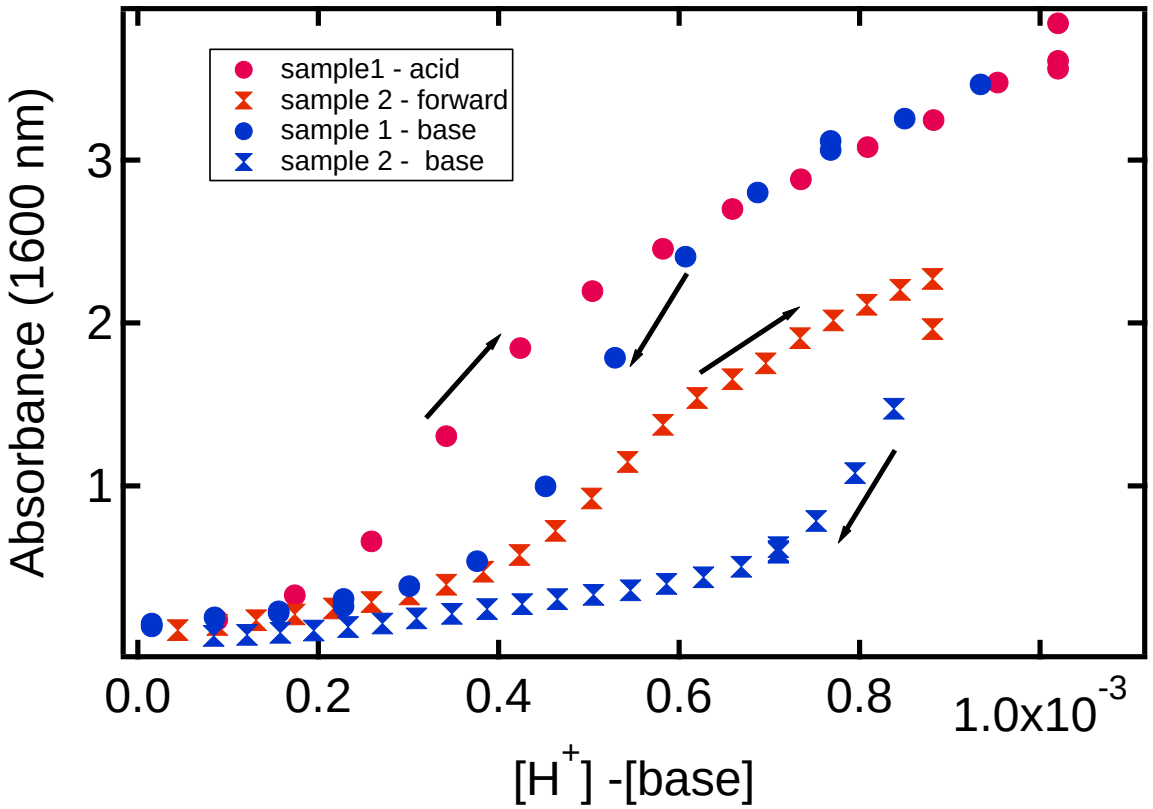

Figure 5.17. Hysteresis of $CoCp^*_2$ with ZnO NCs and acid/base. For two samples of ZnO NCs (d = 3.8 nm, 3.4×10^{-5} M) with excess $CoCp^*_2$, the optical absorbance at 1600 nm is tracked as a function of the net concentration of acid in solution. Acid (as a solution of [DDA-H][BAr^F_4]) and base (a solution of P4-^{t}Bu phosphazene) were added in 10 μL aliquots.

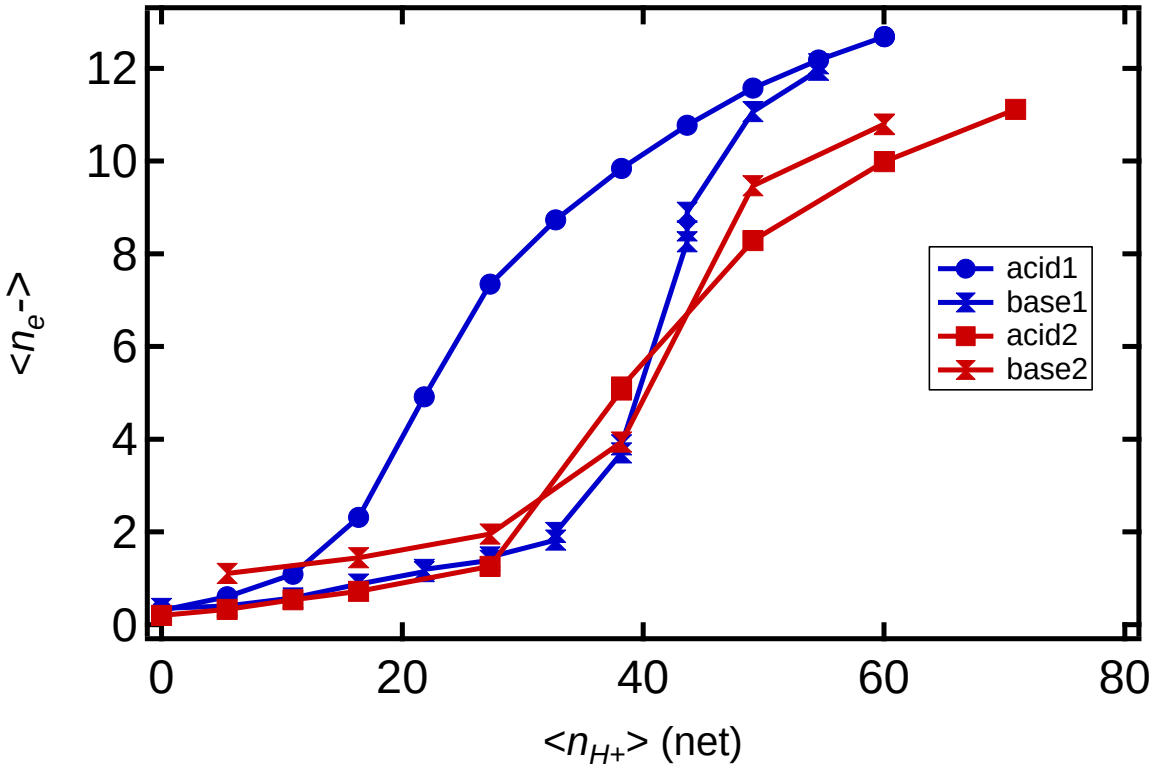

Figure 5.18. Hysteresis cycling with $CoCp^*_2$ and acid/base. For one sample of ZnO NCs (d = 3.8 nm, 1.7×10^{-5} M) with $CoCp^*_2$ added (560 equiv), the optical absorbance at 850 nm is tracked and converted to $\langle n_{e^-} \rangle$ as a function of the net number of protons per NC $\langle n_{H^+} \rangle$. Acid (as a solution of $[DDA\text{-}H][BAr^F{}_4]$) was added and base (a solution of P4-^{t}Bu phosphazene) were added in 10 μL aliquots (blue points), followed by addition of acid and base a second time.

5.6 Electrochemistry Attempts with Zinc Oxide Nanocrystals

In an attempt to determine the position of the conduction band of colloidal ZnO NCs, cyclic voltammetry, spectroelectrochemistry, and rotating ring electrochemistry were attempted. Electrochemistry has been performed on films,[14-16] but we wanted to perform experiments on colloidal NCs and in THF, where the conditions are more similar to what is used for the majority of the experiments described in this thesis.

The first issue with electrochemistry in THF and all non-polar solvents is low conductivity. In an attempt to surpass this issue, 0.4 M solutions of electrolyte (as opposed to the 0.1 M solutions generally used in electrochemistry) were prepared. Spectroelectrochemistry and cyclic

voltammetry of ZnO NCs in THF with tetrabutylammonium hexafluorophosphate [TBA][PF_6] (0.4 M) were attempted using a gold mesh electrode and glassy carbon electrode (respectively), however the NCs were very unstable and precipitated. Further tests determined that the ZnO NCs are unstable with the electrolyte [TBA][PF_6] (a standard electrolyte). Attempts to redissolve the precipitate in toluene, THF, acetonitrile, DMF, or ether were unsuccessful; the NCs were irreversibly aggregated. As an alternative electrolyte, [TBA][BF_4] was tested, and we found that the NCs are stable on the benchtop for up to an hour (although the exact time will vary with the batch of NCs).

With more stable solutions, we wanted to test the solution conductivity and determine if sufficient charge is passed in the solution using controlled potential electrolysis (CPE) (Figure 5.19). The cell was held at -1.0 V and -1.1 V (vs. $Ag/AgNO_3$) (~ -1.6 V vs. Fc/Fc^+) using a Pt mesh electrode, and ~1.4 x 10^{-3} C were passed after 10 minutes with NCs. This equates to 1.2 × 10^{-8} mol of electrons passed in the solution, compared to 8 × 10^{-7} mol of ZnO.

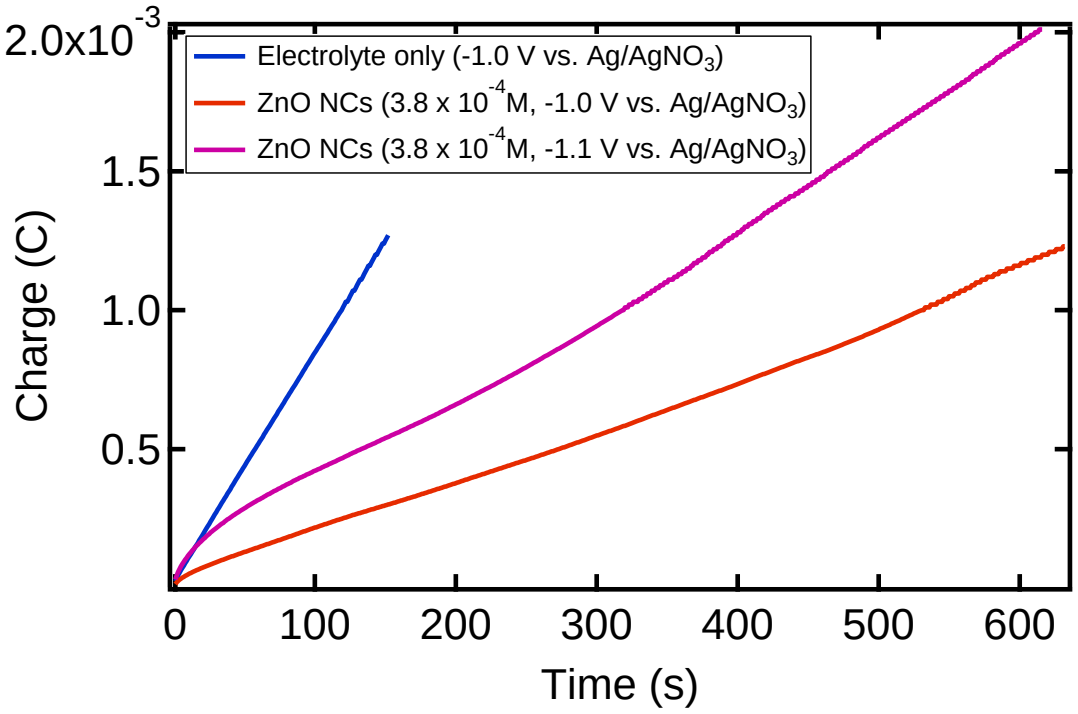

Figure 5.19. Controlled potential electrolysis of ZnO NCs was performed using a Pt mesh electrode and the charge was monitored over time. The blue line is electrode in electrolyte only (0.4 M [TBA][BF4]), the red is with ZnO NCs held at -1.0 V, and the purple is NCs held at -1.1 V.

However, there are several problems with these experiments. (1) A potential of -1.1 V vs. $Ag/AgNO_3$ is likely not reducing enough, based on the more recent observation that $CrCp^*_2$ cannot reduce the NCs. (2) With only 10^{-3} C passed and an epsilon of 1000 $M^{-1}cm^{-1}$ per electron at 850 nm, we would only anticipate an absorbance change of 0.01, likely too small to see. (3) After 30 minutes, the NC solution began to precipitate. Despite these caveats, we have learned that the NCs are more stable to $[BF_4]$ salts than $[PF_6]$ salts and that with THF and 0.4 M electrolyte insufficient charge is passed using a mesh electrode. Future experiments should consider a method to pass more charge, monitor in the region of more intense signal from the NCs (2000 nm, for example) and make more stable solutions.

5.7 Reactivity of ZnO Nanocrystals with CO_2, Benzophenone, and Other Two-Electron Two-Proton Reactions

The ability of ZnO NCs to store electrons (*e*–) and protons (H^+) has been demonstrated using ET and PCET acceptors, but NCs store *more than one e*– and H^+ per NC. One way to utilize this unique property of colloidal semiconductor NCs is to perform multi *e*–/H^+ transformations in solution, as opposed to molecules that can generally donate only one *e*– and/or H^+. Some of the biggest markets for chemical transformations are difficult multi *e*–/H^+ reactions including reduction of N_2 to NH_3 and CO_2 to various reduced products.[17,18] Given that nontoxic and abundant CO_2 may be used both for fuel production and as a C-1 feedstock, research in this field is extensive.[19] In industrial settings, a Cu/ZnO catalyst is used to produce methanol from CO_2 and H_2 at 100 bar and temperatures above 200 °C.[20,21] Recently, it was reported that ZnO alone is active for CO_2 reduction, in contrast to other oxides such as SiO_2 and Al_2O_3.[22,23] Yahaya et al. showed that ZnO, TiO_2, and NiOH powders can reduce CO_2 to methanol and other products,[24] and Wan et al. found that higher surface areas of oxides are more active for photoreduction of CO_2.[25] However, there are very few reports of CO_2 photoreduction using non-titanium nanomaterials with careful control over proton and reducing equivalents.[26]

We believe that an added advantage to using metal oxides (and other semiconducting materials) is that all of the *e*–/H^+ can be delivered at approximately the same potential, like in a battery. While still far away from the fine understanding that can come from small molecule studies, we wanted to use colloidal metal oxides for these transformations because of our ability to track their reactivity and protonation state using optical spectroscopy and the addition of acids/bases to more finely control the equivalents.

Scheme 5.4. Proposed reaction of ZnO NCs with CO_2.

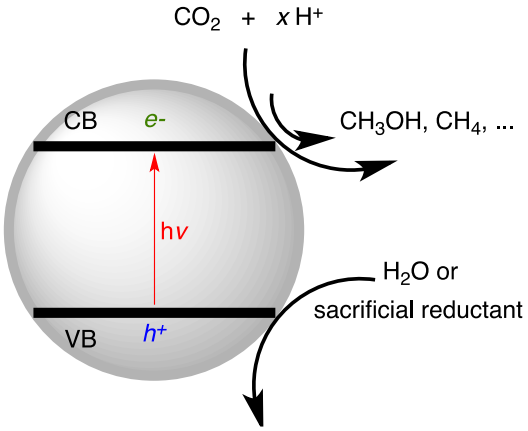

Our experimental design was to generate reduced NCs with UV light and test for reactivity with CO_2 and other multi *e*–/H^+ acceptors, as depicted in Scheme 5.4. Initial studies with undergraduate Ashley Soria in 2012-2013 were performed in standard cuvettes in the glovebox, with aliquots of the *e*–/H^+ acceptor added as a solid or as a concentrated solution in toluene. Using this method, we determined that photoreduced ZnO NCs (1×10^{-4} M, 2 mL) did not react with DMSO (100 μL) or benzophenone (6.0 mg), as indicated by the absence of a color change after approximately 20 minutes, monitored by eye and by optical spectroscopy.

Initial experiments did find that reduced ZnO NCs react with *p*-tolylsulfoxide, most likely to form *p*-tolylsulfide by a concerted two-electron process. Upon addition of *p*-tolylsulfoxide, photoreduced ZnO NCs in toluene changed from blue to clear and optical spectra showed a decrease in absorbance for electrons in ZnO NCs, shown below in Figure 5.20. However there were a few issues with this initial experiment: (1) the number of equivalents was not determined, as this was just a survey test, and (2) I was concerned that there was residual oxygen in the solvent that was used to dissolve the stock solution of *p*-tolylsulfoxide. We also note that these

experiments were performed with DDA-capped ZnO NCs, and because of the reactivity between DDA and CO_2, subsequent experiments were performed with TOPO*-capped ZnO.

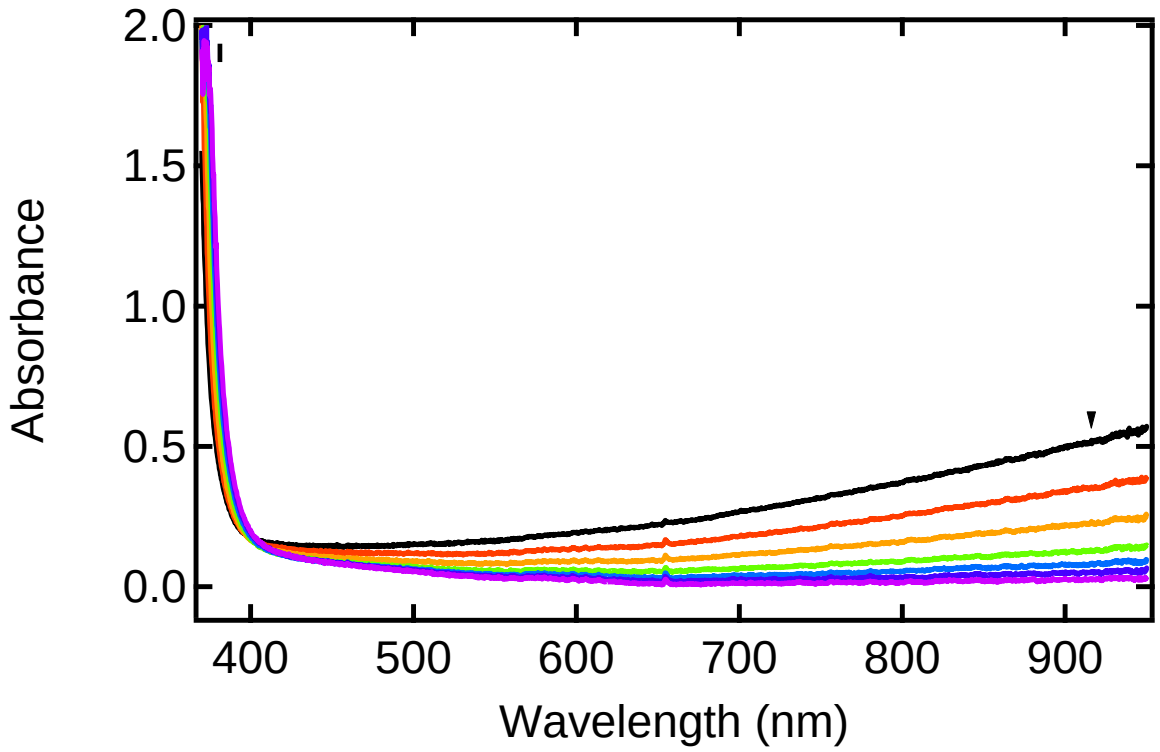

Figure 5.20. Optical absorption spectra of the addition of *p*-tolylsulfoxide to photoreduced ZnO in toluene (d = 3.8 nm, 1.19 × 10^{-4} M, initial trace in black). Absorbance at > 400 nm is attributed to electrons in the conduction band of ZnO. The number of equivalents was not precisely determined, but was approximately 100 per NC per addition.

Another undergraduate, Hayli Larsen, continued this project in 2014. She used TOPO*-capped ZnO NCs and confirmed that photoreduced NCs did not react with DMSO and extended the substrate scope. Photoreduced ZnO NCs (d = 3.8 to 4.2 nm) in toluene/THF did not reduce azobenzene, dimethyl carbonate, acetaldehyde, priopionaldehyde, or the insoluble salts 2,3-dihydroxynaphthalene and *p*-formaldehyde.

It was confirmed that the NCs reacted with *p*-tolylsulfoxide, albeit in a smaller amount than observed above, but no additional products were observed by ^{1}H NMR spectroscopy, except for

a slight increase in a broad peak of the NCs (2.3 ppm, 100 Hz in width), which we associate with capping ligands. This reaction should be investigated in more detail.

There was also some observed reactivity with similar additions of anthraquinone to photoreduced NCs, as well as some slow reactivity with benzaldehyde (that over a day resulted in precipitation). Addition of gaseous CO_2 to a J-Young tube of photoreduced NCs gave no color change, but there was a small peak at 3.1 ppm observed by ^{1}H NMR spectroscopy that may be associated with methanol formation. By ^{13}C NMR spectroscopy, a broad peak at -165.8 ppm appears only in the sample of photoreduced NCs plus $^{13}CO_2$, as opposed to DDA-capped ZnO only (in blue) (Figure 5.21). This experiment should be repeated with TOPO*-capped ZnO.

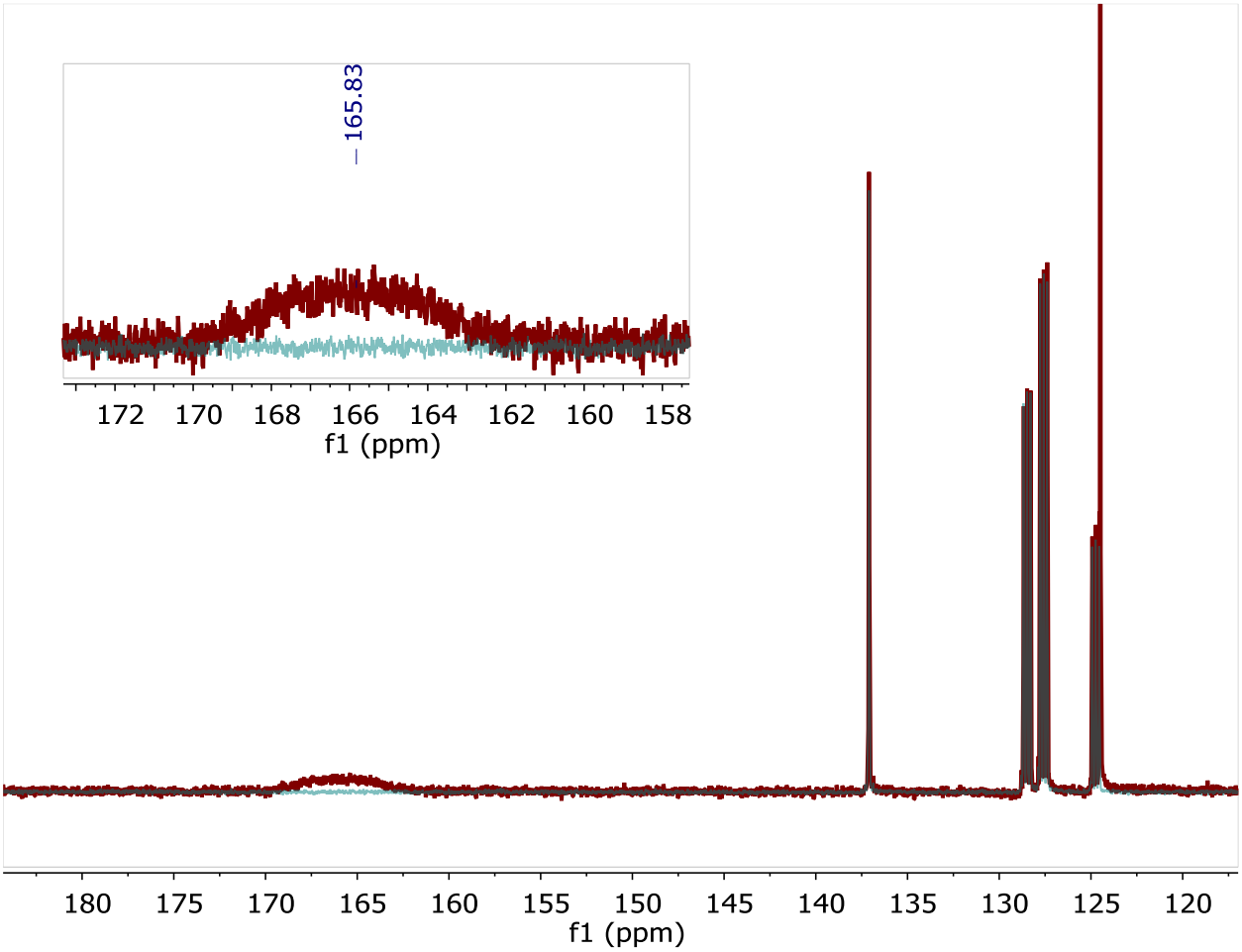

Figure 5.21. ^{13}C NMR spectra of photoreduced ZnO only (d = 3.8 nm, 4.6×10^{-4} M) plus $^{13}CO_2$ (900 equiv added to the headspace, at 4 atm in 1.3 mL of headspace), blue and red, respectively.

5.8 Reaction of Doped ZnO Nanocrystals

As described in detail in Chapter 4, ZnO NCs can be reduced using an outer sphere reductant (MCp^*_2) and protons, which shift the conduction band levels lower in energy. This reduction reaches a maximum at $\langle n_{e^-} \rangle_{max}$, that depends on the volume of the NC, thereby giving a maximum carrier density ($\langle N_{e^-} \rangle_{max}$). This was reported for photoreduced ZnO NCs as well.[10] In collaboration with Dr. Alina Schimpf, we wondered if doping with aliovalent metal ions (Mg^{2+} or Cd^{2+}) would give a different density. Similar to the addition of acid, the inclusion of dopant atoms in the lattice should change the absolute chemical potential of the NCs and change the way that they are reduced by an outer sphere reductant.

Three batches of ZnO NCs that were doped with different amounts of Mg^{2+}, by the method of a mixture of metal salts,[27] were received from Dr. Schimpf and the experiments with chemical reductants are described here. Each sample was characterized in the same manner to determine the Abs(850nm) per electron in order to determine $\langle n_{e^-} \rangle$ in the optical spectrometer. Excess reductant was added to a solution of the NCs in toluene/THF in a glovebox, and acid was added in small aliquots as a solution of [DDA-H][BAr^F_4] until the spectra ceased changing, indicating that $\langle n_{e^-} \rangle_{max}$ was reached. The optical absorbance from 300 to 900 nm was monitored, and later converted to $\langle n_{e^-} \rangle$ versus equivalents of acid per NC ($\langle n_{H^+} \rangle$). An example of this experiment is shown below in Figure 5.22.

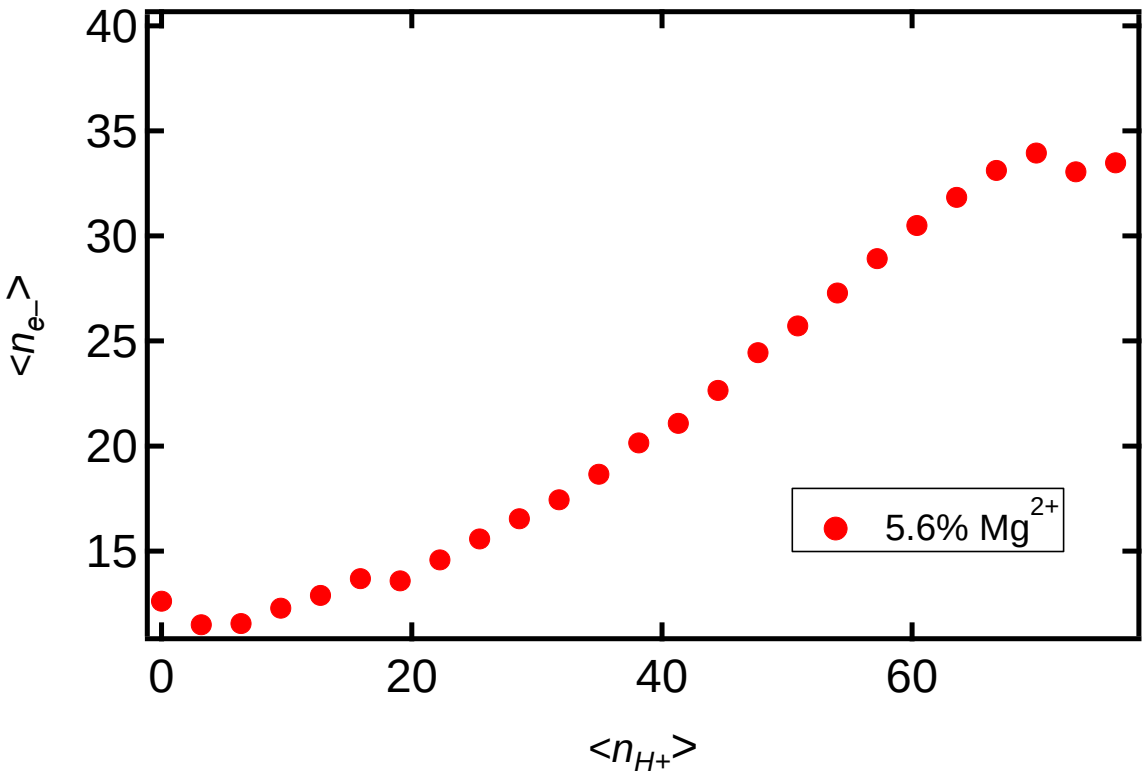

Figure 5.22. The number of electrons per NC $\langle n_{e^-} \rangle$ of Mg^{2+}-doped NCs with excess $CoCp^*_2$ as a function of added protons as $[DDA\text{-}H][BAr^F{}_4]$. $\langle n_{e^-} \rangle_{max}$ is reached at ~35 electrons per NC.

Each sample was analyzed in the same way, and the $\langle n_{e^-} \rangle_{max}$ was converted to $\langle N_{e^-} \rangle_{max}$ using the NC volume, and compared to the $\langle N_{e^-} \rangle_{max}$ obtained for undoped NCs at $4.0(1.0) \times 10^{20}$ cm^{-3} (Figure 5.23), as described in the chemical reductants chapter (Chapter 4). The samples are plotted as a function of the ratio of Mg^{2+}/Zn^{2+}, with the highest at 0.164. We note that although the NCs have different diameters, they are all above the quantum confinement regime and $\langle N_{e^-} \rangle_{max}$ is normalized for NC volume. We find that $\langle N_{e^-} \rangle_{max}$ for the three doped NC batches is much lower than the 100% Zn^{2+} NCs, at $1.8(0.2) \times 10^{20}$ cm^{-3}, independent of the percentage of Mg^{2+} ions. The reason for this effect is unknown, and counter intuitive given the expected shift of E_g with Mg^{2+} doping,[27] but points to a significant effect of the nature of the cation, which appears to be constant above 4% Mg^{2+} doping.

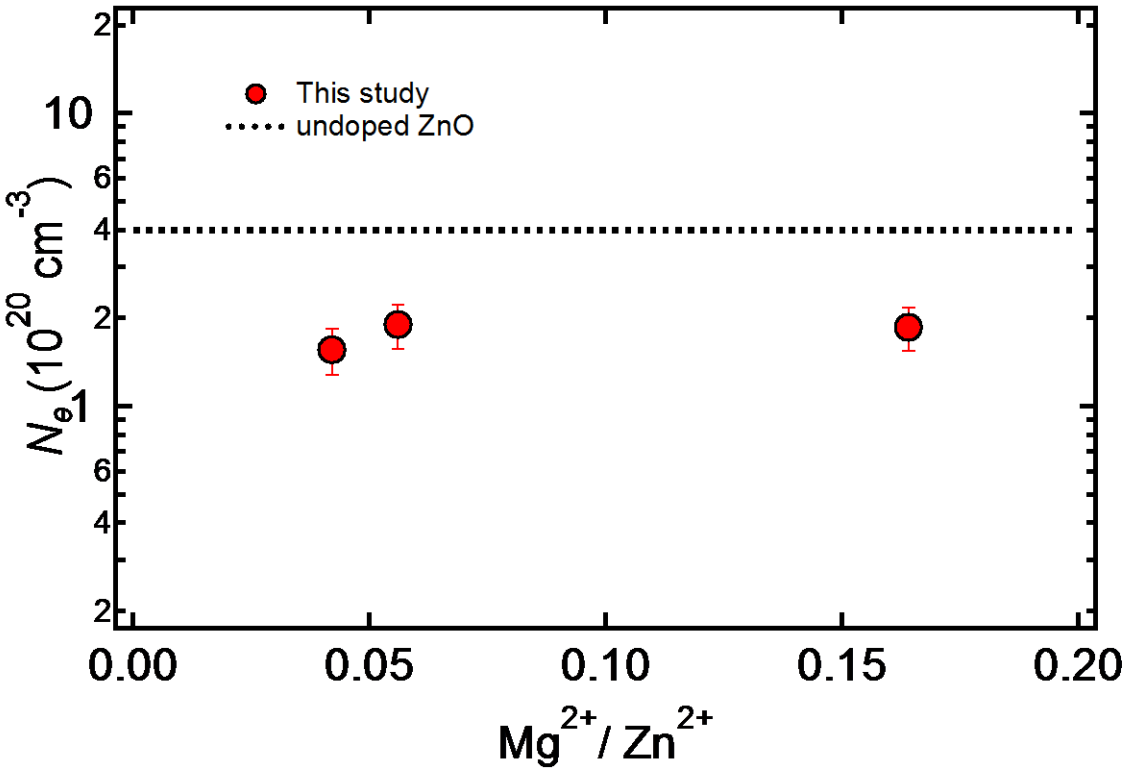

Figure 5.23. Maximum carrier density of Mg^{2+} doped NCs reduced with $CoCp^*_2$ and acid (as [DDA-H][BAr^F_4]) as a function of Mg^{2+} content relative to Zn^{2+}. The dotted line represents a maximum carrier density obtained for undoped ZnO NCs (see Chapter 4), that is more than double the density achieved for these doped samples.

5.9 ORAGNOMETALLIC SYNTHESIS OF NCS

The experiments reported in this thesis were performed with ZnO NCs that were prepared using the previously reported method involving the room temperature, base hydrolysis of zinc acetate salts under air. We wanted to test that observed trends for carrier density, capping ligands, *etc*. held for ZnO NCs synthesized by another method. The zinc precursor was dicylohexylzinc ($Zn(Cy)_2$), prepared using a recently published method via salt metathesis with $ZnCl_2$.[28] Nanocrystals were grown following a preparation developed by Monge et al,[29] via the slow hydrolysis of $Zn(Cy)_2$ over 17 hours with one equiv of DDA, followed by precipitation and washing (Scheme 5.5).

Scheme 5.5. Organometallic synthesis of ZnO NCs using $Zn(Cy)_2$.

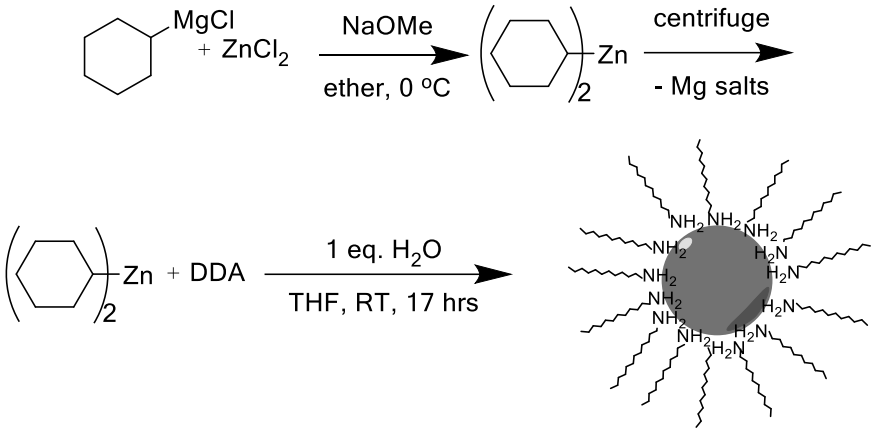

The ^{1}H NMR spectra of the precursor ($Zn(Cy)_2$) was compared to the NCs in toluene-d_8, and show that all of the $Zn(Cy)_2$ is consumed and that there is free DDA as well as DDA bound to the NCs (Figure 5.24). Optical spectroscopy of the NCs shows very similar band edge features compared to the base hydrolysis method, with one intense feature at ~320 nm (Figure 5.25). TEM images of the NCs show monodisperse, relatively spherical NCs with an average diameter of d = 2.5 ± 0.8 nm (Figure 5.26), consistent with the size obtained via optical spectroscopy, at d = 2.9 ± 0.6 nm according to UV-Vis following our typical method of calculating size based on a previously reported relationship of size and the optical spectra.[30]

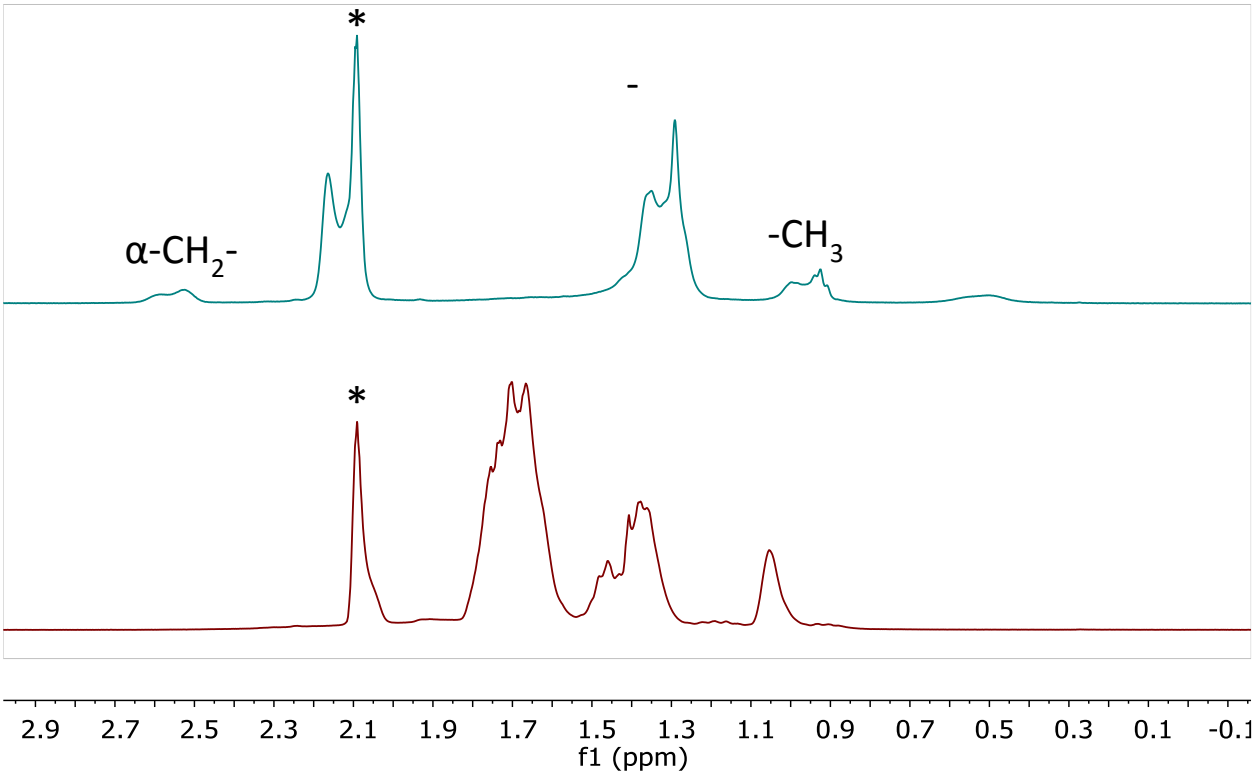

Figure 5.24. ^{1}H NMR spectra of ZnO NCs synthesized via hydrolysis of $Zn(Cy)_2$ and 1 equiv of DDA (blue, top), and $Zn(Cy)_2$ alone in toluene-d_8 (red, bottom).

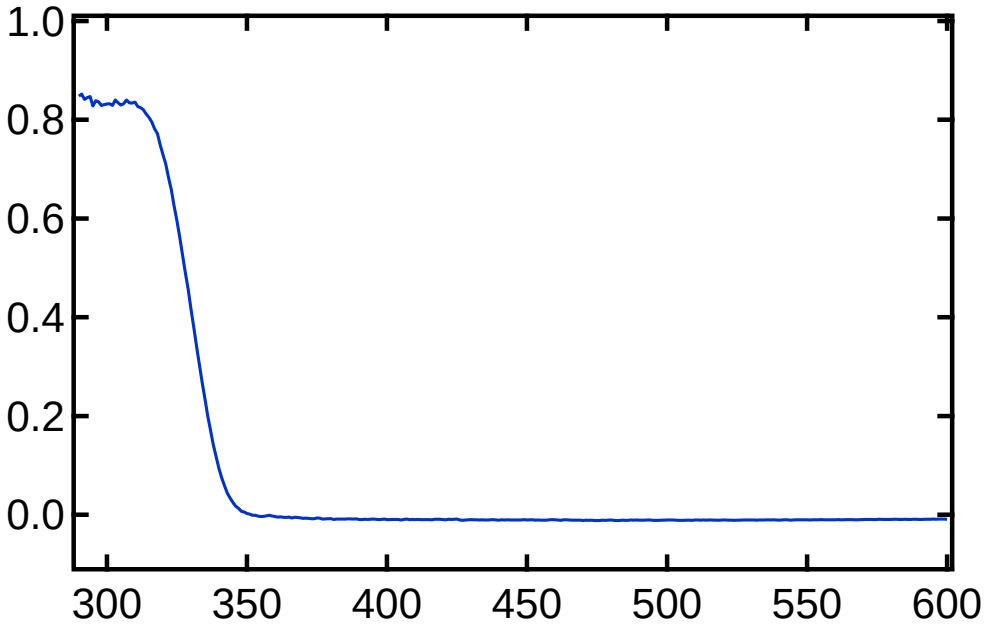

Figure 5.25. Optical absorbance spectrum of ZnO NCs synthesized via hydrolysis of $Zn(Cy)_2$ and 1 equiv of DDA in toluene (approximately 10^{-7} M).

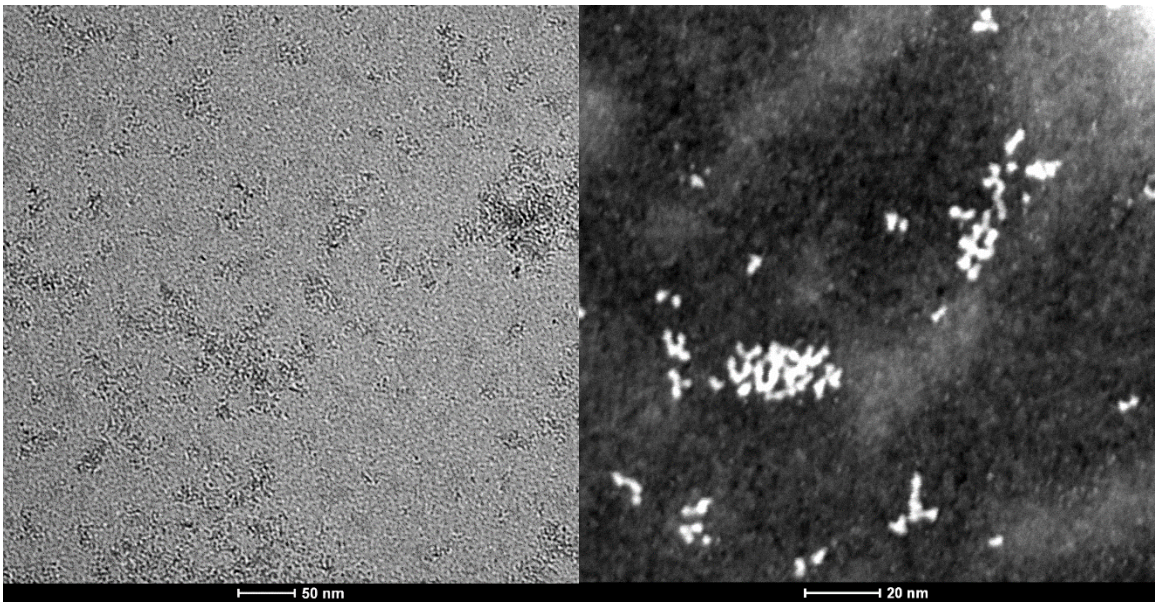

Figure 5.26. TEM and STEM images of ZnO NCs synthesized via hydrolysis of $Zn(Cy)_2$ and 1 equiv of DDA in toluene. Sizing was performed using ImageJ to give $d = 2.5 \pm 0.8$.

Preliminary experiments with excess $CoCp^*_2$ and aliquots of $[Na][BAr^F_4]$ added show a peak in the near IR that corresponds to electrons in the ZnO NCs (Figure 5.27). This indicates that the NCs can be reduced in a similar fashion as NCs synthesized via base hydrolysis. Ongoing experiments are exploring this system to determine the molar absorption coefficient per electron and to calculate the carrier density.

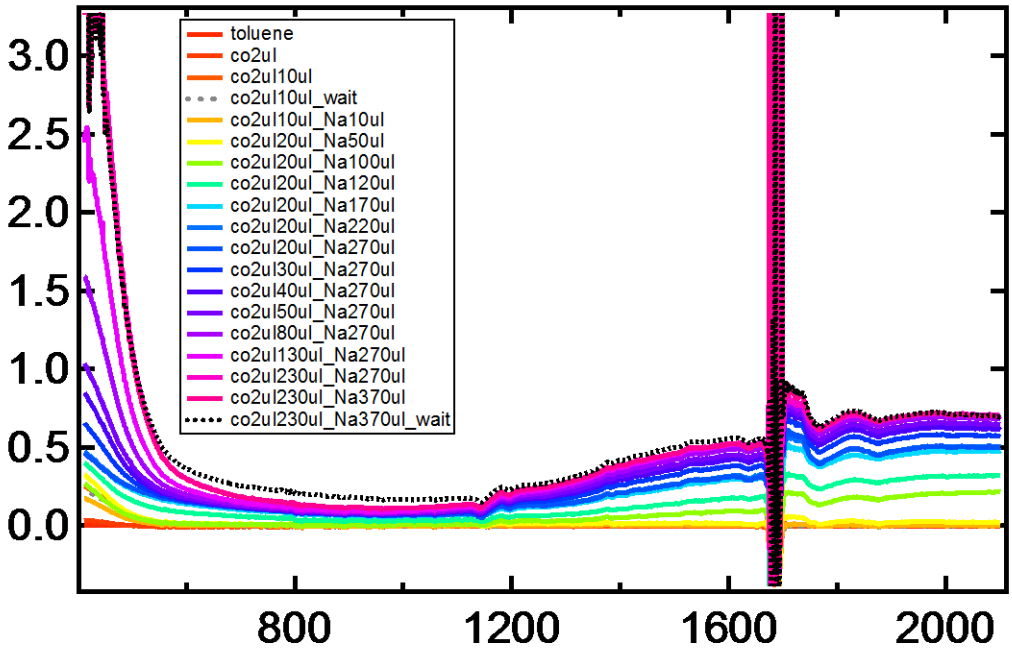

Figure 5.27. Optical absorbance spectrum of ZnO NCs (d = 2.9 nm, 2.1 × 10^{-5} M), synthesized from the hydrolysis of $Zn(Cy)_2$ reduced with excess $CoCp^*_2$ and $[Na][BAr^F_4]$. The choppy region at 1700 nm arises from excess THF added (therefore rendering the zeroing ineffective).

5.10 Quantitative EPR with Chemically Reduced ZnO Nanocrystals

The following experiments were conducted with an undergraduate student who worked with me, Ashley Soria. Our objective was to quantify the number of electrons generated from chemically reduced NCs with acid using EPR spectroscopy. These experiments were successful only because of the valuable assistance of Ellen Hayes in the Stoll lab.

5.10.1 *EPR for Chemically Reduced NCs*

For g-value dependence and quantitative studies, all measurements were performed with three batches of chemically reduced NCs (d = 3.5 nm, 4.1 nm, and 4.7 nm) on a Bruker EMX spectrometer. 2,2,6,6-tetramethylpiperidine 1-oxyl (TEMPO) was chosen as an external spin count standard and a 7.1 mM stock solution of TEMPO in toluene was prepared for use in making a calibration curve. Prior to carrying out any EPR trials, a power saturation experiment was performed on both TEMPO and reduced NCs to determine the optimum power level and avoid saturation. This preliminary step indicated that 33 dB (0.101 mW) should be used for TEMPO and 18 dB (3.19 mW) for reduced ZnO NCs.

To generate a calibration curve for TEMPO, a stock solution of TEMPO was diluted with toluene in the working range of NC concentration (0.1 mM – 1.0 mM). The EPR spectra were processed in Igor Pro and first normalized to correct for the number of scans, power level, and receiver gain (machine settings that often have to be adjusted from sample to sample). The corrected spectra were then integrated and baseline corrected to obtain the area under the peak. The area, otherwise referred to as the integrated intensity, was plotted against TEMPO concentration to produce the calibration curve shown in Figure 5.28.

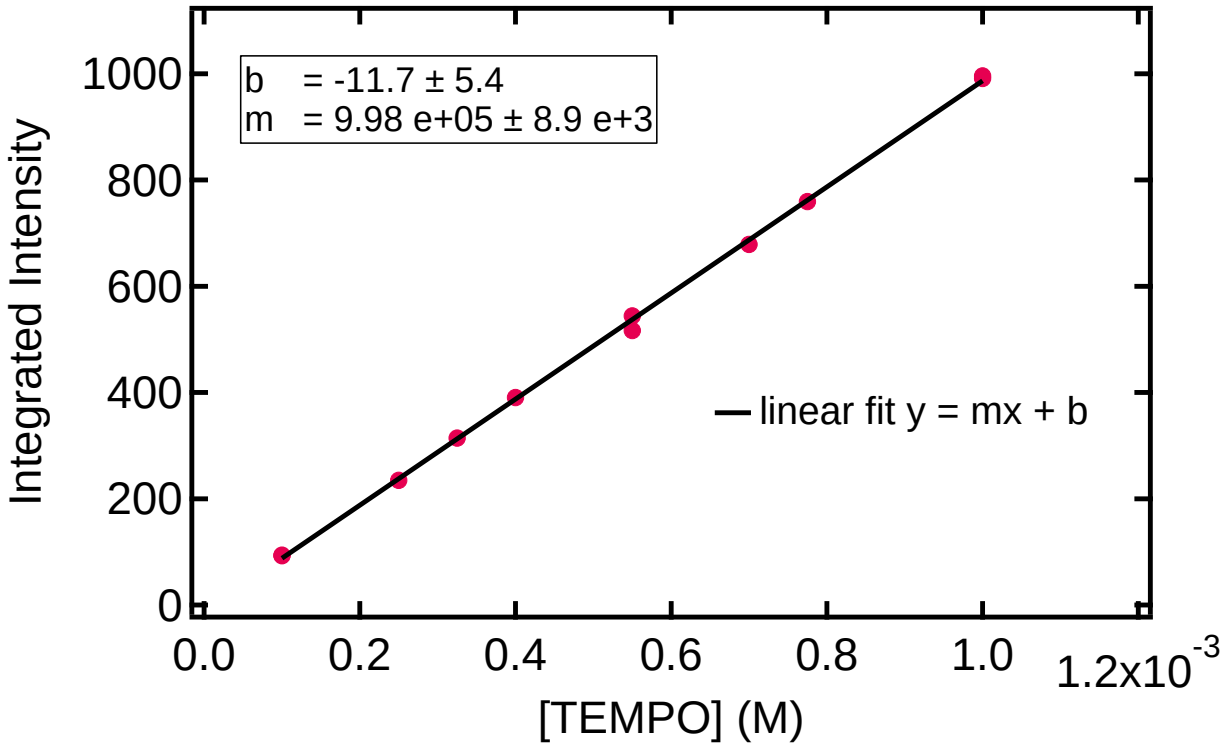

Figure 5.28. TEMPO calibration curve, with integrated intensity (calculated using IgorPro) plotted versus the known concentration of TEMPOin a standard 4 mm quartz EPR tube.

For simultaneous optical spectroscopy and EPR analysis of the NCs, after an optical spectrum was recorded, 400 µL of reduced NCs were transferred to 4 mm EPR tubes after each addition of $CoCp^*_2$ and/or $[HBAr^F_4]$ to yield NC samples with varying $\langle n_{e^-} \rangle$. The tubes were sealed using a septum and Parafilm® to prevent air from contaminating the samples. 2,2-diphenyl-1-picrylhydrazyl (DPPH) was attached to the outside of each tube to be used as a g-value standard, but was removed when integrating under the peak to prevent power saturation issues. An o-ring was placed 10 cm above the center of the sample as a guide to ensure proper placement into the EMX cavity.

5.10.2 *g Factor Versus* $\langle n_{e^-} \rangle$

In photoreduced ZnO NCs, the g factor is inversely related to NC size and rises smoothly with $\langle n_{e^-} \rangle$.[3] The g factor versus $\langle n_{e^-} \rangle$ (obtained from optical spectra) for chemically reduced ZnO using $CoCp^*_2$ and $[HBAr^F_4]$ are shown below in Figure 5.29. We find that within a size of NC,

the g-value is roughly linear with $<n_{e-}>$, similar to photoreduced NCs. At a given $<n_{e-}>$, the g factor is higher for smaller NCs, as expected, indicating that the EPR signal does not arise from deeply trapped electrons. It also suggests that the electrons are delocalized, as the band gap of the NCs (E_g) is size-dependent in this regime and the g factor is sensitive to NC diameter.

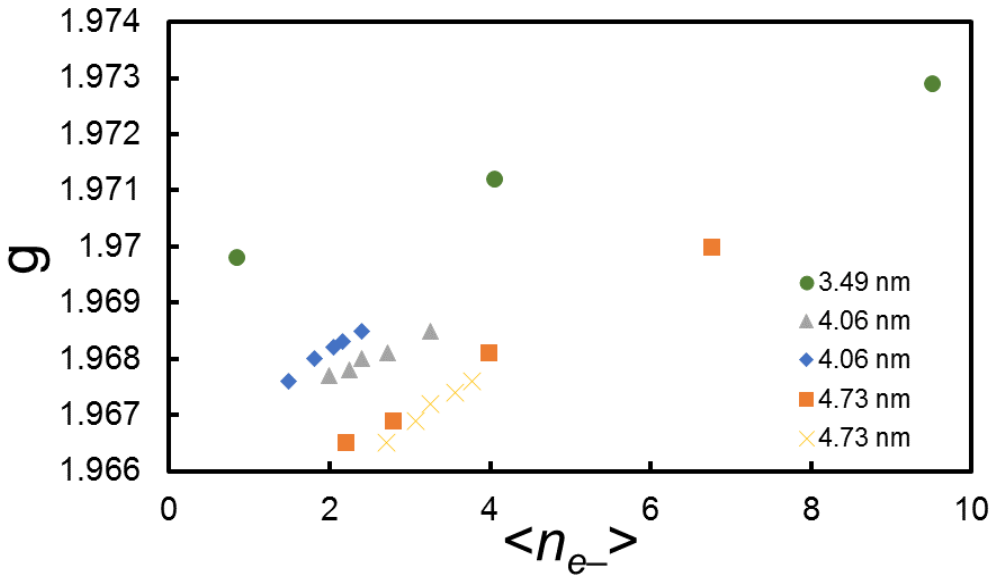

Figure 5.29. The g-value as determined by EPR as a function of $<n_{e-}>$, for four sizes of NCs, ranging from d = 3.49 nm to d = 4.73 nm.

5.10.3 *Spin Quantitation in Chemically Reduced NCs*

The concentration of spins for each sample was quantified from the calibration curve derived from TEMPO measurements as shown in Figure 5.28. The number of carriers per NC from the EPR spectra ($<n_{e-}>_{EPR}$) were compared with the $<n_{e-}>$ determined from the optical spectra. These data are presented below in Figure 5.30. The value of $<n_{e-}>_{EPR}$ is consistent with $<n_{e-}>$, at small numbers of electrons, but deviates at higher values of $<n_{e-}>$. An illustration of this point is to consider the data labeled A, where $<n_{e-}>$ = 7 from the optical spectra and $<n_{e-}>_{EPR}$ = 2.5.

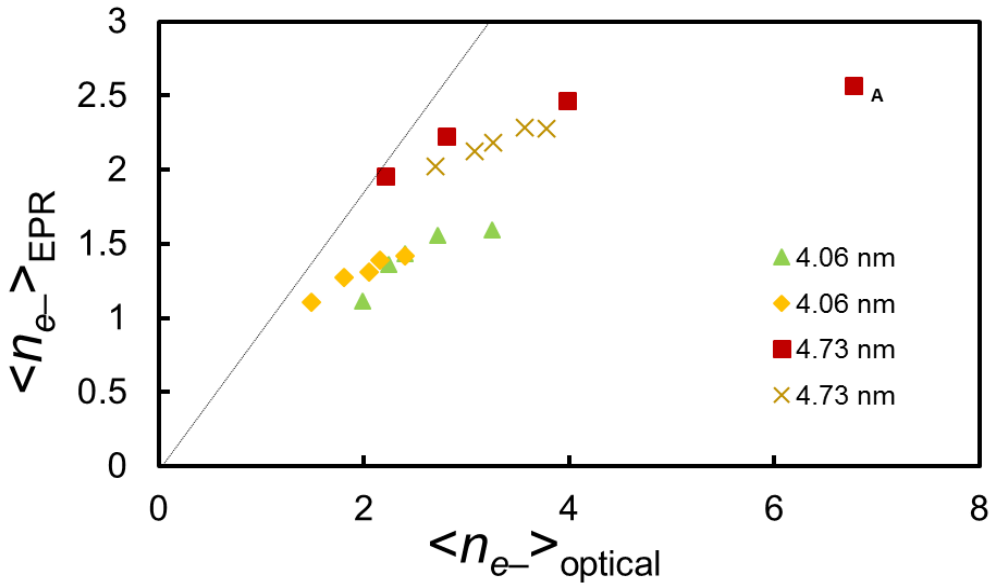

Figure 5.30. $\langle n_{e^-}\rangle_{EPR}$ plotted against $\langle n_{e^-}\rangle$ obtained from the optical spectrafor two sizes of NCs. The dotted line depicts the 1:1 relationship between $\langle n_{e^-}\rangle_{EPR}$ and $\langle n_{e^-}\rangle_{optical}$.

A possible explanation for the surprisingly small value of $\langle n_{e^-}\rangle_{EPR}$ at higher values of $\langle n_{e^-}\rangle$ is that perhaps TEMPO is not an ideal standard for electrons in ZnO NCs. The proximity of the spins in the interior of the NC likely gives rise to spin-spin interactions, which is likely the cause of line broadening in the EPR spectra. It is also likely that the spins are paired in the NCs, decreasing the total observed signal by EPR, but not by optical spectroscopy. However, spin pairing cannot completely explain the small value of $\langle n_{e^-}\rangle_{EPR}$ because point A gives $(\langle n_{e^-}\rangle) \sim 6$, which, with spin pairing of all of the electrons, should give a value of $\langle n_{e^-}\rangle_{EPR} \geq 3$. Temperature may also be an issue because all of the data were recorded at 25 °C, and cooler temperatures may enable a more accurate counting of spins. A similar discussion was described by Liu et al for photochemically reduced NCs, where some curvature in integrated EPR intensity was observed at higher $\langle n_{e^-}\rangle$.[3] They fit the data to a Poissonian filling model including conduction band states with *S*, *P*, and *D* symmetries. We note that $\langle n_{e^-}\rangle_{EPR}$ is in general higher for $CoCp^*_2$/acid reduced NCs than for photochemically reduced NCs, as discussed more extensively in Chapter 4.

5.11 Discussion of Diffusion of H in ZnO

A recurring question in this system is how quickly a proton delivered to the surface of the NCs would be able to diffuse into the NC lattice. In 2006, Nickel stated that in the diffusion of

hydrogen (gas) through ZnO, electrons are more mobile than protons. Therefore electrons diffuse quickly through the lattice and pull the protons along with them. We imagine this could be possible in our system. However, most of the rates of diffusion through nanomaterials are measured in the bulk and at high temperatures and the best we can do is to extrapolate these rates to the nanoscale. Let's take two specific examples of hydrogen diffusion through ZnO. The first, from Thomas and Lander in 1956 where the diffusion coefficient of hydrogen gas in crystalline ZnO was measured from 200 to 650 °C by monitoring changes in the conductivity. The diffusion rate is represented by the classic model of diffusion through an infinite cylinder, in units of cm^2s^{-1}. The diffusion rate varies as a function of temperature, following Equation (5.5).

$$2D = 0.063e^{\frac{-0.91e}{kT}} \tag{5.5}$$

where D is the diffusion constant, e is the elementary charge (in C), k is the Boltzmann constant (in J/K) and T is the temperature. 0.91 eV is E_A, the activation barrier for hydrogen moving through the lattice.

Extrapolating the temperature to 298 K gives a diffusion rate of 2.6×10^{-17} cm^2s^{-1}, or 2.6×10^{-3} nm^2s^{-1}. The mean-squared distance from a single point, x^2, can be related to the two-dimensional diffusion constant[31] according to:

$$< x^2 >= 4Dt \tag{5.6}$$

Assuming that the nanocrystal r = 1.5 nm, solving for t gives approximately 7 minutes for the time it takes for a proton to diffuse over a distance of 1.5 nm.

In 2006 Nickel explored the diffusion of hydrogen through single crystal and polycrystalline ZnO using secondary-ion mass spectrometry (SIMS).[31] For single crystal ZnO, where hydrogen can diffuse faster presumably because it avoids lattice disorder of a polycrystalline material, the diffusion of hydrogen also varies with temperature with a drastically shallower slope of E_A = 0.23 eV.[31] The extrapolated diffusion rate to 298 K gives $D = 1.8 \times 10^{-12}$ cm^2s^{-1}, which corresponds to 3×10^{-3} s to move across a nanocrystal with r = 1.5 nm.

These two studies were done at much higher temperatures than 298 K and give relatively different rates of diffusion of hydrogen through ZnO (7 minutes vs. 3 x 10^{-3} s). However, it is reasonable to conclude that diffusion of protons through small ZnO NCs can occur on the timescale of many of the experiments described here. This assumption should be more accurately

validated with nanocrystalline ZnO, but is useful to consider when analyzing experiments with ZnO.

5.12 Stopped-Flow Reactions with ZnO and $CoCp^*_2$

The majority of the experiments described with the ZnO NCs in this thesis were done under thermodynamic conditions, where we wait until the reaction has completed before collecting measurements. In an attempt to determine the rate of electron injection into the NCs, single mixing stopped-flow optical absorbance spectroscopy was performed. With the help of Miles Braten, stopped flow experiments were used to monitor the reduction of ZnO NCs with $CoCp^*_2$ in toluene using a TgK Double Mixing Cryo Stopped-Flow spectrometer at 0°C and 25°C.

An excess of $CoCp^*_2$ was used relative to the NCs so that the conditions were pseudo-first order (3.9 mM after mixing, 26 equiv per NC). The concentration of NCs was 0.15 mM after dilution in the stopped flow for all spectra discussed here. The absorbance spectra were monitored with $CoCp^*_2$ added to toluene only, and then added to NCs at 0 °C (Figure 5.31) and 25 °C (Figure 5.32). The absorbances at 700 nm and 525 nm were monitored for the absorption of reduced ZnO NCs and the disappearance of $CoCp^*_2$, respectively. Time traces at each wavelength are plotted in Figure 5.33 and Figure 5.34, and for reference, for the control without NCs (Figure 5.35).

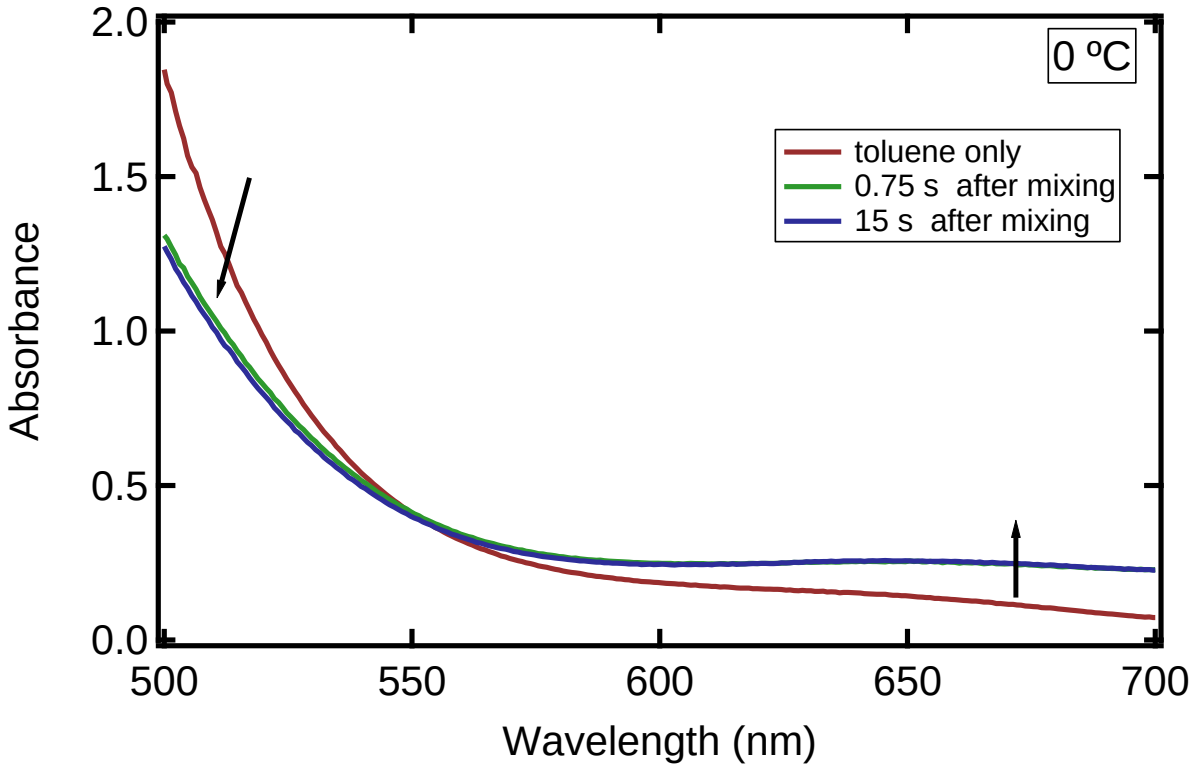

Figure 5.31. Stopped flow optical spectra of $CoCp^*_2$ (3.85 mM after mixing) at 0 °C with the addition of toluene only (red), and ZnO NCs (d = 4.0 nm, 1.5×10^{-4} M after mixing) after 0.75 s (green) and 15 s (blue) after mixing. The tail of a peak from 500 to 550 nm is attributed to $CoCp^*_2$, and the growth of a signal from 550 to longer wavelengths is attributed to electrons in the conduction band of reduced ZnO NCs.

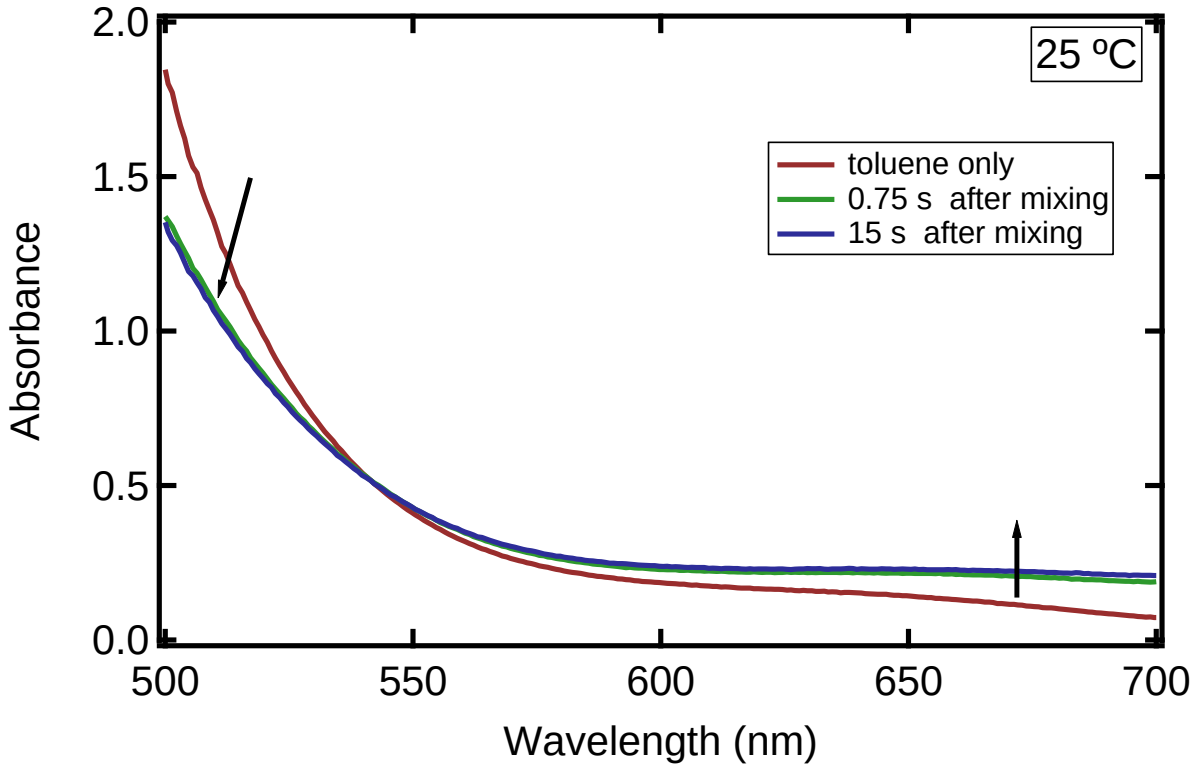

Figure 5.32. Similar to Figure 5.31 above but at room temperature. Stopped flow optical spectra of $CoCp^*_2$ (3.85 mM after mixing) at 25 °C with the addition of toluene only (red), and ZnO NCs (d = 4.0 nm, 1.5×10^{-4} M after mixing) after 0.75 s (green) and 15 s (blue) after mixing. The tail of a peak from 500 to 550 nm is attributed to $CoCp^*_2$, and the growth of a signal from 550 to longer wavelengths is attributed to electrons in the conduction band of reduced ZnO NCs.

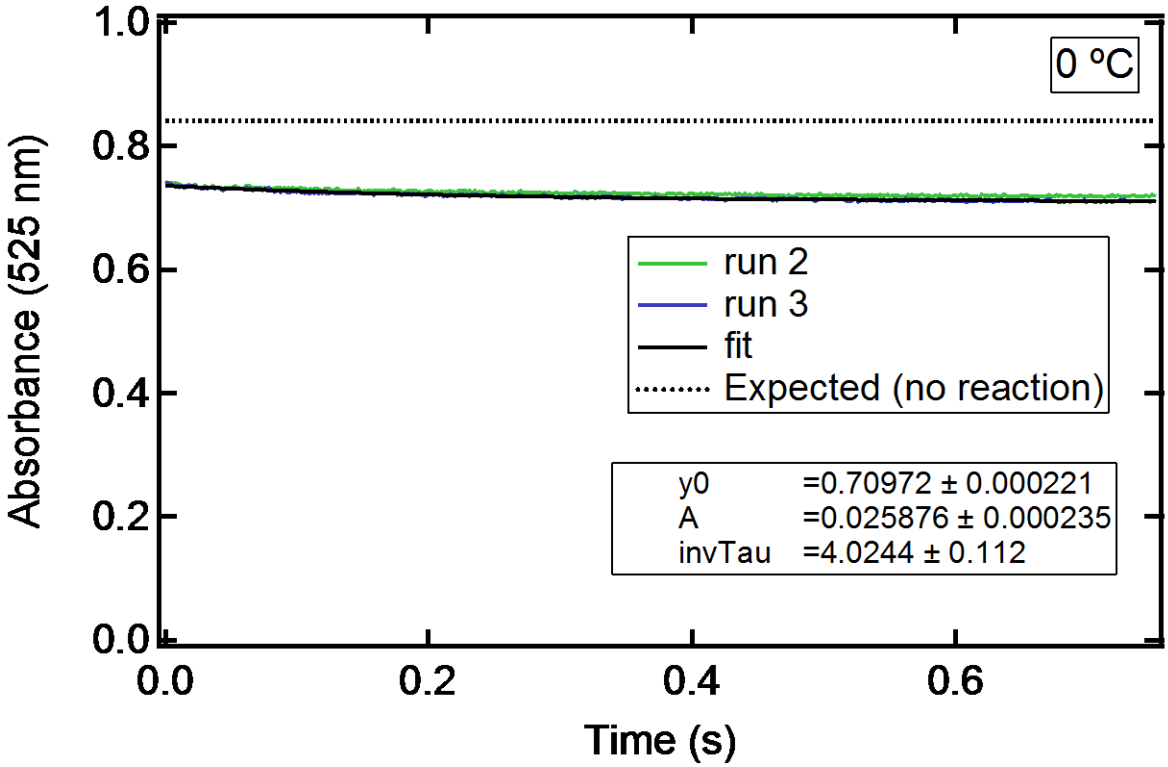

Figure 5.33. Time trace of the absorbance at 525 nm monitored for the reaction of $CoCp^*_2$ (3.85 mM after mixing) and ZnO NCs (d = 4.0 nm, 1.5×10^{-4} M after mixing) shown in Figure 5.31. The absorbance slowly decreases and is fit to an exponential with $k = 1 \times 10^3$ $M^{-1}s^{-1}$. The dotted line at Absorbance = 0.82 corresponds to the expected value if no reaction occurred.

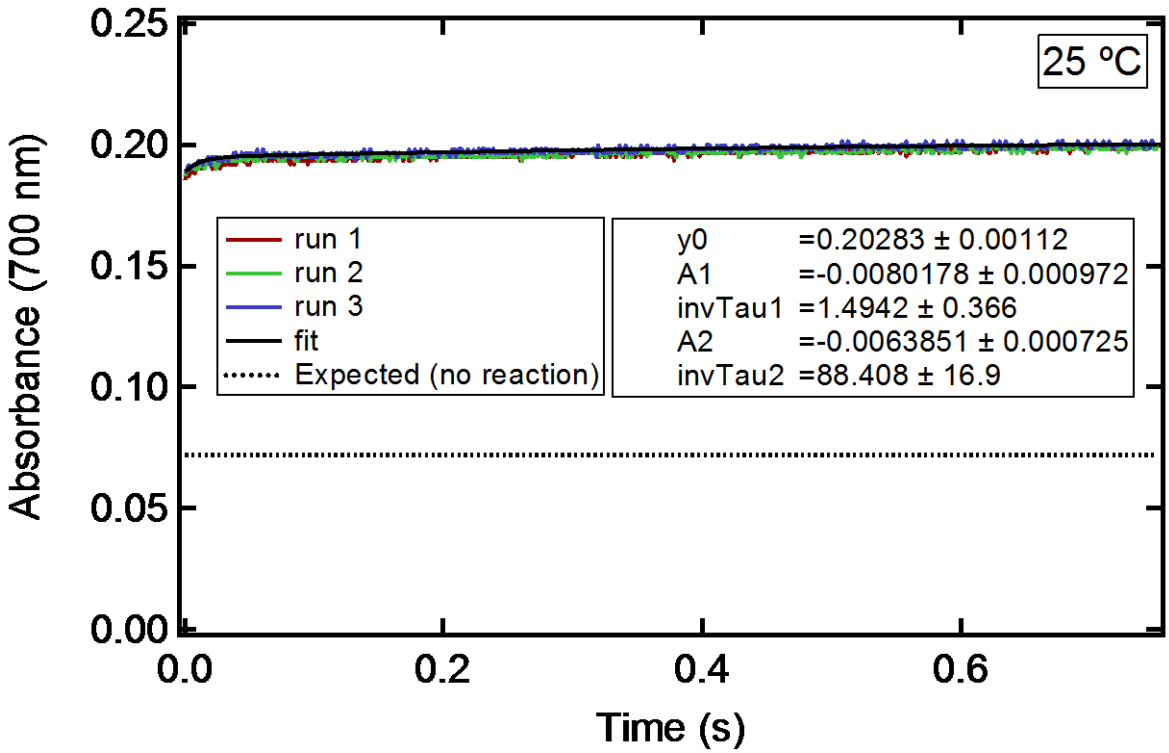

Figure 5.34. Absorbance at 700 nm for the reaction of $CoCp^*_2$ (3.85 mM after mixing) and ZnO NCs (d = 4.0 nm, 1.5×10^{-4} M after mixing) monitored over time (compared to final spectra shown in Figure 5.32). The increase of absorbance at 700 nm is attributed to electrons in ZnO NCs. At the first data point, the reaction is >85% complete. The dotted line at Absorbance = 0.07 corresponds to the expected value if no reaction occurred.

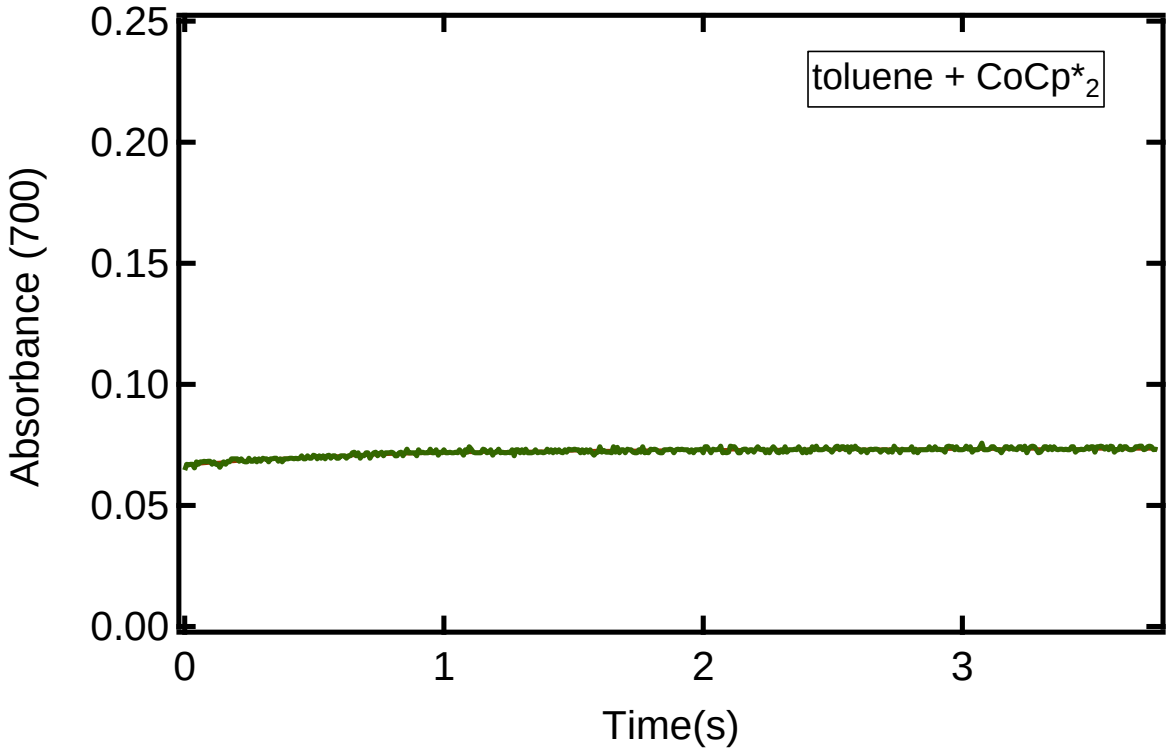

Figure 5.35. Absorbance at 700 nm for the reaction of $CoCp^*_2$ (3.85 mM after mixing) and toluene only, monitored over time. The absorbance is essentially unchanged over the entire time period.

For all of the conditions studied, we find that the reaction between ZnO NCs and $CoCp^*_2$ is approximately 90% complete within the time of mixing. Given the mixing time of the stopped flow (1 ms), the rate constant for the pseudo first-order reaction must be greater than 10^6 M^{-1} s^{-1}. A faster technique must be used to measure the rate of this reaction.

5.13 Discussion of Diffusion Rate of Nanoparticles and Small Molecules

This section was devised with Professor James Mayer in 2012 to address our questions about rates of diffusion of nanoparticles. In general, larger objects will diffuse slower in solution than smaller objects, according to the Stokes-Einstein equation (see below). We wondered how the rate of reaction of nanoparticles would be affected by their size. Of course we note that these

simple calculations do not approach the more complicated topics of ionic diffusion (where species in solution are charged), nanoparticle ligand effects, etc.

5.13.1 *Case 1: Reactions of Two Similar Sized Objects*

The rate constant of a diffusion-controlled reaction, describing in particular a reaction at the boundary condition where when A comes into contact with B, a reaction occurs, and that the reactants are always replenished, is described below in Equation (5.7):[32]

$$k_d = 4\pi\left(D_A + D_B\right)\left(r_A + r_B\right)N_A \tag{5.7}$$

where $D_{A/B}$ is the diffusion coefficients of the each species in solution and $r_{A/B}$ is the radius of each species. The sum of radii (r_A+r_B) is also commonly referred to as the "reaction radius", or R', and N_A is included to convert the units to the standard $M^{-1}s^{-1}$.

The magnitude of a diffusion constant can be estimated by the Stokes-Einstein relation, Equation (5.8) for the diffusion of spherical species in a solution with low Reynold's number:

$$D = \frac{k_B T}{6\pi\eta r} \tag{5.8}$$

where D is the diffusion coefficient, η is the viscosity of the medium, an r is the radius of the spherical particle.

We assume the validity of Stokes-Einstein relation, and this agrees with the measurements discussed in Chapter 2. Then rate constant for a diffusion controlled reaction of two nanoparticles of the same size (r_A = r_B), then the reaction radius R'= $2r_{A/B}$, that react when they touch at a distance $2r_{A/B}$ is given by:

$$k_d = 4\pi N_A\left(2r_{A/B}\right)\left(\frac{k_B T}{6\pi\eta r_{A/B}} + \frac{k_B T}{6\pi\eta r_{A/B}}\right) \tag{5.9}$$

$$k_d = \frac{8}{3}N_A\left(\frac{k_B T}{\eta}\right) \tag{5.10}$$

This predicts that the diffusion-limited rate constant is roughly *independent of the radius of the particle*. The slower diffusion of the larger nanoparticles is compensated by the fact that they react at a larger separation. If this analysis is correct, the diffusion limited rate constant for molecular species (ca. 10^{10} M^{-1} s^{-1}) will also apply to nanoparticles.

5.13.2 *Case 2: Reactions of a Nanoparticle with a Small Molecule*

Consider a nanoparticle with diffusion constant D_P and radius r_P, and a small molecule with diffusion constant D_m and radius r_m. Then the reacting radius R' is roughly $r_P + r_m$ and Equation (5.7) becomes:

$$k_d = 4\pi N_A \left(r_p + r_m\right)\left(D_p + D_m\right) \tag{5.11}$$

Using Stokes-Einstein for the diffusion constants gives:

$$k_d = 4\pi N_A \left(r_p + r_m\right)\left(\frac{k_B T}{6\pi\eta}\right)\left(\frac{1}{r_p} + \frac{1}{r_m}\right) \tag{5.12}$$

$$k_d = \frac{2}{3} N_A \left(\frac{k_B T}{\eta}\right)\left(2 + \frac{r_m}{r_p} + \frac{r_p}{r_m}\right) \tag{5.13}$$

When r_P is, for instance, ten times larger r_m,

$$k_d = \frac{2}{3} N_A \left(\frac{k_B T}{\eta}\right)\left(2 + 0.1 + 10\right) = \frac{24.2}{3} N_A \left(\frac{k_B T}{\eta}\right) \tag{5.14}$$

This gives the counterintuitive result that the diffusion limit is *three times faster* (24.2/3 versus 8/3 in Equation (5.10) as the coefficient) for a nanoparticle + molecule reaction with a tenfold difference in size vs. the reaction of two nanoparticles or of two small molecules. This occurs because the diffusion is dominated by the small molecule while the larger nanoparticle radius means that the molecule does not have to diffuse as far.

It should be emphasized that there are uncertainties in the application of Stokes-Einstein, and that the equation for a diffusion limited rate constant is only approximate. So while the numerical result (factor of three for 10:1 particle sizes) is approximate, it seems likely that the

diffusion limit for unequal sized particles is larger than that for equal particles. This has been discussed similarly for proteins interacting with small molecules.[33]

To be more specific, using 2D ^{1}H diffusion-ordered NMR the approximate diffusion coefficients of nanoparticles and small molecules (ferrocene) are directly measured (Table 5.1). These measurements can be used to estimate the diffusion-limited rates for each reaction in toluene without using the Stokes-Einstein relation. By this calculation, the diffusion-limited rate is at least three times faster for the reaction between a nanoparticle and a small molecule than of either species alone, as predicted above, and the rates of similar species are similar.

Table 5.1. Calculated diffusion-limited rate constants for nanoparticles.

*	R' (r_A+r_B) (m)	ΣD (m^2s^{-1})	k_D ($M^{-1}s^{-1}$)
Nanoparticle+Nanoparticle	6×10^{-9}	1.8×10^{-10}	8.17×10^{9}
Ferrocene+Ferrocene	6×10^{-10}	4×10^{-9}	1.82×10^{10}
Nanoparticle+Ferrocene	3.3×10^{-9}	2.1×10^{-9}	5.24×10^{10}

*The k_D was determined using $k_D = 4\pi R'(D_A+D_B)N_A$, where the estimated radii are based on a d = 6 nm nanoparticle and the accepted hydrodynamic diameter of 0.6 nm for ferrocene.[34] Diffusion coefficients for ferrocene and ZnO nanoparticles capped by dodecylamine were 2×10^{-9} m^2s^{-1} and 9×10^{-11} m^2s^{-1}, respectively, and were an average of three DOSY experiments in toluene-d_8.

5.14 Notes to Chapter 5

(1) Schimpf, A. M.; Thakkar, N.; Gunthardt, C. E.; Masiello, D. J.; Gamelin, D. R. *ACS Nano* **2013**, *8*, 1065.

(2) Koelle, U.; Moser, J.; Graetzel, M. *Inorg. Chem.* **1985**, *24*, 2253.

(3) Liu, W. K.; Whitaker, K. M.; Smith, A. L.; Kittilstved, K. R.; Robinson, B. H.; Gamelin, D. R. *Phys. Rev. Lett.* **2007**, *98*, 186804.

(4) Chávez, I.; Alvarez-Carena, A.; Molins, E.; Roig, A.; Maniukiewicz, W.; Arancibia, A.; Arancibia, V.; Brand, H.; Manuel Manríquez, J. *J. Organomet. Chem.* **2000**, *601*, 126.

(5) Schrauben, J. N.; Hayoun, R.; Valdez, C. N.; Braten, M.; Fridley, L.; Mayer, J. M. *Science* **2012**, *336*, 1298.

(6) Warren, J. J.; Tronic, T. A.; Mayer, J. M. *Chem. Rev.* **2010**, *110*, 6961.

(7) Manner, V. W.; Markle, T. F.; Freudenthal, J. H.; Roth, J. P.; Mayer, J. M. *Chem. Commun.* **2008**, 256.

(8) Germeau, A.; Roest, A.; Vanmaekelbergh, D.; Allan, G.; Delerue, C.; Meulenkamp, E. *Phys. Rev. Lett.* **2003**, *90*, 097401.

(9) Gamelin, D. R., Personal Communication.

(10) Schimpf, A. M.; Gunthardt, C. E.; Rinehart, J. D.; Mayer, J. M.; Gamelin, D. R. *J. Am. Chem. Soc.* **2013**, *135*, 16569.

(11) Meulenkamp, E. A. *J. Phys. Chem. B* **1998**, *102*, 5566.

(12) Schwesinger, R.; Schlemper, H.; Hasenfratz, C.; Willaredt, J.; Dambacher, T.; Breuer, T.; Ottaway, C.; Fletschinger, M.; Boele, J.; Fritz, H.; Putzas, D.; Rotter, H. W.; Bordwell, F. G.; Satish, A. V.; Ji, G.-Z.; Peters, E.-M.; Peters, K.; von Schnering, H. G.; Walz, L. *Liebigs Annalen* **1996**, *1996*, 1055.

(13) Boileau, S.; Illy, N. *Prog. Polym. Sci.* **2011**, *36*, 1132.

(14) Haram, S. K.; Quinn, B. M.; Bard, A. J. *J. Am. Chem. Soc.* **2001**, *123*, 8860.

(15) Guyot-Sionnest, P.; Wang, C. *J. Phys. Chem. B* **2003**, *107*, 7355.

(16) White, M. A.; Weaver, A. L.; Beaulac, R.; Gamelin, D. R. *ACS Nano* **2011**, *5*, 4158.

(17) Chatt, J.; Dilworth, J. R.; Richards, R. L. *Chem. Rev.* **1978**, *78*, 589.

(18) Kumar, B.; Llorente, M.; Froehlich, J.; Dang, T.; Sathrum, A.; Kubiak, C. P. *Annu. Rev. Phys. Chem.* **2012**, *63*, 541.

(19) Samanta, A.; Zhao, A.; Shimizu, G. K. H.; Sarkar, P.; Gupta, R. *Ind. Eng. Chem. Res.* **2012**, *51*, 1438.

(20) Ma, J.; Sun, N.; Zhang, X.; Zhao, N.; Xiao, F.; Wei, W.; Sun, Y. *Catal. Today* **2009**, *148*, 221.

(21) Sakakura, T.; Choi, J.-C.; Yasuda, H. *Chem. Rev.* **2007**, *107*, 2365.

(22) Wambach, J.; Baiker, A.; Wokaun, A. *Phys. Chem. Chem. Phys.* **1999**, *1*, 5071.

(23) Yu, J.; Yu, X. *Environmental Science & Technology* **2008**, *42*, 4902.

(24) Yahaya, A. H.; Gondal, M. A.; Hameed, A. *Chem. Phys. Lett.* **2004**, *400*, 206.

(25) Wan, L.; Wang, X.; Yan, S.; Yu, H.; Li, Z.; Zou, Z. *CrystEngComm* **2012**, *14*, 154.

(26) Navalón, S.; Dhakshinamoorthy, A.; Álvaro, M.; Garcia, H. *ChemSusChem* **2013**, *6*, 562.

(27) Cohn, A. W.; Kittilstved, K. R.; Gamelin, D. R. *J. Am. Chem. Soc.* **2012**, *134*, 7937.

(28) Côté, A.; Charette, A. B. *J. Am. Chem. Soc.* **2008**, *130*, 2771.

(29) Monge, M.; Kahn, M. L.; Maisonnat, A.; Chaudret, B. *Angew. Chem. Int. Ed.* **2003**, *42*, 5321.

(30) Meulenkamp, E. A. *J. Phys. Chem. B* **1998**, *102*, 7764.

(31) Nickel, N. H. *Phys. Rev. B* **2006**, *73*, 195204.

(32) Calef, D. F.; Deutch, J. M. *Annu. Rev. Phys. Chem.* **1983**, *34*, 493.

(33) Berg, O. G.; von Hippel, P. H. *Annu. Rev. Biophys. Biophys. Chem.* **1985**, *14*, 131.

(34) Canzi, G.; Mrse, A. A.; Kubiak, C. P. *J. Phys. Chem. C* **2011**, *115*, 7972.

BIBLIOGRAPHY

Anderson, J.; Van de Walle, C. G. *Rep. Prog. Phys.* **2009**, *72*, 126501.

Anderson, N. C.; Hendricks, M. P.; Choi, J. J.; Owen, J. S. *J. Am. Chem. Soc.* **2013**, *135*, 18536.

Anderson, N. C.; Owen, J. S. *Chem. Mater.* **2012**, *25*, 69.

Anikeeva, P. O.; Madigan, C. F.; Halpert, J. E.; Bawendi, M. G.; Bulović, V. *Phys. Rev. B* **2008**, *78*, 085434.

Astruc, D. *Electron Transfer and Radical Processes in Transition-Metal Chemistry*; John Wiley & Sons, Inc.: New York, 1995.

Bahnemann, D. W.; Kormann, C.; Hoffmann, M. R. *J. Phys. Chem.* **1987**, *91*, 3789.

Berg, O. G.; von Hippel, P. H. *Annu. Rev. Biophys. Biophys. Chem.* **1985**, *14*, 131.

Binstead, R. A.; Moyer, B. A.; Samuels, G. J.; Meyer, T. J. *J. Am. Chem. Soc.* **1981**, *103*, 2897.

Boileau, S.; Illy, N. *Prog. Polym. Sci.* **2011**, *36*, 1132.

Bolts, J. M.; Wrighton, M. S. *J. Phys. Chem.* **1976**, *80*, 2641.

Brookhart, M.; Grant, B.; Volpe, A. F. *Organometallics* **1992**, *11*, 3920.

Bruchez, M.; Moronne, M.; Gin, P.; Weiss, S.; Alivisatos, A. P. *Science* **1998**, *281*, 2013.

Bullen, C.; Mulvaney, P. *Langmuir* **2006**, *22*, 3007.

Buonsanti, R.; Llordes, A.; Aloni, S.; Helms, B.; Milliron, D. *Nano Lett.* **2011**, *11*, 4706.

Calef, D. F.; Deutch, J. M. *Annu. Rev. Phys. Chem.* **1983**, *34*, 493.

Canzi, G.; Mrse, A. A.; Kubiak, C. P. *J. Phys. Chem. C* **2011**, *115*, 7972.

Carlsson, P.; Holmstrom, B. *J. Electrochem. Soc.* **1982**, *129*, 1851.

Chatt, J.; Dilworth, J. R.; Richards, R. L. *Chem. Rev.* **1978**, *78*, 589.

Chávez, I.; Alvarez-Carena, A.; Molins, E.; Roig, A.; Maniukiewicz, W.; Arancibia, A.; Arancibia, V.; Brand, H.; Manuel Manríquez, J. *J. Organomet. Chem.* **2000**, *601*, 126.

Chen, J.; Ruther, R. E.; Tan, Y.; Bishop, L. M.; Hamers, R. J. *Langmuir* **2012**, *28*, 10437.

Chennupati Jagadish, S. J. P. *Zinc Oxide Bulk, Thin Films and Nanostructures*; Elsevier Ltd.: Amsterdam, 2006.

Cohn, A. W.; Janßen, N.; Mayer, J. M.; Gamelin, D. R. *J. Phys. Chem. C* **2012**, *116*, 20633.

Cohn, A. W.; Kittilstved, K. R.; Gamelin, D. R. *J. Am. Chem. Soc.* **2012**, *134*, 7937.

Connelly, N. G.; Geiger, W. E. *Chem. Rev.* **1996**, *96*, 877.

Coppel, Y.; Spataro, G.; Pagès, C.; Chaudret, B.; Maisonnat, A.; Kahn, M. L. *Chem. Eur. J.* **2012**, *18*, 5384.

Côté, A.; Charette, A. B. *J. Am. Chem. Soc.* **2008**, *130*, 2771.

De Roo, J.; Van den Broeck, F.; De Keukeleere, K.; Martins, J. C.; Van Driessche, I.; Hens, Z. *J. Am. Chem. Soc.* **2014**.

De Trizio, L.; Buonsanti, R.; Schimpf, A. M.; Llordes, A.; Gamelin, D. R.; Simonutti, R.; Milliron, D. J. *Chem. Mater.* **2013**, *25*, 3383.

Diroll, B. T.; Gordon, T. R.; Gaulding, E. A.; Klein, D. R.; Paik, T.; Yun, H. J.; Goodwin, E. D.; Damodhar, D.; Kagan, C. R.; Murray, C. B. *Chem. Mater.* **2014**, *26*, 4579.

Dorfs, D.; Härtling, T.; Miszta, K.; Bigall, N. C.; Kim, M. R.; Genovese, A.; Falqui, A.; Povia, M.; Manna, L. *J. Am. Chem. Soc.* **2011**, *133*, 11175.

Ekimov, A. I.; Efros, A. L.; Onushchenko, A. A. *Solid State Commun.* **1985**, *56*, 921.

El-Sayed, M. A. *Acc. Chem. Res.* **2004**, *37*, 326.

Evans, C. M.; Cass, L. C.; Knowles, K. E.; Tice, D. B.; Chang, R. P. H.; Weiss, E. A. *J. Coord. Chem.* **2012**, *65*, 2391.

Semiconductor Electrodes; Finklea, H. O., Ed.; Elsevier: New York, NY, 1988; Vol. 55.

Proton-coupled Electron Transfer: A Carrefour for Chemical Reactivity Traditions; Formosinho, S.; Barroso, M., Eds.; Royal Society of Chemistry: Cambridge, U.K., 2012.

Fritzinger, B.; Moreels, I.; Lommens, P.; Koole, R.; Hens, Z.; Martins, J. C. *J. Am. Chem. Soc.* **2009**, *131*, 3024.

Fujishima, A.; Zhang, X.; Tryk, D. A. *Surf. Sci. Rep.* **2008**, *63*, 515.

Gamelin, D. R., Personal Communication.

Gerischer, H. *Electrochim. Acta* **1989**, *34*, 1005.

Germeau, A.; Roest, A.; Vanmaekelbergh, D.; Allan, G.; Delerue, C.; Meulenkamp, E. *Phys. Rev. Lett.* **2003**, *90*, 097401.

Gomes, R.; Hassinen, A.; Szczygiel, A.; Zhao, Q.; Vantomme, A.; Martins, J. C.; Hens, Z. *J. Phys. Chem. Lett.* **2011**, *2*, 145.

Goodenough, J. B.; Kim, Y. *Chem. Mater.* **2010**, *22*, 587.

Gratzel, M. *Nature* **2001**, *414*, 338.

Green, M. *J. Mater. Chem.* **2010**, *20*, 5797.

Guyot-Sionnest, P.; Wang, C. *J. Phys. Chem. B* **2003**, *107*, 7355.

Haase, M.; Weller, H.; Henglein, A. *J. Phys. Chem.* **1988**, *92*, 482.

Hamann, T. W.; Gstrein, F.; Brunschwig, B. S.; Lewis, N. S. *Chem. Phys.* **2006**, *326*, 15.

Hammes-Schiffer, S. *Chem. Rev.* **2010**, *110*, 6937.

Haram, S. K.; Quinn, B. M.; Bard, A. J. *J. Am. Chem. Soc.* **2001**, *123*, 8860.

Harris, C.; Kamat, P. V. *ACS Nano* **2010**, *4*, 7321.

Hassinen, A.; Gomes, R.; De Nolf, K.; Zhao, Q.; Vantomme, A.; Martins, J. C.; Hens, Z. *J. Phys. Chem. C* **2013**, *117*, 13936.

Hassinen, A.; Moreels, I.; De Nolf, K.; Smet, P. F.; Martins, J. C.; Hens, Z. *J. Am. Chem. Soc.* **2012**, *134*, 20705.

Hayoun, R., University of Washington, 2011.

Hayoun, R. *Studies of Metal Oxides in Organic Redox Reactions: Zinc Oxide Nanoparticles as Chemical Reductants in Electron Transfer and Hydrogen Atom Transfer Reactions and the Use of Osmium Tetroxide to Oxidize Higher Alkanes*, Ph.D. Thesis, University of Washington, 2011.

Hayoun, R.; Whitaker, K. M.; Gamelin, D. R.; Mayer, J. M. *J. Am. Chem. Soc.* **2011**, *133*, 4228.

Henrich, V. E.; Cox, P. A. *The Surface Science of Metal Oxides*; Press Syndicate of the University of Cambridge: Cambridge, 1994.

Hens, Z.; Martins, J. C. *Chem. Mater.* **2013**, *25*, 1211.

Hens, Z.; Moreels, I.; Martins, J. C. *ChemPhysChem* **2005**, *6*, 2578.

Hinterwirth, H.; Kappel, S.; Waitz, T.; Prohaska, T.; Lindner, W.; Lämmerhofer, M. *ACS Nano* **2013**, *7*, 1129.

Hoffmann, M. R.; Martin, S. T.; Choi, W.; Bahnemann, D. W. *Chem. Rev.* **1995**, *95*, 69.

Hofmann, D. M.; Hofstaetter, A.; Leiter, F.; Zhou, H.; Henecker, F.; Meyer, B. K.; Orlinskii, S. B.; Schmidt, J.; Baranov, P. G. *Phys. Rev. Lett.* **2002**, *88*, 045504.

Hoyer, P.; Weller, H. *Chem. Phys. Lett.* **1994**, *221*, 379.

Huss, A. S.; Bierbaum, A.; Chitta, R.; Ceckanowicz, D. J.; Mann, K. R.; Gladfelter, W. L.; Blank, D. A. *J. Am. Chem. Soc.* **2010**, *132*, 13963.

Ip, K.; Overberg, M. E.; Heo, Y. W.; Norton, D. P.; Pearton, S. J.; Stutz, C. E.; Luo, B.; Ren, F.; Look, D. C.; Zavada, J. M. *Appl. Phys. Lett.* **2003**, *82*, 385.

Jagadish, C.; Pearton, S. J. *Zinc Oxide Bulk, Thin Films and Nanostructures*; Elsevier Ltd.: Amsterdam, 2006.

Jakob, M.; Levanon, H.; Kamat, P. V. *Nano Lett.* **2003**, *3*, 353.

Jeong, K. S.; Deng, Z.; Keuleyan, S.; Liu, H.; Guyot-Sionnest, P. *J. Phys. Chem. Lett.* **2014**, *5*, 1139.

Jha, P. P.; Guyot-Sionnest, P. *ACS Nano* **2009**, *3*, 1011.

Kalyuzhny, G.; Murray, R. W. *J. Phys. Chem. B* **2005**, *109*, 7012.

Kambe, S.; Nakade, S.; Kitamura, T.; Wada, Y.; Yanagida, S. *J. Phys. Chem. B* **2002**, *106*, 2967.

Kanehara, M.; Koike, H.; Yoshinaga, T.; Teranishi, T. *J. Am. Chem. Soc.* **2009**, *131*, 17736.

Katari, J. E. B.; Colvin, V. L.; Alivisatos, A. P. *J. Phys. Chem.* **1994**, *98*, 4109.

Khan, M. M.; Adil, S. F.; Al-Mayouf, A. *J. Saudi Chem. Soc.* **2015**, *19*, 462.

Klimov, V. I.; McGuire, J. A.; Schaller, R. D.; Rupasov, V. I. *Phys. Rev. B* **2008**, *77*, 195324.

Klimov, V. I.; Mikhailovsky, A. A.; McBranch, D. W.; Leatherdale, C. A.; Bawendi, M. G. *Science* **2000**, *287*, 1011.

Klingshirn, C. *Chemphyschem* **2007**, *8*, 782.

Knowles, K. E.; Tagliazucchi, M.; Malicki, M.; Swenson, N. K.; Weiss, E. A. *J. Phys. Chem. C* **2013**, *117*, 15849.

Koch, U.; Fojtik, A.; Weller, H.; Henglein, A. *Chem. Phys. Lett.* **1985**, *122*, 507.

Koelle, U.; Moser, J.; Graetzel, M. *Inorg. Chem.* **1985**, *24*, 2253.

Koh, W.-k.; Koposov, A. Y.; Stewart, J. T.; Pal, B. N.; Robel, I.; Pietryga, J. M.; Klimov, V. I. *Sci. Rep.* **2013**, *3*, 2004.

Kumar, B.; Llorente, M.; Froehlich, J.; Dang, T.; Sathrum, A.; Kubiak, C. P. *Annu. Rev. Phys. Chem.* **2012**, *63*, 541.

Kuno, M.; Lee, J. K.; Dabbousi, B. O.; Mikulec, F. V.; Bawendi, M. G. *J. Chem. Phys.* **1997**, *106*, 9869.

Le Bras, J.; Jiao, H.; Meyer, W. E.; Hampel, F.; Gladysz, J. A. *J. Organomet. Chem.* **2000**, *616*, 54.

Lemon, B. I.; Hupp, J. T. *J. Phys. Chem. B* **1997**, *101*, 2426.

Lemon, B. I.; Hupp, J. T. *J. Phys. Chem.* **1996**, *100*, 14578.

Lemon, B. I.; Lyon, L. A.; Hupp, J. T. *In Nanoparticles and Nanostructured Films: Preparation, Characterization, and Applications*; Wiley–VCH: New York, 1998.

Liang, X.; Ren, Y.; Bai, S.; Zhang, N.; Dai, X.; Wang, X.; He, H.; Jin, C.; Ye, Z.; Chen, Q.; Chen, L.; Wang, J.; Jin, Y. *Chem. Mater.* **2014**.

Liu, H.; Keuleyan, S.; Guyot-Sionnest, P. *J. Phys. Chem. C* **2011**, *116*, 1344.

Liu, W. K.; Whitaker, K. M.; Kittilstved, K. R.; Gamelin, D. R. *J. Am. Chem. Soc.* **2006**, *128*, 3910.

Liu, W. K.; Whitaker, K. M.; Smith, A. L.; Kittilstved, K. R.; Robinson, B. H.; Gamelin, D. R. *Phys. Rev. Lett.* **2007**, *98*, 186804.

Lommens, P.; Lambert, K.; Loncke, F.; De Muynck, D.; Balkan, T.; Vanhaecke, F.; Vrielinck, H.; Callens, F.; Hens, Z. *ChemPhysChem* **2008**, *9*, 484.

Look, D. C. *Mater. Sci. Eng., B* **2001**, *80*, 383.

Lyon, L. A.; Hupp, J. T. *J. Phys. Chem. B* **1999**, *103*, 4623.

Lyon, L. A.; Hupp, J. T. *J. Phys. Chem. B* **1999**, *103*, 4623.

Ma, J.; Sun, N.; Zhang, X.; Zhao, N.; Xiao, F.; Wei, W.; Sun, Y. *Catal. Today* **2009**, *148*, 221.

Madelung, O. *Semiconductors: Data Handbook*; 3rd ed.; Springer: New York, 2004.

Majetich, S. A.; Carter, A. C.; Belot, J.; McCullough, R. D. *J. Phys. Chem.* **1994**, *98*, 13705.

Manner, V. W.; Markle, T. F.; Freudenthal, J. H.; Roth, J. P.; Mayer, J. M. *Chem. Commun.* **2008**, 256.

Manthiram, K.; Alivisatos, A. *J. Am. Chem. Soc.* **2012**, *134*, 3995.

Mayer, J. M. *Acc. Chem. Res.* **2011**, *44*, 36.

McCleverty, J. A.; Meyer, T. J. *Comprehensive Coordination Chemistry II*; Elsevier Ltd.: Oxford, UK, 2004; Vol. 6.

Meulenkamp, E. A. *J. Phys. Chem. B* **1998**, *102*, 7764.

Meulenkamp, E. A. *J. Phys. Chem. B* **1998**, *102*, 5566.

Monge, M.; Kahn, M. L.; Maisonnat, A.; Chaudret, B. *Angew. Chem. Int. Ed.* **2003**, *42*, 5321.

Morales, M. V.; Asedegbega-Nieto, E.; Iglesias-Juez, A.; Rodríguez-Ramos, I.; Guerrero-Ruiz, A. *ChemSusChem* **2015**, *8*, 2223.

Moreels, I.; Martins, J. C.; Hens, Z. *ChemPhysChem* **2006**, *7*, 1028.

Morris-Cohen, A. J.; Aruda, K. O.; Rasmussen, A. M.; Canzi, G.; Seideman, T.; Kubiak, C. P.; Weiss, E. A. *Phys. Chem. Chem. Phys.* **2012**, *14*, 13794.

Morris-Cohen, A. J.; Donakowski, M. D.; Knowles, K. E.; Weiss, E. A. *J. Phys. Chem. C* **2010**, *114*, 897.

Morris-Cohen, A. J.; Frederick, M. T.; Cass, L. C.; Weiss, E. A. *J. Am. Chem. Soc.* **2011**, *133*, 10146.

Morris-Cohen, A. J.; Malicki, M.; Peterson, M. D.; Slavin, J. W. J.; Weiss, E. A. *Chem. Mater.* **2012**, 1155.

Morrison, S. R. *Electrochemistry at Semiconductor and Oxidized Metal Electrodes*; Plenum Press: New York, 1980.

Munro, A. M.; Jen-La Plante, I.; Ng, M. S.; Ginger, D. S. *J. Phys. Chem. C* **2007**, *111*, 6220.

Murray, R. W. *Acc. Chem. Res.* **1980**, *13*, 135.

Nakagawa, T.; Beasley, C. A.; Murray, R. W. *J. Phys. Chem. C* **2009**, *113*, 12958.

Navalón, S.; Dhakshinamoorthy, A.; Álvaro, M.; Garcia, H. *ChemSusChem* **2013**, *6*, 562.

Nickel, N. H. *Phys. Rev. B* **2006**, *73*, 195204.

Nilsson, M. *J. Magn. Reson.* **2009**, *200*, 296.

Norberg, N. S.; Gamelin, D. R. *J. Phys. Chem. B* **2005**, *109*, 20810.

O'Regan, B. C.; Durrant, J. R. *Acc. Chem. Res.* **2009**, *42*, 1799.

Ochsenbein, S. T.; Feng, Y.; Whitaker, K. M.; Badaeva, E.; Liu, W. K.; Li, X.; Gamelin, D. R. *Nat Nano* **2009**, *4*, 681.

Palomaki, P. K. B.; Miller, E. M.; Neale, N. R. *J. Am. Chem. Soc.* **2013**, *135*, 14142.

Reddy, M. V.; Subba Rao, G. V.; Chowdari, B. V. R. *Chem. Rev.* **2013**, *113*, 5364.

Reed, M. A. *Scientific American* **1993**, *268*, 118.

Roest, A. L.; Germeau, A.; Kelly, J. J.; Vanmaekelbergh, D. l.; Allan, G.; Meulenkamp, E. A. *ChemPhysChem* **2003**, *4*, 959.

Roest, A. L.; Houtepen, A. J.; Kelly, J. J.; Vanmaekelbergh, D. *Faraday Discuss.* **2004**, *125*, 55.

Roest, A. L.; Kelly, J. J.; Vanmaekelbergh, D.; Meulenkamp, E. A. *Phys. Rev. Lett.* **2002**, *89*, 036801.

Rossetti, R.; Nakahara, S.; Brus, L. E. *J. Chem. Phys.* **1983**, *79*, 1086.

Sakakura, T.; Choi, J.-C.; Yasuda, H. *Chem. Rev.* **2007**, *107*, 2365.

Samanta, A.; Zhao, A.; Shimizu, G. K. H.; Sarkar, P.; Gupta, R. *Ind. Eng. Chem. Res.* **2012**, *51*, 1438.

Samson, S.; Fonstad, C. G. *J. Appl. Phys.* **1973**, *44*, 4618.

Sandström, J. *Dynamic NMR Spectroscopy*; Academic Press Inc.: New York, 1982.

Saouma, C. T.; Kaminsky, W.; Mayer, J. M. *J. Am. Chem. Soc.* **2012**, *134*, 7293.

Schaller, R. D.; Agranovich, V. M.; Klimov, V. I. *Nat Phys* **2005**, *1*, 189.

Schimpf, A. M.; Gunthardt, C. E.; Rinehart, J. D.; Mayer, J. M.; Gamelin, D. R. *J. Am. Chem. Soc.* **2013**, *135*, 16569.

Schimpf, A. M.; Ochsenbein, S. T.; Buonsanti, R.; Milliron, D. J.; Gamelin, D. R. *Chem. Commun.* **2012**, *48*, 9352.

Schimpf, A. M.; Thakkar, N.; Gunthardt, C. E.; Masiello, D. J.; Gamelin, D. R. *ACS Nano* **2013**, *8*, 1065.

Schrauben, J. N.; Hayoun, R.; Valdez, C. N.; Braten, M.; Fridley, L.; Mayer, J. M. *Science* **2012**, *336*, 1298.

Schwartz, D. A.; Gamelin, D. R. *Proc SPIE-Int Soc Opt Eng* **2003**, *5224*, 1.

Schwartz, D. A.; Norberg, N. S.; Nguyen, Q. P.; Parker, J. M.; Gamelin, D. R. *J. Am. Chem. Soc.* **2003**, *125*, 13205.

Schwartz, D. A.; Norberg, N. S.; Nguyen, Q. P.; Parker, J. M.; Gamelin, D. R. *J. Am. Chem. Soc.* **2003**, *125*, 13205.

Schwartz, D. A.; Norberg, N. S.; Nguyen, Q. P.; Parker, J. M.; Gamelin, D. R. *J. Am. Chem. Soc.* **2003**, *125*, 13205.

Schwesinger, R.; Schlemper, H.; Hasenfratz, C.; Willaredt, J.; Dambacher, T.; Breuer, T.; Ottaway, C.; Fletschinger, M.; Boele, J.; Fritz, H.; Putzas, D.; Rotter, H. W.; Bordwell, F. G.; Satish, A. V.; Ji, G.-Z.; Peters, E.-M.; Peters, K.; von Schnering, H. G.; Walz, L. *Liebigs Annalen* **1996**, *1996*, 1055.

Shim, M.; Guyot-Sionnest, P. *Nature* **2000**, *407*, 981.

Shim, M.; Guyot-Sionnest, P. *J. Am. Chem. Soc.* **2001**, *123*, 11651.

Smith, A. M.; Nie, S. *Acc. Chem. Res.* **2009**, *43*, 190.

Song, B.; Reuber, J.; Ochs, C.; Hahn, F. E.; Lügger, T.; Orvig, C. *Inorg. Chem.* **2001**, *40*, 1527.

Stiefel, E. I. *Proc. Natl. Acad. Sci. USA* **1973**, *70*, 988.

Strzhemechny, Y. M.; Mosbacker, H. L.; Look, D. C.; Reynolds, D. C.; Litton, C. W.; Garces, N. Y.; Giles, N. C.; Halliburton, L. E.; Niki, S.; Brillson, L. J. *Appl. Phys. Lett.* **2004**, *84*, 2545.

Talapin, D. V.; Lee, J.-S.; Kovalenko, M. V.; Shevchenko, E. V. *Chem. Rev.* **2010**, *110*, 389.

Theys, B.; Sallet, V.; Jomard, F.; Lusson, A.; Rommeluère, J.-F.; Teukam, Z. *J. Appl. Phys.* **2002**, *91*, 3922.

Thomas, D. G.; Lander, J. J. *J. Chem. Phys.* **1956**, *25*, 1136.

Tian, J.; Cao, G. *Nano Rev* **2013**, *4*, 22578.

Valdez, C. N.; Braten, M.; Soria, A.; Gamelin, D. R.; Mayer, J. M. *J. Am. Chem. Soc.* **2013**, *135*, 8492.

Valdez, C. N.; Schimpf, A. M.; Gamelin, D. R.; Mayer, J. M. *ACS Nano* **2014**, *8*, 9463.

Van de Walle, C. G. *Phys. Rev. Lett.* **2000**, *85*, 1012.

Vohs, J. M. *Chem. Rev.* **2012**, *113*, 4136.

Wambach, J.; Baiker, A.; Wokaun, A. *Phys. Chem. Chem. Phys.* **1999**, *1*, 5071.

Wan, L.; Wang, X.; Yan, S.; Yu, H.; Li, Z.; Zou, Z. *CrystEngComm* **2012**, *14*, 154.

Wang, L.-Q.; Zhou, X.-D.; Exarhos, G. J.; Pederson, L. R.; Wang, C.; Windisch, J. C. F.; Yao, C. *Appl. Phys. Lett.* **2007**, *91*, 173107.

Wang, T.; Radovanovic, P. V. *J. Phys. Chem. C* **2011**, *115*, 406.

Warren, J. J.; Tronic, T. A.; Mayer, J. M. *Chem. Rev.* **2010**, *110*, 6961.

Wehrenberg, B. L.; Guyot-Sionnest, P. *J. Am. Chem. Soc.* **2003**, *125*, 7806.

Weiss, E. A. *Acc. Chem. Res.* **2013**, *46*, 2607.

Wheeler, L. M.; Neale, N. R.; Chen, T.; Kortshagen, U. R. *Nat. Commun.* **2013**, *4*, 2197.

Whitaker, K. M.; Ochsenbein, S. T.; Polinger, V. Z.; Gamelin, D. R. *J. Phys. Chem. C* **2008**, *112*, 14331.

White, M. A.; Weaver, A. L.; Beaulac, R.; Gamelin, D. R. *ACS Nano* **2011**, *5*, 4158.

Wilkinson, G.; Gillard, R. D.; McCleverty, J. A. *Comprehensive Coordination Chemistry*; Pergamon Books Ltd.: Great Britain, 1987; Vol. 5.

Wood, A.; Giersig, M.; Hilgendorff, M.; Vilas-Campos, A.; Liz-Marzán, L. M.; Mulvaney, P. *Aust. J. Chem.* **2003**, *56*, 1051.

Wood, A.; Giersig, M.; Mulvaney, P. *J. Phys. Chem. B* **2001**, *105*, 8810.

Xu, H.; Zhang, R. Q.; Ng, A. M. C.; Djurišić, A. B.; Chan, H. T.; Chan, W. K.; Tong, S. Y. *J. Phys. Chem. C* **2011**, *115*, 19710.

Yahaya, A. H.; Gondal, M. A.; Hameed, A. *Chem. Phys. Lett.* **2004**, *400*, 206.

Yakelis, N. A.; Bergman, R. G. *Organometallics* **2005**, *24*, 3579.

Yan, S. G.; Lyon, L. A.; Lemon, B. I.; Preiskorn, J. S.; Hupp, J. T. *J. Chem. Educ.* **1997**, *74*, 657.

Ye, X.; Fei, J.; Diroll, B. T.; Paik, T.; Murray, C. B. *J. Am. Chem. Soc.* **2014**, *136*, 11680.

Yin, Y.; Alivisatos, A. P. *Nature* **2005**, *437*, 664.

Yu, J.; Yu, X. *Environmental Science & Technology* **2008**, *42*, 4902.

Zhao, Y.; Pan, H.; Lou, Y.; Qiu, X.; Zhu, J.; Burda, C. *J. Am. Chem. Soc.* **2009**, *131*, 4253.

VITA

Carolyn N. Valdez was born and raised in Littlerock, California. She earned her B.S. in Chemistry with a minor in English from California Institute of Technology (2010, *with Honors*), where she performed research in the laboratory of Professor Harry B. Gray. In 2010, Carolyn began graduate studies at the University of Washington working with Professor James M. Mayer. In 2014, she moved with Prof. Mayer to Yale University to complete her doctorate work. Carolyn worked as a short term CENTC postdoctoral research fellow with Prof Mayer at Yale University after the completion of her Ph.D. in 2015.